Міністерство освіти і науки України
Національний університет «Запорізька політехніка»

НОВІ МАТЕРІАЛИ І ТЕХНОЛОГІЇ В МЕТАЛУРГІЇ ТА МАШИНОБУДУВАННІ

НАУКОВИЙ ЖУРНАЛ

ВИХОДИТЬ ЧОТИРИ РАЗИ НА РІК

№ 2’2026

Заснований у грудні 1997 року

Засновник та видавець – Національний університет «Запорізька політехніка»

Запоріжжя
НУ «Запорізька політехніка»
2026

Ministry of Education and Science of Ukraine
National University Zaporizhzhia Polytechnic

NEW MATERIALS AND TECHNOLOGIES IN METALLURGY AND MECHANICAL ENGINEERING

THE SCIENTIFIC JOURNAL

PUBLISHED FOUR TIMES PER YEAR

No 2’2026

Founded in December 1997

Founder and publisher – National University Zaporizhzhia Polytechnic

Zaporizhzhia
NU Zaporizhzhia Polytechnic
2026

p-ISSN 1607-6885
e-ISSN 2786-7358

УДК 669+621.002+621.002.3

Наказом Міністерства освіти і науки України № 1471 від 26.11.2020 р. «Про затвердження рішень Атестаційної колегії Міністерства щодо діяльності спеціалізованих вчених рад від 26 листопада 2020 року» журнал «Нові матеріали і технології в металургії та машинобудуванні» **(скорочена назва – НМТ)** включений до переліку наукових фахових видань України в категрії «Б»**, в яких можуть публікуватися результати дисертаційних робіт на здобуття наукових ступенів доктора наук і доктора філософії (кандидата наук).**

Інтернет-сторінка журналу: https://nmt.zp.edu.ua

Наукове видання включено до міжнародних (INSPEC, CrossRef) і національних («Джерело», Національна бібліотека України імені В. І. Вернадського НАН України) реферативних та наукометричних баз даних.

Опублікованим статтям присвоюється унікальний ідентифікатор цифрового об'єкта DOI.

Науковий журнал друкує оригінальні та оглядові статті науковців ВНЗ і установ України та інших країн відповідно до рубрик:

- теорія будови та структурних змін у металах, сплавах та композитах. Вплив термічної, хіміко-термічної та термомеханічної обробки на характер структури і фізико-механічні властивості матеріалів;
- конструкційні та функціональні матеріали. Механічні властивості сталей, сплавів та композитів. Технологічне забезпечення надійності та довговічності деталей енергетичних установок. Методи механічного оброблення. Технології зміцнювальних обробок. Характеристики поверхневих шарів та захисних покриттів деталей машин і виробів;
- металургійне виробництво. Теплофізика та теплоенергетика. Ресурсозберігальні технології. Порошкова металургія. Промтранспорт. Раціональне використання металів;
- механізація, автоматизація та роботизація. Вдосконалення методів дослідження та контролю якості металів. Моделювання процесів у металургії та машинобудуванні.

РЕДАКЦІЙНИЙ ШТАТ

Рукописи надісланих статей проходять додаткове незалежне рецензування з залученням провідних фахівців України та інших країн, за результатами якого редакційна колегія ухвалює рішення щодо можливості їх опублікування. Рукописи не повертаються.

Рекомендовано до видання Вченою радою Національного університету «Запорізька політехніка»,
протокол № 10 від 28 квітня 2026 року.

Журнал набраний та зверстаний у редакційно-видавничому відділі Національного університету «Запорізька політехніка»

Комп'ютерний дизайн та верстання Наталія Савчук

Адреса редакції: 69011, Запоріжжя, вул. Університетська, 64, тел. (061) 769-82-96, редакційно-видавничий відділ

e-mail: rvv@zp.edu.ua

p-ISSN 1607-6885
e-ISSN 2786-7358

UDC 669+621.002+621.002.3

By order of the Ministry of Education and Science of Ukraine No. 1471 of November 26, 2020 "On approval of decisions of the Attestation Board of the Ministry regarding the activities of specialized scientific councils of November 26, 2020", the journal "New materials and technologies in metallurgy and mechanical engineering" (abbreviated name - NMT) is included in the list of scientific professional publications of Ukraine in the category "B", in which the results of dissertations for the scientific degrees of Doctor of Science and Doctor of Philosophy (candidate of science) can be published.

Internet page of the journal: https://nmt.zp.edu.ua
The scientific publication is included in international (INSPEC, CrossRef) and national (Dzherelo, National Library of Ukraine named after V. I. Vernadsky of the National Academy of Sciences of Ukraine) abstract and scientometric databases.
Published articles are assigned a unique DOI digital object identifier.
The scientific journal publishes original articles by scientists from universities and organizations of Ukraine and other countries in accordance with the headings:
- theory of structure and structural changes in metals, alloys and composites. Influence of thermal, chemical-thermal and thermomechanical treatment on the nature of the structure and physical and mechanical properties of materials;
- structural and functional materials. Mechanical properties of steels, alloys and composites. Technological support of reliability and durability of parts of power plants. Methods of mechanical processing. Hardening technologies. Characteristics of surface layers and protective coatings of machine parts and products;
- metallurgical production. Thermal physics and heat power engineering. Resource-saving technologies. Powder metallurgy. Promtransport. Rational use of metals;
- mechanization, automation and robotization. Improvement of methods for research and quality control of metals. Modeling of processes in metallurgy and mechanical engineering.

EDITORIAL TEAM

Manuscripts of submitted articles undergo additional independent review with the involvement of leading experts from Ukraine and other countries, based on which the editorial board decides on the possibility of their publication. Manuscripts are not returned.

Recommended for publication by the Academic Council of the National University Zaporizhzhia Polytechnic,
Protocol N 10 April 28, 2026.

The journal was typed and typeset in the editorial and publishing department of the National University Zaporizhzhia Polytechnic

Computer design and layout Nataliia Savchuk

Editorial address: 69011, Zaporizhzhia, st. University, 64, tel. (061) 769-82-96, editorial and publishing department e-mail: rvv@zp.edu.ua

ЗМІСТ

СТРУКТУРОУТВОРЕННЯ. ОПІР РУЙНУВАННЮ ТА ФІЗИКО-МЕХАНІЧНІ ВЛАСТИВОСТІ

КОНСТРУКЦІЙНІ І ФУНКЦІОНАЛЬНІ МАТЕРІАЛИ

ТЕХНОЛОГІЇ ОТРИМАННЯ ТА ОБРОБКИ КОНСТРУКЦІЙНИХ МАТЕРІАЛІВ

МОДЕЛЮВАННЯ ПРОЦЕСІВ В МЕТАЛУРГІЇ ТА МАШИНОБУДУВАННІ

CONTENTS

STRUCTURE FORMATION. RESISTANCE TO DESTRUCTION AND PHYSICAL-MECHANICAL PROPERTIES

STRUCTURAL AND FUNCTIONAL MATERIALS

TECHNOLOGIES OF OBTAINING AND PROCESSING OF CONSTRUCTION MATERIALS

MODELING OF PROCESSES IN METALLURGY AND MECHANICAL ENGINEERING

СТРУКТУРОУТВОРЕННЯ. ОПІР РУЙНУВАННЮ ТА ФІЗИКО-МЕХАНІЧНІ ВЛАСТИВОСТІ

STRUCTURE FORMATION. RESISTANCE TO DESTRUCTION AND PHYSICAL-MECHANICAL PROPERTIES

UDC 669.721.5

INFLUENCE OF CHEMICAL COMPOSITION ON MECHANICAL PROPERTIES OF BIORESORBABLE MAGNESIUM ALLOY OF Mg-Nd-Zr SYSTEM FOR OSTEOSYNTHESIS

Viktor Greshta — Candidate of Technical Science, Professor, Rector of the National University Zaporizhzhia Polytechnic, Zaporizhzhia, Ukraine, *e-mail: greshtaviktor@gmail.com,* ORCID: 0000-0002-4589-6811

Purpose. *Determination of the optimal chemical composition of a bioresorbable Mg-Nd-Zr magnesium alloy capable of providing a favourable balance of strength and ductility for osteosynthesis applications.*

Research methods*. The study employed a Box-Behnken experimental design. Specimens were prepared by induction melting followed by heat treatment. Tensile properties were measured in accordance with ISO 6892-1, and the results were processed statistically using the STATISTICA software package.*

Results*. Neodymium was identified as the main contributor to the tensile strength of the Mg-Nd-Zr alloy, with an optimal content of about 3.6 %. Zirconium improved ductility, most likely through the formation of a fine-grained structure, with an optimal content of about 1.8 %. A negative interaction between neodymium and zirconium was observed when content of both elements were increased simultaneously, and this effect should be considered when optimising the alloy composition. Within the zinc range studied (up to 0.8 %), zinc had no statistically significant effect on the mechanical properties. The resulting regression model predicts the mechanical properties of the alloy from the alloying-element content with good accuracy. Overall, the findings provide a basis for optimising the composition of bioresorbable magnesium alloys to achieve a favourable balance of strength and ductility for osteosynthesis.*

Scientific novelty*. The combined effect of Nd, Zr and Zn on the mechanical properties of a bioresorbable Mg-Nd-Zr alloy for osteosynthesis was established. Neodymium was identified as the principal strength-controlling element, whereas zirconium contributes to improved ductility and can also enhance strength. A negative Nd-Zr interaction at elevated concentrations was also revealed, with a substantial effect on the mechanical characteristics of the alloy.*

Practical value*. The regression model makes it possible to predict the mechanical properties of the alloy from the alloying-element content, thereby simplifying the selection of compositions for specific medical applications.*

Key words: *bioresorbable magnesium alloy, osteosynthesis, mechanical properties, chemical composition, neodymium, zirconium, Box-Behnken design, regression model, composition optimization, implants.*

Introduction

The full-scale war in Ukraine has sharply increased the demand for implants and osteosynthesis devices. Preliminary estimates suggest an increase of more than 800 %. This growth is associated with the sharp rise in traumatic injuries involving severe bone damage among both service personnel and civilians. According to the Ministry of Defence of Ukraine, about 40 % of wounded personnel sustain injuries to the extremities, many of which require complex surgery for bone reconstruction.

In the treatment of service personnel with traumatic bone injuries, temporary fixation of fractured bone fragments is often required. Standard clinical practice involves temporary fixation devices made of titanium alloys or special steels. The main drawback of this approach is the need for a second operation to remove the hardware.

A possible alternative is the use of materials that are gradually resorbed by the body, progressively lose their load-bearing capacity, and eventually dissolve completely. Magnesium-based alloys are among the most promising candidates. In particular, an alloy based on the ML10 grade has been developed for use in traumatology, orthopaedics and cardiac surgery, where it functions as a bioresorbable material that slowly dissolves in the surrounding tissue after fulfilling its medical role.

The main challenges associated with this concept are relatively low mechanical properties of magnesium alloys and need to control their dissolution rate in the body. Research aimed at improving these characteristics therefore remains highly relevant.

DOI 10.15588/1607-6885-2026-2-1

Literature review

Because of their biocompatibility and their ability to dissolve gradually in the body, magnesium alloys are widely regarded as promising candidates for temporary osteosynthesis implants [1]. Their comparatively low strength and ductility, however, remain an important limitation. These factors substantially restrict their use in load-bearing components of endoprosthetic systems.

Nevertheless, magnesium, whether used as a pure metal or in alloyed form, is receiving increasing attention in healthcare and biomedical research [2]. Over recent years, the number of publications devoted to magnesium as a temporary implant material has grown steadily owing to its bioresorbable nature. Magnesium degrades readily and does not leave long-term residues in the body [3, 4]. As a bioresorbable material, it gradually breaks down in the biological environment and can support tissue regeneration and the recovery of physiological function. In many medical applications, implants are required only temporarily to support healing. If conventional implants are not removed in time, adverse reactions may occur, including chronic irritation, inflammatory response and, in some cases, biotoxicity.

A considerable literature resources are available on the properties of magnesium alloys and the factors that influence them. Most studies, however, focus on Mg-Ca or Mg-Zn-Ca alloys, whereas Mg-Re systems, including neodymium-alloyed Mg-Nd-Zr [5, 6], have received less attention, particularly with the influence of chemical composition on mechanical properties.

Studies [7, 8] discuss the chemical composition, properties and applications of bioresorbable magnesium alloys and emphasise that a sound understanding of composition is essential for improving biocompatibility and bioresorbability. These studies analyse both chemical composition and corrosion behaviour, with particular attention to how individual alloying elements affect composition and corrosion resistance. In these and in similar studies [9, 10], however, the emphasis is placed on corrosion behaviour and biocompatibility rather than on mechanical properties. The authors of [11] review bioresorbable magnesium alloys as candidate materials for osteosynthesis and show that Ca, Zn, Mn, Sr and Zr are widely used as alloying additions to magnesium because of their non-toxicity. Elements such as Al, Ni, Ag, Cu and the rare earths (Nd, La, Ce) may also be used to improve the corrosion resistance and mechanical properties of magnesium alloys [12]. Lu et al. [13] examines alloying strategies for magnesium alloys intended for orthopaedic use. Zirconium is an efficient grain refiner and improves both strength and ductility. Zinc strengthens the alloy but can reduce ductility at high concentrations. Neodymium provides a pronounced increase in strength together with a favourable balance of strength and ductility. Calcium and strontium promote bioactivity and osteointegration. Compositions such as Mg-Nd-Zn-Zr show promising performance by combining high strength, adequate ductility and a controlled corrosion rate. Chen et al. [14] summarises the effects of critical alloying elements on the structure, mechanical properties and bioresorbable behaviour of magnesium alloys, with a focus on the Mg-Ca, Mg-Zn, Mg-Sr, Mg-Re and Mg-Cu systems. Zinc strengthens the alloy through solid-solution and precipitation hardening, calcium improves biocompatibility, strontium promotes osteogenesis, and rare-earth elements enhance corrosion resistance. Importantly, the content of alloying elements must be carefully controlled in order to maintain a workable balance between mechanical properties, biodegradation rate and biocompatibility.

Taken together, the available literature shows that, despite substantial research on magnesium alloys for medical applications, the selection of an optimal Mg-Nd-Zr composition with specific regard to mechanical properties remains insufficiently studied. Given the strong and complex influence of alloying elements on both strength and ductility, identifying their optimal content remains an important task in the development of bioresorbable materials for osteosynthesis.

Objective

This study is aimed to determine the optimal chemical composition of a bioresorbable Mg-Nd-Zr magnesium alloy that would provide a favourable balance of strength and ductility for osteosynthesis applications. To achieve this aim, an experimental design was developed, ingots of different chemical compositions were produced, the specimens were tested in tension, and the resulting data were analysed statistically.

The study examined how the mechanical properties of an Mg-Nd-Zr alloy – which contains no toxic alloying elements and is therefore a potential candidate for implant applications – depend on the concentration of its alloying elements. The property variables were ultimate tensile strength and elongation to failure under uniaxial tension.

Materials and methods

Ingots of the magnesium alloy were produced by melting in an IPM-500 induction furnace with a capacity of 0.5 t, a power rating of 140 kW and a throughput of 230 kg/h. A gas-fired holding furnace with a capacity of 150 kg was also used. Pre-heated charge materials were loaded into the induction furnace; after melting, the liquid alloy was transferred into removable crucibles at 650–730 °C. The crucibles were then placed in holding furnaces, where the alloy composition was refined with a flux consisting of 38–46 % $MgCl_2$, 32–40 % KCl, 5–8 % $BaCl_2$ and 3–5 % CaF_2 at 740–760 °C.

The cast blanks were heat-treated in a pit-type electric resistance furnace (112 kW, 95 kg/h capacity) and in a PAP-4M furnace (50 kg/h capacity). The heat-treatment regime consisted of solution treatment at 540 ± 5 °C for 15 h followed by air cooling, and ageing at 200 ± 5 °C for 8 h followed by final air cooling.

Tensile testing was performed on a modernised R10 testing machine (Fig. 1) in accordance with ISO 6892-1, using cylindrical specimens with a gauge-section diameter of 4 mm.

The extensometer gauge length was 25 mm. During testing, elongation of the gauge section was measured with

DOI 10.15588/1607-6885-2026-2-1

an accuracy of ±1 μm. Stress in the gauge section was applied by loading the movable crosshead with a force measured by a dynamometer. The measurement accuracy for stress in the gauge section was 3 MPa. The extensometer and elastic dynamometer signals were digitised at 0.01 s intervals. All tests were performed on series of identical specimens. Statistical analysis was conducted at a significance level of 0.05.

a *b* *c*

Figure 1. Specimens for tensile testing (*a*); general view (*b*) and working area (*c*) of the modernised R10 tensile testing machine equipped with a dynamometer

Statistical analysis and mathematical modelling were performed in STATISTICA (StatSoft) using the experimental data obtained from the designed experiments. The workflow combined correlation, analysis of variance and regression methods. Correlation analysis was first used to identify mutually independent factors for further study. ANOVA and Pareto charts were then used to identify the factors with the strongest influence on the response variables properties. Multiple regression analysis was subsequently used to determine the regression coefficients and construct the mathematical models. Model adequacy was assessed by comparing the adequacy variance with the reproducibility variance using Fisher's F-test. Because the number of experimental runs exceeded the number of regression coefficients to be estimated, the design was under-saturated. The reproducibility variance was determined from triplicate experiments at the centre point of the design, and its homogeneity was evaluated using Cochran's criterion.

The reproducibility variance was calculated from:

$$S_y^2 = \frac{\sum_{i=1}^{N}\sum_{j=1}^{n}\left(F_{i,j}^{\exp} - \overline{F_i^{\exp}}\right)^2}{N(n-1)}, \qquad (1)$$

where N is the number of replicate experiments and n is the number of repetitions per experiment.

Assuming uniform replication of experiments, the adequacy variance of the model was calculated from:

$$S_{ad}^2 = \frac{\sum_{i=1}^{N}\sum_{j=1}^{n}\left(T^{calc} - \overline{T^{\exp}}\right)^2}{f_{ad}}, \qquad (2)$$

where n is the number of replicate experiments in each series, T^{calc} is the predicted value of the response parameter, $\overline{T^{\exp}}$ is the mean experimental value from the replicates, and f is the number of degrees of freedom.

The homogeneity of the reproducibility variance was evaluated using Fisher's F-test:

$$F^{\exp} = \frac{S_{ad}^2}{S_y^2}. \qquad (3)$$

Results

To establish how the principal alloying elements influence strength and ductility, the upper concentration limit for each element was selected on the basis of its solubility in magnesium. The upper limits were thus 1.8 % for zirconium, 3.6 % for neodymium and 0.8 % for zinc.

The Box-Behnken design was selected for experimental planning. Compared with a full factorial design, it offers several advantages. It requires substantially fewer experimental points, especially when the number of factors is large, thereby reducing both material consumption and experimental cost. Unlike a first-order full factorial design, it also allows quadratic effects and factor interactions to be estimated, providing a more accurate approximation of the response surface within the region of interest. Because the design is spherically symmetric, the experimental points are distributed uniformly around the centre, which ensures uniform prediction variance throughout the factor space. This arrangement also makes the design more resistant to random disturbances and measurement error than a full factorial design.

The tensile-test results obtained for Mg-Nd-Zr alloy specimens of different chemical composition (Table 1) were used to construct the Box-Behnken experimental matrix with three factors at three levels (Table 2).

Table 1 – Levels of variation of the chemical composition of the experimental specimens

Level	Zr	Nd	Zn
-1	0,2	2,0	0,1
0	1,0	2,8	0,45
+1	1,8	3,6	0,8

Owing to the efficiency of the chosen experimental design, 15 experimental melts were sufficient for analysis of variance (Fig. 2) and for constructing a statistically significant second-order regression model with linear two-factor interaction terms (Tables 3 and 4).

Table 2 – Box-Behnken experimental design matrix (2^3)

Run No.	X_1 (Zr)	X_2 (Nd)	X_3 (Zn)	$\sigma_в$, МПа	δ, %
1	0,20	2,00	0,45	249,3	3,42
2	1,80	2,00	0,45	252,2	5,37
3	0,20	3,60	0,45	290,1	3,32
4	1,80	3,60	0,45	268,6	4,48
5	0,20	2,80	0,10	268,9	3,37
6	1,80	2,80	0,10	259,3	4,92
7	0,20	2,80	0,80	270,4	3,37
8	1,80	2,80	0,80	260,8	4,92
9	1,00	2,00	0,10	249,8	4,39
10	1,00	3,60	0,10	278,8	3,90
11	1,00	2,00	0,80	251,8	4,39
12	1,00	3,60	0,80	280,0	3,90
13	1,00	2,80	0,45	262,5	4,14
14	1,00	2,80	0,45	264,9	4,60
15	1,00	2,80	0,45	266,1	4,00

DOI 10.15588/1607-6885-2026-2-1

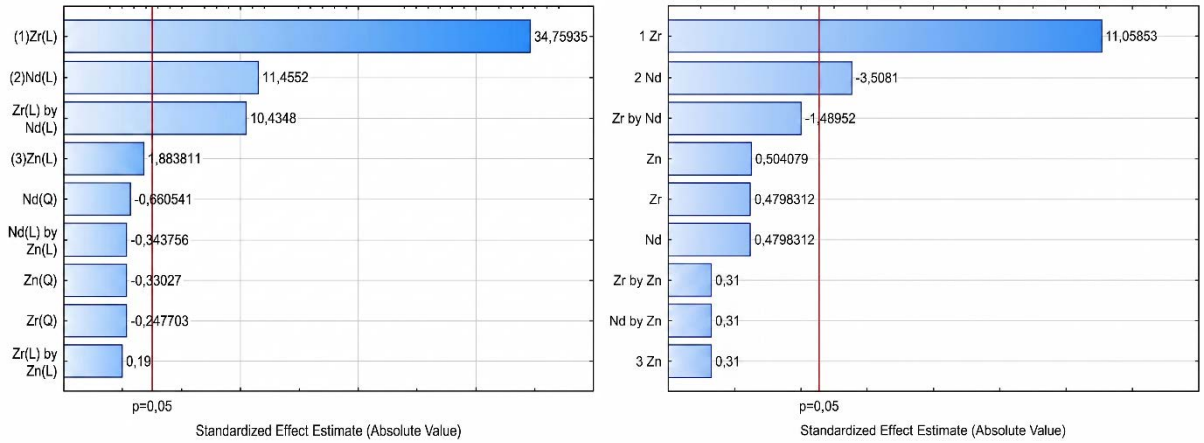

a *b*

Figure 2. Pareto charts showing the effect of the alloying elements on the tensile strength (*a*) and ductility (*b*) of the alloy

Table 3 – Parameters of the regression model for the effect of the alloying elements on tensile strength, including two-factor interaction terms

Factor	Regression coefficient	Standard error	t(5)	p	−95 % CI	+95 % CI
Constant	265.000	0.335907	788.9095	0.000000	264.1365	265.8635
Zr (linear)	−9.4500	0.822800	−11.4852	0.000088	−11.5651	−7.3349
Zr (quadratic)	−0.1500	0.605564	−0.2477	0.814215	−1.7067	1.4067
Nd (linear)	28.6000	0.822800	34.7594	0.000000	26.4849	30.7151
Nd (quadratic)	−0.4000	0.605564	−0.6605	0.538120	−1.9567	1.1567
Zn (linear)	1.5500	0.822800	1.8838	0.118296	−0.5651	3.6651
Zn (quadratic)	−0.2000	0.605564	−0.3303	0.754585	−1.7567	1.3567
Zr·Nd	−12.2000	1.163615	−10.4846	0.000136	−15.1912	−9.2088
Zr·Zn	0.0000	1.163615	0.0000	1.000000	−2.9912	2.9912
Nd·Zn	−0.4000	1.163615	−0.3438	0.745014	−3.3912	2.5912

Notes. Statistically significant values are shown in bold. t(5) is the value of the t-statistic with 5 degrees of freedom, used for hypothesis testing and for assessing statistical significance; p is the probability of observing the given effect under the null hypothesis that the effect is absent. Lower p-values indicate stronger evidence against the null hypothesis.

Table 4 – Parameters of the regression model for the effect of the alloying elements on elongation to failure, including two-factor interaction terms

Factor	Regression coefficient	Standard error	t(5)	p	−95 % CI	+95 % CI
Constant	4.145833	0.057314	72.33581	0.000000	3.998504	4.293163
Zr (linear)	1.552500	0.140389	11.05853	0.000105	1.191618	1.913382
Zr (quadratic)	0.049583	0.103324	0.47988	0.651567	−0.216019	0.315186
Nd (linear)	−0.492500	0.140389	−3.50810	0.017135	−0.853382	−0.131618
Nd (quadratic)	0.049583	0.103324	0.47988	0.651567	−0.216019	0.315186
Zn (linear)	0.000000	0.140389	0.00000	1.000000	−0.360882	0.360882
Zn (quadratic)	0.052083	0.103324	0.50408	0.635627	−0.213519	0.317686
Zr·Nd	−0.395000	0.198541	−1.98952	0.103314	−0.905365	0.115365
Zr·Zn	0.000000	0.198541	0.00000	1.000000	−0.510365	0.510365
Nd·Zn	0.000000	0.198541	0.00000	1.000000	−0.510365	0.510365

DOI 10.15588/1607-6885-2026-2-1

Discussion

Analysis of the contribution of each factor to alloy strength (Fig. 2a) shows that neodymium exerts the strongest positive effect. By contrast, zirconium and Nd·Zr interaction both have a statistically significant negative effect on tensile strength.

The alloying elements affect ductility differently. Increasing the zirconium content improves ductility, whereas increasing the neodymium content reduces it (Fig. 2*b*). The positive effect of zirconium is more than three times larger than the negative effect of neodymium. The Zr·Nd interaction leads to an additional reduction in ductility. As in the case of tensile strength, zinc does not have a statistically significant effect on elongation to failure.

Overall, the results indicate that the strength of Mg-Nd-Zr alloys is governed primarily by neodymium content and by the nature of its interaction with zirconium. Increasing the neodymium content raises tensile strength, whereas an excessive simultaneous increase both Nd and Zr can reduce it because of the negative two-factor interaction. Within the concentration range studied, zinc does not have a statistically significant effect.

According to the regression model, the linear effect of zirconium on tensile strength is negative. This effect, however, cannot be interpreted in isolation, because zirconium also has a strong influence on ductility and participates in a two-factor interaction with neodymium. The low p-value supports the reliability of this estimate. The optimum zirconium content is therefore likely to lie in the upper part of the studied range (about 1.8 %). Tensile strength also increases with neodymium content, as indicated by the statistically significant positive regression coefficient and the low p-value. Its optimum is likewise expected to lie near the upper part of the studied range (about 3.6 %). The regression coefficients for zinc are not statistically significant, indicating that no detectable effect of this element on strength was observed.

The near-linear relation between the model-predicted and experimentally measured values of strength and elongation to failure (Fig. 3) indicates that the estimates are reliable and confirms the adequacy of the model.

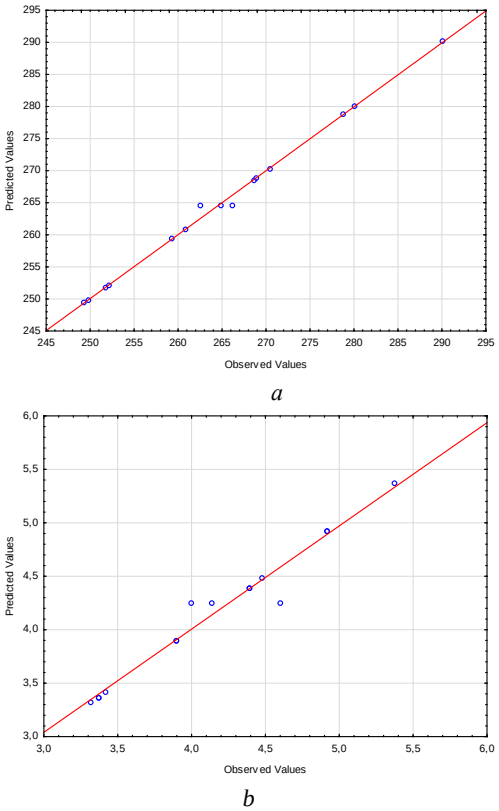

Figure 3. Model-predicted versus experimentally measured values of tensile strength (*a*) and elongation to failure (*b*) of the alloy

Analysis of the dependence of strength (Fig. 4) and ductility (Fig. 5) alloying-element content shows that increasing the neodymium content generally increases tensile strength while reducing ductility.

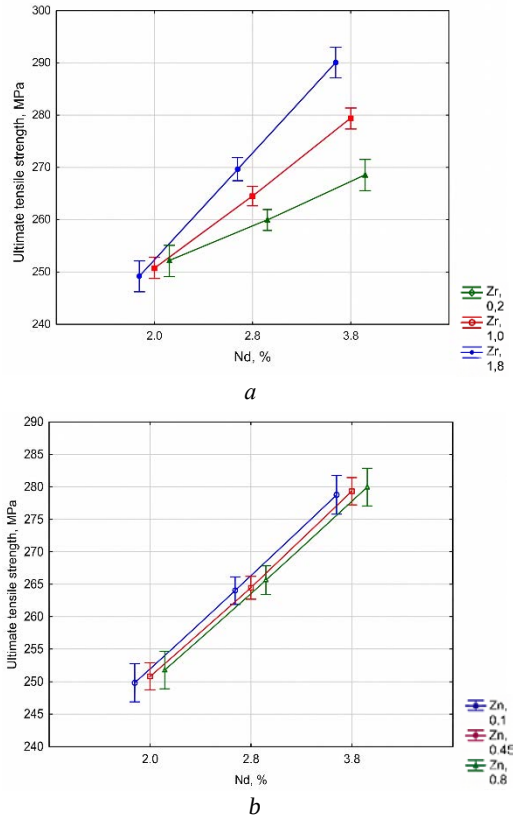

Figure 4. Tensile strength of the alloy as a function of neodymium content at 0.45 % Zn (*a*) and at 1 % Zr (*b*)

The increase in tensile strength most likely reflects two contributions from neodymium: solid-solution strengthening and the formation of strengthening

DOI 10.15588/1607-6885-2026-2-1

intermetallic phases. The solubility of zirconium in magnesium is low; nonetheless, zirconium restricts grain growth and thus promotes the formation of a fine-grained structure. As a result, zirconium can enhance strength and ductility simultaneously, which is particularly important because improvement of one of these properties is often accompanied by deterioration of the other.

Figure 4a shows that higher neodymium content is associated with increased tensile strength. At the same time, a simultaneous increase in neodymium and zirconium reduces strength, most likely because of excessive precipitation of secondary phases.

In the presence of zinc, zirconium may also influence the formation and distribution of secondary phases and thus affect the mechanical properties of the alloy. According to [15], zirconium has a beneficial effect on magnesium-alloy properties when its content remains below about 2 %. Although zinc may also contribute to an increase in strength, no such effect was observed within the zinc concentration range examined in present study.

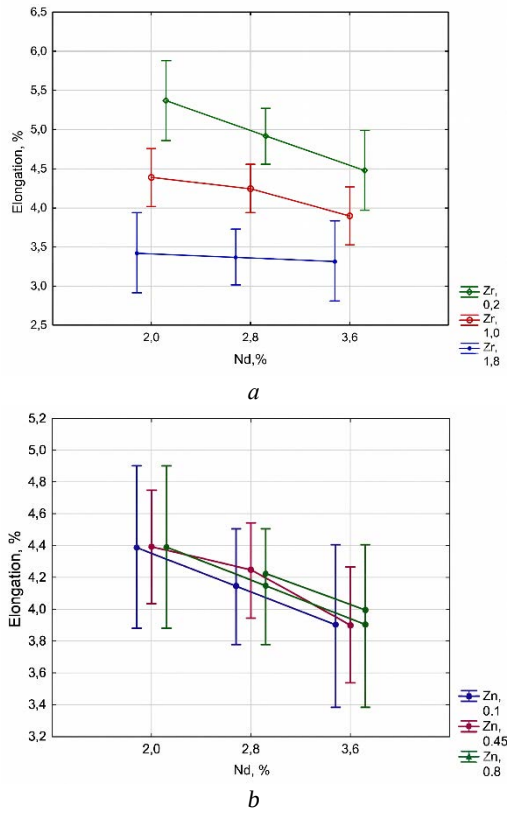

Figure 5. Elongation to failure of the alloy as a function of neodymium content at 0.45 % Zn (*a*) and at 1 % Zr (*b*)

Consistent with the obtained results, Fig. 5a shows that ductility increases with increasing zirconium content, most likely because grain growth is restrained and a fine-grained structure forms. Changes in zinc concentration had almost no effect on alloy ductility.

Conclusions

Neodymium was found to be the key element controlling the tensile strength of Mg-Nd-Zr magnesium alloys, with the optimal content lying close to the upper limit of the studied range (3.6 %).

Increasing the zirconium content improved alloy ductility, most likely through its role in promoting a fine-grained structure. The optimal zirconium content likewise lies close to the upper limit of the range studied (1.8 %).

A negative interaction between neodymium and zirconium was observed at simultaneously elevated concentrations of both elements. This effect should be taken into account when optimising the alloy composition.

Within zinc concentration range (up to 0.8 %), zinc had no statistically significant effect on the mechanical properties of the alloy. Taking into consideration the possible positive effect of zinc on the corrosion resistance of magnesium alloys, however, its addition may still be useful and requires further investigation. At the same time, zinc additions may increase Young's modulus [16].

The regression model developed predicts the mechanical properties of the alloy from its alloying-element content with good accuracy. These results provide a basis for optimising the chemical composition of the bioresorbable magnesium alloy to achieve a favourable balance of strength and ductility for osteosynthesis applications.

Further research should focus on how chemical composition influences the biodegradation rate and biocompatibility of the alloy in order to support its further optimisation for medical applications.

References

1. Zhang, T., Wang, W., Liu, J., Wang, L., Tang, Y., & Wang, K. (2022). A review on magnesium alloys for biomedical applications. Frontiers in Bioengineering and Biotechnology, 10, 953344. https://doi.org/10.3389/fbioe.2022.953344

2. Moosbrugger, C., & Marquard, L. (2017). Engineering Properties of Magnesium Alloys. ASM International.

3. Chakraborty Banerjee, P., Al-Saadi, S., Choudhary, L., Harandi, S. E., & Singh, R. (2019). Magnesium implants: prospects and challenges. Materials, 12(1), 136. https://doi.org/10.3390/ma12010136

4. Chen, J., Tan, L., Yu, X., Etim, I. P., Ibrahim, M., & Yang, K. (2018). Mechanical properties of magnesium alloys for medical application: a review. Journal of the Mechanical Behavior of Biomedical Materials, 87, 68–79. https://doi.org/10.1016/j.jmbbm.2018.07.020

5. Shalomeev, V., Aikin, N., Chorniy, V., & Naumik, V. (2019). Design and examination of the new biosoluble casting alloy of the system Mg-Nd-Zr for osteosynthesis. Eastern-European Journal of Enterprise Technologies, 1(12 (97)), 40–48.

DOI 10.15588/1607-6885-2026-2-1

6. Shalomeiev, V. A., Tsyvirko, E. I., & Aikin, M. D. (2016). Magnesium alloys with an enhanced level of properties for medical implants. Metaloznavstvo ta Obrobka Metaliv, (2), 3–10. [in Ukrainian]

7. Rao, S. S. S., Mohan, A., Suryanarayana, C., & Prabhu, T. R. (2020). Biodegradable magnesium alloys: a review of their chemical composition, properties and applications. Materials, 13(8), 1934. https://doi.org/10.3390/ma13081934

8. Zhang, Y., Xu, J., Ruan, Y. C., Yu, M. K., O'Laughlin, M., Wise, H., & You, L. (2019). Chemical composition and corrosion behavior of biodegradable magnesium alloys. Journal of Alloys and Compounds, 785, 1086–1096. https://doi.org/10.1016/j.jallcom.2019.02.034

9. Li, J., Tan, L., Wan, P., Yu, X., & Yang, K. (2018). Biodegradable magnesium alloys with improved chemical composition for orthopedic applications. Biomaterials, 164, 34–45. https://doi.org/10.1016/j.biomaterials.2018.02.024

10. Wang, J., Witte, F., Xi, T., Zheng, Y., Yang, K., Yang, Y., & Li, Y. (2020). Influence of chemical composition on the biodegradability of magnesium alloys. Acta Biomaterialia, 105, 1–15. https://doi.org/10.1016/j.actbio.2020.02.036

11. Kumar, R., Promila, Kumar, A., Silla, S., & Sarova, A. (2017). Biocompatibility and degradation study of magnesium alloys: a review. Journal of Emerging Technologies and Innovative Research (JETIR), 4(6), 526–536.

12. Hassan, S. F., Islam, M. T., Saheb, N., & Baig, M. M. A. (2022). Magnesium for implants: a review on the effect of alloying elements on biocompatibility and properties. Materials, 15(16), 5669. https://doi.org/10.3390/ma15165669

13. Lu, Y., Deshmukh, S., Jones, I., & Chiu, Y. (2021). Biodegradable magnesium alloys for orthopaedic applications. Biomaterials Translational, 2(3), 214–235. https://doi.org/10.12336/biomatertransl.2021.03.005

14. Chen, Y., Dou, J., Yu, H., & Chen, C. (2019). Degradable magnesium-based alloys for biomedical applications: the role of critical alloying elements. Journal of Biomaterials Applications, 0(0), 1–25. https://doi.org/10.1177/0885328219834656

15. Amukarimi, S., & Mozafari, M. (2021). Biodegradable magnesium-based biomaterials: an overview of challenges and opportunities. MedComm, 2(2), 123–144. https://doi.org/10.1002/mco2.59

16. Chen, J., Xu, Y., Kolawole, S. K., Wang, J., Su, X., Tan, L., & Yang, K. (2022). Systems, properties, surface modification and applications of biodegradable magnesium-based alloys: a review. Materials, 15(14), 5031. https://doi.org/10.3390/ma15145031

Received 15.04.2026
Accepted 23.04.2026
Published 07.05.2026

УДК 669.721.5

ВПЛИВ ХІМІЧНОГО СКЛАДУ БІОРОЗЧИННОГО МАГНІЄВОГО СПЛАВУ СИСТЕМИ Mg-Nd-Zr ДЛЯ ОСТЕОСИНТЕЗУ НА МЕХАНІЧНІ ВЛАСТИВОСТІ

Віктор Грешта	канд. техн. наук, професор, ректор Національного університету «Запорізька політехніка», м. Запоріжжя, Україна, *e-mail: greshtaviktor@gmail.com*, ORCID: 0000-0002-4589-6811

Мета роботи. *Визначення раціонального хімічного складу біорозчинного магнієвого сплаву системи Mg-Nd-Zr, при якому забезпечується оптимальне поєднання міцності та пластичності, для застосування в остеосинтезі.*

Методи дослідження. *Застосовано комплекс методів, що включав планування експерименту за методом Бокса-Бенкена, виготовлення зразків шляхом виплавки та термічної обробки магнієвих сплавів, механічні випробування на розтяг згідно з ISO 6892-1, а також статистичну обробку отриманих даних за допомогою програмного забезпечення STATSOFT.*

Отримані результати. *Встановлено ключову роль неодиму у підвищенні границі міцності магнієвого сплаву системи Mg-Nd-Zr, з оптимальним вмістом близько 3,6 %. Виявлено позитивний вплив цирконію на пластичність сплаву, імовірно через формування дрібнозернистої структури, з оптимальним вмістом близько 1,8 %. Виявлено негативний ефект взаємодії між неодимом та цирконієм при їх одночасному підвищенні концентрації, що потребує врахування при оптимізації складу сплаву. Встановлено, що вплив цинку в досліджуваному діапазоні концентрацій (до 0,8 %) на механічні властивості сплаву є статистично незначущим. На основі отриманих даних розроблено регресійну модель, яка дозволяє з високою точністю прогнозувати*

DOI 10.15588/1607-6885-2026-2-1

механічні властивості сплаву залежно від вмісту легуючих елементів. Ці результати створюють основу для оптимізації хімічного складу біорозчинного магнієвого сплаву з метою досягнення оптимального балансу міцності та пластичності для застосування в остеосинтезі.

Наукова новизна. *Встановлено комплексний вплив легувальних елементів (Nd, Zr, Zn) на механічні властивості біорозчинного магнієвого сплаву системи Mg-Nd-Zr для остеосинтезу. Виявлено, що неодим є ключовим елементом, який підвищує границю міцності сплаву, тоді як цирконій сприяє одночасному зростанню міцності та пластичності. Виявлено негативний ефект взаємодії між Nd та Zr при їх високих концентраціях, що суттєво впливає на механічні характеристики сплаву.*

Практична цінність. *Розроблена регресійна модель дозволяє прогнозувати механічні властивості сплаву залежно від вмісту легуючих елементів, що значно спрощує процес підбору оптимального складу для конкретних медичних застосувань.*

Ключові слова: *біорозчинний магнієвий сплав, остеосинтез, механічні властивості, хімічний склад, неодим, цирконій, план Бокса-Бенкена, регресійна модель, оптимізація складу, імплантати.*

Список літератури

1. A review on magnesium alloys for biomedical applications / Zhang T. et al. *Frontiers in Bioengineering and Biotechnology*. 2022. Vol. 10. P. 953344. DOI: https://doi.org/10.3389/fbioe.2022.953344

2. Moosbrugger C., Marquard L. *Engineering properties of magnesium alloys*. Materials Park (OH): ASM International, 2017. 184 p.

3. Magnesium implants: prospects and challenges / . Chakraborty Banerjee P. et al. *Materials*. 2019. Vol. 12, No. 1. P. 136. DOI: https://doi.org/10.3390/ma12010136

4. Mechanical properties of magnesium alloys for medical application: a review / Chen J. et al. *Journal of the Mechanical Behavior of Biomedical Materials*. 2018. Vol. 87. P. 68–79. DOI: https://doi.org/10.1016/j.jmbbm.2018.07.020

5. Shalomeev V., Aikin N., Chorniy V., Naumik V. Design and examination of the new biosoluble casting alloy of the system Mg-Nd-Zr for osteosynthesis. *Eastern-European Journal of Enterprise Technologies*. 2019. Vol. 1, No. 12 (97). P. 40–48.

6. Шаломєєв В. А., Цивірко Е. І., Айкін М. Д. Магнієві сплави з підвищеним рівнем властивостей для імплантатів в медицині. *Металознавство та обробка металів*. 2016. No. 2. С. 3–10.

7. Biodegradable magnesium alloys: a review of their chemical composition, properties, and applications / Rao S. S. S. et al. *Materials*. 2020. Vol. 13, No. 8. P. 1934. DOI: 10.3390/ma13081934.

8. Chemical composition and corrosion behavior of biodegradable magnesium alloys / Zhang Y. et al. *Journal of Alloys and Compounds*. 2019. Vol. 785. P. 1086–1096. DOI: https://doi.org/10.1016/j.jallcom.2019.02.034

9. Biodegradable magnesium alloys with improved chemical composition for orthopedic applications / Li J. et al. *Biomaterials*. 2018. Vol. 164. P. 34–45. DOI: https://doi.org/10.1016/j.biomaterials.2018.02.024

10. Influence of chemical composition on the biodegradability of magnesium alloys / Wang J. et al. *Acta Biomaterialia*. 2020. Vol. 105. P. 1–15. DOI: https://doi.org/10.1016/j.actbio.2020.02.036

11. Biocompatibility and degradation study of magnesium alloys: a review / Kumar R. et al. *Journal of Emerging Technologies and Innovative Research*. 2017. Vol. 4, No. 6. P. 526–536.

12. Hassan S. F., Islam M. T., Saheb N., Baig M. M. A. Magnesium for implants: a review on the effect of alloying elements on biocompatibility and properties. *Materials*. 2022. Vol. 15, No. 16. P. 5669. DOI: https://doi.org/10.3390/ma15165669

13. Lu Y., Deshmukh S., Jones I., Chiu Y. Biodegradable magnesium alloys for orthopaedic applications. *Biomaterials Translational*. 2021. Vol. 2, No. 3. P. 214–235. DOI: https://doi.org/10.12336/biomatertransl.2021.03.005

14. Chen Y., Dou J., Yu H., Chen C. Degradable magnesium-based alloys for biomedical applications: the role of critical alloying elements. *Journal of Biomaterials Applications*. 2019. Vol. 34, No. 0. P. 1–25. DOI: https://doi.org/10.1177/0885328219834656

15. Amukarimi S., Mozafari M. Biodegradable magnesium-based biomaterials: an overview of challenges and opportunities. *MedComm*. 2021. Vol. 2. P. 123–144. DOI: https://doi.org/10.1002/mco2.59

16. Systems, properties, surface modification and applications of biodegradable magnesium-based alloys: a review / Chen J. et al. *Materials*. 2022. Vol. 15, No. 14. P. 5031. DOI: https://doi.org/10.3390/ma15145031

DOI 10.15588/1607-6885-2026-2-1

p-ISSN 1607-6885 New materials and technologies in metallurgy and mechanical engineering. 2026/2
e-ISSN 2786-7358 New materials and technologies in metallurgy and mechanical engineering. 2026/2

UDC 669.721.5:621.785.7

Mykyta Aikin	Senior lecturer of Physical Materials Science Department, National University Zaporizhzhia Polytechnic, Zaporizhzhia, Ukraine, *e-mail: fitone14@gmail.com*, ORCID: 0000-0001-9513-2804
Vadym Shalomeev	Doctor of Technical Sciences, Professor, National University Zaporizhzhia Polytechnic, Zaporizhzhia, Ukraine, *e-mail: shalomeev@zntu.edu.ua*, ORCID: 0000-0002-6091-837X
Yevhen Vyshenko	Student of group IF-213sp, National University Zaporizhzhia Polytechnic, Zaporizhzhia, Ukraine

MICROSTRUCTURE, MECHANICAL PROPERTIES, AND CONTROLLED DEGRADATION OF A BIORESORBABLE MG-3.15ND-1.25ZR-0.6ZN ALLOY FOR OSTEOSYNTHESIS IMPLANTS: INDUSTRIAL PROCESSING AND BENCHMARKING AGAINST ML10 ALLOY

Purpose. *To evaluate the microstructure, mechanical properties, and degradation behaviour of a bioresorbable Mg-3.15Nd-1.25Zr-0.6Zn (wt.%) alloy produced via an industrially compatible route, and to demonstrate its superiority over the reference alloy ML10 for osteosynthesis applications with degradation synchronized to bone healing.*

Research methods. *Microstructure was examined by optical microscopy (Neophot 32, OLYMPUS IX 70) and SEM/EDS (SELMI REM-106I). Grain size was measured by the intercept method (ISO 643:2024). Mechanical properties were determined on an INSTRON 2801 machine (ASTM B557, ISO 6892-1) in the heat-treated condition and after 90-day immersion in Gelofusine (pH 7.4), Venofundin (pH 5.5), and physiological saline at 36 ± 1 °C. Corrosion rates were obtained by gravimetric mass loss. Heat treatment was performed under argon in Bellevue and PAP-4M furnaces. Industrial trials were conducted on malleolar screws of three sizes at JSC "Motor Sich".*

Results. *After casting into a water-cooled copper mould (25–30 °C/s) and two-stage heat treatment (560 °C/8 h + 200 °C/16 h), the alloy exhibited a grain size of 57 ± 4.7 μm (50% finer than ML10), with clean boundaries containing dispersed Zn_2Zr_3 and β″ precipitates instead of continuous $(Mg,Zn)_{12}Nd$ networks. Ultimate tensile strength reached 309 ± 6.5 MPa, yield strength 252 ± 6.5 MPa, and elongation 7.9 ± 0.65% – improvements of 31%, 33%, and 126% over ML10. Corrosion rates (0.45–0.68 mm/year) were 39–42% lower than ML10. After 90 days the alloy retained 58–76% of initial strength (182–230 MPa), maintaining >180 MPa throughout the critical 12-week healing period, versus 38–42% for ML10. Industrial trials on three screw sizes confirmed reproducibility.*

Scientific novelty. *For the first time, a comprehensive evaluation of the interrelationship between microstructure, mechanical properties, and degradation kinetics of the Mg-3.15Nd-1.25Zr-0.6Zn alloy was performed across three model biological fluids with systematic benchmarking against ML10 and bone healing requirements. It was established that elimination of continuous $(Mg,Zn)_{12}Nd$ grain-boundary networks combined with grain refinement to 57 μm shifts the dominant corrosion mode from catastrophic intergranular attack (150–200 μm penetration in ML10) to uniform surface corrosion (<50 μm penetration), yielding degradation kinetics temporally synchronized with the physiological stages of bone healing.*

Practical value. *An industrially scalable route was validated in pilot production of malleolar screws using standard melting, copper-mould casting, and conventional heat treatment. The alloy provides a sufficient mechanical safety margin throughout all critical healing phases (weeks 0–20), surpassing ML10 and meeting preclinical requirements for biodegradable orthopaedic fixation.*

Key words: *biodegradable magnesium alloy, Mg-Zr-Nd-Zn system, osteosynthesis, microstructure, grain refinement, mechanical properties, biocorrosion, controlled degradation, bone healing, malleolar screw, ML10 alloy.*

Introduction

Biodegradable magnesium alloys represent promising candidates for orthopaedic trauma implants by virtue of three key advantages. First, the elastic modulus of magnesium (41–45 GPa) closely approximates that of cortical bone (10–30 GPa), thereby minimizing stress shielding effects. Second, Mg^{2+} ions actively promote osteogenesis. Third, biodegradation obviates the need for secondary surgical intervention to remove the implant.

Despite these advantages, magnesium alloys present critical limitations. In chloride-containing physiological environments, excessive corrosion rates lead to subcutaneous gas cavity formation, localized pH elevation, and premature loss of mechanical integrity prior to completion

DOI 10.15588/1607-6885-2026-2-2

of the 12–16-week bone healing period. The industrial alloy ML10 (known internationally as part of the Mg-Nd-Zr system developed for aerospace applications), despite acceptable initial properties (σ_{UTS} = 230–240 MPa), retains only 40% of its strength after three months owing to a coarse-grained microstructure with heterogeneous secondary phase distribution.

A critical gap exists between the degradation kinetics of current magnesium alloys and the biomechanical requirements of bone healing. An ideal implant should provide maximal support during early-stage healing (weeks 0–6), progressively transfer load to regenerating bone tissue (weeks 6–16), and maintain load-bearing capacity exceeding 180 MPa throughout the critical 12-week period.

The Mg-Zr-Nd-Zn quaternary system offers considerable promise: zirconium provides grain refinement, neodymium enhances corrosion resistance, and zinc contributes solid solution strengthening. Laboratory investigations have achieved ultimate tensile strengths of 300–365 MPa; however, industrial scalability and systematic validation of biodegradation behaviour remain to be demonstrated.

Analysis of research and publications

Over the past two decades, bioresorbable magnesium alloys have emerged as leading candidates for use in trauma and orthopedic implants. Their growing prominence is primarily attributed to three key advantages over conventional inert metallic materials [1–3]:

1. The elastic modulus of magnesium (41–45 GPa) is much closer to that of cortical bone (10–30 GPa), which helps mitigate stress shielding and the consequent resorption of bone tissue.

2. Mg^{2+} ions exhibit osteoconductive properties, supporting bone growth along the implant surface.

3. Their controlled biodegradation eliminates the need for secondary surgical intervention to remove the implant.

In contrast to stainless steel, cobalt-chromium, and titanium alloys – whose stiffness exceeds that of bone by a factor of 4–10 – magnesium alloys preserve a more physiological distribution of mechanical loads within the bone-implant system. This feature is particularly critical in the talar region of the ankle joint, where stress shielding can delay fracture consolidation, reduce bone mineral density, and increase the risk of clinical recurrence.

However, magnesium-based implants also exhibit inherent limitations. In chloride-containing physiological environments, anodic dissolution of magnesium leads to the formation of $Mg(OH)_2$ and molecular hydrogen. When corrosion proceeds too rapidly, this can result in [4, 5]:

1. Subcutaneous gas cavities due to hydrogen accumulation.

2. Local alkalization (elevated pH), which suppresses cellular activity.

3. Premature loss of the implant's mechanical integrity.

Pure magnesium degrades at an excessively high rate: its load-bearing capacity is typically lost before completion of the 12–16-week bone healing phase [5, 6]. Additional challenges include the presence of coarse-grained microstructures, galvanic microcells between the matrix and secondary phases, and a pronounced susceptibility to corrosion fatigue and stress corrosion cracking [4]. Fig. 1 illustrates the critical mismatch between the degradation kinetics of current magnesium alloys and the biomechanical requirements of bone healing. Conventional Mg alloys lose their strength too rapidly, falling below the critical threshold of 180 MPa as early as week 6. The ML10 alloy provides insufficient mechanical support during the crucial phase of hard callus formation, maintaining only 140–160 MPa between weeks 6 and 12. Even the benchmark alloy WE43, although characterized by relatively controlled degradation, exhibits a low initial strength (about 210 MPa) and approaches the critical threshold too closely (183 MPa at week 8), offering an inadequate safety margin.

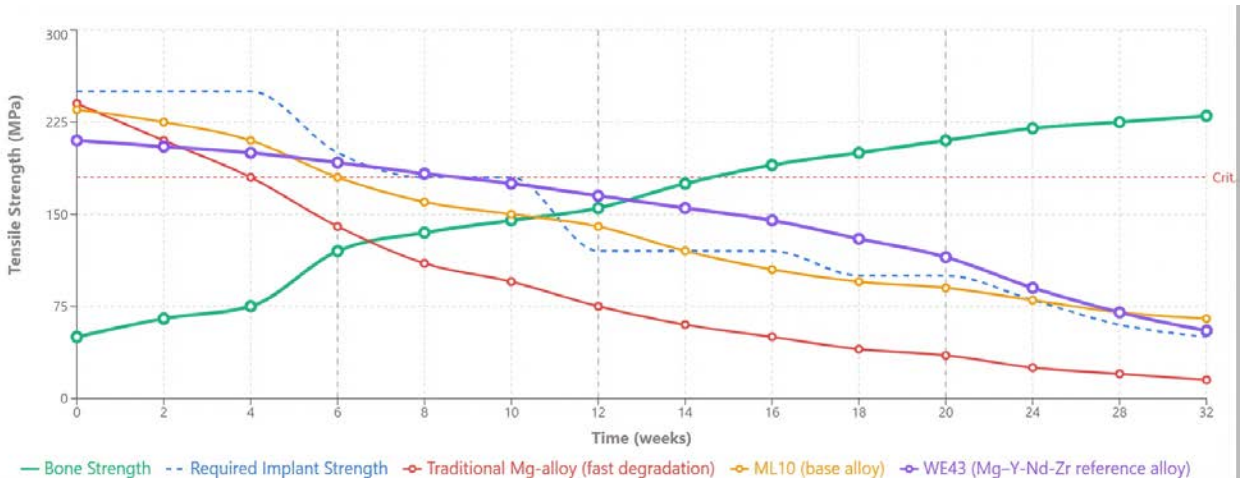

Figure 1. Critical gap in mechanical support: current biodegradable magnesium alloys versus bone healing requirements

DOI 10.15588/1607-6885-2026-2-2

These observations underscore the need to develop a new magnesium alloy with (i) higher initial strength (>250 MPa) and (ii) finely tuned degradation kinetics that are temporally synchronized with the physiological stages of bone tissue regeneration.

Contemporary development of bioresorbable magnesium alloys is centered on three interrelated strategies [3, 5, 7]:

1. Optimizing alloying elements to simultaneously strengthen the matrix and suppress corrosion.

2. Engineering fine-grained, homogeneous microstructures.

3. Designing heat-treatment protocols that homogenize phase distribution and reduce microgalvanic activity without compromising ductility.

The Mg-Zr-Nd-Zn system is particularly promising. Zirconium is the most effective grain refiner in aluminium-free magnesium alloys: it reduces dendritic cell size, promotes a uniform distribution of secondary phases, and improves the isotropy of mechanical properties. Neodymium significantly enhances corrosion resistance and thermal stability while maintaining cytocompatibility. Zinc provides solid-solution strengthening without forming extensive galvanic networks, provided its concentration remains moderate [3, 6, 7]. Experimental studies within this system have already achieved ultimate strengths in the range of 300–365 MPa, combined with acceptable ductility and significantly reduced corrosion rates [1–3]. However, these results have been obtained predominantly at the laboratory scale; industrial scalability, together with standardized validation of biocompatibility and controlled degradation, still require systematic verification.

The industrial reference alloy ML10 exhibits acceptable mechanical properties, but its microstructure is coarse-grained with a non-uniform distribution of large secondary phases. In physiological substitute fluids, this microstructural heterogeneity leads to a more rapid loss of ductility and strength than is desirable for fracture consolidation in the ankle region. Consequently, there remains a clear need for an alloy that [2, 5, 8]:

1. Surpasses ML10 in terms of initial mechanical performance.

2. Maintains critical reserves of strength and ductility throughout the first three months under physiological conditions.

3. Can be reliably produced using standard industrial casting lines.

From a materials science standpoint, microstructural homogeneity and fine grain size are key determinants of corrosion behaviour. Grain refinement enhances the barrier function of grain boundaries, hinders the development of galvanic microcells, and promotes the formation of dense, protective corrosion films. At the same time, excessive dispersion of secondary-phase particles and compositional inhomogeneity can accelerate localized dissolution [3, 5].

Despite encouraging in vitro findings, several critical aspects remain insufficiently documented. It is still unclear to what extent these optimized microstructures can be reliably reproduced under industrial cooling rates and conventional heat-treatment schedules, and whether the mechanical safety margins can be maintained throughout the crucial three-month period in blood-mimicking media. While some studies report ultimate tensile strengths above 300 MPa combined with elongations of 7–10 %, large-scale industrial implementation in actual threaded screw implants remains limited [2, 8].

Standardization of model media is essential. Gelofusine, Venofundin, and physiological saline affect degradation kinetics in distinct ways due to differences in macromolecular and electrolyte composition. Using this spectrum of media enables a more realistic assessment of the time-dependent loss of mechanical properties compared with simpler single-buffer systems [5]. A comprehensive assessment – encompassing initial mechanical properties, microstructural characterization, corrosion dynamics in multiple media, and benchmarking against both cortical bone and the reference alloy ML10 – is consistent with current standards for preclinical validation [3, 8].

The literature points to two parallel trajectories.

The first is scientific and technological: existing studies establish the fundamental feasibility of achieving controlled degradation while retaining high mechanical performance, yet they simultaneously highlight the absence of standardized comparative methodologies and the need for regulatory harmonization [1, 2].

The second is clinical and translational: although preliminary animal and early clinical data support the safety and functional benefits of biodegradable magnesium implants, current evidence is fragmented, dominated by small, heterogeneous cohorts, and often limited to short follow-up periods. This underscores the need for rigorously designed, multicenter studies with unified endpoints (e.g., time to consolidation, complication rates, long-term remodeling of bone and implant remnants), as well as integration of imaging, functional, and patient-reported outcomes to substantiate routine clinical adoption.

Purpose

The aim of this study is to evaluate a bioresorbable Mg-Zr-Nd-Zn alloy that is compatible with standard industrial melting and casting routes, outperforms ML10 in terms of initial mechanical properties, and exhibits controlled degradation in blood-substitute media over a three-month period.

The present study employs a previously developed [8] bioresorbable alloy of composition Mg-1.2…1.3Zr-3.1…3.2Nd-0.5…0.7Zn (wt.%), designed to achieve a synergistic combination of grain refinement (via Zr), corrosion stabilization and dispersion strengthening (via Nd), and solid-solution strengthening (via Zn). The pocessing route was likewise defined on the basis of these earlier investigations [9,10]: melting was carried out in a

DOI 10.15588/1607-6885-2026-2-2

crucible furnace using primary magnesium and master alloys, followed by casting into a water-cooled copper mould (cooling rate 25–30 °C/s). The cast billets were then subjected to a two-step heat treatment consisting of homogenization at 560 ± 5 °C for 8 h with subsequent air cooling, and artificial ageing at 200 ± 5 °C for 16 h.

Industrial trials on ankle screws of three size ranges were conducted to assess the reproducibility of the alloy's microstructure and properties in real components. Degradation behaviour was systematically examined in Gelofusine, Venofundin, and physiological saline, with the loss of strength and ductility quantified after 1, 2, and 3 months of immersion. Comparison with ML10 and with the property range of cortical bone was used to determine whether the alloy retained a sufficient mechanical safety margin to ensure stable fixation throughout the critical healing period [5, 8].

The study demonstrates that an industrially compatible processing route can provide a predictable microstructure and corrosion-mechanical behaviour that meets contemporary preclinical evaluation requirements [1–3]. Successful implementation will provide a foundation for more advanced preclinical studies of biocompatibility and of the systemic effects of degradation products, with a view toward eventual clinical application in the fixation of ankle fractures.

Research material and methodology

Pilot industrial heats of the experimental alloy were carried out in Shop No. 1 of JSC "Motor Sich". Test specimens were manufactured from the new bioresorbable alloy in the form of malleolar screws of different configurations: Type 1 (L = 40 mm, D = 5 mm, d = 3 mm), Type 2 (L = 50 mm, D = 7.5 mm, d = 4.5 mm), and Type 3 (L = 100 mm, D = 7 mm, d = 5.5 mm) (Fig. 2).

The experimental bioresorbable magnesium alloy was developed within the Mg-Zr-Nd-Zn system to balance mechanical strength against biodegradation rate. The target composition comprised 0.4–1.5 wt.% Zr, 2.2–3.4 wt.% Nd, and 0.1–0.7 wt.% Zn. The charge materials consisted of primary ingot magnesium (grades Mg90, Mg95, and Mg96), zinc (grade Ts2), an Mg-Nd master alloy (20–35 wt.% Nd, ≤2.5 wt.% impurities, balance Mg), and an Mg-Zr master alloy (10–20 wt.% Zr, ≤5 wt.% impurities, balance Mg).

Melting was carried out in an IPM-500 crucible furnace (capacity 0.5 t, power 140 kW, throughput 230 kg/h). Preheated charge materials were melted and tapped into removable crucibles at 650–730 °C. The melt was then transferred to holding furnaces, where its composition was adjusted and it was refined with VI-2 flux at 740–760 °C. The VI-2 flux had the following composition: 38–46 wt.% $MgCl_2$, 32–42 wt.% KCl, 5–8 wt.% $BaCl_2$, 3–5 wt.% CaF_2, ≤8 wt.% NaCl + $CaCl_2$, and ≤1.5 wt.% MgO. The Zr-, Nd- and Zn-containing master alloys were then added, and the melt was held at 730 °C prior to casting [11].

For industrial validation, the alloys were cast into water-cooled copper moulds, achieving a cooling rate of 25–30 °C/s. The cooling rate was measured using type-K (Chromel-Alumel) thermocouples, with an operating range from -400 to +1200 °C, positioned in direct contact with the melt.

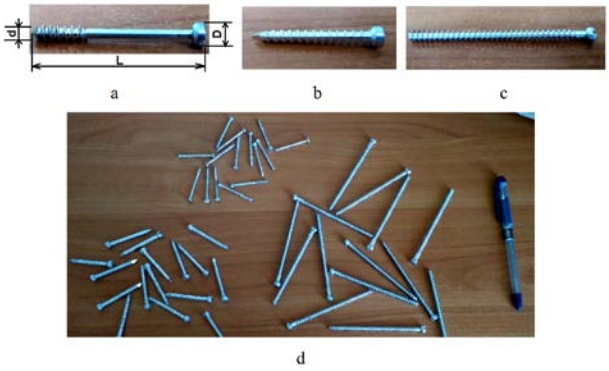

Figure 2. Test specimens of varying length. (a) Type 1; (b) Type 2; (c) Type 3; (d) general view

Heat treatment was carried out in a protective argon atmosphere using either a "Bellevue" pit furnace (112 kW, 95 kg/h) or a PAP-4M furnace (50 kg/h).

The optimized heat-treatment schedule consisted of:

1. Homogenization: 560 ± 5 °C for 8 h, followed by air cooling.

2. Ageing**:** 200 ± 5 °C for 16 h, followed by air cooling.

Optical microscopy. The macro- and microstructure were examined using Neophot 32 and Olympus IX 70 optical microscopes at magnifications of 100×, 200×, 350×, and 500×. Metallographic specimens were prepared after heat treatment and subsequently etched. The etchant composition was: 1 % HNO_3, 20 % CH_3COOH, 19 % distilled water, and 60 % ethylene glycol.

Grain size analysis. The average grain size was determined in accordance with ISO 643:2024 using the intercept method [12]. At 100× magnification, grain boundaries intersected by a test line were counted as following. For each specimen, at least eight representative regions were analysed, with a minimum of two non-parallel measurements per region, each intersecting at least ten grains.

The average grain size D was calculated from:

$$D = L/N, \quad (1)$$

where L is the total length of the test line converted to the image scale (μm), and N is the number of grain boundary intersections along this line.

The standard deviation S was determined as:

$$S = \sqrt{\frac{1}{n}\sum_{i=1}^{n}(D_i - \bar{D})^2}\ , \quad (2)$$

where D_i is the grain size measured in the i-th test, $\bar{D}$ is the arithmetic mean grain size, and n is the number of measurements.

DOI 10.15588/1607-6885-2026-2-2

Ultimate tensile strength and elongation to fracture were determined on an INSTRON 2801 universal testing machine in accordance with ASTM B557 [11] and ISO 6892-1 [13]. Tests were performed both on specimens in the heat-treated condition and after immersion in artificial blood substitutes (Gelofusine, Venofundin, and physiological saline) for 1, 2, and 3 months at 36 ± 1.0 °C [14]. Temperature stability during immersion was maintained using a UT-15 ultra-thermostat.

Specimen preparation. Prior to immersion, the specimens were degreased with ethyl alcohol. After the specified exposure time, the samples were removed and corrosion products were chemically stripped in chromic acid at 18–25 °C for 3 min. The specimens were then rinsed with running water followed by distilled water, dried, and subjected to mechanical testing. For each test condition, three specimens were examined [14].

The compositions of the artificial blood substitutes are summarized in Table 1.

Table 1 – Composition of artificial blood substitutes

Solution	Succinylated gelatin (g/500 mL)	NaCl (g/500 mL)	NaOH (g/500 mL)	Hydroxyethyl starch (g/500 mL)	pH
Gelofusine	20	3,5	0,68	–	7,4
Venofundin	–	4,5	–	30	5,5
Normal saline	–	4,5	–	–	5,5–7,0

Note: Normal saline denotes 0.9% NaCl solution (4.5 g/500 mL).

Specimen quality was assessed by visual inspection and radiographic examination. Visual inspection was used to identify surface defects, damage, and shrinkage cavities, whereas radiographic testing was employed to detect internal defects, porosity, and flux inclusions.

Results and their discussion

The developed Mg-3.15Nd-1.25Zr-0.6Zn alloy exhibited a markedly refined microstructure compared with the reference alloy ML10. Quantitative metallographic analysis revealed an average grain size of 57 ± 4.7 μm, which is approximately 50% smaller than the 115 ± 9.1 μm measured for ML10 (Fig. 3).

Such pronounced grain refinement is consistent with the Hall-Petch relationship, which predicts an improvement in mechanical properties with decreasing grain size [15].

Grain refinement resulted from the synergistic effect of the elevated Zr content (1.25 wt.%) and the optimized heat-treatment parameters. Zirconium acts as a strong grain refiner in magnesium alloys, providing heterogeneous nucleation sites for α-Mg grains during solidification [16]. Differential thermal analysis (DTA) identified the melting temperature of the pseudoeutectic at 571.4 °C, which guided the choice of a homogenization temperature of 560 °C – high enough to ensure complete dissolution of the $(Mg, Zn)_{12}Nd$ eutectic phase while avoiding the risk of incipient melting.

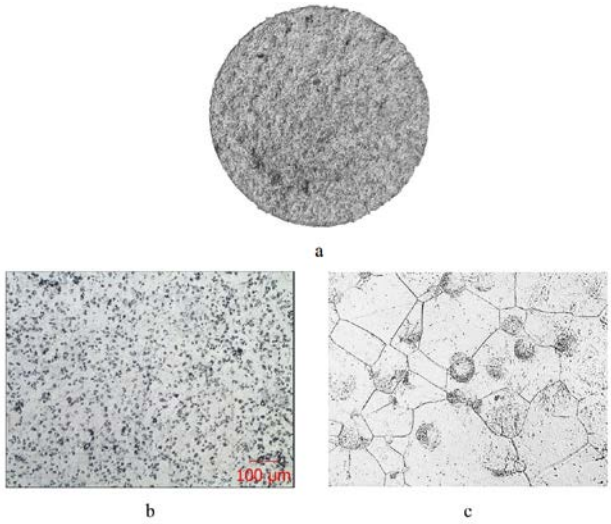

Figure 3. Microstructure of Mg-3.15Nd-1.25Zr-0.6Zn and ML10 alloys. (a) Macrostructure showing uniform grain distribution, ×5; (b) ML10 microstructure with secondary phase particles at grain boundaries, ×100; (c) developed alloy with refined grains and clean boundaries, ×100

The most important microstructural feature of the developed alloy is the presence of clean grain boundaries free from continuous networks of grain-boundary precipitates (Fig. 3*a*). In contrast, ML10 is characterized by extensive decoration of grain boundaries with coarse pseudoeutectic $(Mg, Zn)_{12}Nd$ phases (Fig. 3*b*). These boundary phases act as preferential corrosion sites and stress concentrators [17]. In the developed alloy, the grain boundaries instead contain fine, uniformly distributed Zn_2Zr_3 particles together with metastable β″ secondary-phase precipitates, which provide effective dispersion strengthening without degrading corrosion resistance.

The developed alloy exhibited superior mechanical properties compared with ML10 for all measured parameters (Table 2).

Its ultimate tensile strength of 309 MPa exceeds the threshold typically required for load-bearing orthopaedic applications [18]. More importantly, the yield strength of 252 MPa exceeds the minimum level recommended for osteosynthesis screws in clinical use. The simultaneous improvement in ductility (7.9% elongation compared with 3.5% for ML10) is particularly noteworthy, given that bioresorbable implants are often prone to embrittlement during degradation [17].

These improvements can be attributed to three concurrent strengthening mechanisms:

1. Grain boundary strengthening via the Hall-Petch effect. Grain refinement increases the yield strength in accordance with the Hall-Petch relationship, as the higher grain-boundary area in fine-grained microstructures provides more effective barriers to dislocation motion [15].

DOI 10.15588/1607-6885-2026-2-2

Table 2 – Comparative mechanical properties

Property	Developed alloy	ML10	Improve-ment
Grain size (μm)	57±4,7	115±9,1	−50 %
Ultimate tensile strength (MPa)	309±6,5	235±5,0	+31 %
Yield strength (MPa)	252±6,5	190±5,0	+33 %
Elongation to failure (%)	7,9±0,65	3,5±0,5	+126 %
Residual UTS after 3 months (MPa)	206±24	94±2	+119 %
Strength retention (%)	66±8	40±2	+65 %

2. Solid-solution strengthening. The higher neodymium content (3.15 wt.% vs. 2.5 wt.% in ML10) together with the increased zinc content (0.6 wt.% vs. 0.4 wt.%) markedly contributes to strengthening via lattice distortion. Neodymium has a relatively high solubility in magnesium and, owing to its larger atomic radius, generates significant local lattice strain.

3. Dispersion strengthening. Complete dissolution of the pseudoeutectic during homogenization, followed by controlled ageing, produced a higher volume fraction of fine Zn_2Zr_3 and β″ secondary-phase particles compared with ML10. These coherent or semi-coherent precipitates impede dislocation motion through the Orowan mechanism.

The elimination of coarse secondary-phase particles at grain boundaries also removes preferred crack-initiation sites, which explains the improved ductility. Fractographic analysis revealed predominantly transgranular dimpled fracture in the developed alloy, in contrast to the intergranular brittle fracture observed in ML10, corroborating the beneficial effect of clean grain boundaries on fracture toughness.

Long-term mechanical integrity during degradation represents a critical differentiating factor for bioresorbable orthopaedic implants [19]. The developed alloy retained 58–76 % of its initial strength after three months of immersion in simulated biological fluids – an improvement of 45–90 % relative to the 40% retention observed for ML10 (Fig. 4).

Even under the most aggressive test conditions (Venofundin, pH 5.5), the developed alloy maintained an ultimate tensile strength of 182 ± 18 MPa after 90 days, sufficient for load-bearing function throughout the critical period of ankle fracture consolidation.

This superior property retention can be attributed to two microstructural factors:

First, the absence of continuous secondary-phase particles at grain boundaries eliminates the most aggressive corrosion pathway. In ML10, galvanic couples form between the α-Mg matrix (anode) and $(Mg, Zn)_{12}Nd$ secondary-phase particles (cathode), creating preferential attack channels along grain boundaries [20]. This leads to rapid intergranular corrosion and premature mechanical failure even at modest overall mass loss.

Second, the refined grain structure (57 μm versus 115 μm) paradoxically improves corrosion resistance despite the increased grain boundary area. Finer grains promote more uniform formation of the protective $Mg(OH)_2$/MgO film and reduce the size of local galvanic cells [21].

Bioresorbable implants *in vivo* are exposed to diverse chemical environments ranging from neutral pH in healthy tissue to acidic conditions at sites of inflammation or hematoma [22]. Table 3 summarizes the corrosion kinetics and evolution of mechanical properties.

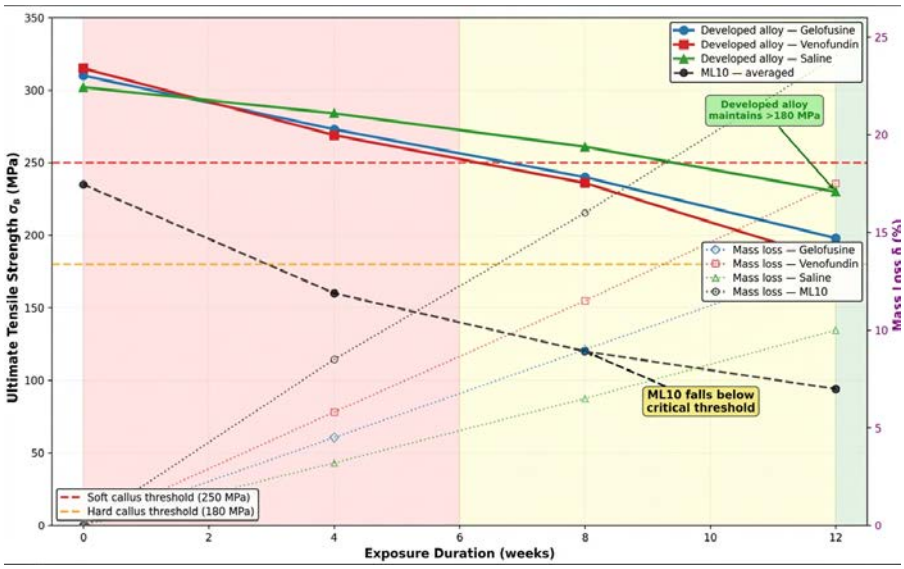

Figure 4. Biaxial plot of ultimate tensile strength retention (MPa) versus time (weeks) for both alloys in all three solutions, with cumulative mass loss (%)

DOI 10.15588/1607-6885-2026-2-2

Table 3 – Degradation characteristics in model biological fluids (90-day immersion)

Solution	CR[a] (mm/year)	Residual UTS (MPa)	Residual El. (%)
Developed Mg–3.15Nd–1.25Zr–0.6Zn			
Gelofusine	0,45±0,05	198±12 (64 %)	5,2±0,8 (65 %)
Normal saline	0,52±0,06	230±15 (76 %)	6,8±1,0 (86 %)
Venofundin	0,68±0,08	182±18 (58 %)	4,0±0,9 (50 %)
ML10			
Gelofusine	0,78±0,08	98±3 (42 %)	1,2±0,2 (40 %)
Normal saline	0,85±0,09	95±2 (40 %)	1,2±0,2 (40 %)
Venofundin	1,12±0,12	89±4 (38 %)	1,1±0,2 (37 %)

Note: [a]Corrosion rate determined by gravimetric mass loss.

Values represent mean ± SD (n = 3). Parenthetical percentages indicate retention relative to initial properties (Table 2). El. = elongation to failure.

The developed alloy consistently exhibited 39–42% lower corrosion rates across all test solutions compared with ML10. This improvement is particularly significant in acidic Venofundin (0.68 mm/year versus 1.12 mm/year for ML10), a 39 % reduction, which simulates the inflammatory microenvironment of early postoperative healing.

Degradation rates varied systematically with solution composition, ranging from slowest in protein-containing Gelofusine (0.45 mm/year), to intermediate in physiological saline (0.52 mm/year), to fastest in acidic Venofundin (0.68 mm/year). This trend reflects three distinct corrosion-modifying mechanisms.

In Gelofusine, albumin and other plasma proteins adsorb onto the magnesium surface, forming a semi-protective organic layer that partially impedes electrolyte access to the underlying metal [22]. For ML10 in this medium, the corrosion rate reached 0.78 mm/year, 73% higher than the experimental alloy, indicating that protein-mediated passivation is less effective on this alloy's surface.

In physiological saline, the absence of proteins eliminates this organic barrier, resulting in moderately accelerated degradation (0.52 mm/year for the developed alloy versus 0.85 mm/year for ML10). Nevertheless, the neutral pH permits rapid formation of a stable $Mg(OH)_2$ layer, which provides partial surface protection.

In acidic Venofundin (pH 5.5), proton reduction becomes the dominant cathodic reaction, accelerating overall corrosion to 0.68 mm/year for the developed alloy and 1.12 mm/year for ML10. Moreover, the acidic environment continuously dissolves the protective $Mg(OH)_2$ layer, preventing the establishment of a stable barrier.

The interrelationship between microstructure, degradation mode, and mechanical property retention is well established in the magnesium alloy literature [20].

Coarse-grained alloys exhibiting extensive secondary phase precipitation along grain boundaries, such as ML10, are susceptible to severe intergranular corrosion, with penetration depths reaching 150–200 μm following prolonged exposure, as the grain boundary networks serve as preferential corrosion pathways. This attack pattern results in catastrophic loss of load-bearing cross-section and premature mechanical failure. In contrast, alloys possessing fine-grained microstructures with homogeneous alloying element distribution exhibit uniform surface corrosion with limited penetration depth (<50 μm), thereby preserving the structural integrity of the bulk material [20].

This difference in corrosion morphology directly accounts for the observed dissolution kinetics in plasma substitute media. Intergranular attack generates internal fissures that act as stress concentrators, inducing brittle fracture at loads substantially below the nominal strength of the residual material, a mechanism consistent with the pronounced strength deterioration of ML10 to 38–42% of initial values across all model solutions. Conversely, uniform surface recession maintains a defect-free cross-section, enabling the material to sustain loads proportional to its remaining cross-sectional area, thus explaining the retention of 58–76% of initial strength in the developed alloy, depending on environmental aggressivity.

The ultimate criterion for success in bioresorbable orthopaedic implants is controlled degradation synchronized with bone healing kinetics. An ideal bioresorbable screw should provide maximal mechanical support during the early healing phase (weeks 0–6), then progressively transfer load to the regenerating bone as it gains strength (weeks 6–16).

Table 4 quantifies the requirements for each healing stage and evaluates both alloys against these benchmarks.

During Phase 1 (weeks 0–6), only a soft fibrous callus with minimal mechanical competence is present at the fracture site; accordingly, the implant must bear virtually 100% of applied loads. Both alloys initially satisfy this requirement, although ML10 affords a narrower safety margin.

The critical distinction emerges in Phase 2 (weeks 6–12), when hard callus formation commences but bone strength remains below 150 MPa. The developed alloy maintains 195–230 MPa throughout this period, sufficient for safe load sharing between implant and healing tissue. In contrast, ML10 degrades to 140–160 MPa, creating a biomechanical mismatch wherein the implant can no longer adequately support applied loads [18].

By Phase 3 (weeks 12–20), the bone has developed sufficient lamellar architecture to assume the majority of loading, requiring only >120 MPa residual strength from the implant. The developed alloy comfortably maintains this threshold (120–180 MPa), whereas ML10 has degraded to 85–95 MPa, below the safety limit.

Phase 4 (weeks 20–32) corresponds to complete bone union, at which point the implant should ideally

DOI 10.15588/1607-6885-2026-2-2

undergo degradation to permit natural bone remodelling. The developed alloy achieves controlled degradation within this timeframe, whereas ML10 frequently fails prematurely.

Table 4 – Healing phase requirements versus alloy performance characteristics

Healing phase	Timeframe	Regenerating bone strength[a]	Implant strength threshold
Healing Phase Requirements			
Inflammation / soft callus	Weeks 0–6	50–80 MPa	>250 MPa
Hard callus formation	Weeks 6–12	120–150 MPa	>180 MPa
Bone remodelling	Weeks 12–20	180–220 MPa	>120 MPa
Complete union	Weeks 20–32	>200 MPa	<100 MPa[c]
Alloy Performance Evaluation			
Healing phase	Developed alloy status	ML10 status	
Inflammation / soft callus	✓ 260–309 MPa	✓ 240–260 MPa[b]	
Hard callus formation	✓ 195–230 MPa	✗ 140–160 MPa	
Bone remodelling	✓ 120–180 MPa	✗ 85–95 MPa	
Complete union	✓ Controlled degradation	✗ Premature failure	

Note: [a]Estimated compressive strength of regenerating fracture callus based on published biomechanical studies.

[b]Marginal compliance; lower-bound values approach threshold.

[c]Upper limit; implant should degrade below this threshold to permit physiological loading of healed bone.

✓ = requirement satisfied; ✗ = requirement not met. Projected implant strengths extrapolated from 90-day immersion data (Table 3).

Conclusions

1. Microstructural achievement. The developed Mg-3.15Nd-1.25Zr-0.6Zn alloy achieved 50% grain refinement (57±4.7 μm versus 115±9.1 μm in ML10) and complete elimination of continuous secondary phase networks at grain boundaries through synergistic effects of elevated Zr content (1.25 wt.%) and optimized two-stage heat treatment (homogenization at 560 °C/8h + ageing at 200 °C/16 h). The resultant microstructure is characterized by clean boundaries with fine, uniformly distributed Zn_2Zr_3 and β" precipitates.

2. Mechanical performance. Ultimate tensile strength of 309±6.5 MPa and elongation of 7.9±0.65% represent improvements of 31% and 126%, respectively, over ML10, while yield strength of 252±6.5 MPa exceeds clinical requirements for load-bearing osteosynthesis screws. These enhancements result from three concurrent strengthening mechanisms: Hall-Petch grain boundary strengthening, solid solution strengthening from Nd and Zn, and Orowan dispersion strengthening from coherent/semi-coherent dispersoids.

3. Controlled degradation synchronized with bone healing. The alloy retained 58–76% of initial strength after three months (depending on solution) versus 38–42% for ML10, maintaining >180 MPa throughout the critical 12-week hard callus formation period across all tested physiological solutions (Gelofusine: 0.45 mm/year; physiological saline: 0.52 mm/year; Venofundin: 0.68 mm/year) – representing a 39–42% reduction in corrosion rate compared with ML10 (0.78–1.12 mm/year). This degradation timeline aligns with bone healing kinetics: adequate support during inflammation/soft callus phases (weeks 0–6), critical load-bearing capacity during hard callus formation (weeks 6–12), and controlled degradation during remodelling (weeks 12–20).

4. Mechanistic understanding. The superior corrosion resistance despite finer grain structure (increased boundary area) results from two interrelated mechanisms: (a) elimination of galvanic corrosion pathways through complete dissolution of anodic $(Mg, Zn)_{12}Nd$ grain boundary networks, and (b) refined grain size promoting uniform protective $Mg(OH)_2/MgO$ film formation while reducing local galvanic cell dimensions. The developed alloy exhibits uniform surface corrosion (<50 μm penetration) versus catastrophic intergranular attack in ML10 (150–200 μm), which accounts for the divergent mechanical property retention despite comparable overall mass loss.

5. Industrial scalability. The processing route: crucible melting, casting into a water-cooled copper mould at 25–30 °C/s, and two-stage heat treatment in standard furnaces, demonstrated reproducible microstructure and properties in industrial trials on threaded malleolar screws of three sizes (Ø3.5, Ø4.0, Ø4.5 mm), confirming compatibility with existing manufacturing infrastructure.

6. Path to clinical translation. Although this study confirms controlled degradation in model biological fluids and biomechanical alignment with bone healing phases, clinical implementation requires: (a) *in vivo* animal studies to evaluate tissue response, hydrogen management, and systemic distribution of degradation products; (b) fatigue property characterization under cyclic physiological loading; (c) evaluation of surface modification strategies (coatings, micro-arc oxidation); and (d) completion of biocompatibility protocols in accordance with ISO 10993 and ASTM F3160.

7. Broader implications. This work demonstrates that rational grain boundary engineering through compositional optimization (Zr modification + Nd stabilization + Zn strengthening) and controlled thermal processing can yield industrially viable biodegradable magnesium alloys with degradation timelines synchronized to tissue healing. The approach is extensible to other temporary load-bearing applications in orthopaedic and cardiovascular devices requiring predictable mechanical support during regeneration followed by controlled resorption.

DOI 10.15588/1607-6885-2026-2-2

References

1. Aikin, M., & Shalomeev, V. (2024). Optimization of heat treatment regime for a new biodegradable Mg-Zr-Nd alloy with enhanced mechanical properties. *Innovative Materials and Technologies in Metallurgy and Mechanical Engineering*, 31–38. https://doi.org/10.15588/1607-6885-2024-3-5

2. Aikin, M., Shalomeev, V., Kukhar, V., Kostryzhev, A., Kuziev, I., Kulynych, V., Dykha, O., Dytyniuk, V., Shapoval, O., & Zagorskis, A. (2025). Recent advances in biodegradable magnesium alloys for medical implants: Evolution, innovations, and clinical translation. *Crystals*, *15*(8), Article 671. https://doi.org/10.3390/cryst15080671

3. Aikin, M., Shalomeev, V., & Lukyanenko, O. (2021). Дослідження впливу високих швидкостей охолодження при кристалізації на структуру та властивості сплаву системи Mg-Zr-Nd [Investigation of the influence of high cooling rates during crystallization on the structure and properties of the Mg-Zr-Nd system alloy]. *Innovative Materials and Technologies in Metallurgy and Mechanical Engineering*. https://doi.org/10.15588/1607-6885-2021-1-4

4. ASTM International. (2004). *Standard guide for laboratory immersion corrosion testing of metals* (ASTM G31-72R04). https://doi.org/10.1520/G0031-72R04

5. ASTM International. (2023). *Standard test methods for tension testing wrought and cast aluminum- and magnesium-alloy products* (ASTM B557-15).

6. Dangwal, S., Edalati, K., Valiev, R. Z., & Langdon, T. G. (2023). Breaks in the Hall-Petch relationship after severe plastic deformation of magnesium, aluminum, copper, and iron. *Crystals*, *13*(3), Article 413. https://doi.org/10.3390/cryst13030413

7. Eddy Jai Poinern, G., Brundavanam, S., & Fawcett, D. (2013). Biomedical magnesium alloys: A review of material properties, surface modifications and potential as a biodegradable orthopaedic implant. *American Journal of Biomedical Engineering*, *2*(6), 218–240. https://doi.org/10.5923/j.ajbe.20120206.02

8. Gracheva, A., Polozov, I., & Popovich, A. (2025). Additive manufacturing of biodegradable metallic implants by selective laser melting: Current research status and application perspectives. *Metals*, *15*(7), Article 754. https://doi.org/10.3390/met15070754

9. International Organization for Standardization. (2019). *Metallic materials-Tensile testing-Part 1: Method of test at room temperature* (ДСТУ ISO 6892-1:2019).

10. International Organization for Standardization. (2024). *Steels-Micrographic determination of the apparent grain size* (ISO 643:2024).

11. Jin, S., Zhang, D., Lu, X., Zhang, Y., Tan, L., Liu, Y., & Wang, Q. (2020). Mechanical properties, biodegradability and cytocompatibility of biodegradable Mg-Zn-Zr-Nd/Y alloys. *Journal of Materials Science & Technology*, *47*, 190–201. https://doi.org/10.1016/j.jmst.2020.02.017

12. Lin, X., Saijilafu, Wu, X., Wu, K., Chen, J., Tan, L., Witte, F., Yang, H., Mantovani, D., & Zhou, H. (2023). Biodegradable Mg-based alloys: Biological implications and restorative opportunities. *International Materials Reviews*, *68*(4), 365–403. https://doi.org/10.1080/09506608.2022.2079367

13. Liu, C., Ren, Z., Xu, Y., Pang, S., Zhao, X., & Zhao, Y. (2018). Biodegradable magnesium alloys developed as bone repair materials: A review. *Scanning*, *2018*, 1–15. https://doi.org/10.1155/2018/9216314

14. Maier, H. J., Julmi, S., Behrens, S., Klose, C., Gartzke, A.-K., Wriggers, P., Waselau, A.-C., & Meyer-Lindenberg, A. (2020). Magnesium alloys for open-pored bioresorbable implants. *JOM*, *72*, 1859–1869. https://doi.org/10.1007/s11837-020-04078-8

15. Morgan, E. F., Unnikrisnan, G. U., & Hussein, A. I. (2018). Bone mechanical properties in healthy and diseased states. *Annual Review of Biomedical Engineering*, *20*, 119–143. https://doi.org/10.1146/annurev-bioeng-062117-121139

16. Müller, E., Schoberwalter, T., Mader, K., Seitz, J.-M., Kopp, A., Baranowsky, A., & Keller, J. (2024). The biological effects of magnesium-based implants on the skeleton and their clinical implications in orthopedic trauma surgery. *Biomaterials Research*, *28*, Article 0122. https://doi.org/10.34133/bmr.0122

17. Shalomeev, V., Aikin, N., Chorniy, V., & Naumik, V. (2019). Design and examination of the new biosoluble casting alloy of the system Mg-Zr-Nd for osteosynthesis. *Materials Science*.

18. Thomas, K. K., Zafar, M. N., Pitt, W. G., & Husseini, G. A. (2023). Biodegradable magnesium alloys for biomedical implants: Properties, challenges, and surface modifications with a focus on orthopedic fixation repair. *Applied Sciences*, *14*(1), Article 10. https://doi.org/10.3390/app14010010

19. Xi, Z., Wu, Y., Xiang, S., Sun, C., Wang, Y., Yu, H., Fu, Y., Wang, X., Yan, J., & Zhao, D. (2020). Corrosion resistance and biocompatibility assessment of a biodegradable hydrothermal-coated Mg-Zn-Ca alloy: An in vitro and in vivo study. *ACS Omega*, *5*, 4548–4557. https://doi.org/10.1021/acsomega.9b03889

20. Yuan, W., Panigrahi, S. K., Su, J.-Q., & Mishra, R. S. (2011). Influence of grain size and texture on Hall-Petch relationship for a magnesium alloy. *Scripta Materialia*, *65*, 994–997. https://doi.org/10.1016/j.scriptamat.2011.08.028

21. Zhang, T., Wang, W., Liu, J., Wang, L., Tang, Y., & Wang, K. (2022). A review on magnesium alloys for biomedical applications. *Frontiers in Bioengineering and Biotechnology*, *10*, Article 953344. https://doi.org/10.3389/fbioe.2022.953344

22. Zhang, X., Yuan, G., Niu, J., Fu, P., & Ding, W. (2012). Microstructure, mechanical properties, biocorrosion behavior, and cytotoxicity of as-extruded Mg-Nd-Zn-Zr alloy with different extrusion ratios. *Journal of the Mechanical Behavior of Biomedical Materials*, *9*, 153–162. https://doi.org/10.1016/j.jmbbm.2012.02.002

Received 12.03.2026
Accepted 20.03.2026
Published 07.05.2026

DOI 10.15588/1607-6885-2026-2-2

УДК 669.721.5:621.785.7

МІКРОСТРУКТУРА, МЕХАНІЧНІ ВЛАСТИВОСТІ ТА КОНТРОЛЬОВАНА ДЕГРАДАЦІЯ БІОРОЗЧИННОГО СПЛАВУ MG-3,15ND-1,25ZR-0,6ZN ДЛЯ ІМПЛАНТІВ ОСТЕОСИНТЕЗУ: ПРОМИСЛОВА ТЕХНОЛОГІЯ ТА ПОРІВНЯЛЬНА ОЦІНКА ЗІ СПЛАВОМ МЛ10

Микита Айкін — старший викладач кафедри фізичного матеріалознавства, Національний університет «Запорізька політехніка», Запоріжжя, Україна, *e-mail: fitone14@gmail.com*, ORCID: 0000-0001-9513-2804

Вадим Шаломєєв — д-р техн. наук, професор, Національний університет «Запорізька політехніка», Запоріжжя, Україна, *e-mail: shalomeev@zntu.edu.ua*, ORCID: 0000-0002-6091-837X

Євген Вишенко — студент групи ІФ-213сп, Національний університет «Запорізька політехніка», Запоріжжя, Україна

Мета. *Оцінити мікроструктуру, механічні властивості та деградаційну поведінку біорозчинного сплаву Mg-3,15Nd-1,25Zr-0,6Zn (мас.%), виготовленого за промислово сумісною технологією, та продемонструвати його переваги над сплавом МЛ10 для остеосинтезу з кінетикою деградації, синхронізованою із загоєнням кістки.*

Методи дослідження. *Мікроструктуру досліджували методами оптичної мікроскопії (Neophot 32, OLYMPUS IX 70) та СЕМ/ЕДС (SELMI РЕМ-106І). Розмір зерна визначали методом перетинів (ISO 643:2024). Механічні властивості вимірювали на машині INSTRON 2801 (ASTM B557, ISO 6892-1) у термічно обробленому стані та після 90-добової витримки у Гелофузині (pH 7,4), Венофундині (pH 5,5) та фізіологічному розчині при 36 ± 1 °C. Швидкість корозії визначали гравіметричним методом. Термічну обробку проводили в атмосфері аргону у печах Bellevue та ПАП-4М. Промислові випробування виконано на кісточкових гвинтах трьох типорозмірів на АТ «Мотор Січ».*

Результати. *Після лиття у водоохолоджувану мідну виливницю (25–30 °C/с) та двоступеневої термічної обробки (560 °C/8 год + 200 °C/16 год) сплав має розмір зерна 57 ± 4,7 мкм (на 50% менше за МЛ10) з чистими межами, що містять дисперсні частинки Zn_2Zr_3 та β″ замість безперервних мереж $(Mg,Zn)_{12}Nd$. Границя міцності — 309 ± 6,5 МПа, границя текучості – 252 ± 6,5 МПа, подовження – 7,9 ± 0,65%, що на 31%, 33% та 126% вище за МЛ10. Швидкості корозії (0,45–0,68 мм/рік) на 39–42 % нижчі за МЛ10. Після 90 діб сплав зберіг 58–76 % початкової міцності (182–230 МПа), підтримуючи >180 МПа протягом критичного 12-тижневого періоду, проти 38–42 % для МЛ10. Промислові випробування на трьох типорозмірах гвинтів підтвердили відтворюваність.*

Наукова новизна. *Вперше систематично оцінено взаємозв'язок мікроструктури, механічних властивостей та кінетики деградації сплаву Mg-3,15Nd-1,25Zr-0,6Zn у трьох біологічних рідинах із порівнянням з МЛ10 та вимогами загоєння кістки. Встановлено, що усунення міжзеренних мереж $(Mg,Zn)_{12}Nd$ разом із подрібненням зерна до 57 мкм змінює механізм корозії з міжкристалітного (150–200 мкм) на рівномірний поверхневий (<50 мкм), забезпечуючи синхронізацію деградації зі стадіями загоєння.*

Практична цінність. *Промислово масштабовану технологію валідовано у дослідному виробництві кісточкових гвинтів трьох типорозмірів із використанням стандартної тигельної плавки, лиття у мідну виливницю та конвенційної термічної обробки. Сплав забезпечує достатній запас міцності протягом усіх критичних фаз загоєння (тижні 0–20), перевершуючи МЛ10 та відповідаючи доклінічним вимогам до біодеградуючих ортопедичних фіксаторів.*

Ключові слова: *біодеградуючий магнієвий сплав, система Mg-Zr-Nd-Zn, остеосинтез, мікроструктура, механічні властивості, біокорозія, контрольована деградація, загоєння кістки, кісточковий гвинт, сплав МЛ10.*

Список літератури

1. Aikin M., Shalomeev V. Optimization of heat treatment regime for a new biodegradable Mg-Zr-Nd alloy with enhanced mechanical properties. *Innovative Materials and Technologies in Metallurgy and Mechanical Engineering*. 2024. С. 31–38. DOI: https://doi.org/10.15588/1607-6885-2024-3-5

2. Aikin M., Shalomeev V., Kukhar V. et al. Recent advances in biodegradable magnesium alloys for medical implants: evolution, innovations, and clinical translation. *Crystals*. 2025. Vol. 15, № 8. Article 671. DOI: https://doi.org/10.3390/cryst15080671

3. Aikin M., Shalomeev V., Lukyanenko O. Дослідження впливу високих швидкостей охолодження при кристалізації на структуру та властивості сплаву системи Mg-Zr-Nd. Innovative

DOI 10.15588/1607-6885-2026-2-2

Materials and Technologies in Metallurgy and Mechanical Engineering. 2021. DOI: https://doi.org/10.15588/1607-6885-2021-1-4

4. ASTM International. Standard guide for laboratory immersion corrosion testing of metals (ASTM G31-72R04). 2004. DOI: https://doi.org/10.1520/G0031-72R04

5. ASTM International. Standard test methods for tension testing wrought and cast aluminum- and magnesium-alloy products (ASTM B557-15). 2023.

6. Dangwal S., Edalati K., Valiev R. Z., Langdon T. G. Breaks in the Hall-Petch relationship after severe plastic deformation of magnesium, aluminum, copper, and iron. *Crystals*. 2023. Vol. 13, № 3. Article 413. DOI: https://doi.org/10.3390/cryst13030413

7. Poinern G. E. J., Brundavanam S., Fawcett D. Biomedical magnesium alloys: a review of material properties, surface modifications and potential as a biodegradable orthopaedic implant. *American Journal of Biomedical Engineering*. 2013. Vol. 2, № 6. P. 218–240. DOI: https://doi.org/10.5923/j.ajbe.20120206.02

8. Gracheva A., Polozov I., Popovich A. Additive manufacturing of biodegradable metallic implants by selective laser melting: current research status and application perspectives. *Metals*. 2025. Vol. 15, № 7. Article 754. DOI: https://doi.org/10.3390/met15070754

9. Metallic materials. Tensile testing. Part 1: Method of test at room temperature (ДСТУ ISO 6892-1:2019). Київ, 2019.

10. Steels – Micrographic determination of the apparent grain size (ISO 643:2024). 2024.

11. Jin S. та ін. Mechanical properties, biodegradability and cytocompatibility of biodegradable Mg-Zn-Zr-Nd/Y alloys. *Journal of Materials Science & Technology*. 2020. Vol. 47. P. 190–201. DOI: https://doi.org/10.1016/j.jmst.2020.02.017

12. Lin X. та ін. Biodegradable Mg-based alloys: biological implications and restorative opportunities. *International Materials Reviews*. 2023. Vol. 68, № 4. P. 365–403. DOI: https://doi.org/10.1080/09506608.2022.2079367

13. Liu C. та ін. Biodegradable magnesium alloys developed as bone repair materials: a review // Scanning. 2018. Vol. 2018. P. 1–15. DOI: https://doi.org/10.1155/2018/9216314

14. Maier H. J. та ін. Magnesium alloys for open-pored bioresorbable implants. *JOM*. 2020. Vol. 72. P. 1859–1869. DOI: https://doi.org/10.1007/s11837-020-04078-8

15. Morgan E. F., Unnikrisnan G. U., Hussein A. I. Bone mechanical properties in healthy and diseased states. *Annual Review of Biomedical Engineering*. 2018. Vol. 20. P. 119–143. DOI: https://doi.org/10.1146/annurev-bioeng-062117-121139

16. Müller E. et al. The biological effects of magnesium-based implants on the skeleton and their clinical implications in orthopedic trauma surgery. *Biomaterials Research*. 2024. Vol. 28. Article 0122. DOI: https://doi.org/10.34133/bmr.0122

17. Shalomeev V., Aikin N., Chorniy V., Naumik V. Design and examination of the new biosoluble casting alloy of the system Mg-Zr-Nd for osteosynthesis. *Materials Science*. 2019.

18. Thomas K. K. et al. Biodegradable magnesium alloys for biomedical implants: properties, challenges, and surface modifications with a focus on orthopedic fixation repair. *Applied Sciences*. 2023. Vol. 14, № 1. Article 10. DOI: https://doi.org/10.3390/app14010010

19. Xi Z. et al. Corrosion resistance and biocompatibility assessment of a biodegradable hydrothermal-coated Mg-Zn-Ca alloy: an in vitro and in vivo study. *ACS Omega*. 2020. Vol. 5. P. 4548–4557. DOI: https://doi.org/10.1021/acsomega.9b03889

20. Yuan W. та ін. Influence of grain size and texture on Hall-Petch relationship for a magnesium alloy. *Scripta Materialia*. 2011. Vol. 65. P. 994–997. DOI: https://doi.org/10.1016/j.scriptamat.2011.08.028

21. Zhang T. et al. A review on magnesium alloys for biomedical applications. *Frontiers in Bioengineering and Biotechnology*. 2022. Vol. 10. Article 953344. DOI: https://doi.org/10.3389/fbioe.2022.953344

22. Zhang X. et al. Microstructure, mechanical properties, biocorrosion behavior, and cytotoxicity of as-extruded Mg-Nd-Zn-Zr alloy with different extrusion ratios. *Journal of the Mechanical Behavior of Biomedical Materials*. 2012. Vol. 9. P. 153–162. DOI: https://doi.org/10.1016/j.jmbbm.2012.02.002

DOI 10.15588/1607-6885-2026-2-2

КОНСТРУКЦІЙНІ І ФУНКЦІОНАЛЬНІ МАТЕРІАЛИ

STRUCTURAL AND FUNCTIONAL MATERIALS

UDC 621.74.045:669.715:669.018.25

Serhii Puchek — Postgraduate student of the Department of Transport Technologies, National University Zaporizhzhia Polytechnic, Zaporizhzhia, Ukraine, *e-mail: puchek777@gmail.com*, ORCID: 0009-0007-8077-6106

Sergiy Byelikov — Doctor of Technical Sciences, Professor of the Department of Transport Technologies, National University Zaporizhzhia Polytechnic, Zaporizhzhia, Ukraine, *e-mail: belikov@zp.edu.ua*, ORCID: 0000-0002-9510-8190

STUDY OF THE STRUCTURE AND PROPERTIES OF WORKING BLADES OF AIRCRAFT GAS TURBINE ENGINES MADE OF HEAT-RESISTANT NICKEL ALLOY ZhS26-VI

Purpose. *To study the macro- and microstructural condition of VK-2500 gas turbine engine rotor blades in their original condition and after various processing stages. To evaluate their mechanical properties and long-term strength.*

Research methods*. The material quality of first-stage gas turbine engine rotor blades made of Zhs26-VI heat-resistant nickel alloy was studied in their original condition and after hot isostatic pressing (HIP), as well as after HIP and standard heat treatment. Luminescence testing of the blades was performed using the LUM1-OV method. Microstructure examination was performed using optical microscopy (Neophot-32 microscope) and scanning electron microscopy (JSM T-300 microscope).*

Mechanical properties at room temperature were determined in accordance with ISO 6892-84 and ST SEV 471-88, and heat resistance parameters were determined in accordance with DSTU ISO 204:2019.

Results*. Metallographic studies revealed that the microstructure of the rotor blades is single-crystalline, with the main structural components being: γ′- solid solution with the presence of the intermetallic γ′- phase, the eutectic (γ-γ′) phase, carbides, and carbonitrides. A reduction in the size of the structural components is observed in the microstructure of the blades after HIP.*

Scientific novelty*. New data on the structure and phase composition of the rotor blade material for aircraft gas turbine engines have been obtained. Heat treatment under standard conditions after HIP corresponds to almost complete recrystallization of the strengthening intermetallic γ′- phase, which consists of dissolution of the γ′- phase in the γ- matrix and its re-precipitation as dispersed particles of cubic morphology.*

Practical value*. It has been shown that hot isostatic pressing in combination with standard heat treatment provides the most favorable combination of strength and ductility properties, as well as long-term durability of blades.*

Key words*: superalloys, gas turbine blades, homogenization, hot isostatic pressing, intermetallic γ′-phase.*

Introduction

The development of aircraft and stationary gas turbine engineering requires improved performance parameters for gas turbine engines (GTEs), specifically turbine inlet temperatures, increased specific power, and increased efficiency and service life [1].

The reliability and durability of a GTE primarily depend on the performance parameters of the materials used to manufacture the most critical GTE components – the rotor blades and nozzle vanes. Heat-resistant nickel-based alloys are the most common materials used to manufacture these components. Such materials are typically referred to as “superalloys” [2–7].

Technological support for the performance characteristics of GTE components shapes approaches to achieving the required material parameters for GTEs [8–10]. For modern GTEs, the optimal material for both cooled and uncooled rotor blades is high-strength cast nickel alloys, one of which is the ZhS26-VI alloy [10, 15].

One of the characteristic defects of the cast structure of blades with very complex geometry is the presence of internal shrinkage defects [13]. Hot isostatic pressing (HIP) is often used to eliminate such defects [12, 14].

Material and Methodology

The chemical composition of the experimental alloys was determined using a spectral analyzer on an ARL-4460 quantometer.

DOI 10.15588/1607-6885-2026-2-3

The material quality of first-stage rotor blades for the VK-2500 gas turbine engine, cast from ZhS26-VI heat-resistant nickel alloy using high-speed directional solidification (HSDS), was studied:

Variant "1" – after hot isostatic pressing (HIP);

Variant "2" – after HIP and heat treatment using the standard procedure (homogenization at 1265±10°C for 1 hour 15 minutes, vacuum).

The studies were compared to similar blades without the HIP procedure – variant "0".

The HIP process was conducted under actual production conditions at Motor Sich JSC using the following procedure [10]:

- Initial pressure in the high-pressure furnace: 51 MPa;
- Heating from room temperature to T=1040±10 °C at a rate of 90 °C/min;
- Holding at 1040 °C for 1 hour;
- Pressure in the high-pressure furnace at 1040 °C: 120 MPa;
- Heating to 1250±10 °C at a rate of 5 °C/min;
- Holding at 1250±10 °C for 1.5 hours;
- Pressure in the high-pressure furnace at 1250 °C: 170 MPa;
- Cooling of castings to 800 °C at a rate of 30 °C/min.

The chemical composition of the rotor blades received for testing (variant "0", "1", and "2") is presented in Table 1.

Luminescence testing of the root axial section and the airfoil cross-section was performed using the LUM1-OV method.

Microstructure was examined using optical (Neophat-32 microscope) and scanning electron microscopy (JSM T-300 microscope) on unetched and etched microsections cut from rotor blades.

The state of the strengthening intermetallic γ′- phase in the axes and interaxial spaces of the airfoil and airfoil dendrites of rotor blades tested in variants "0", "1" and "2" was studied on microsections after electrolytic etching in a reagent consisting of 80 ml of H_3PO_4 and 10g of CrO_3, using a JSM T-300 scanning electron microscope.

Mechanical properties at room temperature (tensile strength, relative elongation and contraction) were determined in accordance with DSTU ISO 6892-84 and ST SEV 471-88, and heat resistance indicators in accordance with DSTU ISO 204:2019 on a DST-500 test bench at a temperature of 975 °C and a load of 260 MPa until complete destruction.

Research Results

Inspection of the blades received for testing revealed that the blade surfaces before HIP (variant "0") and after HIP and heat treatment (variant "2") had a light gray matte color (Fig.1*a*, *b*, *d*, *e*, *f*). After HIP (variant "1"), the blade surfaces were dark gray (Fig.1c, d).

A metallographic examination of the blade surfaces after hot isostatic pressing (variant "1") revealed dark-gray non-metallic inclusions, characteristic for oxides, penetrating to a depth of ~10 μm (Fig. 2).

The blade surfaces before HIP (variant "0") and after HIP + heat treatment at 1265 °C (variant "2") show virtually no oxidation. The absence of oxidation on the surfaces of parts processed using variant 2 is due to the use of micropowder blasting on the outer surface during preparation of the blades for heat treatment, as well as vacuum cleaning of the surface during high-temperature vacuum treatment after HIP.

X- ray spectral microanalysis (XSMA) of rotor blades in their original cast condition (before HIP, without heat treatment – Fig. 3), and those after HIP (without subsequent heat treatment – Fig. 4) showed that the oxygen, aluminum, titanium, and carbon content on the surfaces of the parts after HIP is approximately three times higher than the concentrations of these elements on the surfaces of the original blades (before HIP). The increase in the concentrations of these elements on the surface of blades that underwent HIP indicates oxidation due to the use of insufficiently pure argon during the HIP process.

Furthermore, the simultaneous application of high temperatures (1250 °C) and pressures (170 MPa) during isostatic pressing leads to intense diffusional mass transfer of aluminum and titanium atoms from the center to the surface, forming layers enriched with these elements on the alloy surface. This is also consistent with literature data on the diffusion of aluminum and titanium in nickel [4].

Luminescence testing using the LUM1-OV method in the axial section of the root and the cross-section of the airfoil of the incoming blades revealed that the blades before HIP exhibited a glow in the form of multiple small, brightly luminous dots (Fig. 5*a*, *b*). No phosphor glow was detected in similar sections of blades after HIP (Fig. 5*c*, *d*, *e*).

Metallographic examination revealed that the microstructure of the rotor blades submitted for examination is single-crystal. The main structural components are a γ-solid solution with the presence of intermetallic γ′-phase, a eutectic phase (γ-γ′), carbides, and carbonitrides (Figure 6).

Table 1 – Chemical composition of the rotor blades tested, made of ZhS26-VI alloy

Variant	Contents of elements, %										
	C	Cr	Co	W	Al	Ti	Mo	Fe	Nb	Si	V
0	0,15	4,68	8,95	12,00	6,10	0,89	1,04	<0,5	1,48	<0,2	1,04
1	0,14	4,77	9,03	11,72	6,10	0,90	0,91	<0,5	1,46	<0,2	0,91
2	0,14	4,76	9,07	11,59	5,94	0,90	0,99	<0,5	1,46	<0,2	0,99
Norms ТУ1-92-177-91	0,12-0,18	4,3-5,6	8,0-10,0	10,9-12,5	5,5-6,2	0,8-1,2	0,8-1,4	≤ 1,0	1,4-1,8	≤ 0,3	0,8-1,2

DOI 10.15588/1607-6885-2026-2-3

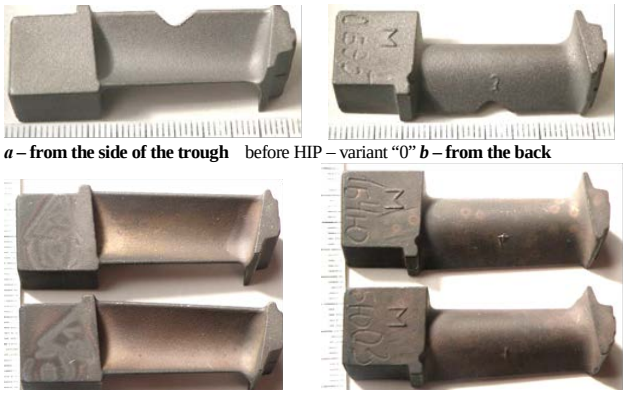

***a* – from the side of the trough** before HIP – variant "0" ***b* – from the back**

c – from the side of the trough **after HIP – variant "1"** *d* – from the back

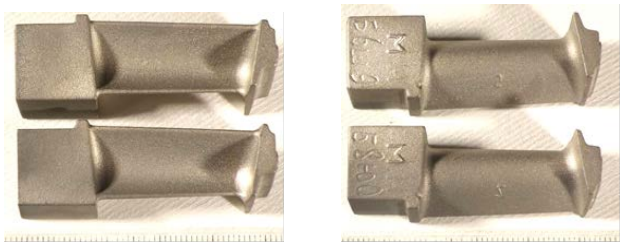

e – from the side of the trough **after HIP + HT – variant "2"** *f* – from the back

Figure 1. External appearance of rotor blades before (*a*, *b*) and after (*c*, *d*) hot isostatic pressing (HIP), as well as after HIP and subsequent heat treatment at 1265 °C (vacuum) (*e*, *f*)

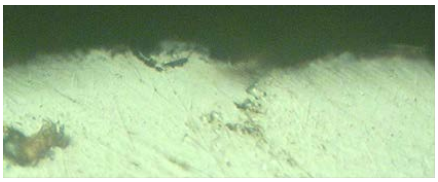

Figure 2. Microstructural condition of the rotor blade surface after HIP – variant "1", ×650

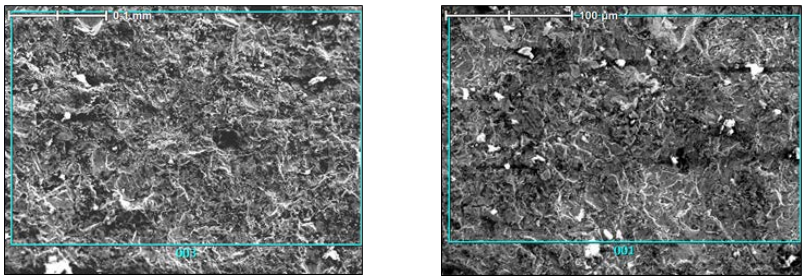

a – ×350 *b* – ×450

№ points	C	O	Al	Ti	V	Cr	Co	Ni	Nb	Fe	Mo	W
001	5,09	5,56	13,89	1,71	0,90	4,54	8,05	54,06	0,83		1,15	4,23
003	5,31	6,92	14,64	1,88		5,75	7,76	48,89		2,19	1,09	5,57

Figure 3. Results of X- ray microanalysis of the surface of a working blade made of ZhS26-VI(HSDS) alloy before the HIP operation: *a* – blade root; *b* – blade airfoil

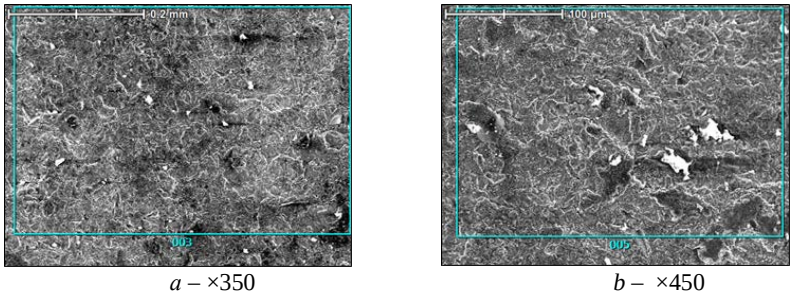

a – ×350 *b* – ×450

№ points	C	O	Al	Ti	V	Cr	Co	Ni	Nb	Mo	W
003	4,87	17,00	33,50	16,91	1,69	6,07		9,12	6,35	1,13	3,35
005	5,37	19,59	31,65	16,78	2,87	3,52	0,86	8,46	6,76	1,60	2,56

Figure 4. Results of X-ray microanalysis of the surface layer of a working blade made of ZhS26-VI(HSDS) alloy after the HIP operation: *a* – blade root; *b* – blade airfoil

DOI 10.15588/1607-6885-2026-2-3

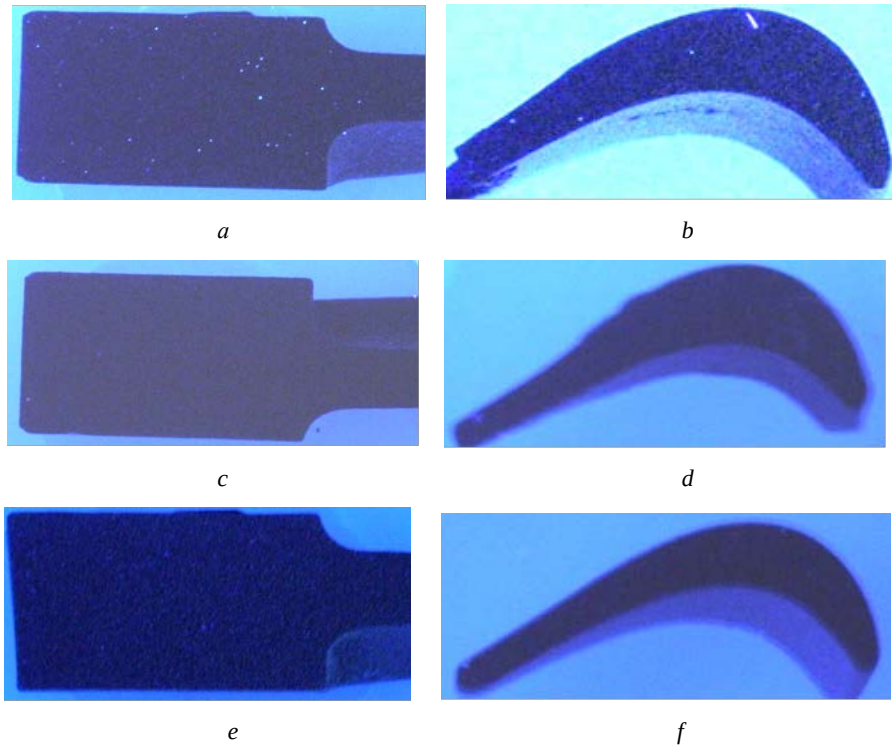

Figure 5. External appearance of rotor blades in the axial section of the root section (*a*, *c*, *e*) and in the cross-section of the airfoil (*b*, *d*, *f*) under a radiation source:
a, *b* – variant "0" – before HIP; *c*, *d* – variant "1" – after HIP; *e*, *f* – variant "2" – after HIP and heat treatment

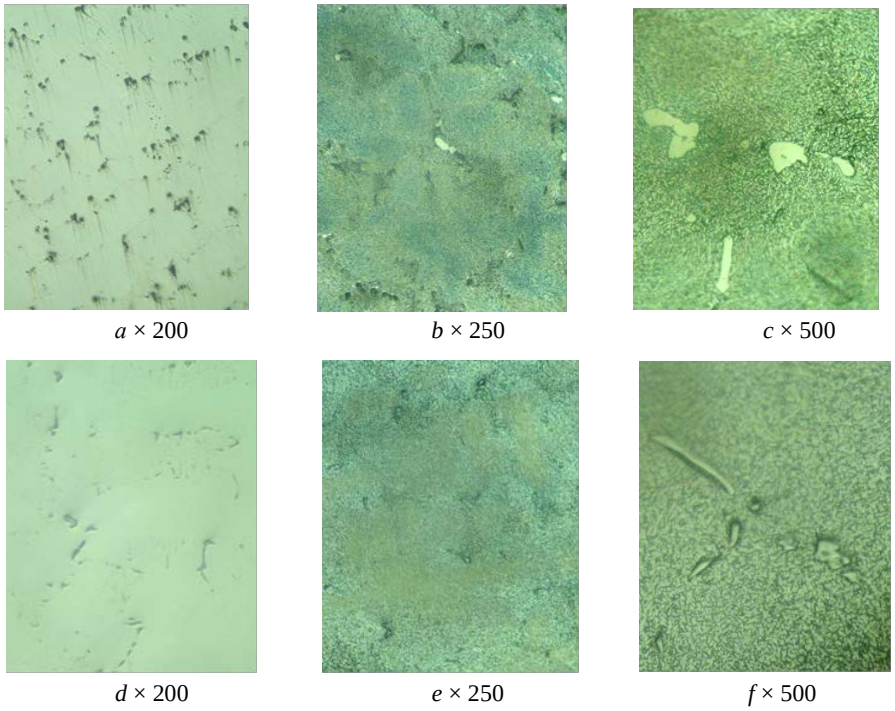

Figure 6. Microstructure of a rotor blade before the HIP operation – variant "0": *a*, *b*, *c* – airfoil; *d*, *e*, *f* – root

The microstructure of rotor blades after HIP shows a reduction in the size of the structural components compared to the blades before the HIP operation. The size of the structural components, as well as the distance between the axes of the second-order dendrites in the blade airfoil, differs slightly from the microstructure parameters in the root section (Table 2).

DOI 10.15588/1607-6885-2026-2-3

A microstructural study revealed that during hot isostatic pressing (HIP) at 1250 °C and 170 MPa (variant 1), significant dissolution and recrystallization of the eutectic phase (γ-γ′) occurred. Coagulated γ′- phase particles were observed in the interdendritic spaces. The microstructure of the rotor blade material after HIP is satisfactory, corresponding to the approved microstructure scale without overheating (Figure 7).

During a microstructural study using optical and scanning electron microscopy on etched microsections cut from rotor blades that had undergone the HIP operation (variant "1"), crater-shaped zones in the form of concentrically located elongated particles of the strengthening intermetallic γ′-phase, characteristic of a "raft" structure [10] (Figure 8), were identified in areas of complete or partial "healing" of micropores. Similar areas characterized by the formation of a "raft" structure were also found around some MC-type carbides (Figure 9). It was found that, as the center of these regions approaches, corresponding to the direction of the resulting stresses, an increase in the density and distortion of intermetallic particles, whose size ranges from 0.22 to 0.27 μm, is observed. Consequently, as a result of plastic deformation initiated by the hot isostatic pressing process, the concentration of distortions of structural components within the local volume of the material, in zones adjacent to micropores, carbides, etc., increases significantly.

Table 2 – Parameters of the structural components of rotor blades made of ZhS26-VI(HSDS) alloy

Material condition		Dimensions of structural components, μm			
		carbides		eutectic type (γ-γ′)	micropores
		globular type MS	eutectic type M_6C		
original (without HIP) before heat treatment	airfoil	2…6	8…15 (single up to 35)	8…14	6…43
	root	3…15	10…18 (single up to 40)	8…16	10…60
after HIP without heat treatment	airfoil	1,5…8	8…14 (single up to 28)	6…12	-
	root	2…12	8…16 (single up to 30)	8…15	-
after HIP without heat treatment heat treatment	airfoil	1,5…6	6…14 (single up to 20)	4…10	-
	root	2…12	8…16 (single up to 35)	5…14	-

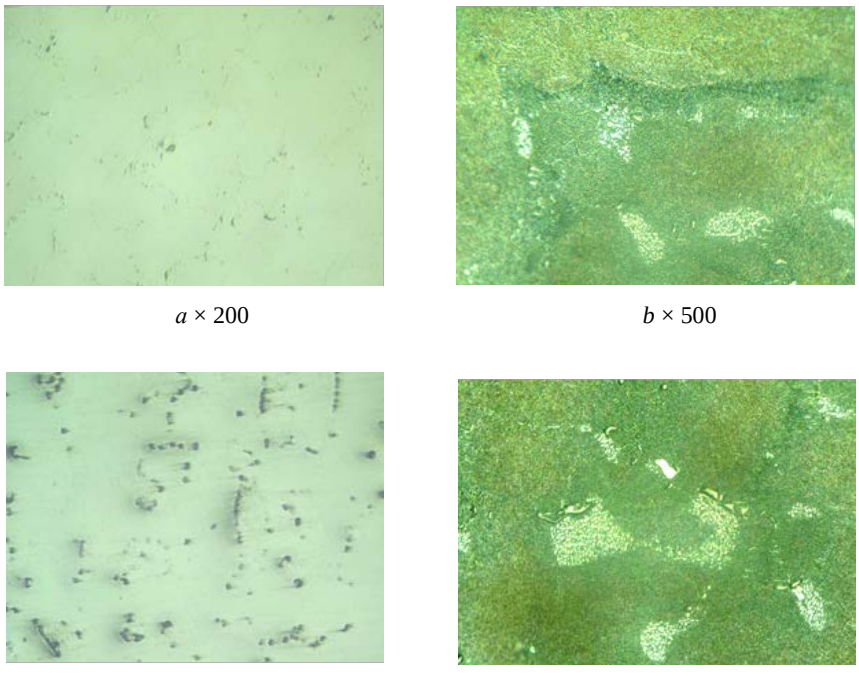

a × 200 *b* × 500

c × 200 *d* × 500

Figure 7. Microstructure of the airfoil (*a*, *b*) and root (c, d) of a rotor blade after HIP – variant "1": *a*, *c* – before etching; *b*, *d* – after etching

DOI 10.15588/1607-6885-2026-2-3

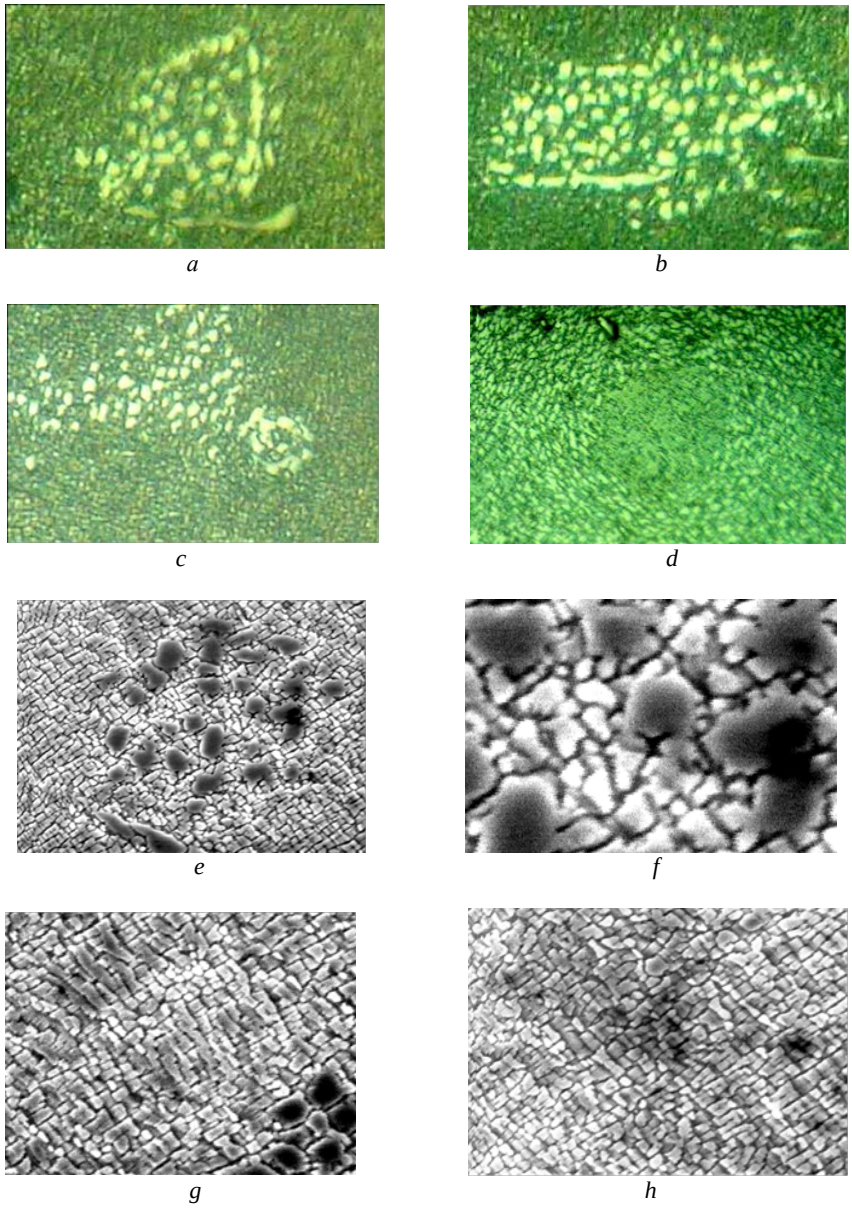

Figure 8. "Raft" structure in the material of working blades after the HIP operation in the areas of "healing" of micropores: *a*, *b*, *c*, *d* – optical microscopy – × 700; *e*, *f*, *g*, *h* – scanning electron microscopy – × 7500

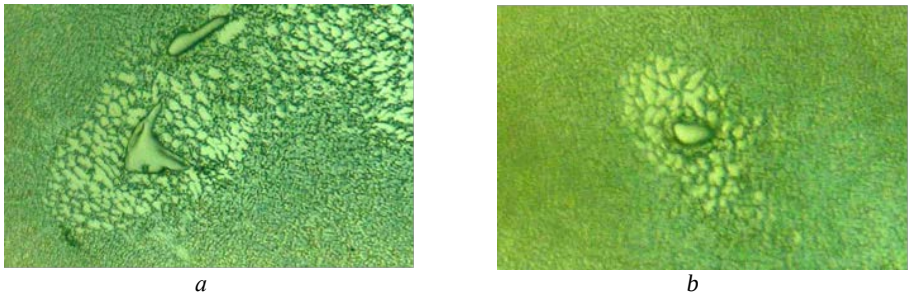

Figure 9. "Raft" structure in rotor blade material after HIP around MC-type carbides, × 700

DOI 10.15588/1607-6885-2026-2-3

In the “healed” zones of micropores, along with small intermetallic particles, a cluster of coagulated elongated γ′-phase particles measuring 1.1–2.2 μm is also observed.

The size of individual micropores detected after HIP does not exceed ~ 0.2 μm, which is approximately 100–300 times smaller than the pores found in the blades before HIP. Heat treatment according to the standard mode after gas-static treatment (variant “2”) promotes almost complete recrystallization of the strengthening intermetallic γ′-phase, which consists of dissolution of the γ′- phase in the γ′- matrix and its repeated precipitation in the form of dispersed particles of cubic morphology with the presence of a small amount of coagulated intermetallic γ′- phase precipitated in the interdendritic spaces (Figure 10).

The study of the state of the strengthening intermetallic γ′- phase in the axes and interaxial spaces of the airfoil and root dendrites of rotor blades processed according to variants “0”, “1”, and “2” revealed that in the original material of cast blades (before HIP), the γ′- phase particles have a cubic morphology and form blocks consisting of four particles. The size of the γ- particles, measured along the side of a square equivalent in area, in the dendrite axes is mainly 0.38...0.57 μm (Fig. 11*a*; Table 3). In the interaxial spaces of the dendrites, along with γ′- particles measuring ~ 0.6 μm, there is a significant amount of coagulated phase up to 1.5 μm (Figure 11*b*).

No significant differences in the morphology and size of the intermetallic phase precipitated in the blade's root compared to its airfoil are observed.

In the blade structure after isostatic pressing, a refinement of the intermetallic γ′- phase is observed (Fig. 11*c*, *d*). The size of the γ′- particles is approximately half that of the original alloy (see Table 3). In the blade material after isostatic pressing, the precipitation of a small amount of γ′-phase microparticles measuring 0.07–0.1 μm was detected, as well as zonal interdendritic precipitates of coagulated intermetallic particles reaching 2.57 μm in size.

During homogenization at 1265 °C for 1 hour 15 minutes, carried out after the isostatic pressing operation, the particle sizes of the γ′- intermetallic phase in the axes and interaxial spaces of the dendrites were equalized (Fig. 11*e*, *f*). It should be noted that the alloy structure retains zonal areas with the presence of coagulated γ′- particles measuring 1.1...2.86 μm, located between the axes (Fig. 12). The mechanical and heat-resistant properties were determined on unheat-treated samples (Ø15 mm; L=135 mm), cast using the directional solidification method, as well as after heat treatment according to the standard mode (homogenization at a temperature of 1265±10 °C for 1 hour 15 minutes). The results of mechanical tests and long-term strength tests are presented in Table 4.

Heat treatment according to the standard mode after HIP (variant “2”) promotes increased ductility of the alloy, while maintaining its strength and heat-resistant properties, which is due to an increase in the structural homogeneity of the alloy and the relaxation of stresses induced during hot isostatic pressing.

The most favorable combination of strength and ductility characteristics, as well as long-term strength, was achieved in samples processed using the second method (HIP + standard heat treatment).

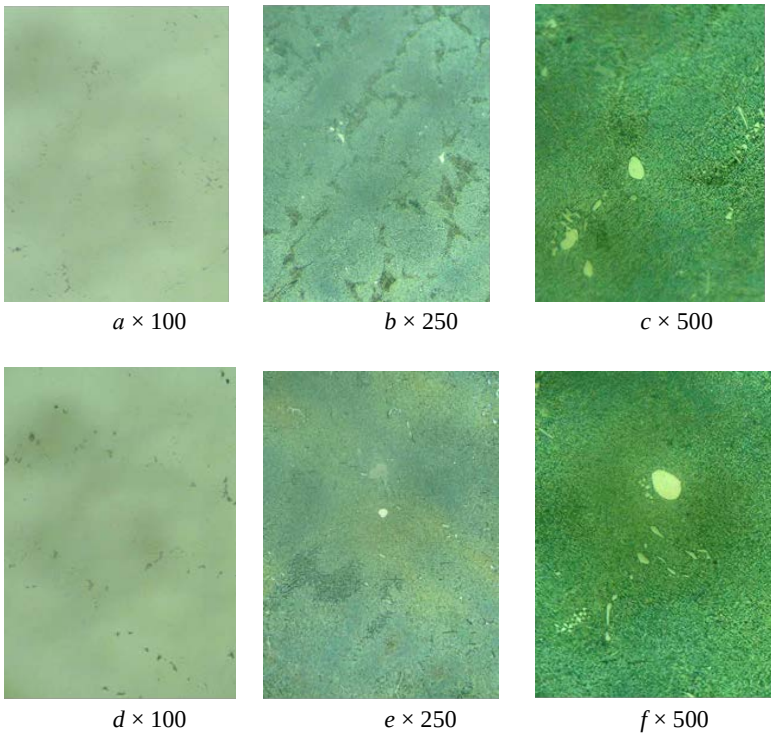

a × 100 *b* × 250 *c* × 500

d × 100 *e* × 250 *f* × 500

Figure 10. Microstructure of rotor blades after HIP and heat treatment – variant “2”: *a*, *b*, *c* – airfoil; *d*, *e*, *f* – root

DOI 10.15588/1607-6885-2026-2-3

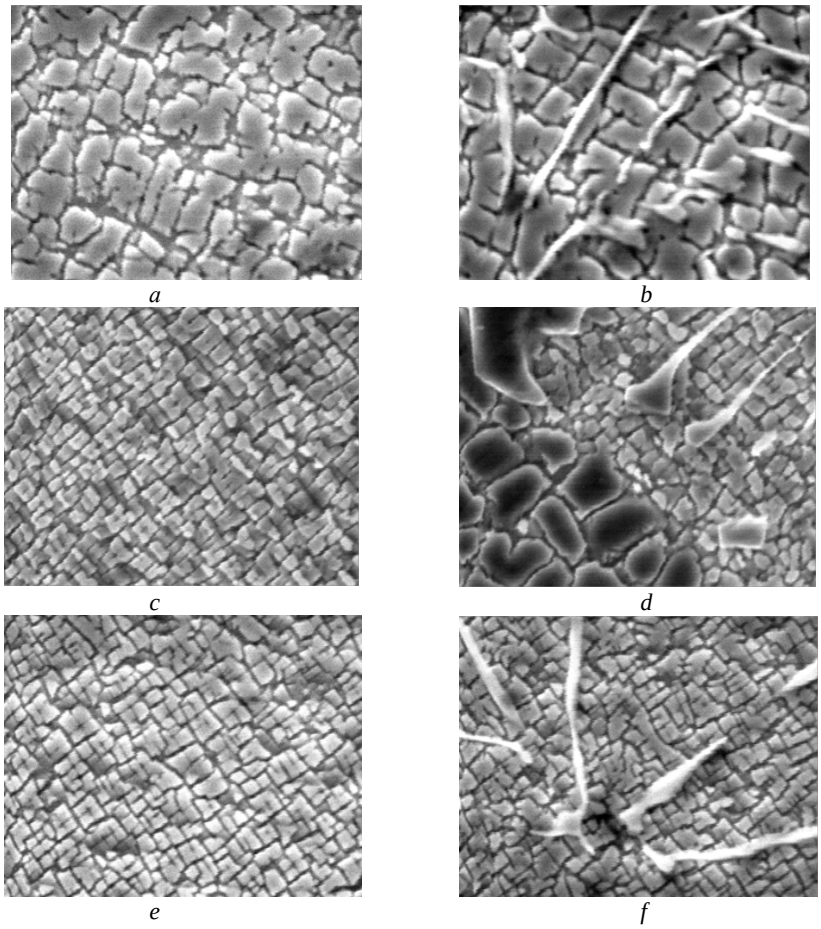

Figure 11. State of the intermetallic γ′- phase in the axes (a, c, e) and interaxial spaces of dendrites (*b*, *d*, *f*) of rotor blades cast from the ZhS26-VI (HSDS) alloy, × 10000:

a, *b* – before the HIP operation (without heat treatment) – variant "0"; *c*, *d* – after the HIP operation (without heat treatment) – variant "1"; *e*, *f* – after the HIP operation and heat treatment –variant "2"

Table 3 – Sizes of γ′-phase particles in the material of rotor blades made of the ZhS26-VI alloy, manufactured in accordance with variants "0", "1"and "2"

Measurement area		Particle size of the particles γ′-phase, μm		
		before HIP	after HIP	after the HIP + HT
airfoil	axes	0,35…0,52	0,20…0,27 (microparticles – 0.07…0.09 μm)	0,20…0,25
	interaxle	0,058…0,93 (coagulated particles – up to 1.5 microns)	0,24…0,50 (microparticles – 0.08…0.1 μm)	0,22…0,38 (coagulated particles – 1.1…2.8 μm)
root	axes	0,38…0,57	0,21…0,29 (microparticles – 0.07…0.09 μm)	0,21…0,25
	interaxle	0,06…1,0 (coagulated particles – up to 1.5 microns)	0,24…0,57 (microparticles – 0.08…0.1 μm)	0,24…0,38 (coagulated particles – 1.1…2.86 μm)

Figure 13 shows the fractographic structure of fractures obtained during tensile testing of specimens cast from the ZhS26-VI(HSDS) alloy – before the HIP operation, after HIP, and after HIP and standard heat treatment. It was established that fracture of the specimens processed according to different options during testing occurred along the [001] crystallographic plane.

DOI 10.15588/1607-6885-2026-2-3

Table 4 – Mechanical and heat-resistant properties of the ZhS26-VI alloy before and after hot isostatic pressing

Material condition	Mechanical properties at t=20°C			Time to failure ($T_{исп.}$=975 °C, и σ= 260 MPa), τ_r, hours
	$\sigma_в$, MPa	δ, %	Ψ, %	
original (without HIP) without heat treatment	96,5	6,0	-	70^{20}
original (without HIP) after standard heat treatment	92,5 120,7	24,0 12,8	18,5 10,7	54^{30} 59^{30}
after HIP	103,2 104,3	6,4 6,2	8,99 9,36	57^{30} 57^{00}
after hot-pressing and standard heat treatment	102,8 102,9	8,0 11,2	11,2 11,6	56^{00} 63^{00}
Norms H28ТУ-190	≥ 85,0	≥ 6,0	-	≥ 40,0

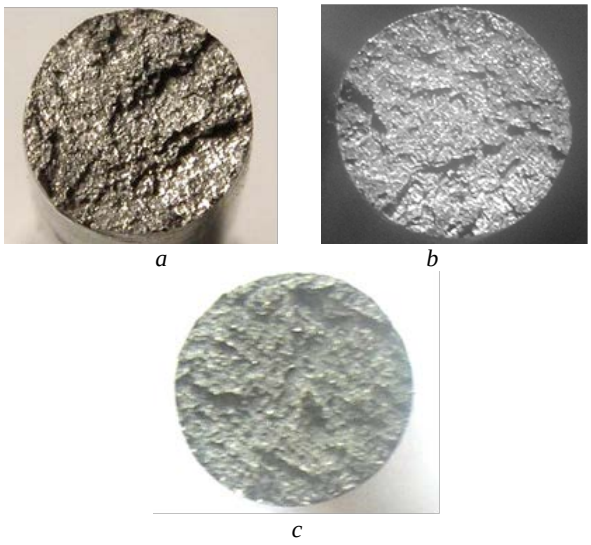

a *b* *c*

Figure 13. Fracture structure of specimens cast from the ZhS26-VI (HSDS) alloy:
a – before the HIP operation (variant "0"); *b* – after the HIP operation (variant "1"); *c* – after the HIP operation and heat treatment (variant "2")

Conclusions

1. Hot isostatic pressing (HIP) at 1250°C and 170 MPa (Variant 1) improves the quality of turbine blade castings made from ZhS26-VI (HSDS) alloy by stabilizing the structure and properties due to a reduction in microporosity during pore healing.

2. Heat treatment using the standard regime (homogenization at 1265 °C for 1 hour 15 minutes) after overpressure treatment (Variant 2) improves the structural homogeneity of the alloy and relaxes stresses induced during HIP, which has a positive effect on the ductility of the alloy while maintaining its strength and heat-resistant properties.

3. Processing according to the 2nd option (HIP + homogenization at a temperature of 1265 °C for 1 hour 15 minutes) ensures the most favorable combination of strength and plasticity characteristics, as well as long-term strength.

References

1. Chigrin, V. S. (2017). Design and strength of aircraft engines. KhAI, 420.

2. Miller, H. E., & Chambers, W. L. (1987). Constructions of gas turbines and superalloys. In C. T. Sims, N. S. Stoloff, & W. C. Hagel (Eds.), Superalloy II: High temperature materials for aerospace and industrial power (2nd ed., pp. 27–56). John Wiley & Sons.

3. Reed, R. C. (2006). The superalloys: Fundamentals and applications. Cambridge University Press.

4. Birosca, S., & Kolisnychenko, S. (Eds.). (2020). Superalloys II. Trans Tech Publications.

5. Hoppin G.S., Danak W.P. (1987). Future of Superalloys. Superalloys II: High-Temperature Materials for Aerospace and Industrial Power Ed. By Chester T. Sims, Norman S. Stoloff, William C. Hagel. New York, 543–561.

6. Betteridge W., Shaw S. W. K. (1987). Development of superalloys. *Materials Science and Technology*. Vol. 3. P. 682–694.

7. Hauffe K. (1981). Super Werkstoffe und ihre Verfügbarkeit in der Zukunft. *Metallő* 35, 8, 737–744.

8. Boguslaev, V. A., Muravchenko, F. M., Zhemanyuk, P. D., et al. (2007). Technological support of operational characteristics of gas turbine engine parts. Turbine blades (Part 2, 2nd ed.). Motor Sich.

9. Zhemanyuk, P. D., Klochihin, V. V., Gnatenko, V. O., et al. (2013). Study of the influence of hot isostatic pressing and heat treatment on the structure and properties of castings from heat-resistant nickel alloy ZhS6K-VI. *Gas Turbine Technologies*, (6), 20–24.

10. Zhemanyuk, P. D., Klochihin, V. V., Lysenko, N. A., & Naumik, V. V. (2015). Structure and properties of cast blades of aircraft engines from heat-resistant nickel alloy ZhS26-VI after hot isostatic pressing. *Bulletin of Engine Building*, (1), 139–146.

11. Zhemanyuk, P. D., Klochikhin, V. V., Hnatenko, O. V., et al. (2013). Study of the effect of hot isostatic pressing on the structure and properties of cast parts of aircraft engines made of the heat-resistant nickel alloy ZhS6K-VI. *Gas Turbine Technologies*, (6), 20–24.

DOI 10.15588/1607-6885-2026-2-3

12. Ospennikova, O. G., & Orlov, M. R. (2007). Improving the properties of the heat-resistant alloy ZhS6U-VI by hot isostatic pressing and subsequent heat treatment. Materials Science, (9), 32–36.

13. Orlov, M. R. (2008). Formation of pores in single-crystal turbine blades during directional solidification. *Metals*, (1), 70–75.

14. Myalnitsa, G. P., Verkhovlyuk, A. M., Narivsky, A. V., Shynsky O. Y., Maksyuta I. I. (2023). Materials and technologies for blades of industrial gas turbine engines. Naukova Dumka, 180. https://doi.org/10.15407/978-966-00-1810-5

15. Puchek, S., & Byelikov, S. (2025). Structure and properties of ZhS26-VI superalloy for production of responsible parts of gas turbine engines. New Materials and Technologies in Metallurgy and Mechanical Engineering, (4), 14–21. https://doi.org/10.15588/1607-6885-2025-4-2

Received 06.04.04.2026
Accepted 14.04.2026
Published 07.05.2026

УДК 621.74.045:669.715:669.018.25

ДОСЛІДЖЕННЯ СТРУКТУРИ ТА ВЛАСТИВОСТЕЙ РОБОЧИХ ЛОПАТОК АВІАЦІЙНИХ ГАЗОТУРБІННИХ ДВИГУНІВ ІЗ ЖАРОМІЦНОГО НІКЕЛЕВОГО СПЛАВУ ЖС26-ВІ

Сергій Пучек — аспірант кафедри транспортних технологій Національного університету «Запорізька політехніка», м. Запоріжжя, Україна, *e-mail: puchek777@gmail.com*, ORCID: 0009-0007-8077-6106

Сергій Бєліков — д-р техн. наук, професор, професор кафедри транспортних технологій Національного університету «Запорізька політехніка», м. Запоріжжя, Україна, *e-mail: belikov@zp.edu.ua*, ORCID: 0000-0002-9510-8190

Мета роботи. *Вивчити макро- та мікроструктурний стан робочих лопаток газотурбінного двигуна ВК-2500 у вихідному стані та після різної технологічної обробки. Оцінити рівень механічних характеристик і тривалої міцності.*

Методи дослідження. *Досліджували якість матеріалу робочих лопаток 1-го ступеня ГТД із жароміцного нікелевого сплаву ЖС26-ВІ у вихідному стані та після гарячого ізостатичного пресування (ГІП), а також після ГІП і стандартної термічної обробки. Люмінесцентний контроль лопаток здійснювали методом ЛЮМ1-ОВ. Дослідження мікроструктури проводили методами оптичної (мікроскоп «Neophot-32») та растрової електронної мікроскопії (мікроскоп «JSM T-300»). Механічні властивості при кімнатній температурі визначали відповідно до ISO 6892-84 та СТ РЕВ 471-88, а показники жароміцності – відповідно до ДСТУ ISO 204:2019.*

Отримані результати. *Металографічними дослідженнями встановлено, що мікроструктура робочих лопаток є монокристалічною з основними структурними складовими: γ′- твердий розчин із наявністю інтерметалідної γ′- фази, евтектичної (γ-γ′) фази, карбідів і карбонітридів. У мікроструктурі лопаток після ГІП спостерігається зменшення розмірів структурних складових.*

Наукова новизна. *Отримано нові дані про структуру та фазовий склад матеріалу робочих лопаток авіаційного ГТД. Термічна обробка за стандартним режимом після ГІП забезпечує практично повну перекристалізацію зміцнювальної інтерметалідної γ′- фази, що полягає у розчиненні γ′- фази в γ- матриці з повторним її виділенням у вигляді дисперсних частинок кубічної морфології.*

Практична цінність. *Показано, що гаряче ізостатичне пресування у комбінації зі стандартною термічною обробкою забезпечує отримання найбільш сприятливого поєднання міцнісних і пластичних характеристик, а також тривалої міцності лопаток.*

Ключові слова: *суперсплави, лопатки газової турбіни, гомогенізація, гаряче ізостатичне пресування, інтерметалідна γ′- фаза.*

Список літератури

1. Чигрин В. С. Конструкция и прочность авиационных двигателей. Харьков : ХАИ, 2017. 420 с.

2. Miller H. E., Chambers W. L. Constructions of gas turbines and superalloys. Superalloy II: High temperature materials for aerospace and industrial power / ed. by Sims C. T., Stoloff N. S., Hagel W. C. 2nd ed. New York : John Wiley & Sons, 1987. P. 27–56.

3. Reed R. C. The superalloys. Fundamentals and applications. Cambridge : Cambridge University Press, 2006. 372 p.

DOI 10.15588/1607-6885-2026-2-3

4. Superalloys II / ed. by Birosca S., Kolisnychenko S. Switzerland : Trans Tech Publications Ltd., 2020. 520 p.

5. Hoppin G.S., Danak W.P. Future of Superalloys. Superalloys II: High-Temperature Materials for Aerospace and Industrial Power / Ed. By Chester T. Sims, Norman S. Stoloff, William C. Hagel. New York, 1987. P. 543–561.

6. Betteridge W., Shaw S. W. K. Development of superalloys. *Materials Science and Technology*. 1987. Vol. 3. P. 682–694.

7. Hauffe K. Super Werkstoffe und ihre Verfügbarkeit in der Zukunft. *Metall.* 1981. H. 35. No 8. P. 737–744.

8. Технологическое обеспечение эксплуатационных характеристик деталей ГТД. Лопатки турбины. Ч. 2 : монография / Богуслаев В. А. та ін. 2-е изд. Запорожье : Мотор Сич, 2007. 496 с.

9. Исследование влияния горячего изостатического прессования и термообработки на структуру и свойства отливок из жаропрочного никелевого сплава ЖС6К-ВИ / Жеманюк П. Д. и др. *Газотурбинные технологии*. 2013. № 6. С. 20–24. 2013.

10. П. Д. Жеманюк, В. В. Клочихин, Н. А. Лысенко, В. В. Наумик. Структура и свойства литых лопаток авиационных двигателей из жаропрочного никелевого сплава ЖС26-ВИ после горячего изостатического прессования. *Вісник двигунобудування*. 2015. № 1. P. 139–146.

11. Исследование влияния горячего изостатического прессования на структуру и свойства литых деталей авиационных двигателей из жаропрочного никелевого сплава ЖС6К-ВИ / Жеманюк П. Д. и др. *Газотурбинные технологии*. 2013. № 6 (117). С. 20–24.

12. Оспенникова О. Г., Орлов М. Р. Повышение свойств жаропрочного сплава ЖС6У-ВИ путем горячего изостатического прессования и последующей термической обработки. *Материаловелдение.* 2007. № 9. – С. 32–36.

13. Орлов М. Р. Образование пор в монокристаллических рабочих лопатках турбины в процессе направленной кристаллизации. *Металлы*. 2008. № 1. С. 70–75.

14. Матеріали і технології для лопаток вітчизняних промислових газотурбінних двигунів / Мяльніца Г. П. та ін. ; за ред. Вероцької В. В. Київ : Наукова думка, 2023. 180 с. https://doi.org/10.15407/978-966-00-1810-5

15. Puchek S., Byelikov S. Structure and properties of ZhS26-VI superalloy for production of responsible parts of gas turbine engines. *Нові матеріали і технології в металургії та машинобудуванні*. 2025. No. 4. C. 14–21. https://doi.org/10.15588/1607-6885-2025-4-2

DOI 10.15588/1607-6885-2026-2-3

p-ISSN 1607-6885 New materials and technologies in metallurgy and mechanical engineering. 2026/2
e-ISSN 2786-7358 New materials and technologies in metallurgy and mechanical engineering. 2026/2

UDC 620.175.2:669.15

Diana Hlushkova — Doctor of Technical Sciences, Professor, Head of the Department of Metal Technology and Materials Science, Kharkiv National Automobile and Highway University, Kharkiv, Ukraine, *e-mail: diana@khadi.kharkov.ua*, ORCID: 0000-0001-8612-6584

Volodymyr Volchuk — Doctor of Technical Sciences, Professor, Head of the Department of Materials Science and Materials Processing, Ukrainian State University of Science and Technology, Dnipro, Ukraine, *e-mail: volchuk.volodymur@gmail.com*, ORCID: 0000-0001-7199-192X

PREDICTION OF MECHANICAL PROPERTIES OF 40KHMFA STEEL BASED ON MULTIFRACTAL ANALYSIS OF MICROSTRUCTURE

Purpose. *The purpose of the study is to develop and scientifically substantiate a method for quantitative assessment and prediction of mechanical properties (tensile strength, yield strength, relative elongation) and resistance to hydrogen sulfide corrosion-mechanical destruction of 40KHMFA steel based on multifractal analysis of the parameters of its bainite-martensitic microstructure after various heat treatment regimes.*

Research methods. *The research was carried out on 40KHMFA steel (0.42% C; 0.87% Cr; 0.25% Mo; 0.14% V). The samples were quenched from 860 °C in oil with subsequent high tempering in the temperature range of 660–740 °C (step 20 °C) with holding times of 5, 30, 60 and 90 minutes. Mechanical tests included static tensile testing on standard cylindrical samples, determination of impact strength on Charpy samples with a V-shaped notch and hardness measurements by the Rockwell and Vickers methods. Microstructural analysis was performed using optical metallography after mechanical grinding, polishing, electrolytic polishing and etching in 4 % nital. Multifractal analysis of microstructure images was performed by calculating the generalized Renyi dimensions (Dq), the singularity spectrum f(α) and the derived parameters: D_0, Δ, K and the spectral width Δf(α) separately for the bainite and martensitic components. Resistance to hydrogen sulfide cracking was assessed according to standardized methods in an environment saturated with H_2S.*

Results. *With increasing temperature and duration of tempering, a regular decrease in strength characteristics ($\sigma_в$ and σ_t) and an increase in plasticity (δ_5) is observed. Multifractal parameters sensitively reflect the evolution of the microstructure: a decrease in D_0 contributes to improving plasticity, and an increase in the parameters Δ and K – to increasing resistance to plastic deformation. Regression models with high coefficients of determination (R^2 = 0.86–0.95) have been developed, which allow reliable prediction of mechanical properties exclusively from the multifractal characteristics of the microstructure. It is shown that long-term tempering at 700 °C preserves the acicular morphology, but is accompanied by coagulation growth of carbide particles.*

Scientific novelty. *The scientific novelty of the work lies in the first systematic application of multifractal analysis for the quantitative characterization of the bainite-martensitic microstructure of 40KHMFA steel in order to predict its mechanical properties and resistance to hydrogen sulfide corrosion-mechanical destruction. For the first time, quantitative correlations between the parameters D_0, Δ, K, Δf(α) and the indicators of strength and ductility were established, and regression dependencies were developed that allow for non-destructive assessment of material properties. The higher informativeness of the multifractal approach compared to traditional methods of quantitative metallography in the analysis of substructural changes was proven.*

Practical value. *The developed multifractal method and regression models can be used to create digital systems for non-destructive quality control and predict the durability of pipelines and structural elements operating in aggressive hydrogen sulfide environments of the oil and gas and nuclear power industries. The proposed optimal heat treatment regime – of quenching from 860 °C in oil with subsequent tempering at (700 ± 10) °C for 90 minutes – provides a rational balance of strength, ductility and corrosion resistance of 40KHMFA steel. This makes it possible to reduce the volume of destructive mechanical tests in the production of dual-purpose pipes.*

Key words: *multifractal analysis, 40KHMFA steel, bainite-martensitic structure, heat treatment, mechanical properties, hydrogen sulfide corrosion-mechanical destruction, regression modeling, forecasting, non-destructive testing, pipeline steels.*

Introduction

Resistance to hydrogen sulfide corrosion cracking (HSCC) is one of the main problems for pipeline steels operated in aggressive environments of the oil and gas industry. HSCC occurs due to the combined action of corrosion, mechanical stresses and diffusion of atomic hydrogen into the metal, which leads to the formation of

DOI 10.15588/1607-6885-2026-2-4

cracks and premature failure of structures. Low-alloy steels of the 40KHMFA type (analogs of Cr-Mo-V steels) are particularly sensitive to this type of failure due to the peculiarities of the phase composition, the presence of non-metallic inclusions and microstructural inhomogeneities.

Heat treatment significantly affects the balance of strength and ductility of such steel, as well as its corrosion resistance. Therefore, it is urgent to find effective methods for quantitative assessment of the microstructure, which would allow predicting operational properties without conducting destructive mechanical tests.

Analysis of research and publications

The mechanical and corrosion properties of alloyed steels depend on the microstructure, distribution of alloying elements and non-metallic inclusions. Sulfides and oxides often become the sites of crack initiation in environments containing H_2S.

NACE TM0177 and TM0284 are used to assess resistance to SCR and hydrogen cracking. Studies show that tempering in the range of 700–715 °C provides the best compromise between strength and embrittlement resistance for Cr-Mo steels.

Recently, fractal and multifractal methods have been actively used for quantitative characterization of complex structures, corrosion defects and failure mechanisms. Multifractal analysis, unlike classical fractal, allows for a more detailed assessment of the heterogeneity, order and regularity of the microstructure through the spectrum of generalized Renyi dimensions (Dq) and the spectrum of singularities f(α).

Despite the significant number of works on fractal analysis of corrosion and inclusions, there is a lack of systematic research on the application of the multifractal approach specifically to 40KHMFA steel for predicting resistance to SCR. This necessitates the development of an appropriate methodology. The performance characteristics and durability of alloyed steels are largely determined by the features of their microstructural structure, phase composition, the nature of the distribution of alloying components, as well as the presence and morphology of non-metallic inclusions [1–5]. Inclusions of non-metallic nature, in particular sulfide and oxide particles, play the role of local stress concentrations and can act as centers of crack initiation in environments containing hydrogen sulfide. This, in turn, intensifies localized corrosion processes and contributes to the accumulation of diffuse hydrogen in the metal [1, 2]. It has been established that hydrogen sulfide corrosion cracking is activated in aggressive acidic environments (pH < 4) under conditions of increased partial pressure of H_2S (over 0.0034 bar), when atomic hydrogen penetrates the crystal lattice of steel and causes its brittle fracture [7, 8].

To quantify the resistance of materials to this type of fracture, standardized test methods are widely used, in particular NACE TM0177 (uniaxial tensile method) and NACE TM0284 (determination of susceptibility to hydrogen-induced cracking, HIC). These approaches are focused on determining both mechanical characteristics and corrosion resistance of the material [2, 7, 8]. In particular, for low-alloy steels, it has been shown that an increase in the nickel content above 1 wt.% can lead to a decrease in the SCR resistance due to the formation of unstable phase components [1, 9]. At the same time, for Cr-Mo steels, a significant effect of the tempering temperature on the formation of the martensitic-bainite structure and the corresponding susceptibility to fracture has been established: the optimal range of 700–715 °C provides a favorable combination of strength and ductility with a reduction in the risk of embrittlement [10].

In modern research, digital approaches to materials analysis are becoming increasingly widespread, including mathematical modeling, the concept of digital twins, and machine learning methods. Such tools allow predicting the behavior of materials under operating conditions with increased accuracy [6, 9]. Among them, fractal and multifractal methods occupy a special place, which are used to quantitatively describe the complexity of the microstructure, the geometry of corrosion damage, and the mechanisms of fracture [11–13].

The fractal approach, in particular the use of fractal dimension D, is effectively used to analyze heterogeneous corrosion processes in pipeline steels. For example, for steel grade X80, it was found that the parameters of the fractal geometry of corrosion defects allow estimating the fracture pressure and predicting the development of cracks [14–18]. Similarly, when studying the corrosion behavior of 316L stainless steel, a clear relationship was found between the value of the fractal dimension and its resistance to hypochlorite environments [19].

The use of fractal analysis to assess the influence of non-metallic inclusions on the properties of structural steels, in particular of the S355J2 type, has shown a close correlation between the fractal characteristics of the structure and the indicators of strength and impact toughness [2]. Similar results have been obtained in the study of surface-modified materials: fractal modeling after ion-plasma chromium plating or TiN-type coatings indicates an increase in wear resistance, which is due to changes in the morphology of the surface layer [20, 21].

Multifractal analysis is a further development of the fractal approach and allows the study of complex heterogeneous systems by determining the spectrum of singularities f(α) and generalized dimensions Dq. This provides a deeper characterization of the structure, including the degree of its homogeneity, order, and statistical regularity [6, 13]. In the field of pipeline transport, such methods have already demonstrated their effectiveness in analyzing the failure processes of composite pipes and predicting their mechanical behavior [6].

DOI 10.15588/1607-6885-2026-2-4

However, despite a significant number of studies, the issue of using multifractal analysis to assess the resistance to hydrogen sulfide corrosion cracking of 40KHMFA steels remains insufficiently addressed. This is especially important given the specificity of their bainite-martensitic microstructure and the role of non-metallic inclusions in the fracture processes [20–22]. Traditional analysis methods often do not take into account the complex multifractal nature of corrosion damage, which can lead to underestimation of the risk of crack initiation [22–24].

In this context, the application of a multifractal approach to predicting the mechanical properties and resistance of 40KHMFA steel to hydrogen sulfide based on the analysis of its microstructure opens up new prospects for optimizing heat treatment regimes and improving the efficiency of quality control systems in industry.

Purpose of work

The aim of the work is to develop a method for predicting the mechanical properties and resistance to hydrogen sulfide corrosion-mechanical destruction of 40KHMFA steel based on the multifractal characteristics of its bainite-martensitic microstructure.

To achieve the goal, the following tasks were solved:

- conduct heat treatment of 40KHMFA steel (quenching from 860°C in oil and high tempering in the range of 660–740°C with different holding times) and perform microstructural analysis;
- apply multifractal analysis to bainite and martensitic components and establish correlations between the parameters D_0, Δ, K, $\Delta f(\alpha)$ and mechanical characteristics ($\sigma_в$, σ_t, δ_5);
- develop regression models for predicting properties exclusively based on multifractal indicators and assess their accuracy.

Research material and methodology

The object of the study was 40KHMFA steel with the following chemical composition (wt. %): C – 0.42; Mn – 0.59; Si – 0.26; Cr – 0.87; Ni – 0.30; Mo – 0.25; V – 0.14.

The samples were quenched from 860 °C in oil, after which they were tempered at temperatures of 660, 680, 700, 720 and 740 °C with holding times of 5, 30, 60 and 90 min. The temperature was controlled by a thermocouple built into the sample.

Mechanical tests included tensile testing on standard cylindrical specimens, determination of impact strength on Charpy V-notch specimens, and Rockwell and Vickers hardness measurements.

The microstructure was studied after mechanical grinding, polishing, electrolytic polishing and etching in 4% nital. The size of the former austenite grain was determined by etching in picric acid with the additive "Sintol". Resistance to SCR was assessed according to standardized methods in an environment saturated with hydrogen sulfide.

Research results

With increasing temperature and duration of tempering, there is a natural decrease in strength ($\sigma_в$ and σ_t) and an increase in plasticity (δ_5). At temperatures around 700 °C, the effect of holding time on strength is less pronounced due to the acceleration of diffusion processes (Fig. 1).

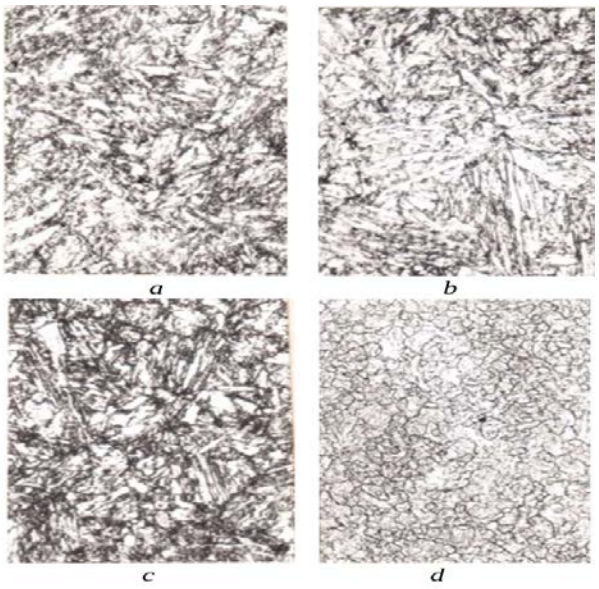

Figure 1. Structure of 40KHMFA steel after heat treatment : *a* – 630 …660 ° C ; *b* – 650…670 ° C ; *c* – 670…690 ° C , ×1250; *d* – austenitic structure , ×400

With increasing tempering temperature and holding time, there is a systematic decrease in strength characteristics and a corresponding increase in ductility. At higher tempering temperatures, the effect of holding time on the decrease in strength is less pronounced compared to lower temperatures. In the as-delivered state, the steel had a tempered acicular bainite-martensitic structure. Long-term tempering leads to coarsening of carbide particles, but retains the acicular morphology (Fig. 2).

The results of mechanical tests are shown in Fig. 3 (the relative elongation after heat treatment was ~ ~ 65–70 % and therefore was not shown in the graphs).

DOI 10.15588/1607-6885-2026-2-4

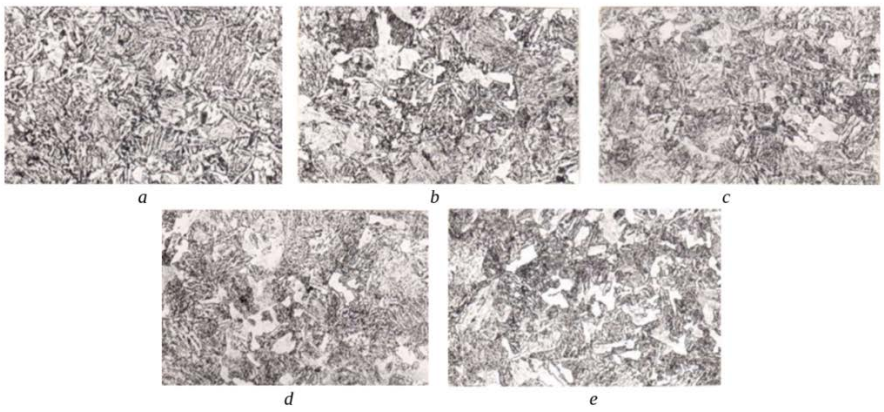

Figure 2. Microstructure of 40KHMFA steel in the as-delivered state and after tempering at 700 °C (holding time × 500-fold increase): *a* – as-delivered state; *b* – 5 min; *c* – 30 min; *d* – 60 min; *e* – 90 min

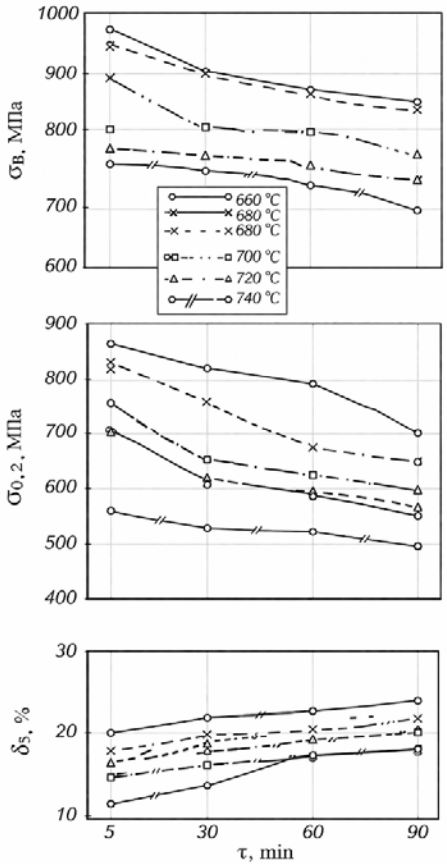

Figure 3. The relationship between tempering temperature, holding time on the mechanical characteristics of 40KHMFA steel after quenching

Multifractal analysis of the microstructure was performed using Renyi dimensions :

$$D(q) = \frac{1}{q-1} \cdot \lim_{\delta \to \infty} \frac{\ln \sum_{i=1}^{N} p_i^q}{\ln \delta}, \quad (1)$$

where δ –the size of the side of the square cell (box) that covers the studied image of the microstructure (in classical notation this parameter corresponds to ε); p_i –the probability that a certain part of the object (e.g., pixel intensity, area of a particular phase or structural element) falls into the i -th grid cell; q –the order of the statistical moment (exponent), which can take on any real values in the range from –∞ to +∞.

The spectrum of singularities f(α) was obtained through the Legendre transformation:

$$\alpha = d\tau(q)/dq, \quad (2)$$

$$f(\alpha) = q\alpha - \tau(q). \quad (3)$$

Based on the spectrum, the parameters of homogeneity, order (Δ), and regularity (K) were calculated.

The results of multifractal characteristics for bainite and martensite are given in Table 1 (the batch numbering corresponds to the different processing regimes).

Table 1 – Multifractal characteristics of the structure of 40KHMFA steel

Batch number	Bainite D_0	Bainite Δ	Beinit K	Bainite Δf(α)	Martensite D_0	Martensite Δ	Martensite K	Martensite Δf(α)
1	1.81	0.55	1.38	0.05	1.68	0.47	1.35	0.11
2	1.85	0.57	1.44	0.02	1.73	0.49	1.40	0.34
3	1.88	0.73	1.51	0.11	1.72	0.52	1.43	0.39
4	1.91	0.68	1.50	0.17	1.77	0.58	1.45	0.36
5	1.90	0.82	1.56	0.18	1.80	0.55	1.52	0.59
6	1.96	0.79	1.60	0.26	1.83	0.59	1.60	0.68
7	1.97	0.85	1.62	0.29	1.88	0.65	1.70	0.69

DOI 10.15588/1607-6885-2025-4-

Regression dependences have been developed:

$\sigma_B = 821.32 - 112.21\ D_0 + 111.26\ \Delta + 216.78\ K - 17.24\ \Delta f(\alpha)$ ($R^2 = 0.95$) –for martensite;

$\sigma_T = 695.75 - 469.87\ D_0 - 190.04\ \Delta + 573.35\ K + 286.82\ \Delta f(\alpha)$ ($R^2 = 0.86$) –for bainite;

$\delta_5 = 20.99 + 16.35\ D_0 + 28.03\ \Delta - 23.15\ K + 5.28\ \Delta f(\alpha)$ ($R^2 = 0.88$) –for bainite.

The analysis shows that bainite has higher D_0, Δ and K values compared to martensite, indicating greater ordering. With changing processing regimes, the structure becomes more multifractal, which correlates well with changes in mechanical properties.

The proposed models allow for reliable prediction of properties based on microstructural analysis data, which is especially important for non-destructive quality control.

Conclusions

1. Multifractal analysis is an effective tool for quantitatively assessing the bainite-martensitic microstructure of 40KHMFA steel after various heat treatment regimes.

2. The parameters D_0, Δ, K, and $\Delta f(\alpha)$ sensitively reflect changes in the heterogeneity and ordering of the structure and allow for the prediction of strength and ductility.

3.The developed regression models with high coefficients of determination make it possible to evaluate mechanical characteristics without conducting mechanical tests.

4. The optimum quenching regime for 40KHMFA steel intended for dual-purpose pipes is 860°C in oil followed by tempering at (700 ± 10)°C for 90 minutes. This regime provides the best balance of strength, ductility and resistance to hydrogen sulfide cracking.

5. The multifractal approach surpasses traditional metallographic methods in sensitivity to substructural changes and opens up prospects for creating digital systems for predicting the service life of structural elements operating in aggressive environments.

References

1. Wang, Y., Karasev, A., Park, J. H., & Jönsson, P. G. (2021). Non-metallic inclusions in different ferroalloys and their effect on steel quality: A review. Metallurgical and Materials Transactions B, 52, 2892–2925. https://doi.org/10.1007/s11663-021-02259-7

2. Volchuk, V. M., Uzlov, O. V., Puchikov, O. V., & Ivantsov, S. V. (2021). Fractals theory application for evaluation of influence of non-metallic inclusions on mechanical properties of S355J2 steel. IOP Conference Series: Materials Science and Engineering, 1021, 012053. https://doi.org/10.1088/1757-899X/1021/1/012053

3. Andrenko, P., Rogovyi, A., Hrechka, I., Khovanskyi, S., & Svynarenko, M. (2021). Characteristics improvement of labyrinth screw pump using design modification in screw. Journal of Physics: Conference Series, 1741(1), 012024. https://doi.org/10.1088/1742-6596/1741/1/012024

4. Migal, V., Lebedev, A., Shuliak, M., Kalinin, E., Arhun, S., & Korohodskyi, V. (2021). Reducing the vibration of bearing units of electric vehicle asynchronous traction motors. Journal of Vibration and Control, 27(9–10), 1123–1131. https://doi.org/10.1177/1077546320937634

5. Sergiyenko, O., Hernández Balbuena, D., Rosas-Méndez, P. L. A., Rivas Lopez, M., Hernandez, W., Podrygalo, M., & Gurko, A. (2011). Analysis of jitter influence in fast frequency measurements. Measurement, 44, 1229–1242. https://doi.org/10.1016/j.measurement.2011.04.001

6. Vafaeva, K. M., Vatin, N. I., Karpov, D. F., & Romanovski, V. (2025). Monitoring hybrid glass-basalt plastic pipes: A fractal approach to failure analysis. Materials Research Express, 12, 075307. https://doi.org/10.1088/2053-1591/adf161

7. Xiang, N., Yang, M., Sun, W., et al. (2026). Dynamic response of grain rotation and slipping system activity in Al6014 tailor heat treated blank after non-uniform loading via crystal plasticity finite element method. Journal of Materials Science and Technology, 251, 39–58. https://doi.org/10.1016/j.jmst.2025.05.065

8. Wang, B., Zeng, W., Zhao, Z., et al. (2026). Near-α Ti60 alloy dwell fatigue basal slip-induced cracking: Faceted crack initiation and local strain evolution. Journal of Materials Science and Technology, 244, 313–330. https://doi.org/10.1016/j.jmst.2025.03.105

9. Borovkov, A. I., Vafaeva, K. M., Vatin, N. I., & Ponyaeva, I. (2024). Synergistic integration of digital twins and neural networks for advancing optimization in the construction industry: A comprehensive review. Construction Materials and Products, 7(4), 7. https://doi.org/10.58224/2618-7183-2024-7-4-7

10. Hlushkova, D. B., & Volchuk, V. M. (2023). Fractal study of the effect of ion plasma coatings on wear resistance. Functional Materials, 30(3), 453. https://doi.org/10.15407/fm30.03.453

11. Volchuk, V. M., & Hlushkova, D. B. (2024). Application of new plasma coatings for restoration of the surface of material. Functional Materials, 31(2), 205–209. https://doi.org/10.15407/fm31.02.205

12. Hlushkova, D. B., Volchuk, V. M., Polyansky, P. M., Saenko, V. A., & Efimenko, A. A. (2023). Fractal modeling of the mechanical properties of the metal surface after ion-plasma chrome plating. Functional Materials, 30(2), 275. https://doi.org/10.15407/fm30.02.275

13. Hlushkova, D. B., Bagrov, V. A., Demchenko, S. V., Volchuk, V. M., Kalinin, O. V., & Kalinina, N. E. (2022). Structure and properties of powder gas-plasma coatings based on nickel. Problems of Atomic Science and Technology, 4(140), 125–130. https://doi.org/10.46813/2022-140-125

14. Kalinina, N. E., Hlushkova, D. B., Hrinchenko, O. D., et al. (2019). Hardening of leading edges of turbine blades by electrospark alloying. Problems of Atomic Science and Technology, 2(120), 151–154.

DOI 10.15588/1607-6885-2026-2-4

15. Mahajan, U., Dhonde, M., Sahu, K., Ghosh, P., & Shirage, P. M. (2024). Titanium nitride (TiN) as a promising alternative to plasmonic metals: A comprehensive review of synthesis and applications. Materials Advances, 5, 846–895. https://doi.org/10.1039/D3MA00965C

16. Vafaeva, K. M., Dhyani, M., Acharya, P., Parik, K., & Ledalla, S. (2024). Glass-basalt-plastic materials for construction in temperate and Arctic climatic regions. Bio Web of Conferences, 86, 01111. https://doi.org/10.1051/bioconf/20248601111

17. Zheng, Y., Li, X., Pi, C., Song, H., Gao, B., Chu, P. K., et al. (2020). Recent advances of two-dimensional transition metal nitrides for energy storage and conversion applications. FlatChem, 19, 100149. https://doi.org/10.1016/j.flatc.2019.100149

18. Hlushkova, D. B., Ryzhkov, Y. V., Kostina, L. L., & Demchenko, S. V. (2018). Increase of wear resistance of the critical parts of hydraulic hammer by means of ion-plasma treatment. Problems of Atomic Science and Technology, 1(113), 208–211.

19. Xu, D., Yu, R., Li, M., Zhang, Y., Ren, J., Ren, H., Huang, J., & Lian, F. (2024). Microstructure evolution and nitriding mechanism of Ti-6Al-4V alloy in alumina-based refractories. International Journal of Applied Ceramic Technology, 22(2), e14975. https://doi.org/10.1111/ijac.14975

20. Das, A., Nanao, Y., Rajan, A., Di Falco, A., & Schulz, S. A. (2025). Low-temperature fabrication of plasmonic titanium nitride thin films by electron beam evaporation. Journal of Physics: Photonics, 7(2), 025032. https://doi.org/10.1088/2515-7647/adcddc

21. Kalinina, N. E., Glushkova, D. B., Voronkov, A. I., & Kalinin, V. T. (2019). Influence of nanomodification on structure formation of multicomponent nickel alloys. Functional Materials, 26(3), 514–518. https://doi.org/10.15407/fm26.03.514

22. Hlushkova, D. B., Kalinin, A. V., Kalinina, N. E., Volchuk, V. M., Saenko, V. A., & Efimenko, A. A. (2023). Study of nanomodification of nickel alloy GS3 with titanium carbide. Problems of Atomic Science and Technology, 2(144), 126. https://doi.org/10.46813/2023-144-126

Received 25.03.2026
Accepted 01.04.2026
Published 07.05.2026

УДК 620.175.2:669.15

ПРОГНОЗУВАННЯ МЕХАНІЧНИХ ВЛАСТИВОСТЕЙ СТАЛІ 40ХМФА НА ОСНОВІ МУЛЬТИФРАКТАЛЬНОГО АНАЛІЗУ МІКРОСТРУКТУРИ

Діана Глушкова — д-р техн. наук, професор, завідувач кафедри технології металів та матеріалознавства Харківського національного автомобільно-дорожнього університету, м. Харків, Україна, *e-mail: diana@khadi.kharkov.ua*, ORCID: 0000-0001-8612-6584

Володимир Волчук — д-р техн. наук, професор, завідувач кафедри матеріалознавства та обробки матеріалів Українського державного університету науки і технологій, м. Дніпро, Україна, *e-mail: volchuk.volodymur@gmail.com*, ORCID: 0000-0001-7199-192X

Мета роботи. *Метою дослідження є розробка та наукове обґрунтування методу кількісної оцінки й прогнозування механічних властивостей (межі міцності на розрив, межі текучості, відносного подовження) та стійкості до сірководневого корозійно-механічного руйнування сталі 40ХМФА на основі мультифрактального аналізу параметрів її бейнітно-мартенситної мікроструктури після різних режимів термічної обробки.*

Методи дослідження. *Дослідження проводили на сталі 40ХМФА (0,42 % C; 0,87 % Cr; 0,25 % Mo; 0,14 % V). Зразки піддавали гартуванню з 860 °C в олії з подальшим високим відпуском у діапазоні температур 660–740 °C (крок 20 °C) з витримками 5, 30, 60 та 90 хвилин. Механічні випробування включали статичний розтяг на стандартних циліндричних зразках, визначення ударної в'язкості на зразках Шарпі з V-подібним надрізом та вимірювання твердості за методами Роквелла і Віккерса. Мікроструктурний аналіз виконували за допомогою оптичної металографії після механічного шліфування, полірування, електролітичного полірування та травлення в 4 % ніталі. Мультифрактальний аналіз зображень мікроструктури здійснювали шляхом розрахунку узагальнених розмірностей Реньї (Dq), спектру сингулярностей f(α) та похідних параметрів: D_0, Δ, K і ширини спектру Δf(α) окремо для бейнітної та мартенситної складових. Стійкість до сірководневого розтріскування оцінювали відповідно до стандартизованих методик у середовищі, насиченому H_2S.*

Отримані результати. *Зі збільшенням температури та тривалості відпуску спостерігається закономірне зниження міцнісних характеристик ($\sigma_в$ і $\sigma_т$) та зростання пластичності (δ_5). Мультифрактальні параметри чутливо відображають еволюцію мікроструктури: зменшення D_0 сприяє покращенню пластичності, а зростання параметрів Δ та K – підвищенню опору пластичній деформації. Розроблено регресійні моделі з високи-*

DOI 10.15588/1607-6885-2026-2-4

ми коефіцієнтами детермінації (R^2 = 0,86–0,95), які дозволяють достовірно прогнозувати механічні властивості виключно за мультифрактальними характеристиками мікроструктури. Показано, що тривалий відпуск при 700 °C зберігає ацикулярну морфологію, але супроводжується коагуляційним ростом карбідних частинок.

Наукова новизна. *Наукова новизна роботи полягає в першому системному застосуванні мультифрактального аналізу для кількісної характеристики бейнітно-мартенситної мікроструктури сталі 40ХМФА з метою прогнозування її механічних властивостей і стійкості до сірководневого корозійно-механічного руйнування. Вперше встановлено кількісні кореляції між параметрами D_0, Δ, K, $\Delta f(\alpha)$ та показниками міцності й пластичності, а також розроблено регресійні залежності, які дозволяють проводити безруйнівну оцінку властивостей матеріалу. Доведено вищу інформативність мультифрактального підходу порівняно з традиційними методами кількісної металографії при аналізі субструктурних змін.*

Практична цінність. *Розроблений мультифрактальний метод і регресійні моделі можуть бути використані для створення цифрових систем безруйнівного контролю якості та прогнозування довговічності трубопроводів і елементів конструкцій, що працюють в агресивних сірководневих середовищах нафтогазової та атомної енергетики. Запропонований оптимальний режим термічної обробки – гартування з 860 °C в олії з подальшим відпуском при (700 ± 10) °C протягом 90 хвилин – забезпечує раціональний баланс міцності, пластичності та корозійної стійкості сталі 40ХМФА. Це дає змогу скоротити обсяг руйнівних механічних випробувань у виробництві труб подвійного призначення.*

Ключові слова: *мультифрактальний аналіз, сталь 40ХМФА, бейнітно-мартенситна структура, термічна обробка, механічні властивості, сірководневе корозійно-механічне руйнування, регресійне моделювання, прогнозування, безруйнівний контроль, трубопровідні сталі.*

Список літератури

1. Wang Y., Karasev A., Park J. H., Jönsson P. G. Non-metallic inclusions in different ferroalloys and their effect on the steel quality: a review. *Metallurgical and Materials Transactions* B. 2021. Vol. 52. P. 2892–2925. DOI: https://doi.org/10.1007/s11663-021-02259-7

2. Volchuk V. M., Uzlov O. V., Puchikov O. V., Ivantsov S. V. Fractals theory application for evaluation of influence of non-metallic inclusions on mechanical properties of S355J2 steel. IOP Conference Series: Materials Science and Engineering. 2021. Vol. 1021. P. 012053. DOI: https://doi.org/10.1088/1757-899X/1021/1/012053

3. Andrenko P., Rogovyi A., Hrechka I., Khovanskyi S., Svynarenko M. Characteristics improvement of labyrinth screw pump using design modification in screw. Journal of Physics: Conference Series. 2021. Vol. 1741, No. 1. P. 012024. DOI: https://doi.org/10.1088/1742-6596/1741/1/012024

4. Migal V., Lebedev A., Shuliak M., Kalinin E., Arhun S., Korohodskyi V. Reducing the vibration of bearing units of electric vehicle asynchronous traction motors. *Journal of Vibration and Control*. 2021. Vol. 27, No. 9–10. P. 1123–1131. DOI: https://doi.org/10.1177/1077546320937634

5. Sergiyenko O., Hernández Balbuena D., Tyrsa V., Rosas-Méndez P. L. A., Rivas Lopez M., Hernandez W., Podrygalo M., Gurko A. Analysis of jitter influence in fast frequency measurements. *Measurement*. 2011. Vol. 44. P. 1229–1242. DOI: https://doi.org/10.1016/j.measurement.2011.04.001

6. Vafaeva K. M., Vatin N. I., Karpov D. F., Romanovski V. Monitoring hybrid glass-basalt plastic pipes: a fractal approach to failure analysis. *Materials Research Express*. 2025. Vol. 12. P. 075307. DOI: https://doi.org/10.1088/2053-1591/adf161

7. Xiang N., Yang M., Sun W. et al. Dynamic response of grain rotation and slipping system activity in Al6014 tailor heat treated blank after non-uniform loading via crystal plasticity finite element method. *Journal of Materials Science and Technology*. 2026. Vol. 251. P. 39–58. DOI: https://doi.org/10.1016/j.jmst.2025.05.065

8. Wang B., Zeng W., Zhao Z. et al. Near-α Ti60 alloy dwell fatigue basal slip-induced cracking: faceted crack initiation and local strain evolution. *Journal of Materials Science and Technology*. 2026. Vol. 244. P. 313–330. DOI: https://doi.org/10.1016/j.jmst.2025.03.105

9. Borovkov A. I., Vafaeva K. M., Vatin N. I., Ponyaeva I. Synergistic integration of digital twins and neural networks for advancing optimization in the construction industry: a comprehensive review. *Construction Materials and Products*. 2024. Vol. 7, No. 4. P. 7. DOI: https://doi.org/10.58224/2618-7183-2024-7-4-7

10. Hlushkova D. B., Volchuk V. M. Fractal study of the effect of ion plasma coatings on wear resistance. *Functional Materials*. 2023. Vol. 30, No. 3. P. 453. DOI: https://doi.org/10.15407/fm30.03.453

11. Volchuk V. M., Hlushkova D. B. Application of new plasma coatings for restoration of the surface of material. Functional Materials. 2024. Vol. 31, No. 2. P. 205–209. DOI: https://doi.org/10.15407/fm31.02.205

12. Hlushkova D. B., Volchuk V. M., Polyansky P. M., Saenko V. A., Efimenko A. A. Fractal modeling of the mechanical properties of the metal surface after ion-plasma chrome plating. *Functional Materials*. 2023. Vol. 30, No. 2. P. 275. DOI: https://doi.org/10.15407/fm30.02.275

13. Hlushkova D. B., Bagrov V. A., Demchenko S. V., Volchuk V. M., Kalinin O. V., Kalinina N. E. Structure and properties of powder gas-plasma coatings based

DOI 10.15588/1607-6885-2025-4-4

on nickel. *Problems of Atomic Science and Technology*. 2022. No. 4 (140). P. 125–130. DOI: https://doi.org/10.46813/2022-140-125

14. Kalinina N. E., Hlushkova D. B., Hrinchenko O. D. et al. Hardening of leading edges of turbine blades by electrospark alloying. *Problems of Atomic Science and Technology*. 2019. No. 2 (120). P. 151–154.

15. Mahajan U., Dhonde M., Sahu K., Ghosh P., Shirage P. M. Titanium nitride (TiN) as a promising alternative to plasmonic metals: a comprehensive review of synthesis and applications. *Materials Advances*. 2024. Vol. 5. P. 846–895. DOI: https://doi.org/10.1039/D3MA00965C

16. Vafaeva K. M., Dhyani M., Acharya P., Parik K., Ledalla S. Glass-basalt-plastic materials for construction in temperate and Arctic climatic regions. Bio Web of Conferences. 2024. Vol. 86. P. 01111. DOI: https://doi.org/10.1051/bioconf/20248601111

17. Zheng Y., Li X., Pi C., Song H., Gao B., Chu P. K. et al. Recent advances of two-dimensional transition metal nitrides for energy storage and conversion applications. *FlatChem*. 2020. Vol. 19. P. 100149. DOI: https://doi.org/10.1016/j.flatc.2019.100149

18. Hlushkova D. B., Ryzhkov Y. V., Kostina L. L., Demchenko S. V. Increase of wear resistance of the critical parts of hydraulic hammer by means of ion-plasma treatment. *Problems of Atomic Science and Technology*. 2018. No. 1 (113). P. 208–211.

19. Xu D., Yu R., Li M., Zhang Y., Ren J., Ren H., Huang J., Lian F. Microstructure evolution and nitriding mechanism of Ti-6Al-4V alloy in alumina-based refractories. *International Journal of Applied Ceramic Technology*. 2024. Vol. 22, No. 2. P. e14975. DOI: https://doi.org/10.1111/ijac.14975

20. Das A., Nanao Y., Rajan A., Di Falco A., Schulz S. A. Low-temperature fabrication of plasmonic titanium nitride thin films by electron beam evaporation. *Journal of Physics*: «Photonics». 2025. Vol. 7, No. 2. P. 025032. DOI: https://doi.org/10.1088/2515-7647/adcddc

21. Kalinina N. E., Glushkova D. B., Voronkov A. I., Kalinin V. T. Influence of nanomodification on structure formation of multicomponent nickel alloys. *Functional Materials*. 2019. Vol. 26, No. 3. P. 514–518. DOI: https://doi.org/10.15407/fm26.03.514

22. Hlushkova D. B., Kalinin A. V., Kalinina N. E., Volchuk V. M., Saenko V. A., Efimenko A. A. Study of nanomodification of nickel alloy GS3 with titanium carbide. *Problems of Atomic Science and Technology*. 2023. No. 2 (144). P. 126. DOI: https://doi.org/10.46813/2023-144-126.

DOI 10.15588/1607-6885-2025-4-4

ТЕХНОЛОГІЇ ОТРИМАННЯ ТА ОБРОБКИ КОНСТРУКЦІЙНИХ МАТЕРІАЛІВ

TECHNOLOGIES OF OBTAINING AND PROCESSING OF CONSTRUCTION MATERIALS

UDC 669.15.194.56

Volodymyr Grabovskyi — Candidate of Technical Sciences, Associate Professor, Associate Professor of the Department of Physical Materials Science, National University Zaporizhzhia Polytechnic, Zaporizhzhia, Ukraine, *e-mail: vladimirgr45@ukr.net*, ORCID: 0000-0003-0936-6132

Igor Bilonik — Candidate of Technical Sciences, Associate Professor, Associate Professor of the Department of Integrated Welding Technologies and Structural Modelling, National University Zaporizhzhia Polytechnic, Zaporizhzhia, Ukraine, *e-mail: bilonikim@gmail.com*, ORCID: 0000-0002-3873-5307

Anatoliy Ershov — Doctor of Technical Sciences, Professor, Professor of the Department of Physics, National University Zaporizhzhia Polytechnic, Zaporizhzhia, Ukraine, *e-mail: ershov@zntu.edu.ua*, ORCID: 0000-0003-0878-6434

Olena Lysytsya — Senior Lecturer, Department of Physical Materials Science, National University Zaporizhzhia Polytechnic, Zaporizhzhia, Ukraine, *e-mail: ov_li@i.ua*, ORCID: 0000-0002-9588-245

DETERMINATION OF TEMPERATURE REGIMES FOR HOT DEFORMATION AND ANNEALING OF NEW 4Kh3N3G7M7F STAMPING STEEL WITH CONTROLLED AUSTENITIC TRANSFORMATION DURING OPERATION AND DISPERSION HARDENING

Purpose. *Determination of heating modes that ensure high technological plasticity during hot pressure treatment and the lowest possible hardness after annealing of new 4Kh3N3G7M7F stamping steel with controlled austenitic transformation during operation and dispersion hardening.*

Research methods. *Torsion and impact bending tests. Hardness measurement. Optical microscopy. X-ray structural analysis.*

Results. *According to the results of torsion and impact bending tests of 4Kh3N3G7M7F steel in the temperature range of 900...1225 °C, it was found that the obtained dependencies have the form of curves with a maximum in the temperature range of 1150...1175 °C at a number of twists about 5 and impact toughness of about 92 J/cm^2. The torque decreases monotonically as the temperature increases (from 2590 N·m at 900 °C to 739 N·m at 1225 °C). Based on the obtained data, the recommended temperature regime for hot pressure treatment of the steel under study is such that the maximum heating temperature of the billets (ingots) should not exceed 1175 °C and not be lower than 950 °C. After forging and cooling in air, the steel has a bainite-martensite structure with a hardness of 44 HRC.*

Based on the results of the effect of full two-stage and incomplete annealing on the reduction of hardness, it was established that the dependence of hardness on annealing in the temperature range of Ac_1-Ac_3 has the form of a curve with a minimum. Full annealing of the studied steel reduces the hardness to 35 HRC and is recommended to be performed according to the following mode: 800 °C, 2 hours, cooling with the furnace + 680 °C, 2 hours, cooling with the furnace. A reduction in steel hardness to 33 HRC is achieved after incomplete annealing at a temperature of 680 °C for 6 hours and cooling with the furnace. After annealing to minimum hardness, 4Kh3N3G7M7F steel acquires a predominantly fine-grained pearlite structure.

Scientific novelty. *After hot deformation and air cooling, 4Kh3N3G7M7F steel with controlled austenitic transformation during operation and dispersion hardening has a bainite-martensite structure with a hardness of 44 HRC. It has been established that during annealing, the dependence of hardness on the increase in the holding temperature of 4Х3Н3Г7М7Ф steel in the range of Ac_1-Ac_3 has the form of a curve with a minimum at a temperature of 680 °C. This is explained by a change in the ratio of steel components with the decomposition of the initial bainite-martensite structure and the restoration of this structure during the cooling of the austenite component. In the annealed state, the steel has a predominantly fine-grained pearlite structure.*

DOI 10.15588/1607-6885-2026-2-5

Practical value. *Based on the results of torsion and impact bending tests, it has been determined that the hot pressure treatment temperature of 4Kh3N3G7M7F steel should be within the range of 1150...950 °C. To improve machinability and obtain a more balanced structure, complete and incomplete annealing modes for 4Kh3N3G7M7F steel have been developed, which reduce the hardness value to 33...35 HRC (compared to 44 HRC after hot deformation). The lowest hardness is achieved by incomplete annealing according to the following mode: 680 °C, holding for 6 hours, cooling in the furnace.*

Key words*: 4Kh3N3G7M7F steel, technological plasticity, temperature, annealing, hardness, structure.*

Introduction

The maximum operating temperature of the best heat-resistant martensitic stamping steels is no higher than 700 °C, which is due to the fundamental characteristics of their base structure. At the same time, during hot metal processing under pressure, the heating of the working parts of tools can significantly exceed these temperatures [1]. This has necessitated the search for other types of stamping materials for use at high temperatures. In particular, steels and alloys based on a BCC crystal lattice with dispersion hardening are proposed as substitutes for standard stamping steels [2–4]. However, their widespread use is limited by their cost and poor machinability [5]. These shortcomings are largely eliminated in new stamping steels with Continuous Annealing Treatment (CAT), the nature and development of which are discussed, in particular, in [6–15]. They have an FCC crystal lattice at room temperature, which gives them satisfactory machinability, and acquire an BCC crystal lattice when heated above 500…600 °C, which increases their resistance to high-temperature embrittlement. This is achieved by lowering their critical points by 200…300 °C compared to standard heat-resistant stamping steels. As a result, steels with CAT offer advantages for the manufacture of pressing tools with operating temperatures above 700 °C. An additional increase in the high-temperature strength of such steels is achieved due to their dispersion hardening after quenching and ageing. A prerequisite for the dispersion hardening of steels with CAT is that after quenching (treatment with a solid solution), they must have a predominantly austenitic rather than martensitic structure [8, 9].

As a result of the search for effective alloying, a new stamping steel with CAT grade 4Kh3N3G7M7F [10] has been developed, which is capable of strengthening by dispersion hardening due to the precipitation of intermetallic particles of the Fe_2Mo type Laves phase and VC type carbides. Its strengthening heat treatment consists of quenching (treatment in a supersaturated solid solution) from a temperature of 1150 °C and subsequent ageing at 725 °C for 2 hours. This provides a significant increase in the high-temperature (750 °C and above) strength of this steel – 2…3 times compared to heat-resistant serial martensitic stamping steels. It has been established [10] that in order to maintain its advantages, 4Kh3N3G7M7F steel must have the following component content limits (in % by mass): 0,39...0,46 C; 2,7...3,6 Cr; 2,7...3,5 Ni; 6,1...6,9 Mn; 6,3...7,1 Mo; 1,1...1,8 V; 0,25...0,36 Si; Fe – the rest. The production and use of 4Kh3N3G7M7F steel requires knowledge of the correct temperature regimes for hot pressure treatment and annealing. The temperature range for heating billets during hot pressure treatment must ensure satisfactory deformability of steels and technological plasticity to prevent the formation of cracks during deformation. Determining the annealing regime, which involves obtaining an equilibrium structure with the lowest possible hardness, is important for ensuring satisfactory machining of steel. Usually, for this purpose, an attempt is made to obtain a pearlite-type structure in alloy steels after annealing. Solving this problem for steels with CAT is not easy due to the high stability of supercooled austenite and, accordingly, the complexity of obtaining such an equilibrium structure. All this indicates the need to carry out appropriate experiments to solve such problems.

Purpose of the work

To determine the heating modes that ensure high technological plasticity during hot pressure treatment and the lowest possible hardness after annealing of new 4Kh3N3G7M7F stamping steel with controlled austenitic transformation during operation and dispersion hardening.

Materials and research methods

4Kh3N3G7M7F steel was smelted in an open induction furnace with a capacity of 50 kg and poured into square-section ingots. The alloying element content of the steel melts was within the grade composition specified above.

Samples for torsion and impact bending tests were made from steel ingots. First, the ingots were cut lengthwise into 15 mm thick plates, and then cut into square-section bars with a side length of 15 mm. Samples for torsion and impact bending tests were made from these bars.

In accordance with GOST 3565-80, the torsion test specimens had a diameter of 10 mm and a working length of 100 mm. The nature of the tests was that one end of the specimen was fixed in place, while a pair of forces was applied to the other end in a plane perpendicular to the axis of the specimen. One end of the sample was fixed, while the other rotated at a selected speed. This meant that the second end of the sample was able to perform longitudinal gradual movements, which excluded the possibility of axial tensile stresses forming in the sample. The samples were twisted on a KM-50 testing machine. The tests were performed at a speed of 20 revolutions per minute until the specimens were destroyed. Based on the test results, the number of revolutions until the destruction of the specimens and the corresponding value of the torque M_t were determined.

DOI 10.15588/1607-6885-2026-2-5

The impact bending test was performed on standard Menage specimens with a U-shaped notch with a radius of 1 mm.

To study the annealing modes, the ingots were forged into square-section bars with a side length of 20 mm, which were cooled in air. The bars were cut into cubic samples.

Research results and discussion

When assessing the technological plasticity of 4Kh3N3G7M7F steel, it was taken into account that it was necessary to determine the temperature range of the highest values of plasticity, resistance to destruction and the lowest resistance to high-temperature deformation in order to predict the best deformability during forging or pressing. Torsion and impact bending tests were carried out on samples in the temperature range of 900…1225 °C. The resulting dependencies are shown in Fig. 1. It can be seen that during torsion tests, the value of the torsional moment M_t monotonically decreases as the temperature increases (from 2590 N·m at 900 °C to 740 N·m at 1225 °C), which corresponds to the natural temperature dependence of steel resistance to plastic deformation. The torque M_t decreases most intensively up to a temperature of 1150 °C. The temperature dependence of the number of revolutions has the form of a curve with a maximum in the temperature range 1150...1175 °C at a value of about 5 revolutions. The curve of the temperature dependence of impact toughness has a similar appearance, the maximum value of which (about 92 J/cm^2) corresponds to testing at temperatures of 1100...1150 °C. That is, the best combination of technological plasticity characteristics is achieved when heated to a temperature of 1150 °C. Higher heating temperatures cause structural changes that significantly reduce the technological plasticity of steel and can lead to metal destruction during hot pressure treatment.

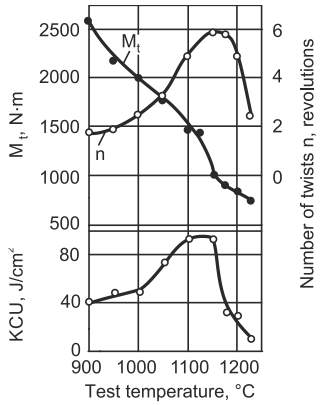

Figure 1. Dependence of torque (M_t), number of twists (n) and impact toughness (KCU) of 4Kh3N3G7M7F steel on test temperature

Thus, based on the results of determining the highest values of the number of twists and impact toughness, the maximum heating temperature of billets (ingots) during hot pressure treatment of 4Kh3N3G7M7F steel should not exceed 1150 °C. At the same time, the torque value is significantly reduced, which ensures good high-temperature deformability of steel. The lower value of the hot deformation temperature is about 950 °C and can be adjusted depending on the power of the stamping equipment and the size of the forgings. Taking into account the obtained results and structural features, the following heating scheme for ingots of new 4Kh3N3G7M7F stamping steel during hot pressure treatment is proposed. First, the blank is loaded into a furnace at a temperature of 800 °C (taking into account that the temperature of Ac_3 = 795 °C) and, after complete heating, is held for 1 hour to complete the polymorphic $\alpha \rightarrow \gamma$ transformation. Next, the blank is heated at a rate of 50 °C per hour to a forging temperature of 1150 °C, held for 1 hour and subjected to forging. The forging completion temperature is not lower than 950 °C. During the forging process, intermediate heating to 1150 °C is possible. The use of this heating scheme ensured the production of high-quality 4Kh3N3G7M7F steel forgings.

Let us consider the results of determining the annealing modes that provide 4Kh3N3G7M7F steel with the lowest hardness values and, accordingly, better machinability. The initial state of processing was forging and air cooling. In this state, the steel had a predominantly bainite-martensite structure, as shown in Fig. 2. The hardness was 44 HRC, which is too high for satisfactory machining of steel.

The study of the effect of different annealing modes on the reduction of the hardness of 4Kh3N3G7M7F steel was carried out taking into account its relatively low critical points: Ac_1 at about 530 °C, Ac_3 at 795 °C , Ar_1 at 220 °C, M_s at 135 °C, M_f – 40 °C. Full annealing of samples was carried out using a two-stage mode with a sequential decrease in temperature, and incomplete single annealing at different temperatures.

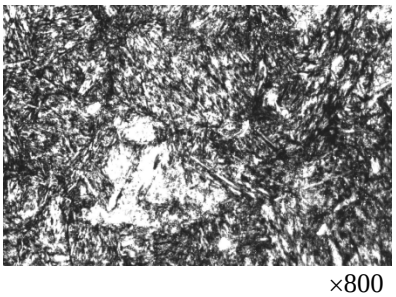

×800

Figure 2. Microstructure of 4Kh3N3G7M7F steel after forging and air cooling

First, the effectiveness of two-stage annealing was investigated. The first annealing corresponded to complete annealing and consisted of heating the samples to temperatures of 800…900 °C (i.e. above Ac_3) with a holding time of 2 hours and cooling with the furnace (100 °C/hour to 300 °C, then in air). This was followed by a second annealing at temperatures ranging from 580 to 730 °C (in the Ac_1–Ac_3 region) with the same holding

DOI 10.15588/1607-6885-2026-2-5

time and cooling as in the first annealing. It was assumed that after the first annealing, the austenitic structure would transform into bainite-martensite, which is due to the high stability of supercooled austenitic steel. The purpose of the second annealing was to break down the bainite-martensite structure, i.e. to obtain a more equilibrium state and, accordingly, lower steel hardness. The results of this experiment are shown in Fig. 3. Each curve corresponds to a specific temperature of the previous first annealing (indicated on the graph). According to the data obtained, the hardness after the first annealing is in the range of 39...41 HRC and increases with higher annealing temperatures. This is explained by the increase in the concentration of carbon and alloying elements in the solid solution due to the more complete dissolution of excess carbide phases with increasing heating temperature.

A typical microstructure after the first annealing (heating above Ac_3 and cooling with the furnace) is shown in Fig. 4, *a*.

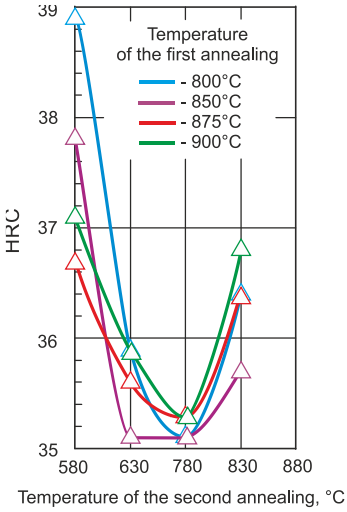

Figure 3. Hardness dependence on the temperature of the second annealing after different temperatures of the first annealing (indicated for each curve in the graph)

It is similar to the microstructure after forging (see Fig. 2), i.e. it is also characterised as bainitic-martensitic, but with a slightly smaller austenite grain size, which is the result of complete recrystallisation during heating.

As can be seen from Fig. 3, all curves of hardness dependence on the temperature of the second annealing have a minimum in the region of 680 °C, which can be explained as follows. The decrease in hardness with an increase in the holding temperature to 680 °C is due to the decomposition of the initial bainite-martensite structure formed after the first annealing. As the temperature increases from 680 °C to 730 °C, the proportion of the austenitic component in the steel increases significantly, and subsequent cooling to room temperature will lead to its transformation according to bainite-martensite kinetics. The increase in hardness due to the formation of such a structure during cooling will prevail over the decrease in hardness due to the decay of the initial bainite-martensite component of the structure. Accordingly, the closer to the temperature Ac_3 (795 °C), the greater the proportion of the bainite-martensite structure in the cooled state, which is characterised by increased hardness.

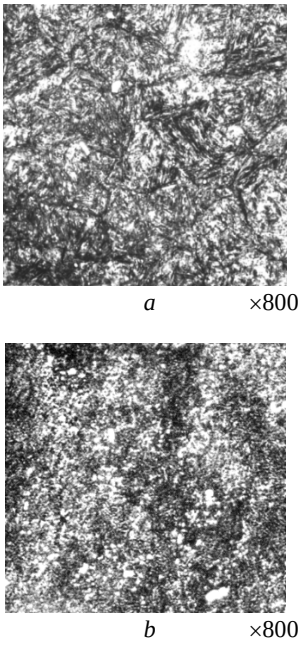

Figure 4. Microstructures of 4Kh3N3G7M7F steel after complete step annealing:
a – first annealing at 800 °C; *b* – second annealing at 680 °C

The hardness values in the minimum range for different annealing temperatures are slightly different. The lowest hardness was obtained for samples that were pre-annealed at temperatures of 800…850 °C (average – 825 °C), equal to 35,1 HRC. This is 9 HRC units less than after cooling the forgings in the furnace. The microstructure after such annealing is shown in Fig. 4, *b* and mainly corresponds to fine-grained pearlite formed as a result of furnace cooling of the decomposition products of the initial bainite-martensite structure. There are also areas of bainite-martensite structure formed during the cooling of the austenite component, which occurs when heated above Ac_1, and a small amount of residual austenite. X-ray phase analysis has established that after the second annealing to minimum hardness, the base of the steel is α-iron, and the amount of residual austenite does not exceed 6%. Phase analysis showed the presence of MC and $M_{23}C_6$ carbides in the structure.

Thus, complete annealing (which is usually used to obtain a more perfect structure) to a hardness of 35 HRC is recommended to be performed in a stepwise mode: 825 °C, 2 hours, cooling with the furnace + 680 °C, 2 hours, cooling with the furnace.

Let us consider the results of a study of single annealing for the possibility of reducing the hardness of steel. The change in steel hardness after heating and holding samples in the temperature range of 580...850 °C

DOI 10.15588/1607-6885-2026-2-5

for 2 hours with cooling both in the furnace and in air was investigated. For the selected temperature range, such annealing is considered incomplete. Figure 5 shows that the dependencies obtained for both cooling methods are curves with a minimum at 680 °C, as for complete step annealing. When the heating temperature is increased to 800 °C, the hardness reaches its maximum value and then stops increasing. This is due to the fact that above ac_3 (795 °C), the steel becomes completely austenitic, and when cooled, it acquires a bainite-martensite structure. The presence of a minimum on the curves is explained in the same way as in the case of the complete step annealing considered above. Naturally, the cooling curve with the furnace is lower than that with air cooling. Accordingly, if in the first case the minimum hardness value is 34,7 HRC, then in the second case it is 35,6 HRC.

The possibility of achieving even lower hardness after single annealing by increasing the holding time to 6 hours at temperatures around 680 °C, i.e. 630...700 °C, was also investigated. The results obtained are shown in Table 1.

It can be seen that as the holding time increases, the hardness values at all temperatures decrease slightly. Moreover, for all annealing temperatures after cooling in the furnace, the hardness is 0,8...1,5 HRC units lower compared to air cooling. The lowest hardness of 32,5 HRC is achieved by annealing at 680 °C for 6 hours and cooling in the furnace. This incomplete annealing mode can be recommended for 4Kh3N3G7M7F steel to ensure better machinability. The microstructure after such annealing is similar to that shown in Fig. 4, *b*, i.e. It is mainly fine-grained pearlite with areas of bainite-martensite and residual austenite. The difference is the larger grain size of austenite and the heterogeneity of the structure, which is characteristic of annealing when heated to temperatures of incomplete recrystallisation.

Thus, to reduce the hardness of the new 4Kh3N3G7M7F steel after hot deformation, annealing can be performed, depending on the complex requirements for structure and hardness, either with complete (full annealing) or partial (incomplete annealing) recrystallisation.

Full annealing, which is usually used to obtain a more perfect structure, is performed in a stepwise mode: 825 °C, 2 hours, cooling with the furnace + 680 °C, 2 hours, cooling with the furnace. The hardness after such annealing is about 35 HRC. Incomplete annealing reduces the hardness to 33 HRC and is performed according to the following mode: 680 °C, 6 hours, cooling with the furnace.

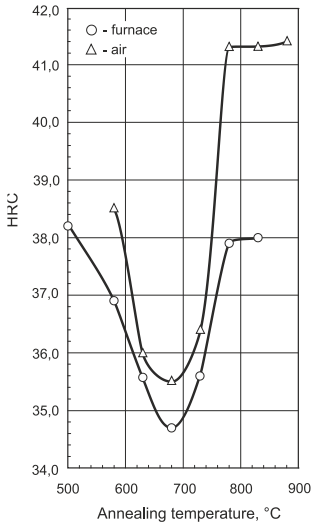

Figure 5. Effect of annealing temperature (2 hours holding time) on hardness after different cooling of steel

Table 1 – Hardness values of 4Kh3N3G7M7F steel after different temperatures and times of incomplete annealing

Annealing temperature, °C	Exposure time, hours	Cooling method	Hardness, HRC
650	2	with a furnace	34,5
		in the air	35,2
	4	with a furnace	34,1
		in the air	34,5
	6	with a furnace	32.8
		in the air	33,5
680	2	with a furnace	33,8
		in the air	35,1
	4	with a furnace	32,6
		in the air	34,3
	6	with a furnace	32,5
		in the air	33,3
700	2	with a furnace	34,5
		in the air	35,1
	4	with a furnace	33,5
		in the air	34,7
	6	with a furnace	33,1
		in the air	34,0

DOI 10.15588/1607-6885-2026-2-5

Conclusions

During hot pressure treatment of new 4Kh3N3G7M7F stamping steel with **C**AT and dispersion hardening, the maximum heating temperature of billets (ingots) should not exceed 1150…1175 °C. This temperature corresponds to the maximum values of the technological plasticity of steel according to the results of torsion and impact bending tests and a significant reduction in torque. The lower value of the hot deformation temperature is recommended to be at least 900 °C.

After hot deformation and air cooling, 4Kh3N3G7M7F steel has a bainite-martensite structure with a hardness of 44 HRC. Full annealing of the tested steel reduces the hardness to 35 HRC and is recommended to be performed according to the following regime: 850 °C, 2 hours, cooling with the furnace + 680 °C, 2 hours, cooling with the furnace. A reduction in steel hardness to 33 HRC is achieved after incomplete annealing according to the following regime: 680 °C, 6 hours, cooling with the furnace. The dependence of hardness on annealing in the temperature range Ac_1–Ac_3 has the form of a curve with a minimum, which is due to a change in the ratio of particles of the bainite-martensite structure that disintegrated and formed during the cooling of austenite. In the annealed state, 4Kh3N3G7M7F steel has a predominantly fine-grained pearlite structure at minimum hardness.

References

1. Grabovskyi, V. Ya. (2000). Structural transformations of matrices during hot pressing of titanium and steel profiles. Metallurgy and Metal Processing, (3), 17–21.

2. Grabovskyi, V. Ya., Belikov, S. B., & Trikoz, G. G. (2002). Research on the performance of press dies made of nickel alloy ZhS6K during hot pressing of heat-resistant materials. New Materials and Technologies in Metallurgy and Mechanical Engineering, (2), 37–40.

3. Grabovskyi, V. Ya. (2003). Testing of matrices made of heat-resistant alloy KhN60VMUT (EP539) during hot pressing of stainless steels. New Materials and Technologies in Metallurgy and Mechanical Engineering, (1), 35–38.

4. Grabovskyi, V. Ya., Kaniuka, V. I., Trykoz, G. G., & Semenyuk, T. P. (2005). Influence of alloying on the performance of nickel alloys for press dies. New Materials and Technologies in Metallurgy and Mechanical Engineering, (1), 32–36.

5. Grabovskyi, V. Ya., & Lysytsya, O. V. (2020). Heat treatment as a method for improving the machinability of tool alloys with a BCC lattice. New Materials and Technologies in Metallurgy and Mechanical Engineering, (1), 88–89. https://doi.org/10.15588/1607-6885-2021-1-13

6. Gogayev, K. O., Sydorchuk, O. M., & Radchenko, O. K. (2016). Tool stamping steels for hot forming (review). Metallurgy and Metal Processing, (3), 18–24.

7. Grabovskyi, V. Ya., Kolisnyk, O. P., & Ostrovska, A. Ye. (2008). Features of the structure and properties of austenitic-martensitic stamping steel. Metallurgy and Metal Processing, (1), 35–38.

8. Perepelkina, M. V., & Grabovskyi, V. Ya. (2016). Selection of effective alloying of new stamped steels with austenitic transformation during operation. New Materials and Technologies in Metallurgy and Mechanical Engineering, (1), 11–15.

9. Grabovskyi, V. Ya., & Lysytsya, O. V. (2023). On the dispersion hardening ability of new stamping steel with controlled austenitic transformation. Metallurgy and Metal Processing, (3), 9–11. https://doi.org/10.15407/mom2023.03.003

10. Grabovskyi, V. Ya., Ershov, A. V., & Lysytsya, O. V. (2025). Operational high-temperature strength of controlled austenite-transformed and dispersion-hardenable die steel. Strength of Materials, 56(6). https://doi.org/10.1007/s11223-025-00728-x

11. Sydorchuk, O. M. (2021). Steel with regulation of austenitic transformation during operation. Metallurgy and Metal Processing, (2), 47–53. https://doi.org/10.15407/mom2021.02.047

12. Krugljakow, A. A., Rogachev, S. O., Lebedeva, N. V., Sokolov, P. Yu., Arsenkin, A. M., & Khatkevich, V. M. (2022). On the nature of hot work hardening phenomenon in die steel with regulated austenitic transformation during exploitation. Materials Science and Engineering: A, 833, 142548. https://doi.org/10.1016/j.msea.2021.142548

13. Gogaev, K. O., & Sydorchuk, O. M. (2022). Die steel with regulated austenitic transformation for hot deformation of copper-nickel alloy. Science and Innovation, 18(3), 23–27. https://doi.org/10.15407/scine18.03.023

14. Krugljakow, A. A., Rogachev, S. O., Sokolov, P. Y., Khatkevich, V. M., & Priupolin, D. V. (2024). Evaluation of hot hardening resource of die steel with controlled austenitic transformation during exploitation. Metallurgist, 68, 187–194. https://doi.org/10.3103/s0967091225700445

15. Sydorchuk, O. M., Myslyvchenko, O. M., Gogaev, K. O., & Hongguang, Y. (2022). Structure and properties of forged steel with regulated austenite transformation. Materials Science, 58, 119–125. https://doi.org/10.1007/S11003-022-00639-1

Received 09.03.2026
Accepted 19.03.2026
Published 07.05.2026

DOI 10.15588/1607-6885-2026-2-5

УДК 669.15.194.56

ВИЗНАЧЕННЯ ТЕМПЕРАТУРНИХ РЕЖИМІВ ГАРЯЧОЇ ДЕФОРМАЦІЇ ТА ВІДПАЛУ НОВОЇ ШТАМПОВОЇ СТАЛІ 4Х3Н3Г7М7Ф З РЕГУЛЬОВАНИМ АУСТЕНІТНИМ ПЕРЕТВОРЕННЯМ ПРИ ЕКСПЛУАТАЦІЇ ТА ДИСПЕРСІЙНОМУ ТВЕРДІННЮ

Володимир Грабовський — канд. техн. наук, доцент, доцент кафедри фізичного матеріалознавства Національного університету «Запорізька політехніка», м. Запоріжжя, Україна, *e-mail: vladimirgr45@ukr.net*¸ ORCID: 0000-0003-0936-6132

Ігор Білоник — канд. техн. наук, доцент, доцент кафедри «Інтегровані технології зварювання та моделювання конструкцій» Національного університету «Запорізька політехніка», м. Запоріжжя, Україна, *e-mail: bilonikim@gmail.com*, ORCID: 0000-0002-3873-5307

Анатолій Єршов — д-р техн. наук, професор, професор кафедри фізики Національного університету «Запорізька політехніка», м. Запоріжжя, Україна, *e-mail: ershov@zntu.edu.ua*, ORCID: 0000-0003-0878-6434

Олена Лисиця — старший викладач кафедри фізичного матеріалознавства Національного університету «Запорізька політехніка», м. Запоріжжя, Україна, *e-mail: ov_li@i.ua*, ORCID: 0000-0002-9588-2450

Мета роботи. *Визначення режимів нагріву, що забезпечують високу технологічну пластичність при гарячій обробці тиском та якомога меншу твердість після відпалу нової штампової сталі 4Х3Н3Г7М7Ф з регульованим аустенітним перетворенням при експлуатації та дисперсійному твердінню.*

Методи дослідження. *Випробування на кручення та ударний згин. Вимірювання твердості. Оптична мікроскопія. Рентгеноструктурний аналіз.*

Отримані результати*. За даними випробувань сталі 4Х3Н3Г7М7Ф на кручення та ударний згин в інтервалі температур 900…1225 °С встановлено, що отримані залежності мають вигляд кривих з максимумом в області температур 1150…1175 °С при числу обертів біля 5 та ударної в'язкості біля 92 Дж/см^2. Величина крутного моменту монотонно зменшується по мірі зростання температури (від 2590 Н·м при 900 °С до 739 Н·м при 1225 °С). Відповідно отриманим даним рекомендовано температурний режим гарячої обробки тиском дослідженої сталі, за яким максимальна температура нагріву заготовок (зливків) повинна бути не вище 1175 °С та не нижче 950 °С. Після кування і охолодження на повітрі сталь має бейнітно-мартенситну структуру з твердістю 44 HRC.*

За результатами впливу на зниження твердості повного двоступеневого та неповного відпалів встановлено, що залежність твердості від відпалу в області температур Ac_1-Ac_3 має вигляд кривої з мінімумом. Повний відпал дослідженої сталі забезпечує зниження твердості до 35 HRC і рекомендовано виконувати за таким режимом: 800 °С, 2 години, охолодженні з піччю + 680 °С, 2 години, охолодженні з піччю. Зниження твердості сталі до 33 HRC досягається після неповного відпалу при температурі 680 °С протягом 6 годин і охолодження з піччю. Після відпалу на мінімальну твердість сталь 4Х3Н3Г7М7Ф набуває переважно структуру дрібнодисперсного зернистого перлиту.

Наукова новизна. *Після гарячої деформації та охолодження на повітрі сталь 4Х3Н3Г7М7Ф з регульованим аустенітним перетворенням при експлуатації та дисперсійним твердінням має бейнітно-мартенситну структуру з твердістю 44 HRC. Встановлено, що при відпалі залежність твердості від зростання температури витримки сталі 4Х3Н3Г7М7Ф в інтервалі Ac_1-Ac_3 має вигляд кривої з мінімумом при температурі 680 °С. Пояснюється це зміною співвідношення складових часток сталі з розпадом вихідної бейнітно-мартеситної структури та з поновленням такої структури при охолодженні аустенітної складової. У відпаленому стані сталь має переважно структуру дрібнодисперсного зернистого перлиту.*

Практична цінність. *За результатами випробувань на кручення та ударний згин визначено, що температура гарячої обробки тиском сталі 4Х3Н3Г7М7Ф повинна знаходитися в межах 1150…950 °С. Для покращення обробки різанням та отримання більш рівновагової структури розроблені режими повного та неповного відпалів сталі 4Х3Н3Г7М7Ф, які знижують значення твердості до 33…35 HRC (порівняно з 44 HRC після гарячої деформації). Найменшу твердість забезпечує неповний відпал за режимом: 680 °С, витримка 6 годин, охолодження з піччю.*

Ключові слова: *сталь 4Х3Н3Г7М7Ф, технологічна пластичність, температура, відпал, твердість, структура.*

DOI 10.15588/1607-6885-2026-2-5

Список літератури

1. Грабовський В. Я. Структурні перетворення матриць при гарячому пресуванні титанових та сталевих профілів. *Металознавство та обробка металів*. 2000. № 3. С. 17–21.

2. Грабовський В. Я., Бєліков С. Б., Трикоз Г. Г. Дослідження працездатності пресових матриць з ливарного нікельового сплаву ЖС6К при гарячому пресуванні жароміцних матеріалів. *Нові матеріали і технології в металургії та машинобудуванні*. 2002. № 2. С. 37–40.

3. Грабовський В. Я. Випробування матриць з жароміцного сплаву ХН60ВМЮТ (ЕП539) при гарячому пресуванні нержавіючих сталей. *Нові матеріали і технології в металургії та машинобудуванні*. 2003. № 1. С. 35–38.

4. Грабовський В. Я., Канюка В. І., Трикоз Г. Г., Семенюк Т. П. Вплив легування на працездатність нікелевих сплавів для пресових матриць. *Нові матеріали і технології в металургії та машинобудуванні*. 2005. № 1. С. 32–36.

5. Грабовський В. Я., Лисиця О. В. Термічна обробка як спосіб покращення оброблюваності різанням інструментального сплаву з ГЦК ґраткою. *Нові матеріали і технології в металургії та машинобудуванні*. 2020. № 1. С. 88–89. DOI: https://doi.org/10.15588/1607-6885-2021-1-13.

6. Гогаєв К. О., Сидорчук О. М., Радченко О. К. Інструментальні штампові сталі для гарячого деформування (огляд). Металознавство та обробка металів. 2016. № 3. С. 18–24.

7. Грабовський В. Я., Колісник О. П., Островська А. Є. Особливості структури та властивостей штампової сталі аустенітно-мартенситного класу. *Металознавство та обробка металів*. 2008. № 1. С. 35–38.

8. Перепьолкіна М. В., Грабовський В. Я. Вибір ефективного легування нових штампових сталей з аустенітним перетворенням при експлуатації. *Нові матеріали і технології в металургії та машинобудуванні*. 2016. № 1. С. 11–15.

9. Грабовський В. Я., Лисиця О. В. До здатності дисперсійного твердіння нової штампової сталі з регульованим аустенітним перетворенням. *Металознавство та обробка металів*. 2023. № 3. С. 9–11. DOI: https://doi.org/10.15407/mom2023.03.003

10. Grabovskyi V. Ya., Ershov A. V., Lysytsya O. V. Operational high-temperature strength of controlled austenite-transformed and dispersion-hardenable die steel. *Strength of Materials*. 2025. Vol. 56, No. 6. DOI: https://doi.org/10.1007/s11223-025-00728-x

11. Сидорчук О. М. Сталь з регулюванням аустенітного перетворення при експлуатації. *Металознавство та обробка металів*. 2021. № 2. С. 47–53. DOI: https://doi.org/10.15407/mom2021.02.047

12. Krugljakow A. A., Rogachev S. O., Lebedeva N. V. et al. On the nature of hot work hardening phenomenon in die steel with regulated austenitic transformation during exploitation. *Materials Science and Engineering*. 2022. Vol. 833. DOI: https://doi.org/10.1016/j.msea.2021.142548

13. Gogaev K. O., Sydorchuk O. M. Die steel with regulated austenitic transformation for hot deformation of copper-nickel alloy. *Science and Innovation*. 2022. Vol. 18, No. 3. P. 23–27. DOI: https://doi.org/10.15407/scine18.03.023

14. Krugljakow A. A., Rogachev S. O., Sokolov P. Y. et al. Evaluation of hot hardening resource of die steel with controlled austenitic transformation during exploitation. *Metallurgist*. 2024. Vol. 68. P. 187–194. DOI: https://doi.org/10.3103/s0967091225700445.

15. Sydorchuk O. M., Myslyvchenko O. M., Gogaev K. O., Hongguang Ye. Structure and properties of forged steel with regulated austenite transformation. *Materials Science*. 2022. Vol. 58. P. 119–125. DOI: https://doi.org/10.1007/S11003-022-00639-1

DOI 10.15588/1607-6885-2026-2-5

МОДЕЛЮВАННЯ ПРОЦЕСІВ В МЕТАЛУРГІЇ ТА МАШИНОБУДУВАННІ

MODELING OF PROCESSES IN METALLURGY AND MECHANICAL ENGINEERING

UDC 621.941.08

Pavlo Tryshyn — PhD, Associate Professor of the Department of Mechanical Engineering Technology, National University Zaporizhzhia Polytechnic, Zaporizhzhia, Ukraine, *e-mail: trishin@zp.edu.ua*, ORCID: 0000-0002-3301-5124

Olena Kozlova — Candidate of Technical Sciences, Associate Professor of the Department of Mechanical Engineering Technology, National University Zaporizhzhia Polytechnic, Zaporizhzhia, Ukraine, *e-mail: kozlova@zp.edu.ua*, ORCID: 0000-0002-3478-5913

Yuriy Vnukov — Doctor of Technical Sciences, Professor, Independent scientist, California, USA, *e-mail: ypahar@ukr.net*, ORCID: 0000-0002-4297-9646

Andriy Levchenko — Graduate student of the Department of Mechanical Engineering Technology, National University Zaporizhzhya Polytechnic, Zaporizhzhya, Ukraine, *e-mail: andrey.levchenko.zp@gmail.com*, ORCID: 0009-0006-3615-867X

INFLUENCE OF DISCONTINUOUS CHIP FORMATION ON THE EXCITATION OF REGENERATIVE SELF-OSCILLATIONS DURING TURNING

Purpose. *The objective of this study is to investigate the influence of discontinuous chip formation on the excitation of regenerative self-oscillations during turning, to compare the vibration for continuous and discontinuous chip formation mechanisms, and to improve the prediction of machining stability for brittle materials.*

Research methods. *The study was carried out under conditions of continuous orthogonal turning using a CNC lathe. Vibration was investigated with a single degree of freedom cutter–oscillator designed in the direction of chip thickness variation. The displacement of the cutting edge during machining was measured using an inductive sensor, and the signals were recorded through a multi-channel data acquisition system and processed on a computer. Oscillograms were analyzed to determine vibration amplitude and static deflection.*

Results. *The experimental results showed that the type of chip formation has a significant influence on vibration during turning. When machining steel AISI 1045, characterized by continuous chip formation, pronounced regenerative chatter was observed in the cutting speed range of v=100–250 m/min, with vibration amplitude increasing as cutting speed increased. In contrast, during machining of gray cast iron GG35, which produces discontinuous chips, no regenerative chatter was detected; only low-amplitude random vibrations were present, and their level remained nearly constant over the entire cutting speed range. For bronze CuSn3Zn13Pb4, also characterized by discontinuous chip formation, regenerative chatter occurred only at higher cutting speeds (v=150–250 m/min), and the vibration amplitude increased with cutting speed similarly to steel.*

Scientific novelty. *The scientific novelty of this study lies in establishing the influence of discontinuous chip formation on the suppression and excitation conditions of regenerative self-oscillations during turning.*

Practical value. *The practical significance of this study lies in improving the prediction of machining stability when processing materials with different chip formation mechanisms. The obtained results can be used to select optimal cutting conditions that reduce or prevent regenerative self-oscillations, especially when machining brittle materials.*

Key words: *vibration, regenerative self-oscillations, chip formation, cutter-oscillator, chip type.*

Introduction

Vibration during turning remains a key problem in machining, as it significantly impacts surface quality, part accuracy, and cutting tool life [1]. The most undesirable type of vibration during machining is considered to be regenerative self-oscillations, the mechanism of which is associated with cutting along a vibrational wavy trace that arose during the previous revolution of the part, leading to a change in the thickness of the cut layer over time during cutting [2].

DOI 10.15588/1607-6885-2026-2-6

Chip formation can also significantly influence cutting dynamics. Depending on the properties of the workpiece material and machining conditions, chip formation varies significantly, resulting in the formation of various chip types: continuous, discontinuous, and segmental chips [3]. In continuous chip formation, plastic deformation of the material occurs more continuously. Segmented chip formation is accompanied by the periodic formation of shear segments and the occurrence of high-frequency oscillations in cutting force. In discontinuous chip formation, the cutting process has a pronounced intermittent nature, caused by brittle fracture of the material and the formation of individual chip fracture elements. In this case, chip formation is accompanied by sharp surges in cutting forces and brief unloading of the cutting tool, which leads to pulsed excitation of oscillations. This specificity of the interaction between the tool and the workpiece can both limit the development of classical regenerative self-oscillations due to the break in feedback and, under certain conditions, initiate complex non-stationary vibration modes that require separate theoretical and experimental analysis.

Different chip formation types differ significantly in the mechanism of plastic deformation of the material, the frequency of chip formation, and the nature of cutting force changes. Most existing theoretical and experimental studies focus on the machining of plastic materials, which are characterized by continuous chip formation. Meanwhile, when machining brittle materials, such as gray cast iron, discontinuous chip formation occurs. Despite this, the influence of discontinuous chips on the excitation of regenerative self-oscillations has been insufficiently studied, and the applicability of classical models developed for continuous chip formation remains controversial.

Thus, there is need to expand the theory of cutting process dynamics to the class of brittle materials with discontinuous chip formation, which will allow for more accurate prediction of the stability of the turning process and the development of effective methods for vibration suppression.

Literature review

The problem of vibration during turning has been studied for a long time, but its physical nature still does not have an unambiguous interpretation. In early works, the main attention was paid to phenomena associated with contact processes on the cutting edge of the tool. In particular, one of the first explanations for the occurrence of vibrations was based on the periodic formation and breakdown of built up edge. In studies [4, 5] it was shown that the built up edge is cyclically formed and destroyed, causing a change in cutting forces and, as a result, excitation of vibrations of the technological system.

Most scientists associate the appearance of vibrations with the regenerative effect, which is considered the main source of self-oscillations during turning [6–9]. However, in work [10] it was established that waviness on the cutting surface is not the cause of regenerative self-oscillations, but rather their consequence. At the same time, vibrations occur as a result of the resonance of the frequency of chip formation and the natural frequency of the cutter during cutting.

In parallel with the development of the theory of regenerative self-oscillations, considerable attention was paid to the study of the chip formation process itself as a source of vibration excitation. It was found that chip segmentation is accompanied by fluctuations in cutting forces, which can act as a source of vibration excitation.

In [10], when turning steel AISI 1040, it was found that the frequency of formation of secondary and primary waves on the free side of the chip increases almost linearly with cutting speed. The vibration amplitude increases sharply when the chip segmentation frequency curve approaches the corresponding curve of the natural frequency of the cutter (at approximately 100 m/min).

In [11], graphs of the dependence of chip type on cutting speed were constructed during a study of various steels and a titanium alloy. It was found that when the chip formation frequency coincides with one of the natural oscillation frequencies of the machine's elastic system, resonance can occur, leading to intense vibrations. To avoid instability of the chip formation process in the local shear plane, the tool oscillation frequency must exceed the segmental chip formation frequency.

In [12], vibrations during milling of gray cast iron were studied. Based on the results, a stability lobe diagram in the frequency domain was constructed. In the study, the oscillator was a component with one degree of freedom along the z-axis. Milling was performed using a multi-tooth face mill with a 45° cutting angle. This research method does not allow for the study of regenerative self-oscillations alone.

The study [13] presents a hybrid methodology based on an artificial neural network, specifically developed for predicting the surface roughness of GG-25 gray cast iron workpieces processed during turning. These studies did not consider the effect of vibration on roughness.

In [14], a comprehensive model for predicting vibrations during turning of cast iron brake discs was developed, and a stability lobe diagram was constructed. A test cutting method was proposed for identifying vibrations during radial turning using continuous cutting at variable speed. It was established that the intensity of vibrations is affected by cutting speed; vibrations occur in a specific speed range in which the peak amplitude of oscillations is observed.

In [15], the influence of cutting parameters and the chemical composition of cast iron on the excitation of regenerative self-oscillations was established. It was found that a higher C-Si content in cast iron helps suppress the resulting vibrations; turning cast iron with a high carbon content with a lower C-Si content at low cutting speeds is accompanied by intense regenerative self-oscillations.

DOI 10.15588/1607-6885-2026-2-6

Despite the considerable amount of research, most of them focus on continuous or segmented chip formation, or use a methodology that is not able to separately study only regenerative self-oscillations. At the same time, the processes characteristic of the processing of brittle materials with the formation of discontinuous chips remain less studied. This limits the possibilities of applying classical models of cutting dynamics and necessitates the further development of the theory taking into account the peculiarities of discontinuous chip formation.

The aim of the study is to investigate the influence of discontinuous chip formation on the excitation of regenerative self-oscillations during turning.

Research methodology

The experiments were carried out under continuous orthogonal turning conditions on a Zenitech WL 320 CNC lathe [16]. A cutter-oscillator with one degree of freedom in the direction of change in the thickness of the cut layer was used to study the vibrations [17]. The natural frequency of the cutter-oscillator oscillations was f_n=500Hz. The cutter-oscillator was installed in the tool holder of the machine using a special device, in the housing of which an inductive displacement sensor Schneider Electric XS4-P12AB110 was installed (Fig. 1). Vibrations of the cutting edge during the turning process were recorded by this sensor and fed to a multichannel analog-to-digital converter L-Card E140 and transmitted in digital form to a personal computer. Signal processing was performed in PowerGraph 3.3 software. The obtained oscillograms were used to determine the cutting edge oscillation amplitude A_x and the static deflection B_x. Additionally, a spectral analysis of the oscillograms was performed using the fast Fourier transform method to determine the frequency of self-oscillations f_{SO}.

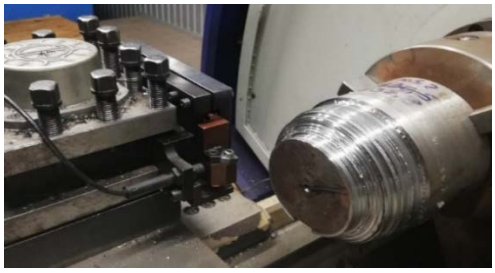

Figure 1. Workplace for vibration research [18]

The workpieces were cylindrical, D=120mm, L=100mm, ensuring high system rigidity during continuous turning. To compare the effects of different chip formation types on vibration excitation during turning, the following workpieces were used: grade steel AISI 1045 with continuous chips, gray cast iron GG35, and bronze CuSn3Zn13Pb4 – materials characterized by discontinuous chip.

Turning was performed under the following cutting conditions: cutting speed v=50-250m/min, feed rate S=0.2mm/rev, depth of cut t=1mm, without cooling.

The cutting carbide insert T15K6 (P30) has the following geometric parameters: γ=0°, α=10°, φ=90°, λ=0°, r=0.15 mm. The wear area on the flank surface of the cutter was maintained in the range of 0.05...0.1 mm.

Results and discussion

As a result of the research during turning of different materials, oscillograms of the cutting edge oscillations were recorded (Fig. 2–4), according to which the oscillation amplitude A_x and the static deflection of the cutter-oscillator B_x and the frequency of self-oscillations f_{SO} were measured (Table 1–3).

When turning steel AISI 1045 with the cutter-oscillator, intense regenerative self-oscillations were observed in the cutting speed range of v=100–250 m/min. The oscillation amplitude increased with increasing cutting speed. When turning cast iron GG35, regenerative self-oscillations were absent; oscillograms showed random oscillations whose amplitude remained virtually unchanged with increasing cutting speed. When turning bronze CuSn3Zn13Pb4, regenerative self-oscillations were observed at cutting speeds of v=150–250 m/min. With increasing cutting speed, the oscillation amplitude increased, similar to that observed for steel AISI 1045.

Table 1 – Results of the study when turning steel AISI 1045

v, m/min	A_x, mm	B_x, mm	f_{SO}, Hz
50	0.03…0.035	0.25…0.283	-
100	0.040…0.048	0.18…0.216	625
150	0.050…0.063	0.16…0.2	625
200	0.066…0.075	0.16…0.183	625
250	0.075…0.091	0.166…0.2	625

Table 2 – Results of the study during turning of bronze CuSn3Zn13Pb4

v, m/min	A_x, mm	B_x, mm	f_{SO}, Hz
50	0.018…0.023	0.043…0.046	-
100	0.016…0.025	0.046…0.050	-
150	0.021…0.028	0.046…0.050	582
200	0.050…0.075	0.046…0.050	570
250	0.083…0.100	0.043…0.046	581

Table 3 – Results of the study during turning of cast iron GG35

v, m/min	A_x, mm	B_x, mm	f_{SO}, Hz
50	0.011…0.016	0.183…0.19	-
100	0.008…0.014	0.15…0.166	-
150	0.006…0.014	0.156…0.163	-
200	0.006…0.013	0.16…0.17	-
250	0.008…0.012	0.16…0.166	-

DOI 10.15588/1607-6885-2026-2-6

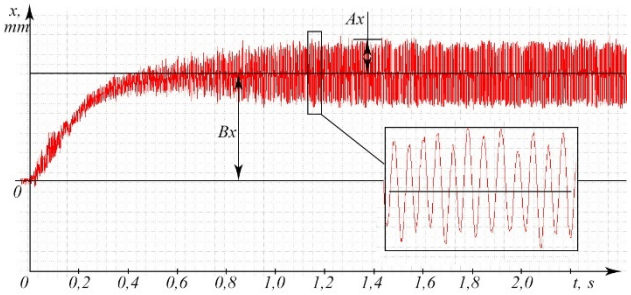

Figure 2. Oscillogram of steel AISI 1045 turning at a speed of v =150 m/min

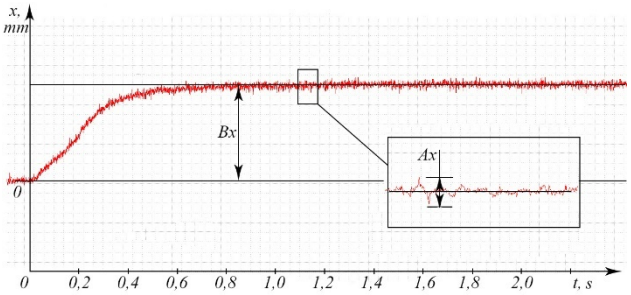

Figure 3. Oscillogram of turning cast iron GG35 at a speed of v =150 m/min

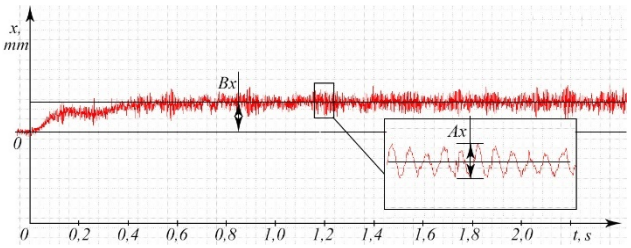

Figure 4. Oscillogram of turning bronze CuSn3Zn13Pb4 at a speed of v =150 m/min

The chips when turning steel AISI 1045 had a wave on the free surface, which confirmed the presence of regenerative self-oscillations (Fig. 5*a*). And the chips of cast iron GG35 and bronze CuSn3Zn13Pb4 were formed from numerous pieces of irregular shape, not connected or weakly connected with each other, from which it was not possible to decide the nature of vibration (Fig. 4*bc*).

The amplitude of the regenerative self-oscillations of the cutting edge of the cutter-oscillator was reflected in the vibration patterns of the machined surface (Fig. 6). On the surface of steel AISI 1045, there was a clear wave from the oscillations of the cutter tip; on bronze CuSn3Zn13Pb4, the wave was much smaller, and on cast iron GG35, the wave was absent.

An analysis of the amplitude-frequency spectra (Fig.7) revealed that a dominant oscillation frequency was observed when turning steel AISI 1045 at cutting speeds of 100-250 m/min and bronze CuSn3Zn13Pb4 at cutting speeds of 150-250 m/min. The dominant frequency in the spectrum was slightly higher than the natural frequency of the cutter-oscillating. This confirms that the observed vibration is regenerative self-oscillation. When turning cast iron GG35 the dominant frequency was absent across the entire cutting speed range, indicating the absence of regenerative self-oscillations.

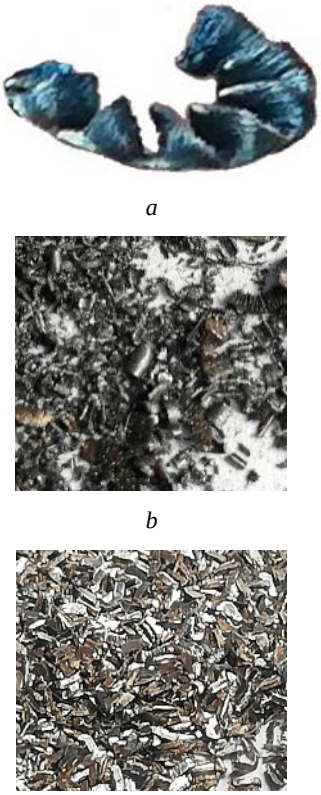

a

b

c

Figure 5. Chips during turning of steel AISI 1045 (*a*), cast iron GG35 (*b*), bronze CuSn3Zn13Pb4 (*c*) at a speed of v=150 m/min

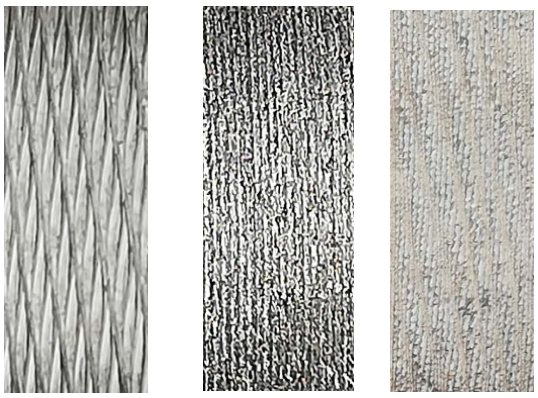

a *b* *c*

Figure 6. Vibration pattern on the machined surface of steel AISI 1045 (*a*), cast iron GG35 (*b*), bronze CuSn3Zn13Pb4 (*c*) at a speed of v=150 m/min

DOI 10.15588/1607-6885-2026-2-6

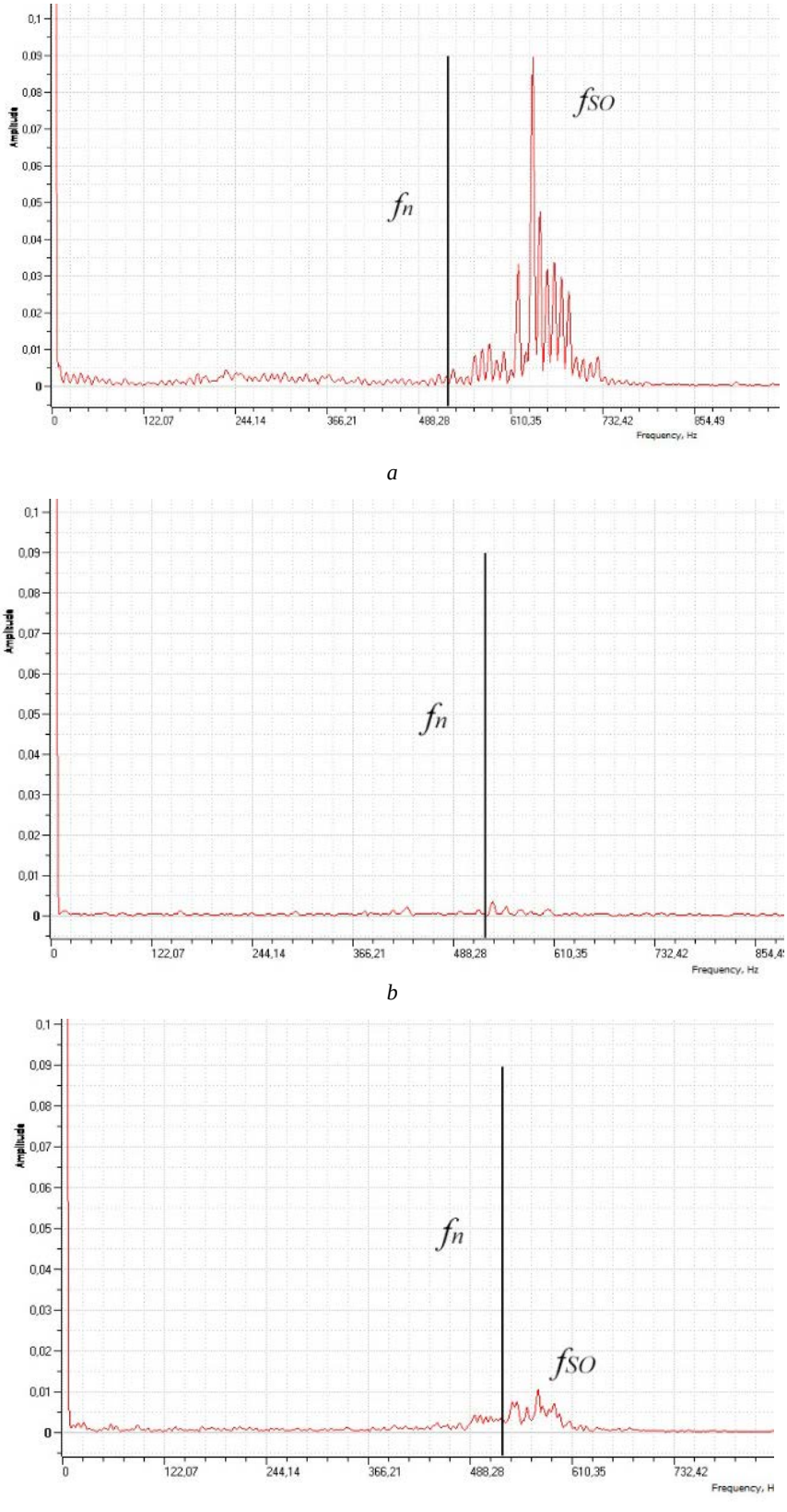

a

b

c

Figure 7. Amplitude-frequency spectrum during turning of steel AISI 1045 (*a*), cast iron GG35 (*b*), bronze CuSn3Zn13Pb4 (*c*) at a speed of *v*=150 m/min

DOI 10.15588/1607-6885-2026-2-6

Conclusion

The conducted studies have shown that the type of chip formation has a significant impact on the excitation of regenerative oscillations during turning. It was found that regenerative oscillations are excited during turning of steel AISI 1045, which produces continuous chips. This is due to the relatively continuous nature of plastic deformation and the stable formation of the shear layer, which facilitates the development of positive feedback between the cutting process and the cutter-oscillator.

At the same time, materials characterized discontinuous chip formation (cast iron GG35, bronze CuSn3Zn13Pb4) dampen regenerative oscillations. The discontinuous, random nature of chip formation, caused by brittle fracture of the material, dampens the oscillator's oscillations via the feedforward coupling and prevents the oscillatory system from oscillating via the feedback coupling.

References

1. Cai, Y., Zhuang, K., Zhu, K., & Wang, X. (2025). Stability analysis of finite amplitude chatter in turning considering tool wear and process damping effects. Journal of Manufacturing Processes, 141, 773–788. https://doi.org/10.1016/j.jmapro.2025.03.019

2. Wang, A., Zhou, B., & Jin, W. (2024). Dynamics of the regenerative turning chatter with little mass eccentricity. International Journal of Non-Linear Mechanics, 166, 104851. https://doi.org/10.1016/j.ijnonlinmec.2024.104851

3. Shouckry, A. S. (1981). Zones and boundaries between different types of chip. Wear, 69(3), 345–353. https://doi.org/10.1016/0043-1648(81)90324-0

4. Ernst, H., & Martellotti, M. (1938). The formation of the built-up edge. ASME Mechanical Engineering, 57, 478–498.

5. Jatakar, K., Shah, V., Binali, R., Salur, E., Sağlam, H., Mikolajczyk, T., & Patange, A. D. (2023). Monitoring built-up edge, chipping, thermal cracking, and plastic deformation of milling cutter inserts through spindle vibration signals. Machines, 11(8), 790. https://doi.org/10.3390/machines11080790

6. Sureshbabu, D. M., & Thyla, P. R. (2023). A novel control strategy for suppression of regenerative chatter in conventional lathe. The International Journal of Advanced Manufacturing Technology, 125, 1917–1926. https://l doi.org /10.1007/s00170-022-09044-z

7. Tobias, S. A., & Fishwick, W. (1958). Theory of regenerative machine tool chatter. The Engineer, 205(7), 199–203.

8. Altintas, Y., Stepan, G., Budak, E., Schmitz, T., & Kilic, Z. M. (2020). Chatter stability of machining operations. Journal of Manufacturing Science and Engineering, 142(11), 110801. https://doi.org/10.1115/1.4047391

9. Schmitz, T. L., & Smith, K. S. (2019). Machining dynamics. Springer. https:// doi.org/10.1007/978-3-319-93707-6

10. Nurulamin, A. K. M., Jaafar, I. H., Patwari, A. U., & Zubaire, W. W. D. (2010). Role of discrete nature of chip formation and natural vibrations of system components in chatter formation during metal cutting. IIUM Engineering Journal, 11(1), 124–138. https://doi.org/10.31436/iiumej.v11i1.53

11. Zhou, W. (2021). *Intensification of turning machining of difficult-to-machine materials based on modeling of chip formation process*. Dissertation.

12. Sahoo, P., & Rout, S. (2019). Chatter investigation on machining of gray cast iron considering the damping effect. International Journal of Recent Contributions from Engineering Science & IT (iJES), 7(3), 64. https://doi.org/10.3991/ijes.v7i3.11376

13. Aguado, S., Pueo, M., Acero, R., Majarena, A. C., & Santolaria, J. (2025). Surface roughness prediction in turning processes for grey cast iron: A hybrid machine learning approach integrating infrared thermography. Engineering Applications of Artificial Intelligence, 161, 112180. https://doi.org/10.1016/j.engappai.2025.112180

14. Djaka, K. S., Moufki, A., Nouari, M., Laheurte, P., & Tidu, A. (2018). A semi-analytical modelling of cutting using crystal plasticity theory and flow line approach. International Journal of Mechanical Sciences, 141, 49–59. https://doi.org/10.1016/j.ijmecsci.2018.10.006

15. Soman, A. S., & Subbiah, S. (2016). Process planning in additive manufacturing: A state-of-the-art review. Procedia CIRP, 49, 146–151. https://doi.org/10.1016/j.procir.2016.04.005

16. Tryshyn, P., & Kozlova, O. (2025). Experimental studies of vibration excitation during turning. Shock and Vibration, 2025, 6157874. https://doi.org/10.1155/vib/6157874

17. Tryshyn, P. (2025). Theory of the cutter-oscillators design. Shock and Vibration, 2025, 6679342. https://doi.org/10.1155/vib/6679342

18. Tryshyn, P. R. (2025). Investigation of cutting conditions based on vibration trace in turning. Vibratsii v tekhnitsi ta tekhnolohiiakh, (1)(116), 40–47. https://doi.org/10.37128/2306-8744-2025-1-5

Received 06.04.2026
Accepted 14.04.2026
Published 07.05.2026

DOI 10.15588/1607-6885-2026-2-6

УДК 621.941.08

ВПЛИВ СТРУЖКОУТВОРЕННЯ, ЩО СТВОРЮЄ СТРУЖКУ НАДЛОМУ, НА ЗБУДЖЕННЯ РЕГЕНЕРАТИВНИХ АВТОКОЛИВАНЬ ПРИ ТОЧІННІ

Павло Тришин — д-р філософії, доцент кафедри технології машинобудування Національного університету «Запорізька політехніка», м. Запоріжжя, Україна, *e-mail: trishin@zp.edu.ua*, ORCID: 0000-0002-3301-5124

Олена Козлова — канд. техн. наук, доцент, доцент кафедри технології машинобудування Національного університету «Запорізька політехніка», м. Запоріжжя, Україна, *e-mail: kozlova@zp.edu.ua*, ORCID: 0000-0002-3478-5913

Юрій Внуков — д-р техн. наук, професор, незалежний науковець, Каліфорнія, США, *e-mail: ypahar@ukr.net*, ORCID: 0000-0002-4297-9646

Андрій Левченко — аспірант кафедри технології машинобудування Національного університету «Запорізька політехніка», м. Запоріжжя, Україна, *e-mail: andrey.levchenko.zp@gmail.com*, ORCID: 0009-0006-3615-867X

Мета роботи. *Метою цього дослідження є вивчення впливу стружкоутворення на збудження регенеративних автоколивань при точінні, порівняння поведінки автоколивань при стружкоутворенні, яке створює зливну стружку та стружку надлому, а також прогнозування стабільності обробки крихких матеріалів.*

Методи дослідження. *Дослідження проводилося в умовах безперервного ортогонального точіння на токарному верстаті з ЧПК. Вібрацію досліджували за допомогою різця-осцилятора з одним ступенем свободи в напрямку зміни товщини шару, що зрізається. Зміщення різальної кромки під час обробки вимірювали за допомогою індуктивного датчика, а сигнали записували за допомогою багатоканальної системи збору даних та обробляли на комп'ютері. Осцилограми аналізували для визначення амплітуди та статичного відхилення.*

Результати. *Експериментальні результати показали, що тип утворення стружки має значний вплив на вібрацію під час точіння. Під час обробки сталі 45, що характеризується зливним стружкоутворенням, у діапазоні швидкостей різання v = 100–250 м/хв спостерігалися регенеративні автоколивання, при цьому амплітуда їх зростала зі збільшенням швидкості різання. Натомість, під час обробки сірого чавуну СЧ35, який утворює стружку надлому, регенеративних автоколивань не виявлено; були наявні лише випадкові коливання низької амплітуди, рівень яких залишався майже постійним у всьому діапазоні швидкостей різання. Для бронзи БрО3Ц13С4, що також утворює стружку надлому, регенеративні автоколивання виникали лише при вищих швидкостях різання (v=150–250 м/хв), амплітуда їх зростала зі швидкістю різання, подібно до сталі.*

Наукова новизна. *Наукова новизна цього дослідження полягає у встановленні впливу стружкоутворення на умови пригнічення та збудження регенеративних автоколивань при точінні.*

Практична цінність. *Практичне значення цього дослідження полягає в покращенні прогнозування стабільності при обробці матеріалів з різними механізмами стружкоутворення. Отримані результати можуть бути використані для вибору оптимальних умов різання, які зменшують або запобігають виникненню регенеративних автоколивань, особливо під час обробки крихких матеріалів.*

Ключові слова: *вібрація, регенеративні автоколивання, стружкоутворення, різець-осцилятор, форма стружки.*

Список літератури

1. Cai Y., Zhuang K., Zhu K., Wang X. Stability analysis of finite amplitude chatter in turning considering tool wear and process damping effects // *Journal of Manufacturing Processes*. 2025. Vol. 141. P. 773–788. DOI: https://doi.org/10.1016/j.jmapro.2025.03.019

2. Wang A., Zhou B., Jin W. Dynamics of the regenerative turning chatter with little mass eccentricity // *International Journal of Non-Linear Mechanics*. 2024. Vol. 166. 104851. DOI: https://doi.org/10.1016/j.ijnonlinmec.2024.104851

3. Shouckry A. S. Zones and boundaries between different types of chip // *Wear*. 1981. Vol. 69, No. 3. P. 345–353. DOI: https://doi.org/10.1016/0043-1648(81)90324-04

4. Ernst H., Martellotti M. The formation of the built-up edge // *ASME Mechanical Engineering*. 1938. Vol. 57. P. 478–498.

5. Jatakar K., Shah V., Binali R. et al. Monitoring built-up edge, chipping, thermal cracking, and plastic deformation of milling cutter inserts through spindle vibration signals // *Machines*. 2023. Vol. 11, No. 8. 790. DOI: https://doi.org/10.3390/machines11080790

DOI 10.15588/1607-6885-2026-2-6

6. Sureshbabu D. M., Thyla P. R. A novel control strategy for suppression of regenerative chatter in conventional lathe // *International Journal of Advanced Manufacturing Technology*. 2023. Vol. 125. P. 1917–1926. DOI: https:// doi.org/10.1007/s00170-022-09044-z

7. Tobias S. A., Fishwick W. Theory of regenerative machine tool chatter // *The Engineer*. 1958. Vol. 205, No. 7. P. 199–203.

8. Altintas Y., Stepan G., Budak E. et al. Chatter stability of machining operations // *Journal of Manufacturing Science and Engineering*. 2020. Vol. 142, No. 11. 110801. DOI: https://doi.org/10.1115/1.4047391

9. Schmitz T. L., Smith K. S. Machining dynamics. — Cham: Springer, 2019. — 382 p. DOI: https:// doi.org/10.1007/978-3-319-93707-6

10. Nurulamin A. K. M., Jaafar I. H., Patwari A. U., Zubaire W. W. D. Role of discrete nature of chip formation and natural vibrations of system components in chatter formation during metal cutting // *IIUM Engineering Journal*. 2010. Vol. 11, No. 1. P. 124–138. DOI: https://doi.org/10.31436/iiumej.v11i1.53

11. Zhou W. Intensification of turning machining of difficult-to-machine materials based on modeling of chip formation process. Dissertation. 2021.

12. Sahoo P., Rout S. Chatter investigation on machining of gray cast iron considering the damping effect // *International Journal of Recent Contributions from Engineering Science & IT*. 2019. Vol. 7, No. 3. 64 p. DOI: https://doi.org/10.3991/ijes.v7i3.11376

13. Aguado S., Pueo M., Acero R. et al. Surface roughness prediction in turning processes for grey cast iron: A hybrid machine learning approach integrating infrared thermography // *Engineering Applications of Artificial Intelligence*. 2025. Vol. 161. 112180. DOI: https://doi.org/10.1016/j.engappai.2025.112180

14. Djaka K. S., Moufki A., Nouari M. et al. A semi-analytical modelling of cutting using crystal plasticity theory and flow line approach // *International Journal of Mechanical Sciences*. 2018. Vol. 141. P. 49–59. DOI: https://doi.org/10.1016/j.ijmecsci.2018.10.006

15. Soman A. S., Subbiah S. Process planning in additive manufacturing: A state-of-the-art review // *Procedia CIRP*. 2016. Vol. 49. P. 146–151. DOI: https://doi.org/10.1016/j.procir.2016.04.005

16. Tryshyn P., Kozlova O. Experimental studies of vibration excitation during turning // *Shock and Vibration*. 2025. 6157874. DOI: https://doi.org/10.1155/vib/6157874

17. Tryshyn P. Theory of the cutter-oscillators design // *Shock and Vibration*. 2025. 6679342. DOI: https://doi.org/10.1155/vib/6679342

18. Tryshyn P. R. Дослідження умов різання за вібраційним слідом при точінні // *Вібрації в техніці та технологіях*. 2025. № 1 (116). С. 40–47. DOI: https://doi.org/10.37128/2306-8744-2025-1-5

.

DOI 10.15588/1607-6885-2026-2-6

UDC 621.914.2:621.762

Vitalii Kolesnyk — PhD, Associate professor, Department of Manufacturing Engineering, Machines and Tools, Sumy State University, Sumy, Ukraine, *e-mail: v.kolesnik@tmvi.sumdu.edu.ua*, ORCID: 0000-0002-0417-3801

Oleksandr Berezniak — PhD Student, Department of Manufacturing Engineering, Machines and Tools. Sumy State University, Sumy, Ukraine, *e-mail: o.bereznyak@tmvi.sumdu.edu.ua*, ORCID: 0009-0005-2275-035X

THERMO-MECHANICAL EFFECTS OF CUTTING PARAMETERS ON HOLE PERFORMANCE AND TOOL WEAR IN CARBON POLIMER / TITANIUM ALLOY STACK

Purpose. *To systematize and summarize the results of scientific studies on the influence of cutting parameters on hole accuracy, machined surface quality, tool wear intensity, and built-up edge formation during drilling of Carbon Fiber-Reinforced Polymer (CFRP)/titanium alloy stacks.*

Research methods. *A comparative parametric analysis was applied to evaluate the influence of feed rate and cutting speed on drilling thrust force, temperature in the cutting zone, delamination intensity in the composite layer, burr height in the titanium layer, surface roughness, and tool wear progression. Experimental and numerical results reported in recent scientific publications were analyzed and integrated to determine cause-and-effect relationships between cutting parameters, thermomechanical processes in the cutting zone, and hole quality indicators.*

Results. *Feed rate was identified as the primary factor governing mechanical loading during drilling and therefore determining the extent of delamination in the CFRP layer. Cutting speed mainly affects the thermal state of the cutting zone and adhesion phenomena in the titanium alloy. Built-up edge formation and adhesive material transfer to the cutting edge modify the effective tool micro-geometry, leading to increased axial forces, reduced hole accuracy, and decreased drilling stability.*

Scientific novelty. *The synthesis of previously published results substantiates the need for an integrated approach to evaluating drilling of CFRP/titanium alloy stacks as a unified thermomechanical system. Within this framework, cutting parameters, tool wear evolution, and built-up edge formation are considered interrelated factors governing the transition between abrasive, adhesive, and diffusion wear mechanisms depending on process conditions.*

Practical value. *The obtained generalizations may guide further research in machining CFRP/titanium alloy stacks, particularly for extending tool life, stabilizing the drilling process, and optimizing cutting parameters to improve hole quality.*

Key words: *drilling, CFRP/titanium alloy stacks, cutting parameters, delamination, built-up edge, tool wear, thermomechanical interaction, comparative parametric analysis.*

Introduction

Carbon Fiber-Reinforced Polymer (CFRP) and Ti-6Al-4V alloy stacks are widely used in aerospace structures due to their high specific strength and durability. Despite these advantages, drilling assembly holes in such multi-material systems remains technologically challenging. The composite layer exhibits anisotropic behavior and limited interlaminar strength, while titanium exhibits low thermal conductivity, strong plasticity, and a high affinity for cutting tools. The abrupt transition between these materials during drilling generates complex thermo-mechanical interactions that often lead to delamination, burr formation, dimensional inaccuracy, accelerated tool wear, and built-up edge (BUE) formation.

Existing research has established that drilling performance in CFRP/Ti stacks is strongly dependent on cutting parameters. Feed rate primarily influences thrust force and interlaminar stress development in the composite layer, whereas cutting speed governs temperature rise and deformation behavior in titanium. Elevated mechanical loading intensifies composite damage, while excessive thermal accumulation promotes titanium plastic flow and adhesion to the cutting edge. Consequently, hole quality, surface integrity, and tool degradation are controlled by the combined action of mechanical and thermal effects rather than by isolated parameters.

Numerous experimental and numerical studies have addressed force prediction, temperature distribution, damage mechanisms, and wear behavior in stack drilling. Assisted technologies such as ultrasonic vibration, helical milling, and hybrid cooling strategies have demonstrated reductions in thrust force or thermal concentration. However, reported optimal parameter ranges remain inconsistent, particularly under varying lubrication and assistance conditions. Furthermore, many investigations analyze dimensional accuracy, surface quality, or tool wear independently, although these phenomena are inherently interrelated.

DOI 10.15588/1607-6885-2026-2-7

Adhesion-induced BUE formation represents a key transitional mechanism linking temperature rise, wear progression, and geometric instability. Modification of the cutting edge by adhered titanium alters contact mechanics, affecting hole accuracy and surface morphology. Despite advances in finite element and data-driven modeling, comprehensive approaches that simultaneously relate cutting parameters to wear evolution, BUE dynamics, and resulting hole quality in CFRP/Ti stacks remain limited.

Therefore, a systematic and integrated assessment of the influence of cutting parameters on the thermo-mechanical behavior, tool wear, and hole performance is required. Such analysis is essential for establishing predictive and stable drilling strategies for aerospace-grade multi-material structures.

Analysis of research and publications

Recent studies have extensively examined the mechanisms of drilling-induced damage in CFRP and stack configurations. Delamination and matrix cracking in CFRP are strongly influenced by thrust force and temperature rise [1-3], while burr formation and plastic deformation dominate the titanium layer, particularly at elevated temperatures [2, 4]. Surface roughness and hole dimensional accuracy are governed by cutting speed–feed combinations and tool geometry, as well as by thermal softening and chip–wall interaction effects [5, 6]. Helical milling and ultrasonic-assisted drilling have demonstrated reduced thrust forces and improved chip evacuation compared to conventional drilling [7], yet parameter sensitivity remains high.

Tool wear behavior in stack drilling is complex and often dominated by adhesive and diffusion mechanisms in titanium and abrasive wear in CFRP [6, 8, 9]. Adhesion of titanium to the cutting edge frequently results in BUE or build-up layer (BUL) formation, altering tool geometry, increasing forces, and accelerating wear progression [4, 9, 10]. Cooling and lubrication strategies such as MQL, Cryo-MQL, and ultrasonic-assisted cryogenic systems have shown potential to mitigate temperature rise and adhesion wear [11-14], but their effectiveness depends strongly on the selection of cutting parameters.

Although numerous works have addressed isolated aspects of temperature fields [15], stress distribution [16], tool geometry [5, 6], coating performance [6, 9], lubrication systems [12, 14], and AI-based predictive modeling [17], the majority of studies treat hole quality, tool wear, and BUE formation as partially independent phenomena. However, in CFRP/Ti stack drilling, these effects are inherently interrelated: cutting parameters influence temperature and stress distribution, which govern adhesion behavior and BUE stability. These, in turn, modify the effective cutting-edge radius and contact mechanics, ultimately affecting hole accuracy and surface integrity.

Feed rate is generally the dominant parameter controlling thrust force and delamination [3, 6], whereas cutting speed primarily governs thermal softening and adhesion in titanium [2, 10, 18]. However, contradictory findings exist regarding optimal speed-feed windows, particularly under hybrid lubrication and ultrasonic assistance [12, 19, 20]. Moreover, while modeling efforts using finite element approaches [2, 21], hybrid analytical–numerical frameworks [16], and data-driven prediction methods [17, 22] have advanced force and temperature prediction, robust coupling between cutting parameters, tool wear progression, and BUE formation in stack drilling remains insufficiently addressed.

Purpose of work

Despite significant progress, there is still a lack of integrated analysis that simultaneously links cutting parameters to tool wear evolution, BUE dynamics, and resulting dimensional deviations, particularly in CFRP/Ti alloy stacks. Most studies focus either on hole damage or on wear mechanisms separately, without establishing mechanistic interdependencies. In particular, the parameter-dependent transition between adhesive wear and thermally activated diffusion wear in titanium, and its feedback effect on delamination and surface integrity in the CFRP layer, is not yet comprehensively understood. Therefore, more solid, systematic research is required to clarify how cutting speed–feed combinations influence tool wear mechanisms and BUE formation during drilling of CFRP/Ti stacks, and how these wear-induced geometric changes propagate into hole quality deterioration. Such understanding is essential for developing predictive, parameter-optimized, and damage-controlled drilling strategies for aerospace-grade multi-material structures.

Research material and methodology

This work presents a structured analytical review of peer-reviewed studies on the drilling of CFRP/Ti-6Al-4V stacks. The methodological framework was developed to enable systematic comparison of mechanical, thermal, and tribological process characteristics and to identify interdependencies between cutting parameters and drilling performance.

The analysis included experimental and validated numerical studies that explicitly reported feed rate and cutting speed and provided quantitative evaluation of thrust force, temperature, delamination, burr height, surface roughness, tool wear, or built-up edge formation. Both conventional and assisted techniques, namely ultrasonic drilling, helical milling, cryogenic, and hybrid cooling, were considered to assess parameter sensitivity under different processing conditions.

The selected publications were classified into four domains. These domains are mechanical response, thermal behavior, hole quality and surface integrity, and tool wear with adhesion phenomena. A comparative-parametric approach was applied to evaluate consistent trends, focusing on correlations between feed rate and thrust force, cutting speed and interface temperature, and the transition of wear mechanisms under different thermo-mechanical modes.

DOI 10.15588/1607-6885-2026-2-7

Reported quantitative indicators were used to support trend validation.

An integrative interpretation was adopted to consider mechanical load, temperature evolution, adhesion stability, and wear progression. Cross-comparison of experimental and modeling results ensured consistency and strengthened the reliability of the derived conclusions.

Research results

Drilling of CFRP/Ti stacks is characterized by thermomechanical heterogeneity resulting from the abrupt transition between the anisotropic brittle composite and the ductile titanium alloy. The chisel edge region operates at near-zero cutting speed, where extrusion and ploughing mechanisms dominate over pure shearing. Hybrid analytical–numerical modeling demonstrates that during the initial penetration stage, the contact area increases rapidly. In contrast, the contact pressure decreases due to localized thermal softening, particularly when the interfacial temperature approaches the matrix glass transition temperature [16]. This phenomenon intensifies interlaminar stresses in CFRP and contributes to thrust-force-driven delamination.

Experimental investigations of CFRP/Ti stacks report exit temperatures in the titanium layer ranging from approximately 182 °C to 356 °C, depending on cutting parameters [2]. Within this interval, titanium burr height increased by about 56.6 %, confirming the strong temperature sensitivity of plastic deformation in Ti-6Al-4V. Simultaneously, matrix tensile damage variables in CFRP increased significantly when the temperature rose from 248 °C to nearly 300 °C, indicating progressive thermal degradation of the polymer matrix [2, 3]. These findings demonstrate that temperature is not merely a by-product of drilling but a governing variable influencing damage evolution in both materials.

Chip formation mechanisms further complicate process mechanics. CFRP produces fragmented, brittle chips, whereas titanium produces continuous or segmented, ductile chips with a strong tendency toward adhesion. Accumulated titanium chips increase torque oscillation and radial force components, particularly at low cutting speeds and elevated feeds [16, 23]. Ultrasonic-assisted drilling has been shown to reduce thrust force by approximately 23–27 % relative to conventional drilling and to decrease the delamination factor by 12–16 % through improved chip fragmentation and intermittent cutting [20]. These quantitative outcomes confirm that the combined influence of mechanical loading, thermal accumulation, and chip evacuation efficiency governs drilling mechanics in stacks.

Cutting speed predominantly governs thermal effects and adhesion phenomena during stack drilling. Across several experimental studies, increasing cutting speed within typical industrial ranges (15–30 m/min for coated drills) reduced thrust force in titanium by approximately 10–15%, primarily due to thermal softening and reduced specific cutting energy [6]. However, the accompanying temperature increase modifies tool-chip interaction conditions.

Measurements of drill temperature during Ti machining show that the peak temperature is concentrated near the drill center and increases markedly under dry conditions compared with compressed-air cooling [10].

Thermal sensitivity of titanium is further evidenced by cryogenic machining studies, which identified a transition zone near −60 °C where force direction and torque behavior changed due to altered material deformation characteristics [18]. Although this result pertains to milling, it illustrates the strong dependence of Ti deformation behavior on temperature state and supports the interpretation of speed-driven thermal effects in drilling.

In CFRP layers, higher cutting speeds generally reduce thrust force and may reduce delamination at moderate feeds [3]. Nevertheless, when the temperature exceeds the matrix glass transition range, softening and resin smearing intensify, potentially increasing subsurface damage [2]. Finite element method (FEM) simulations confirm that elevated interface temperature correlates with increased burr formation in titanium and higher tensile damage variables in CFRP [2]. These observations indicate that cutting speed influences drilling performance through a thermally mediated trade-off between force reduction and thermal degradation.

Feed rate is consistently identified as the dominant factor affecting thrust force and delamination severity. Statistical analyses of CFRP/Ti drilling confirm that feed rate is the most influential parameter on thrust force, with determination coefficients ranging from 0.87 to 0.90 in regression models [6]. Increasing the feed from 0.025 to 0.1 mm/rev resulted in substantial increases in thrust force and corresponding enlargement of delamination damage.

In composite drilling studies, increasing feed from 0.1 to 0.2 mm/rev reduced free-hole area preservation from approximately 99 % to 53 % under unfavorable speed conditions, indicating severe exit damage [3]. Similar trends are reported in stack drilling, where elevated feed increased titanium burr height and composite delamination factors [2, 5]. These results confirm that feed rate directly controls undeformed chip thickness, axial force magnitude, and the distribution of contact stress.

Tool wear progression also correlates with feed intensity. Larger feed values increase normal load on cutting edges and accelerate flank wear development [9]. Under cryogenic conditions with coated drills, higher feed rates led to an approximately 11 % increase in adiabatic shear band thickness in titanium chips, indicating intensified localized deformation and more aggressive wear. Moreover, increased feed rate increases contact pressure and the frictional area, promoting titanium adhesion and facilitating BUE formation [4, 10].

The combined influence of cutting speed and feed determines the dominant damage mechanism and wear mode during drilling. Low cutting speed combined with high feed generally results in elevated thrust force and intensified adhesive wear, promoting unstable BUE accumulation [4]. Conversely, high speed at moderate feed reduces me-

DOI 10.15588/1607-6885-2026-2-7

chanical loading but increases interface temperature, facilitating diffusion wear mechanisms and thermal matrix degradation [9].

Multi-objective optimization studies confirm that balanced parameter windows provide improved overall performance. Analytical hierarchy process-based optimization simultaneously reduced axial force and surface roughness in CFRP/Ti drilling by selecting intermediate parameters [15]. Ultrasonic peck drilling further demonstrated thrust-force reductions of up to 35% compared with conventional drilling under optimized conditions [19].

A comparative analysis with helical milling indicates that a distributed cutting load substantially modifies parameter sensitivity. Helical milling reduced thrust force in titanium from approximately 435 N to 117 N, corresponding to a 73% reduction, thereby decreasing thermally induced damage and improving dimensional stability [23]. Although this represents an alternative process, it underscores the central role of load distribution in determining how cutting parameters influence damage evolution. Key findings is summarized in Table 1.

Hole accuracy in CFRP/Ti stack drilling is affected by the combined influence of thrust force magnitude, thermal expansion, adhesion-induced edge modification, and tool wear. Unlike monolithic materials, dimensional deviation in stacks emerges from the superposition of composite delamination, titanium plastic flow, and temperature-driven geometric instability of the drill.

Diameter deviation in stack drilling results from both mechanical deflection and thermal-adhesive effects. Experimental observations indicate that increasing the feed rate significantly increases thrust force, enhancing radial displacement of the drill and promoting overcut in titanium layers [3]. Statistical analyses confirm feed rate as the dominant contributor to axial load variation, which directly influences dimensional stability [6].

Thermal effects further modify hole diameter. FEM analysis demonstrated that increasing the interface temperature from ~182 °C to ~356 °C resulted in a pronounced increase in burr height and plastic deformation in titanium [2]. Since titanium has relatively low thermal conductivity, localized heat accumulation near the drill margin can cause transient thermal expansion of both the tool and the workpiece, contributing to oversizing.

Adhesion-related phenomena also affect diameter consistency. Titanium build-up layer formation alters the effective cutting edge radius, thereby changing local cutting geometry and increasing dimensional scatter [4]. As adhesion accumulates, cutting becomes intermittently unstable, promoting micro-variations in hole diameter.

Roundness deviation in CFRP/Ti stacks is closely associated with torque fluctuation and radial force asymmetry. Chip accumulation in titanium at low cutting speeds intensifies torque oscillations and increases the drill's dynamic instability [23]. Such oscillatory loading contributes to out-of-roundness and localized wall irregularities.

Table 1 – Key outcomes of investigation relevant for cutting parameters effect on the drilling process

Reference	Topic addressed	Key conclusions
Chen et al. [15]	CFRP/Ti stack drilling; force-based optimization	Axial force decreases with increasing spindle speed and increases with feed rate. Multi-objective optimization indicates that parameter balancing is required to simultaneously control thrust force and surface roughness
Shariar et al. [16]	Thermo-mechanical stress modeling in composite drilling	Thermally induced softening modifies contact pressure distribution during tool engagement. Stress evolution is governed by temperature-dependent material properties rather than purely mechanical loading
Zhaoju et al. [10]	Drill temperature distribution under different cooling methods	Peak temperature localizes near the drill center. Increasing the cutting speed increases the thermal load, whereas higher feed rates above ~ 0.13 mm/rev reduce temperature due to enhanced chip evacuation. Compressed air cooling improves temperature uniformity
Moran et al. [20]	Ultrasonic-assisted drilling (UAD) of CFRP/Ti	UAD stabilizes thrust force, improves chip fragmentation, and reduces adhesive transfer to the tool compared to conventional drilling
Gururaj et al. [24]	Drilling vs helical milling (dry)	Helical milling reduces mechanical and thermal loading, improving surface roughness and subsurface microhardness while mitigating adhesion and wear

Step drilling strategies reduce peak thrust and improve hole stability; however, repeated engagement may introduce cyclic thermomechanical variations that affect cylindricity at elevated feeds [5]. Ultrasonic-assisted drilling reduces radial force magnitude and improves hole geometry by decreasing chip packing, yet the improvement remains parameter-sensitive [20]. The reduction of thrust force through distributed load strategies, such as helical milling, resulted in significantly improved dimensional stability compared to conventional drilling, supporting the interpretation that load concentration directly affects geometric accuracy.

Drill wandering at the hole entry is primarily governed by thrust force magnitude and composite anisotropy. Feed increase intensifies axial force, elevating entry delamination and potentially shifting drill alignment during initial penetration [3]. Thermal softening of the CFRP matrix at elevated interface temperatures further reduces local stiffness, increasing susceptibility to entry instability [2].

Temperature concentration near the drill center also influences positional stability. Experimental temperature measurements revealed peak thermal zones at the chisel

DOI 10.15588/1607-6885-2026-2-7

edge region under dry conditions [10]. Such thermal gradients can asymmetrically modify contact stiffness, potentially contributing to slight angular deviation during drilling.

Although assisted technologies reduce thrust magnitude, they do not fully eliminate positional deviation when feed remains high [19, 20], indicating that mechanical loading remains the principal driver of drill runout. Key finding are summarized in Table 2.

Table 2 – Analysis of process parameters affecting hole accuracy and quality

Reference	Topic addressed	Key conclusions
Li F. et al. [19]	Ultrasonic peck drilling (UPD) of CFRP/Ti laminates	UPD achieves hole diameter within H9 tolerance and reduces CFRP hole roughness compared to conventional and standard ultrasonic drilling.
Chen C. et al. [5]	Variable-parameter stack drilling	Layer-specific adjustments to speed and feed reduce exit delamination and burr formation, improving the geometric stability of the drilled hole.
Chen et al. [2]	Thermal influence on exit deformation	Increasing the exit temperature significantly enhances titanium plastic deformation, resulting in greater burr formation and distortion at the hole exit.
Gururaj et al. [24]	Helical milling vs conventional drilling	Reduced load concentration in helical milling improves dimensional stability and mitigates geometric distortion of hole walls.

Influence of Cutting Parameters on Surface Quality and Surface Integrity

Surface quality in CFRP/Ti stack drilling is governed by the coupled effects of thrust force magnitude, interface temperature, chip-wall interaction, and tool condition. Unlike monolithic drilling, surface integrity in stacks must be evaluated separately for the CFRP and titanium layers, as the governing mechanisms differ substantially.

Surface roughness in titanium layers is strongly dependent on the feed rate, as it is directly related to the undeformed chip thickness and the theoretical surface profile. Statistical analysis confirmed feed rate as the dominant parameter influencing thrust force and, consequently, surface roughness in CFRP/Ti drilling [6]. Increasing feed leads to higher axial load and increased ploughing at the margin region, producing rougher hole walls.

Cutting speed influences roughness indirectly through thermal effects. At moderate speeds, thermal softening reduces cutting resistance and may improve surface finish. However, excessive temperature intensifies adhesion and the formation of a built-up layer, altering the effective cutting edge radius and introducing irregular surface morphology [4, 10]. Experimental temperature measurements revealed peak thermal concentration near the drill center, particularly under dry conditions, increasing adhesion tendency [10].

Ultrasonic-assisted drilling reduced thrust force and improved chip evacuation, resulting in a better surface finish than conventional drilling[20]. Nevertheless, improvements remained sensitive to feed magnitude, indicating that mechanical loading still governs roughness formation.

Helical milling experiments demonstrated a substantially reduced thrust force (~73% lower than conventional drilling), which correlated with improved surface finish and reduced wall irregularities [23]. This supports the interpretation that load distribution and mechanical stability are critical for surface integrity.

Surface integrity in CFRP is not limited to roughness but includes subsurface matrix cracking, fiber pull-out, and interlaminar damage. FEM analysis revealed that an increase in interface temperature from approximately 248 °C to 299 °C significantly amplified tensile damage variables in the composite layer [2]. Since polymer matrix properties degrade rapidly above T_g, cutting speed becomes a critical thermal control parameter.

Feed rate amplifies interlaminar stresses by increasing thrust force, directly intensifying peel-up and push-out damage. Composite drilling studies confirm that higher feed values significantly reduce free-hole area preservation, reflecting increased subsurface damage severity [3].

The combination of high feed and elevated temperature results in the most severe integrity degradation, due to simultaneous mechanical overload and matrix softening. Assisted technologies (ultrasonic or cryogenic) reduce mechanical load or temperature but do not eliminate parameter sensitivity[12, 19, 20].

Burr formation in titanium layers is strongly temperature-dependent. FEM-based analysis reported that increasing exit temperature from ~182 °C to ~356 °C increased burr height by approximately 56.6% [2]. This indicates that cutting speed–induced thermal accumulation directly governs plastic deformation behavior at hole exit.

Feed rate also contributes to burr formation by increasing plastic strain at the exit zone. Higher undeformed chip thickness promotes larger deformation volume before chip separation, intensifying burr size [6].

Cryogenic and hybrid cooling strategies reduce interface temperature and modify plastic flow behavior, but their effectiveness depends on maintaining moderate feed levels [12, 18]. Adhesion phenomena further aggravate burr irregularity; the formation of a titanium build-up layer alters edge sharpness and increases surface tearing at the exit [4] (Table 3).

Tool wear evolution in CFRP/Ti stack drilling is governed by the combined action of abrasive interaction in the composite layer and adhesive-diffusive mechanisms in the titanium layer. The abrupt transition between materials with contrasting thermal conductivity, hardness, and chemical reactivity results in complex wear patterns, often characterized by flank wear, adhesion layers, and unstable BUE formation.

DOI 10.15588/1607-6885-2026-2-7

Table 3 – Analysis of process parameters effecting hole quality and surface integrity

Reference	Topic addressed	Key conclusions
Yu et al. [1]	Temperature field and drilling damage in composites	Dynamic temperature field correlates with drilling-induced microstructural damage and wall surface defects in fiber-reinforced composites
Zhaoju et al. [10]	Temperature distribution and cooling strategies	Elevated cutting speed increases thermal concentration near the drill center, promoting adhesion risk and surface instability; improved cooling reduces peak temperature and thermal gradients
Moran et al. [20]	Ultrasonic-assisted drilling	Intermittent cutting improves wall morphology and reduces adhesive transfer compared to conventional drilling
Joy et al. [4]	Adhesion layer formation in stack drilling	Adhesion layer formation is influenced by drill geometry and contributes to surface irregularity in stack materials

Tool wear evolution in CFRP/Ti stack drilling is governed by the combined action of abrasive interaction in the composite layer and adhesive-diffusive mechanisms in the titanium layer. The abrupt transition between materials with contrasting thermal conductivity, hardness, and chemical reactivity results in complex wear patterns, often characterized by flank wear, adhesion layers, and unstable BUE formation.

Feed rate directly governs undeformed chip thickness and contact pressure along the cutting edge, thereby influencing flank wear progression. Statistical analysis in CFRP/Ti drilling confirms feed rate as the most significant parameter affecting thrust force and mechanical loading [6]. Increased feed intensifies normal stress at the tool-workpiece interface, accelerating abrasive wear in the CFRP layer and adhesive wear in titanium.

Composite drilling studies indicate that higher feed increases thrust force and delamination severity [3], which indirectly affects tool wear by increasing mechanical resistance during penetration. Elevated feed also promotes thicker adiabatic shear bands in titanium chips under cryogenic conditions, indicating intensified localized deformation and higher stress concentration at the cutting edge [9].

Therefore, feed rate primarily controls mechanical wear intensity and contributes to edge degradation through increased ploughing and frictional contact.

Cutting speed influences tool wear predominantly through temperature-dependent mechanisms. Temperature measurements reveal that increasing cutting speed elevates peak temperature near the drill center, particularly under dry conditions [10]. Elevated interface temperature promotes adhesion of titanium to the tool surface and accelerates coating degradation.

Thermal modeling demonstrates that exit temperature may reach approximately 356 °C under certain conditions [2], indicating sufficient thermal activation for diffusion-assisted wear processes. Cryogenic machining studies confirm that altering thermal regime significantly modifies deformation behavior in titanium [18], implying that wear mechanisms transition depending on temperature state.

Under cryogenic cooling with coated tools, wear mechanisms shift depending on thermal conditions and feed intensity [9]. This suggests that cutting speed must be interpreted in conjunction with thermal control strategy when evaluating wear progression.

BUE formation in stack drilling is primarily associated with titanium adhesion. Adhesive transfer modifies the effective cutting edge radius and alters local cutting geometry, resulting in force instability and accelerated wear [4]. Energy-dispersive spectroscopy in ultrasonic-assisted drilling confirmed reduced titanium transfer onto the tool compared to conventional drilling, indicating that mechanical vibration can mitigate adhesion [20].

Temperature concentration near the chisel edge region increases adhesion probability [10]. At elevated thermal conditions, titanium softens and adheres more readily to tool surfaces, facilitating unstable BUE formation.

Helical milling under dry conditions demonstrated reduced adhesion and improved wear stability due to distributed load and lower thermal concentration [23], supporting the interpretation that mechanical load intensity and thermal accumulation jointly govern adhesion-driven wear.

The interaction between feed and cutting speed determines the dominant wear regime. High feed combined with low speed intensifies mechanical loading, promoting abrasive and adhesive wear. Increasing cutting speed reduces mechanical resistance but elevates temperature, which may accelerate diffusion wear and coating degradation [2, 9, 10].

Cooling strategy modifies this interaction. Compressed air reduces peak temperature compared to dry drilling, while ultrasonic assistance reduces adhesion and stabilizes wear progression [20]. However, parameter sensitivity remains pronounced even under assisted conditions (Table 4).

The influence of feed rate on CFRP/Ti stack drilling extends beyond simple force amplification and represents the primary mechanical driver of process instability. Increasing feed enlarges undeformed chip thickness and elevates contact pressure along the cutting edge, resulting in higher thrust force [6]. Elevated thrust intensifies interlaminar stresses in the composite layer and increases the severity of entry and exit delamination. At the same time, increased normal and radial stresses at the drill margin accelerate abrasive wear in the CFRP layer and adhesive wear in the titanium layer.

DOI 10.15588/1607-6885-2026-2-7

Table 4 – Effect of cutting parameters on wear rate and built-edge formation

Reference	Topic addressed	Key conclusions
Samsudeensadham S. et al. [6]	Statistical influence of parameters on drilling performance	Feed rate significantly increases thrust force and accelerates mechanical wear progression. Moderate cutting speed reduces force but intensifies thermal exposure of the cutting edge
Chen et al. [2]	Thermal damage modeling	An elevated exit temperature (up to ~356 °C) promotes plastic deformation in titanium and increases the risk of thermally activated wear mechanisms
Zhaoju Z. Et al. [10]	Drill temperature distribution	A peak temperature localized near the drill center increases the probability of adhesion. Dry drilling conditions exacerbate thermal load and wear risk
Sharma P. [9]	Coated tool wear under cryogenic conditions	Wear mechanism transitions depend on thermal regime and feed intensity; increased feed enhances localized shear deformation and flank wear progression
Jebaratnam Joy, M. [4]	Adhesion layer formation in stack drilling	Adhesion layer formation modifies cutting edge geometry and contributes to wear instability, which is influenced by tool geometry and contact conditions
Moran, X., et al. [20]	Ultrasonic-assisted drilling	Reduced titanium transfer to the tool surface under ultrasonic assistance indicates a reduction in adhesion-driven wear compared to conventional drilling
Hiremath, A. [23]	Helical milling and wear behavior	Distributed load and reduced thermal concentration mitigate adhesion and improve wear stability under dry conditions
Yang D. [18]	Thermal regime in Ti machining	The deformation behavior of titanium is temperature-dependent because of its thermal state, which affects plastic flow and, consequently, the activation of the wear mechanism
(Khashaba & Mashhour, 2026)	Feed influence on drilling damage	Higher feed rates increase mechanical loading and, in turn, intensify tool wear through higher thrust force and resistance

In titanium, greater plastic strain accumulation before chip separation enhances burr formation and exit deformation [2]. This deformation alters the hole geometry and contributes to dimensional deviation. Consequently, mechanical load intensification initiated by feed rate simultaneously affects geometric stability, surface integrity, and wear progression. The mechanical component of the process therefore, acts as the initiating factor in the coupled degradation sequence.

Cutting speed primarily influences drilling performance through its effect on temperature evolution. Experimental measurements indicate that peak temperature is concentrated near the drill center and increases with spindle speed under dry conditions [10]. Numerical analysis shows that the interface temperature may reach approximately 356 °C, significantly increasing the titanium burr height and composite tensile damage variables [2].

At elevated temperature, the polymer matrix in CFRP softens, reducing stiffness and increasing susceptibility to thermally assisted cracking. In titanium, enhanced plastic flow at high temperatures intensifies exit deformation and promotes unstable chip formation. Thermal accumulation also increases the probability of adhesion between titanium and the cutting tool surface [4, 25]. Thus, temperature does not independently initiate instability but amplifies mechanically induced degradation by modifying material properties and interfacial conditions.

Adhesion and built-up edge formation constitute the critical link between tool wear and hole quality. The deposition of adhered titanium on the cutting edge increases the effective edge radius and alters rake and clearance geometry. This geometric alteration alters local cutting mechanics, leading to fluctuating force responses and unstable material removal conditions. Surface roughness increases due to intermittent tearing during adhesion-detachment cycles, while dimensional consistency deteriorates as variations in cutting-edge geometry introduce irregular cutting behavior.

Repeated adhesion and removal events accelerate wear progression through cyclic mechanical loading and coating degradation. As wear progresses, contact conditions continue to change, further reinforcing adhesion tendency and geometric instability. Ultrasonic assistance reduces adhesive transfer compared to conventional drilling, demonstrating that adhesion is sensitive to mechanical vibration; however, adhesion dynamics remain dependent on feed-speed interaction and thermal state [20].

The reviewed studies collectively indicate that CFRP/Ti stack drilling operates as a coupled thermo-mechanical feedback system. Feed rate affects the mechanical load intensity and determines the magnitude of the thrust force. Cutting speed controls the thermal state and modifies deformation behavior in both the composite and the titanium layers. Adhesion influences tool geometry, which in turn affects force response and accelerates wear evolution. Progressive wear further modifies contact mechanics, reinforcing dimensional instability and surface irregularity.

Process modification strategies, such as helical milling, redistribute mechanical loads and reduce localized thermal concentration, improving surface finish and stabilizing wear progression [23]. Ultrasonic and peck drilling reduce peak

DOI 10.15588/1607-6885-2026-2-7

thrust or temperature under optimized conditions [19, 20], yet the fundamental coupling between mechanical loading, thermal accumulation, adhesion formation, and geometric stability persists. These observations confirm that drilling performance in CFRP/Ti stacks cannot be optimized by addressing individual quality metrics in isolation (Table 5).

Table 5 –Summarizing troubleshooting evaluation

Process variable	Mechanism	Consequence
Increased feed rate	Higher undeformed chip thickness and contact pressure	Increased thrust force, intensified delamination, and accelerated flank wear progression
Increased cutting speed	Elevated interface temperature	Matrix softening, enhanced titanium plastic flow, and increased adhesion tendency
Elevated temperature	Thermally activated plastic deformation in Ti	Burr height increase (~56.6 %) and exit deformation
Adhesion formation	Modification of cutting-edge geometry due to titanium transfer	Surface irregularity, dimensional instability, accelerated wear through adhesion–detachment cycles
Load redistribution (helical milling)	Reduced mechanical and thermal concentration	Improved surface finish and wear stability
Ultrasonic assistance	Intermittent cutting and reduced adhesive transfer	Lower thrust force and improved wall morphology

The reviewed literature demonstrates substantial progress in understanding individual aspects of CFRP/Ti stack drilling, including thrust force evolution, temperature distribution, surface damage, and tool wear behavior. However, despite this advancement, several critical research gaps remain, particularly concerning the integrated influence of cutting parameters on tool wear and built-up edge formation.

First, most studies investigate force development or temperature evolution independently of progressive tool wear. Statistical analyses identify feed rate as a dominant contributor to thrust force variation [3, 6], while thermal modeling highlights the significant influence of cutting speed on temperature rise and burr formation [2, 10]. Nevertheless, systematic correlation between parameter-induced thermal states and long-term wear evolution in CFRP/Ti stacks remains limited. Existing investigations often evaluate wear at discrete parameter combinations without establishing continuous wear-parameter interaction models.

Second, adhesion and BUE formation are typically examined qualitatively or as secondary observations rather than as primary process variables. Although evidence indicates that titanium adhesion modifies the cutting edge geometry and influences surface integrity[4, 20], the dynamic evolution of BUE under varying feed-speed combinations has not been sufficiently quantified in stack-drilling conditions. In particular, the interaction between elevated temperature, mechanical load, and adhesion stability in alternating CFRP/Ti cutting remains insufficiently characterized.

Third, geometric accuracy and dimensional deviation are rarely linked directly to tool wear progression. While studies report improvements in hole tolerance under ultrasonic or optimized drilling strategies [19], the coupling between progressive flank wear, adhesion-induced edge modification, and hole diameter consistency has not been systematically modeled. As a result, predictive capability for dimensional stability during long drilling sequences remains limited.

Fourth, most modeling approaches address either thermo-mechanical stress distribution [16] or temperature evolution, but few frameworks integrate wear kinetics and adhesion dynamics into unified predictive models. The absence of integrated thermo-mechanical-tribological modeling restricts the development of robust optimization strategies capable of simultaneously controlling force, temperature, wear, and geometric stability [2].

Furthermore, process-assistance strategies such as ultrasonic drilling and helical milling mitigate thrust force and adhesion intensity [20, 23]. Yet, their long-term impact on the transition of the wear modes under varying cutting parameters has not been comprehensively evaluated. Comparative studies often focus on short drilling intervals and do not fully assess progressive edge degradation and its feedback on dimensional accuracy.

Overall, the current body of literature reflects fragmentation between mechanical, thermal, tribological, and geometric perspectives. Integrated investigations that simultaneously analyze cutting parameter selection, tool wear evolution, built-up edge formation, and hole quality metrics in CFRP/Ti stacks remain scarce. This limitation constrains both mechanistic understanding and industrial process optimization.

Future research should therefore focus on developing unified experimental and modeling frameworks that can couple mechanical loading, temperature evolution, adhesion dynamics, and wear progression. Particular attention should be devoted to quantifying the interaction between cutting parameters and built-up edge stability over extended drilling cycles, as well as to establishing predictive relationships between wear state and dimensional deviation. Such integrated approaches are essential for achieving reliable, reproducible hole quality in multi-material stack drilling, where thermomechanical coupling governs overall process stability.

Discussion

Overall, available quantitative evidence demonstrates that cutting parameters govern drilling performance through coupled thermo-mechanical mechanisms. Cutting

DOI 10.15588/1607-6885-2026-2-7

speed primarily controls temperature-dependent adhesion and diffusion phenomena, whereas feed rate dictates mechanical loading intensity and delamination propensity. Their interaction shifts the balance between adhesive, abrasive, and diffusion wear modes, establishing the mechanistic foundation for tool wear evolution and built-up edge formation, which are examined in subsequent sections.

Across the reviewed literature, feed rate consistently emerges as the primary parameter influencing dimensional accuracy by controlling thrust force and radial load. Cutting speed influences hole geometry indirectly by altering thermal conditions, which in turn affect plastic deformation in titanium and the matrix stiffness in CFRP. Adhesion and built-up layer formation introduce additional geometric variability by modifying tool edge geometry. Therefore, dimensional deviation in CFRP/Ti drilling cannot be attributed to a single parameter but results from the coupled interaction of mechanical load, thermal expansion, and adhesion-driven instability.

Surface quality in CFRP/Ti drilling emerges from the interaction between mechanical loading and temperature evolution. Feed rate primarily governs roughness amplitude and composite subsurface damage by controlling thrust force and contact pressure. Cutting speed modulates surface integrity via thermal mechanisms that influence matrix softening in CFRP and plastic flow in titanium. Adhesion and built-up layer formation introduce additional irregularity by modifying the tool geometry. Therefore, surface quality cannot be optimized by isolated parameter adjustment. Instead, balanced speed-feed combinations are required to control both mechanical and thermal contributions to surface degradation.

Coupled mechanical and thermal effects govern tool wear and built-up edge formation in CFRP/Ti drilling. Feed rate controls contact pressure and mechanical stress intensity, accelerating abrasive and adhesive wear. Cutting speed influences temperature-dependent adhesion and diffusion mechanisms. Built-up edge formation arises primarily from titanium adhesion and is amplified under elevated temperature and mechanical load. Consequently, wear evolution cannot be described solely by kinematic parameters; it must be interpreted through the thermomechanical interactions among cutting speed, feed, and the thermal control strategy.

The majority of existing investigations analyze thrust force, temperature, wear, or damage parameters separately. Integrated studies that simultaneously correlate cutting parameter selection with wear progression, adhesion dynamics, and dimensional deviation remain limited. The fragmentation of current approaches restricts predictive capability and constrains the development of unified optimization frameworks. Therefore, further research should focus on integrated thermo-mechanical models that explicitly couple cutting parameters with tool wear evolution and built-up edge formation while accounting for their combined influence on hole accuracy and surface integrity.

Conclusions

This review analyzed the influence of cutting parameters on drilling performance in CFRP/Ti alloy stacks with emphasis on hole accuracy, surface integrity, tool wear, and built-up edge formation. Based on the synthesized literature, the following conclusions can be drawn.

1. The analysis of drilling mechanics shows that feed rate is the primary mechanical driver of thrust force, while cutting speed predominantly influences the thermal state of the drilling zone. Mechanical loading governs delamination severity and contact pressure at the tool-workpiece interface, whereas temperature amplification modifies deformation behavior and adhesion tendency. The interaction between these parameters defines the fundamental thermo-mechanical response of the stack system.

2. The evaluation of hole accuracy indicates that geometric stability is strongly affected by thrust force magnitude and temperature-induced plastic deformation in titanium. Elevated feed increases delamination and radial instability, while high interface temperature promotes burr growth and exit deformation. However, quantitative studies directly correlating wear progression with dimensional deviation remain limited.

3. The combined action of mechanical stress and thermal accumulation governs surface quality and integrity. Feed-driven load intensification increases ploughing effects and composite subsurface damage, whereas cutting-speed-induced temperature rise accelerates matrix softening and titanium plastic flow. Adhesion and built-up edge formation introduce additional instability by altering cutting geometry and increasing surface irregularity.

4. Coupled mechanical and thermal mechanisms control tool wear and built-up edge formation. Feed rate intensifies contact stress and accelerates flank wear, while cutting speed elevates interface temperature and promotes adhesion-driven wear processes. Built-up edge formation represents a transitional mechanism linking wear progression with geometric and surface instability, particularly under elevated thermal conditions.

5. The integrated analysis confirms that CFRP/Ti stack drilling operates as a coupled thermo-mechanical feedback system. Cutting parameters influence not only force and temperature independently but also adhesion stability, wear evolution, and dimensional consistency through cyclic interaction mechanisms. Optimization strategies that address isolated performance metrics are therefore insufficient to ensure stable drilling performance.

6. Despite significant advances in modeling and experimental investigation, the literature remains fragmented. Few studies simultaneously correlate cutting parameter selection with wear evolution, adhesion dynamics, and dimensional deviation under extended drilling conditions. The development of unified thermo-mechanical–tribological models capable of predicting tool wear progression and built-up edge formation in relation to cutting parameters remains an open research challenge.

DOI 10.15588/1607-6885-2026-2-7

Further research should focus on integrated experimental methodologies and predictive modeling frameworks that couple mechanical load intensity, thermal evolution, adhesion stability, and progressive wear mechanisms. Such approaches are essential for improving process reliability and achieving consistent hole quality in multi-material stack drilling applications.

Acknowledgement

The research was conducted within the framework of the research stay "Research of Built-up Formation Effect on Cutting-Edge Radius When Drilling CFRP/Ti Alloy Stacks.", funded by National Scholarship Program of the Slovak Republic (NSP SAIA) and scientific research "Research of Built-up Edge Formation and Wear Effect on Cutting-Edge Radius When Drilling CFRP/Ti Alloy Stacks" in the frame of research grant "Research into Innovative, Unconventional Methods of Preparation of Cutting Edge Microgeometry to Increase the Tool Life of Cutting Tools" (VEGA 1/0266/23).

The article was prepared with the assistance and technical support of the non-governmental organization "INDUSTRY 5.UA.".

References

1. Yu, J. J., Pan, Z. X., Ye, W., Li, Q. C., & Wu, Z. Y. (2023). Dynamic temperature field and drilling damage mechanism of plain woven carbon/glass hybrid composites. Composite Structures, 304, 116375. https://doi.org/10.1016/j.compstruct.2022.116375

2. Chen, C., Zhao, Q., Wang, A., Shi, Z., & Bai, Y. (2024). Numerical study on the heat effect on the drilling damage of Ti/CFRP stacks. Polymer Composites, 45(10), 9487–9500. https://doi.org/10.1002/pc.28422

3. Khashaba, U. A., & Mashhour, A. A. (2026). Thermo-mechanical damage and cutting forces analysis in drilling UD-GFRP composites. Composites Part A, 201, 109415. https://doi.org/10.1016/j.compositesa.2025.109415

4. Jebaratnam Joy, M., Choo Then, X., Muhammad Hafiz, H., & Gérald, F. (2025). Influence of drill geometry on adhesion layer formation in AFRP/Al7075-T6 stacks. Journal of Manufacturing Processes. https://doi.org/10.3390/jcs9120658

5. Chen, C., Qing, Z., Wang, A., Shi, Z., Yang, Y., & Bao, Y. (2024). Experimental study on step drill geometry and pecking drilling with variable parameters processing method for CFRP and Ti stacks. Journal of Manufacturing Processes, 117, 355–365. https://doi.org/10.1016/j.jmapro.2024.03.011

6. Samsudeensadham, S., & Krishnaraj, V. (2025). Comparative tool wear study on drilling of CFRP/Ti stacks using TiAlN and AlTiSiN coated drill bits. Engineering Research Express, 7(3), 035550. https://doi.org/10.1088/2631-8695/adf8b3

7. Zhang, S., Wang, W., Jiang, R., Xu, Y., Hu, B., & Wang, J. (2023). Multi-objective optimization for machining performance during ultrasonic vibration-assisted helical grinding hole of thin-walled CF/BMI composite laminates. Thin-Walled Structures, 192, 111086. https://doi.org/10.1016/j.tws.2023.111086

8. Aditya, K., Nitin, T., Gopal, A. V., & Krishna, V. (2024). An assessment of machining performance of CAPVD-coated carbide tools in face milling of Ti-6Al-4V. Ceramics International. https://doi.org/10.1016/j.ceramint.2024.02.152

9. Sharma, P., Mishra, S. K., & Ramkumar, J. (2025). Damage mechanisms and wear progression of advanced AlTiSiN coatings deposited on WC/Co cemented carbide cutting tools under cryogenic machining conditions. Ceramics International, 51(27), 54530–54548. https://doi.org/10.1016/j.ceramint.2025.09.183

10. Zhaoju, Z., Albert, J. S., & Lei, C. (2025). Cutting edge temperature and drill wear in dry and minimum quantity lubrication drilling of titanium alloy. Journal of Materials Research and Technology, 39. https://doi.org/10.1016/j.jmrt.2025.12.010

11. Zhang, L., & Zhang, X. (2023). Effect of cooling and lubrication conditions on variable-angle milling of unidirectional CFRP with PCD tools. Journal of Materials Processing Technology, 319, 1–11. https://doi.org/10.1016/j.jmatprotec.2023.118073

12. Ibrahim, M., Yusoff, S., Jaharah, A. G., Hadi, J., Nizaroyani, S., & Mohammad, A. (2024). State-of-the-art hybrid lubrication (Cryo-MQL) supply systems, performance evaluation, and optimization studies in machining processes. Results in Engineering, 22, 102090. https://doi.org/10.1016/j.rineng.2024.102090

13. Shi, Z., Chen, C., Gong, Y., Yang, Z., & Bao, Y. (2024). Sustainable and environmentally friendly longitudinal-torsional ultrasonic cryogenic cooling drilling system. Journal of Cleaner Production, 468, 143001. https://doi.org/10.1016/j.jclepro.2024.143001

14. Deng, Z., et al. (2025). Tool wear in enhanced minimum quantity lubrication assisted milling: From mechanism to application. Chinese Journal of Aeronautics. https://doi.org/10.1016/j.cja.2025.103597

15. Chen, C., Wang, A., Zheng, Z., Zhao, Q., Shi, Z., & Bao, Y. (2023). A study on drilling of CFRP/Ti stacks: Temperature field and thermal damage of the interface region. Materials, 16(7), 2586. https://doi.org/10.3390/ma16072586

16. Shariar, F., Karagüzel, U., & Karpat, Y. (2025). A hybrid model to analyze stress distributions at the tool–workpiece interface during drilling of thick CFRP laminates considering thermal effects. International Journal of Advanced Manufacturing Technology. https://doi.org/10.1007/s00170-025-15717-2

17. Ge, J., et al. (2025). Intelligent machining of CFRP composites via data-driven prediction and optimization: Advances, challenges and future prospects. Materials Science. https://doi.org/10.26434/chemrxiv-2025-b1jjg

18. Yang, D., Liu, G., & Li, X. (2025). Cryogenic temperature-dependent machining forces and surface

DOI 10.15588/1607-6885-2026-2-7

integrity of Ti-6Al-4V titanium alloy. Advanced Engineering Materials. https://doi.org/10.1002/adem.202502270

19. Li, F., Chen, T., Deng, Z., Sun, Y., & Zhang, C. (2023). Ultrasonic assisted pecking drilling process for CFRP/Ti laminated materials. Journal of Manufacturing Processes, 108, 834–851. https://doi.org/10.1016/j.jmapro.2023.11.042

20. Moran, X., et al. (2024). Experimental, modeling, and numerical simulation of ultrasonic assisted drilling of CFRP/Ti stacks. Journal of Manufacturing Processes, 133, 97–117. https://doi.org/10.1016/j.jmapro.2024.11.045

21. Xu, J., et al. (2025). A critical review on numerical modeling of cutting-induced damage for CFRP composites. Composite Structures. https://doi.org/10.1016/j.compstruct.2025.119839

22. Yang, T., Zhang, L., Sun, W., Qian, S., Chen, M., & Qiu, Q. (2025). Cutting force prediction of longitudinal-torsional ultrasonic assisted milling based on ensemble learning: A case study on CFRP. Composites Part A, 190, 108702. https://doi.org/10.1016/j.compositesa.2024.108702

23. Hiremath, A., Malghan, R. L., Bolar, G., & Polishetty, A. (2025). Comprehensive machinability assessment of Ti6Al4V alloy during drilling and helical milling using sustainable dry condition. International Journal on Interactive Design and Manufacturing, 19, 1987–2002. https://doi.org/10.1007/s12008-024-01964-2

24. Gururaj, B., Anoop Aroor, D., Ashwin, P., Raviraj, S., Anupama, H., & Neelakantha, V. L. (2024). Performance analysis of helical milling and drilling operations in CFRP/Ti stacks. Journal of Manufacturing and Materials Processing, 8(3). https://doi.org/10.3390/jmmp8030113

25. Norbert, G. (2025). Fibre-orientation-driven defect probability mapping for machining-induced delamination and burr minimisation in carbon fibre-reinforced polymer composites. Composites Part C: Open Access. https://doi.org/10.1016/j.jcomc.2025.100636

Received 09.03.2026
Accepted 06.04.2026
Published 07.05.2026

УДК 621.914.2:621.762

ТЕРМОМЕХАНІЧНИЙ ВПЛИВ РЕЖИМІВ РІЗАННЯ НА ТОЧНІСТЬ ОТВОРІВ ТА ЗНОШЕННЯ ІНСТРУМЕНТУ ПРИ СВЕРДЛІННІ ПАКЕТІВ ВУГЛЕПЛАСТИК/ТИТАНОВИЙ СПЛАВ

Віталій Колесник — канд. техн. наук, доцент, доцент кафедри технології машинобудування, верстатів та інструментів, Сумський державний університет, м. Суми, Україна, *e-mail: v.kolesnik@tmvi.sumdu.edu.ua*, ORCID: 0000-0002-0417-3801

Олександр Березняк — аспірант, кафедра технології машинобудування, верстатів та інструментів, Сумський державний університет, м. Суми, Україна,*e-mail: o.berezniak@tmvi.sumdu.edu.ua*, ORCID: 0009-0005-2275-035X

Мета роботи. *Систематизувати та узагальнити результати досліджень щодо впливу режимів різання під час свердління пакетів вуглепластик/титановий сплав на точність отворів, якість обробленої поверхні, інтенсивність зношування різального інструменту та утворення наросту на ріжучій кромці.*

Методи дослідження. *Використано порівняльно-параметричний аналіз впливу подачі та швидкості різання на осьову силу свердління, температуру у зоні різання, інтенсивність розшарування композиційного матеріалу, висоту заусенця у шарі титанового сплаву, параметри шорсткості поверхні та інтенсивність зношування інструменту. Узагальнено результати експериментальних досліджень і числового моделювання з сучасних наукових публікацій для встановлення причинно-наслідкових зв'язків між режимами різання, термомеханічними процесами у зоні різання та показниками якості отворів.*

Отримані результати. *Встановлено, що подача є основним фактором механічного навантаження під час свердління та визначає інтенсивність розшарування вуглепластику. Швидкість різання переважно впливає на температуру у зоні різання та адгезійні явища у титановому сплаві. Показано, що утворення наросту та адгезійне перенесення матеріалу на ріжучу кромку змінюють її мікрогеометрію, спричиняють зростання осьових сил, погіршення точності отворів і зниження стабільності процесу свердління.*

Наукова новизна*. Обґрунтовано інтегрований підхід до оцінювання процесу свердління пакетів вуглепластик/титановий сплав як єдиної термомеханічної системи, у якій режими різання, розвиток зношування інструменту та утворення наросту розглядаються як взаємопов'язані чинники переходу між абразивним, адгезійним і дифузійним механізмами зношування.*

Практична цінність. *Отримані узагальнення можуть бути використані для визначення напрямів подальших досліджень, підвищення ресурсу різального інструменту, стабілізації процесу свердління та оптимізації режимів різання.*

Ключові слова: *свердління, пакет вуглепластик/титановий сплав, режими різання, розшарування, наріст, зношування інструменту, термомеханічна взаємодія, порівняльно-параметричний аналіз.*

DOI 10.15588/1607-6885-2026-2-7

Список літератури

1. Yu J. J. et al. Dynamic temperature field and drilling damage mechanism of plain woven carbon/glass hybrid composites *Composite Structures*. – 2023. – Vol. 304. – Art. 116375. DOI: https://doi.org/10.1016/j.compstruct.2022.116375

2. Chen C., Zhao Q., Wang A. Numerical study on the heat effect on the drilling damage of Ti/CFRP stacks. *Polymer Composites.* 2024. Vol. 45. No. 10. P. 9487–9500. DOI: https://doi.org/10.1002/pc.28422

3. Khashaba U. A., Mashhour A. A. Thermo-mechanical damage and cutting forces analysis in drilling UD-GFRP composites. Composites Part A. 2026. – Vol. 201. – Art. 109415. DOI: https://doi.org/10.1016/j.compositesa.2025.109415

4. Jebaratnam Joy M., Choo Then X., Muhammad Hafiz H., Gérald F. Influence of drill geometry on adhesion layer formation in AFRP/Al7075-T6 stacks. *Journal of Composites Science*. 2025. DOI: https://doi.org/10.3390/jcs9120658

5. Chen C. et al. Experimental study on step drill geometry and pecking drilling with variable parameters processing method as drilling of CFRP and Ti stacks. *Journal of Manufacturing Processes.* 2024. Vol. 117. P. 355–365. DOI: https://doi.org/10.1016/j.jmapro.2024.03.011.

6. Samsudeensadham S., Krishnaraj V. Comparative tool wear study on drilling of CFRP/Ti stacks using TiAlN and AlTiSiN coated drill bits. *Engineering Research Express*. 2025. Vol. 7, No. 3. Art. 035550. DOI: https://doi.org/10.1088/2631-8695/adf8b3

7. Shengguo Z., Wenhu W., Ruisong J., Yifeng X., Bo H., Jiaxing W. Multi-objective optimization for the machining performance during ultrasonic vibration-assisted helical grinding hole of thin-walled CF/BMI composite laminates. Thin-Walled Structures. 2023. Vol. 192. Art. 111086. DOI: https://doi.org/10.1016/j.tws.2023.111086

8. Aditya K., Nitin T., Gopal A. V., Krishna V. An assessment of machining performance of CAPVD-coated carbide tools in face milling of Ti-6Al-4V. Ceramics International. 2024. DOI: https://doi.org/10.1016/j.ceramint.2024.02.152

9. Sharma P., Mishra S. K., Ramkumar J. Damage mechanisms and wear progression of advanced AlTiSiN coatings deposited on WC/Co cemented carbide cutting tools for machining under cryogenic conditions. Ceramics International. 2025. Vol. 51, No. 27. P. 54530–54548. DOI: https://doi.org/10.1016/j.ceramint.2025.09.183

10. Zhaoju Z., Albert J. S., Lei C. Cutting edge temperature and drill wear in dry and minimum quantity lubrication environmentally-friendly drilling of titanium alloy. Journal of Materials Research and Technology. 2025. Vol. 39. DOI: https://doi.org/10.1016/j.jmrt.2025.12.010

11. Zhang L., Zhang X. Effect of cooling and lubrication conditions on the variable angle milling of unidirectional CFRP with PCD tools. Journal of Materials Processing Technology. 2023. Vol. 319. P. 1–11. DOI: https://doi.org/10.1016/j.jmatprotec.2023.118073

12. Maria I. et al. State-of-the-art hybrid lubrication (Cryo-MQL) supply systems, performance evaluation, and optimization studies in various machining processes. Results in Engineering. 2024. Vol. 22. Art. 102090. DOI: https://doi.org/10.1016/j.rineng.2024.102090

13. Shi Z. et al. Sustainable and environmentally friendly longitudinal-torsional ultrasonic cryogenic cooling drilling system. Journal of Cleaner Production. 2024. Vol. 468. Art. 143001. DOI: https://doi.org/10.1016/j.jclepro.2024.143001

14. Zhenjing D. et al. Tool wear in enhanced minimum quantity lubrication assisted milling: from mechanism to application. Chinese Journal of Aeronautics. 2025. DOI: https://doi.org/10.1016/j.cja.2025.103597

15. Chen C. et al. A study on drilling of CFRP/Ti stacks: temperature field and thermal damage of the interface region. Materials. 2023. Vol. 16, No. 7. Art. 2586. DOI: https://doi.org/10.3390/ma16072586

16. Shariar F., Karagüzel U., Karpat Y. A hybrid model to analyze stress distributions at the tool and workpiece interface during drilling of thick CFRP laminates considering thermal effects. *The International Journal of Advanced Manufacturing Technology*. 2025. DOI: https://doi.org/10.1007/s00170-025-15717-2

17. Ge J. et al. Intelligent machining of CFRP composites via data-driven prediction and optimization: advances, challenges and future prospects. ChemRxiv. 2025. DOI: https://doi.org/10.26434/chemrxiv-2025-b1jjg

18. Yang D., Liu G., Li X. Cryogenic temperature-dependent machining forces and surface integrity of Ti-6Al-4V titanium alloy. Advanced Engineering Materials. 2025. https://doi.org/10.1002/adem.202502270

19. Li F. et al. Ultrasonic assisted pecking drilling process for CFRP/Ti laminated materials. *Journal of Manufacturing Processes*. 2023. Vol. 108. P. 834–851. https://doi.org/10.1016/j.jmapro.2023.11.042

20. Moran X. et al. Experimental, modeling, and numerical simulation of ultrasonic assisted drilling of CFRP/Ti stacks. *Journal of Manufacturing Processes*. 2024. Vol. 133. P. 97–117. https://doi.org/10.1016/j.jmapro.2024.11.045

21. Xu J et al. A critical review on numerical modeling of cutting-induced damage for CFRP composites. *Composite Structures*. 2025. https://doi.org/10.1016/j.compstruct.2025.119839

22. Yang T. et al. Cutting force prediction of longitudinal-torsional ultrasonic assisted milling based on ensemble learning: A case study on CFRP. Composites Part A. 2025. Vol. 190. 108702. https://doi.org/10.1016/j.compositesa.2024.108702

23. Comprehensive machinability assessment of Ti6Al4V alloy during drilling and helical milling using sustainable dry condition. Hiremath A., Malghan R. L., Bolar G., Polishetty A. *International Journal on Interactive Design and Manufacturing*. 2025. Vol. 19. P. 1987–2002. https://doi.org/10.1007/s12008-024-01964-2

24. Gururaj B. et al. Performance analysis of helical milling and drilling operations in CFRP/Ti stacks. *Journal of Manufacturing and Materials Processing*. 2024. Vol. 8, No. 3. DOI: https://doi.org/10.3390/jmmp8030113

25. Norbert G. Fibre-orientation-driven defect probability mapping for machining-induced delamination and burr minimisation in carbon fibre-reinforced polymer composites. Composites Part C: Open Access. 2025. DOI: https://doi.org/10.1016/j.jcomc.2025.100636

DOI 10.15588/1607-6885-2024-2-7

UDC 621.43.013:621.43.038

Natalya Yevsyeyeva	Candidate of Technical Science, Associate Professor, Department of Automobiles, Heat Engines and Hybrid Energy Plants, National University Zaporizhzhia Polytechnic, Zaporizhzhia, Ukraine, *e-mail: korskovanat@ukr.net*, ORCID: 0000-0002-3398-6537
Roman Sukhonos	Senior Lecturer, Department of Automobiles, Heat Engines and Hybrid Energy Plants, National University Zaporizhzhia Polytechnic, Zaporizhzhia, Ukraine, *e-mail: romevs@zp.edu.ua*, ORCID: 0000-0001-9683-3389
Natalya Ryaboshapka	Senior Lecturer, Department of Automobiles, Heat Engines and Hybrid Energy Plants, National University Zaporizhzhia Polytechnic, Zaporizhzhia, Ukraine, *e-mail: ryaboshapka.ne@gmail.com*, ORCID: 0000-0003-0334-8363
Vladyslav Timoshenko	Student of Department of Automobiles, Heat Engines and Hybrid Energy Plants, National University Zaporizhzhia Polytechnic, Zaporizhzhia, Ukraine, *e-mail: vladtimoha0@gmail.com*

RESEARCH OF THE EFFECT OF RAM AIR BOOSTING ON THE PERFORMANCE OF AN INTERNAL COMBUSTION ENGINE

Purpose. *To investigate the influence of gas exchange parameters, in particular ram air boosting, on the indicated and effective performance of a four-stroke spark-ignition internal combustion engine using the high-performance engine of the Kawasaki Ninja ZX-10R motorcycle as a case study.*

Research methods. *A combination of theoretical and analytical-calculation methods was employed. The magnitude of ram air boosting was analyzed by determining the dynamic air pressure as a function of vehicle speed within the range of 0–300 km/h. A thermodynamic cycle calculation of the spark-ignition engine operating at the rated condition was performed using the Engine Calculation software environment. The analysis was carried out for both naturally aspirated conditions and with ram air boosting, taking into account variations in intake pressure, charge density, cyclic air and fuel mass, as well as the thermodynamic state of the working charge at the beginning of the cycle.*

Results. *It has been established that with increasing vehicle speed, the dynamic air pressure rises according to a quadratic relationship and exceeds 4 kPa at speeds above 300 km/h. This results in an increase in intake pressure, a higher mass of air per cycle, and a corresponding increase in fuel supply. Consequently, the engine effective power increases by up to 4.2%, while average effective pressure shows a similar rise. At the same time, the indicated and effective thermal efficiencies, as well as the specific fuel consumption, remain practically unchanged. It has been found that the increase in engine power is primarily due to the increased mass of the working charge in the cylinder, whereas the main gas exchange coefficients exhibit only minor variations.*

Scientific novelty. *A methodology has been developed for evaluating the effect of ram air boosting on the indicated and effective performance of a spark-ignition internal combustion engine, taking into account variations in gas exchange parameters and intake conditions. The proposed approach enables a quantitative assessment of power gain as a function of vehicle speed.*

Practical value. *The proposed methodology and obtained results can be applied in the design and optimization of intake systems for high-speed vehicles, including motorcycles, sports cars, and aircraft, as well as in the modernization of existing engines to enhance their power output without significant structural complexity.*

Key words: *internal combustion engine, gas exchange, ram air boosting, intake system, dynamic pressure, effective power.*

Introduction

The use of internal combustion engines (ICE) as a power source for various types of machinery has both advantages and disadvantages. The advantages include compactness of the power unit, high specific power output, ease of refueling, and relatively long driving range. The primary disadvantages are associated with environmental impact, namely the harmful emissions resulting from fuel combustion and the pollution of the environment by combustion products. In addition, a vehicle is a source of vibroacoustic and electromagnetic emissions [1].

The main trends in the development and improvement of ICEs over recent decades have been focused on enhancing fuel and lubricant efficiency, increasing reliability, reducing exhaust emissions, improving the level of automation and diagnostic

DOI 10.15588/1607-6885-2026-2-8

capabilities, and decreasing mass and overall dimensions. These parameters determine the technological advancement and competitiveness of various applications (automobiles, motorcycles, marine vessels, locomotives, power generators, etc.), as well as the efficient utilization of key operating materials (lubricants, fuels, metals, etc.) and the associated maintenance and repair costs [2–4].

There are numerous approaches to improving the performance of internal combustion engines, which can be achieved by optimizing the operation of various subsystems. In the absence of boosting devices (such as superchargers or turbochargers), an internal combustion engine is referred to as naturally aspirated. One of the methods to increase the amount of air supplied to the intake system in such engines is the application of ram air boosting.

Analysis of research and publications

There are numerous methods for improving specific performance parameters of ICEs; however, each of them has certain drawbacks, such as complexity, cost, and reduced reliability. The possibilities for boosting ICEs installed on motorcycles are significantly limited. In addition to the conventional requirements of fuel efficiency, reliability, and environmental performance, rather strict constraints are also imposed on mass and dimensional characteristics.

Thus, one of the most obvious ways to increase ICE power – namely, the use of mechanical supercharging (supercharger) or gas-turbine boosting (turbocharger) – becomes complicated or even impractical. However, ram air boosting systems exhibit a certain level of effectiveness. Their efficiency is limited; however, their use in high-speed motorcycles does not lead to a significant increase in mass, and such systems are most effective at high vehicle speeds [5]. In contrast to “conventional” boosting systems (with superchargers or turbochargers), ram air systems have been less studied in the scientific literature; therefore, the research topic is relevant.

Ram air boosting systems have been widely used in aviation since the emergence of aircraft capable of reaching significant speeds (above 140–160 km/h), and later in high-speed automobiles (e.g., Ford Fairlane Thunderbolt, Porsche Panamera GTS) and motorcycles (Kawasaki ZX-11). The effectiveness of ram air boosting in passenger cars is limited due to the large length and significant curvature of intake ducts.

In motorcycles, the air intake is installed in the front part of the vehicle body, within the fairing. According to the study conducted by the authors [6], the increase in intake system pressure due to ram air boosting in a high-speed motorcycle is about 4 kPa. The best results (maximum pressure increase) are obtained with maximum smoothing of the intake duct, which has no sharp corners or abrupt bends.

According to data from [7, 8], the intake pressure of passenger car ICEs increases by 3–6 kPa at vehicle speeds of about 200 km/h.

Based on the analysis of sources [5, 9–12], it can be concluded that the implementation of ram air boosting requires:

- the presence of dynamic pressure (incoming airflow);
- a properly designed and optimally positioned air intake.

Purpose

The purpose of this work is to research the influence of gas exchange parameters on the indicated and effective performance of a four-stroke spark-ignition engine with ram air boosting, using the engine of the Kawasaki Ninja ZX-10R motorcycle as an example.

To achieve this objective, the following tasks were solved:

- determination of the main parameters characterizing intake gas exchange processes; consideration of the main structural elements of the intake system; analysis of aspects related to the application of the ram air effect to improve ICE performance; review of existing methods for studying the influence of ram air boosting on engine performance;
- development of a methodology for determining the effect of ram air boosting on the performance of a high-speed motorcycle spark-ignition engine;
- calculation of the magnitude of ram air boosting, i.e., the dynamic air pressure, at different vehicle speeds;
- performing a thermodynamic cycle calculation of the engine operating at rated conditions, both in the presence and absence of ram air boosting, and determining the indicated and effective performance parameters;
- conclusions based on the analysis of the obtained results.

Material and Methodology

The study employed theoretical (analysis, synthesis, induction, deduction) and practical (analytical-calculation) methods.

To investigate the effect of ram air boosting on the performance of a high-speed motorcycle spark-ignition engine, the engine of the Kawasaki Ninja ZX-10R motorcycle was choosen.

The engine is an inline four-cylinder, liquid-cooled unit with a displacement of 998 cm³, mounted transversely in the motorcycle frame (Fig. 1, 2). The valvetrain is of the DOHC type, with four valves per cylinder. The intake system is designed with reduced flow resistance and incorporates ram air boosting. The air filter element is of the viscous paper type.

DOI 10.15588/1607-6885-2026-2-8

Figure 1. Air intake of the Kawasaki Ninja ZX-10R motorcycle engine [13]

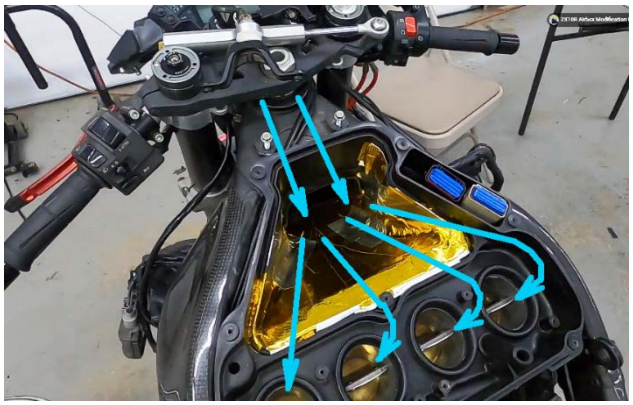

Figure 2. Schematic of the intake system and airflow path in the Kawasaki Ninja ZX-10R motorcycle (air filter not shown) [14]

Technical specifications of the Kawasaki Ninja ZX-10R engine [13, 14]:

- number of cylinders – 4;
- stroke – 76.0 mm;
- bore – 55.0 mm;
- compression ratio – 13;
- maximum effective power – 146 kW (197 hp) at 13,000 rpm;
- maximum torque – 113.5 N·m at 11,500 rpm.

Ambient air is drawn from outside through an intake duct (Figure 1), which is installed in the front part of the motorcycle fairing. The duct is protected by a mesh to prevent large debris from entering.

Then, the horizontal airflow is deflected upward, passes over the upper part of the engine, turns downward, and is directed toward the air filter and throttle valves (Figure 2).

Due to the large cross-sectional area of the air ducts and the orientation of the air intake in the direction of motorcycle motion, an increase in intake air pressure is achieved at high speeds as a result of ram air boosting. The maximum speed of the Kawasaki Ninja ZX-10R motorcycle, depending on the modification, can reach 304 km/h.

The methodology for determining the effect of ram air boosting on the performance of a high-speed motorcycle spark-ignition engine includes:

- calculation of the magnitude of ram air boosting by determining the dynamic air pressure at possible vehicle speeds;
- performing a thermodynamic cycle calculation of the engine operating at rated conditions using the physical and mathematical model of Prof. Yehorov, implemented in the Engine Calculation software [15–17], both without ram air boosting and with ram air boosting at vehicle speeds of 100, 200, and 300 km/h; calculation of indicated and effective performance parameters;
- analysis of the obtained results and formulation of conclusions and recommendations regarding the effectiveness and feasibility of using ram air boosting in engines of ground and aircraft vehicles.

Unlike existing studies, this research considers the influence of ram air boosting on the engine working cycle and indicated performance parameters, not only on effective performance.

Research results

In the course of the study, the nature of the dependence of the increase in dynamic (ram air) pressure on the vehicle speed was determined, i.e., $p_D = f(\upsilon)$ (Fig. 3). A quadratic equation was obtained that allows calculating the value of p_D for any value of υ within the range from 0 to 350 km/h:

$$p_D = 46{,}46 \cdot 10^{-6} \cdot \upsilon^2 - 0{,}8214 \cdot 10^{-6} \cdot \upsilon + 112{,}5 \cdot 10^{-6}. \quad (1)$$

A thermodynamic calculation of the working cycle of the four-stroke spark-ignition engine of the Kawasaki Ninja ZX-10R at rated operating conditions was performed. The calculation was carried out using the Engine Calculation software according to a methodology [16].

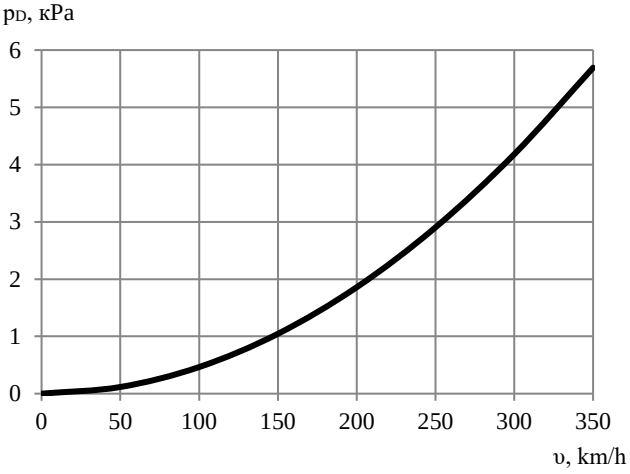

Figure 3. Variation of dynamic air pressure p_D as a function of vehicle speed υ under standard temperature and pressure conditions

DOI 10.15588/1607-6885-2026-2-8

The engine performance parameters, taking into account the magnitude of ram air boosting, were calculated with the following variable parameters:

- boost pressure p_k';
- charge density at the cylinder inlet ρ_k;
- intake pressure losses Δp_{int};
- volumetric efficiency η_v;
- cyclic air mass in the cylinder Δm_{air};
- cyclic fuel mass supply Δm_{fuel};
- pressure in the cylinder at the beginning of the cycle p_a;
- mass of the in-cylinder working medium at the beginning of the cycle m_a.

The intake air temperature T_o was assumed constant.

Table 1 shows the initial data for the thermal calculation of the Kawasaki Ninja ZX10R engine at rated conditions, taking into account ram air boosting.

Table 1 – Input data for the thermodynamic calculation of the Kawasaki Ninja ZX-10R engine at rated conditions taking into account ram air boosting

Parameter	Values			
υ, km/h	0	100	200	300
p_k, Pa	101325			
p_D, Pa	0	464,6	1858,5	4181,6
p_k', Pa	101325	101789,6	103183,5	105506,6
ρ_k, kg/m^3	1,204	1,210	1,226	1,254
Δp_{int}, Pa	4053,0	4071,6	4127,3	4220,3
p_a, Pa	97272	97718	99056	101286
$\Delta m_{air} \cdot 10^6$, kg/cycle	254	255	259	265
$\Delta m_{fuel} \cdot 10^6$, kg/cycle	19,31	19,40	19,67	20,11
$m_a \cdot 10^{-6}$, kg/cycle	272	273	277	283

The indicated performance parameters of the engine are presented in Table 2.

Table 2 – Indicated performance of the Kawasaki Ninja ZX-10R engine at rated conditions without (υ = 0 km/h) and with ram air boosting (υ = 300 km/h)

Parameter	Values			
υ, km/h	0	100	200	300
L_i, J/cycle	419,903	421,835	426,960	437,531
p_i, MPa	1,6853	1,6931	1,7137	1,7561

From Table 2, it follows that at a vehicle speed of Kawasaki Ninja ZX10R υ = 300 km/h under rated operating conditions, compared to υ = 0 km/h, the indicated performance parameters of the engine change as follows:

- indicated work L_i increases by 4.2%;
- indicated average effective pressure p_i increases by 4.2%;
- indicated specific fuel consumption g_i shows no significant change;
- indicated efficiency η_i shows no significant change.

The effective performance parameters of the engine are presented in Table 3.

From Table 3, it follows that at a vehicle speed of υ = 300 km/h under rated conditions, compared to υ = 0 km/h, the effective performance parameters change as follows:

- effective power N_e increases by 4.2% (Fig. 4);
- effective average effective pressure p_e increases by 4.2%;
- effective specific fuel consumption g_e shows no significant change;
- effective efficiency η_e shows no significant change.

Table 3 – Effective performance of the Kawasaki Ninja ZX-10R engine at rated conditions without (υ = 0 km/h) and with ram air boosting (υ = 300 km/h)

Parameter	Values			
υ, km/h	0	100	200	300
N_e, kW	145,57	146,24	148,01	151,68
p_e, MPa	1,348	1,354	1,371	1,405

As the speed of the Kawasaki Ninja ZX-10R motorcycle increases from 0 to 300 km/h, changes occur in the engine working cycle due to ram air boosting. In particular, this leads to an increase in the maximum in-cylinder pressure p_{max} by 0.597 MPa (4.2%) and an increase in the maximum temperature T_{max} by 3.3 K (0.1%).

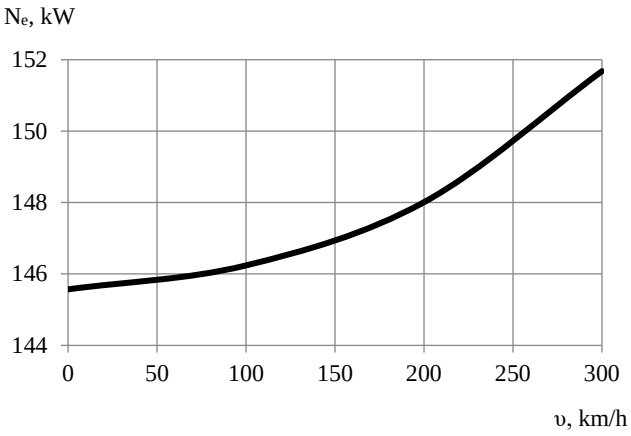

Figure 4. Dependence of the maximum effective power of the Kawasaki Ninja ZX-10R engine on vehicle speed due to ram air boosting

Conclusions

The study has established that motorcycle Kawasaki Ninja ZX10R at a vehicle speed of υ = 300 km/h under rated operating conditions, compared to υ = 0 km/h, the engine performance parameters change as follows:

- effective power Ne and average effective pressure pe increase by 4.2%;
- effective specific fuel consumption ge and effective efficiency ηe remain practically unchanged;

DOI 10.15588/1607-6885-2026-2-8

- maximum in-cylinder pressure p_{max} increases by 0.597 MPa (4.2%);

- maximum temperature T_{max} of the working charge remains practically unchanged.

It is shown that the main parameters characterizing gas exchange in the cylinder and the intake process – residual gas fraction γ, excess air ratio α, and volumetric efficiency η_v – remain practically unchanged when ram air boosting is applied. The increase in engine power is primarily due to the increase in the cyclic air mass Δm_{air} and the cyclic fuel mass Δm_{fuel}.

The results confirm that ram air boosting can provide a noticeable increase in effective power without additional complexity or increase in engine mass, which is critically important for motorcycles and related applications, including aircraft. The obtained results are recommended for experimental validation.

References

1. Chmyr, V. (2025). Analysis of methods for increasing the efficiency of piston internal combustion engines during their use in automotive technology for the organization of vehicle transportation. Collection of scientific works of the National Academy of the State Border Guard Service of Ukraine. Series: Military and Technical Sciences, 2(99), 142–151. https://doi.org/10.32453/3.v99i2.1858

2. Tsymbal, S. V., Zakorchevsky, A. V., Berezovsky, E. E. & Kozak, R. O. (2023). Perspektivni tendenciyi rozvitku porshnevih DVZ i agregativ na yihnij bazi [Promising trends in the development of piston internal combustion engines and units based on them]. VNTU, 8. https://atm.vntu.edu.ua/articles/15.pdf

3. Marchenko, A. P., Ryazancev, M. K. & Shehovcov, A. F. (2004). Dviguni vnutrishnogo zgorannya: Seriya pidruchnikiv u 6 tomah. T. 1. Rozrobka konstrukcij forsovanih dviguniv nazemnih transportnih mashin [Internal combustion engines: A series of textbooks in 6 volumes. Vol. 1. Development of designs of forced engines for ground transport vehicles]. Prapor, 384.

4. Slynko, G., Sukhonos, R., Slinko, V. & Lukyanenko, V. (2024). Research on the Influence of Resonant Charging of a Two-Stroke Gasoline Engine on its Power Curve. New materials and technologies in metallurgy and mechanical engineering, 4, 59–66 https://doi.org/10.15588/1607-6885-2024-4-6

5. Kee, R. J., Maynes, B. D. J., Kenny, R. G., Mackey, D. & Foley, L. (2002). Prediction of Formula 1 Engine and Airbox Performance using Coupled Virtual 4-Stroke and CFD Simulations. SAE Technical Papers. 2002-01-3318 https://doi.org/10.4271/2002-01-3318

6. Cabello, S. & Baz, P. (2013). Sistema aerodinámico Ram-Air: funcionamiento. Motociclismo. https://www.motociclismo.es/industria/el-ram-air_176725_102.html

7. Airboxes and Ram Effect (2008). Autosport. https://forums.autosport.com/topic/103265-airboxes-and-ram-effect

8. Does ram air work? (2012). Grassroots Motorsports. https://grassrootsmotorsports.com/forum/grm/article-topic-does-ram-air-work/48999/page1

9. Abramchuk, F. I., Gutarevich, Yu. F., Dolganov, K. E. & Timchenko, I. I. (2006). Avtomobilni dviguni [Automobile engines]. Aristei, 476.

10. Parry, L., Könözsy, L. & Temple, C. (2018). Airbox design, analysis and improvement for a highperformance road racing sidecar. Vehicle and Automotive Engineering. Lecture Notes in Mechanical Engineering, 2. 545–562. https://doi.org/10.1007/978-3-319-75677-6_48

11. Tan, J. & Abu Bakar, N. Z. (2021). Design improvement of an airbox for a passenger vehicle. Journal of Physics: Conference Series. https://doi.org/10.1088/1742-6596/2120/1/012010

12. Teck Yap, J., Abu Bakar, N. Z., Shaikh Dawood, N. F. & Rosli, M. A. (2021). Design Improvements of Acoustic Response of an Automotive Air Intake System. MATEC Web of Conferences, 335, 10. https://doi.org/10.1051/matecconf/202133503017

13. Kawasaki Ninja ZX-10R Motorcycle Service Manual (2008). Kawasaki Heavy Industries, Ltd., 694.

14. Kawasaki Ninja ZX-10R Racing Kit Manual (2006). Kawasaki Heavy Industries, Ltd., 82.

15. Slynko, G., Sukhonos, R. & Ivanov. P. (2019). Komp'yuterna programa dlya teplovogo rozrahunku robochogo ciklu dviguna vnutrishnogo zgorannya [Computer Program for Calculation of the Operating Cycle of Internal Combustion Engine]. Information technologies: theory and practice: II All-Ukrainian Internet Conference of Higher Education Applicants and Young Scientists, April 4, 2019. Zaporizhzhia. ZNTU, 96–97.

16. Slynko, G. I., Sukhonos, R. F. & Slynko, V. V. (2024). Thermal and dynamic calculation of internal combustion engines: a textbook for course design. National University "Zaporizhzhia Polytechnic", 130.

17. Slynko, G., Sukhonos, R. & Ivanov. P. (2019). Computer Program for Calculation of the Operating Cycle of Internal Combustion Engine. Science Week-2019. Faculty of Transport: annual scientific and practical conference, April 15-19, 2019: abstracts. Zaporizhzhia: ZNTU, 74–75.

18. Dziubak, T. & Karczewski, M. (2022). Experimental Study of the Effect of Air Filter Pressure Drop on Internal Combustion Engine Performance. Energies, 15(9). https://doi.org/10.3390/en15093285

Received 27.03.2026
Accepted 08.04.2026
Published 07.05.2026

DOI 10.15588/1607-6885-2026-2-8

УДК 621.43.013:621.43.038

ДОСЛІДЖЕННЯ ВПЛИВУ ДИНАМІЧНОГО НАДДУВУ НА ПОКАЗНИКИ ДВИГУНА ВНУТРІШНЬОГО ЗГОРАННЯ

Наталія Євсєєва — канд. техн. наук, доцент, доцент кафедри автомобілів, теплових двигунів та гібридних енергетичних установок Національного університету «Запорізька політехніка», м. Запоріжжя, Україна, *e-mail: korskovanat@ukr.net*, ORCID: 0000-0002-3398-6537

Роман Сухонос — старший викладач кафедри автомобілів, теплових двигунів та гібридних енергетичних установок Національного університету «Запорізька політехніка», м. Запоріжжя, Україна, *e-mail: romevs@zp.edu.ua*, ORCID: 0000-0001-9683-3389

Наталя Рябошапка — старший викладач кафедри автомобілів, теплових двигунів та гібридних енергетичних установок Національного університету «Запорізька політехніка», м. Запоріжжя, Україна, *e-mail: ryaboshapka.ne@gmail.com*, ORCID: 0000-0003-0334-8363

Владислав Тимошенко — студент кафедри автомобілів, теплових двигунів та гібридних енергетичних установок Національного університету «Запорізька політехніка», м. Запоріжжя, Україна, *e-mail: vladtimoha0@gmail.com*

Мета роботи. *Дослідити вплив параметрів газообміну, зокрема динамічного (швидкісного) наддуву, на індикаторні та ефективні показники бензинового чотиритактного двигуна внутрішнього згоряння на прикладі високофорсованого двигуна мотоцикла Kawasaki Ninja ZX-10R.*

Методи дослідження. *Для досягнення поставленої мети використано комплекс теоретичних та аналітично-розрахункових методів. Проведено аналіз величини динамічного наддуву шляхом визначення динамічного тиску повітря залежно від швидкості руху транспортного засобу в діапазоні 0–300 км/год. Виконано термодинамічний розрахунок робочого циклу бензинового двигуна на номінальному режимі з використанням програмного середовища Engine Calculation. Розрахунок проведено для умов відсутності та наявності динамічного наддуву з урахуванням зміни тиску на впуску, густини заряду, маси повітря та палива в циклі, а також параметрів робочого тіла на початку циклу.*

Отримані результати. *Встановлено, що зі зростанням швидкості руху мотоцикла величина динамічного тиску повітря зростає за квадратичним законом і при швидкості понад 300 км/год досягає значення понад 4 кПа. Це призводить до підвищення тиску на впуску, збільшення циклового заряду повітря та відповідного зростання подачі палива. У результаті ефективна потужність двигуна збільшується до 4,2 %, а середній ефективний тиск – на аналогічну величину. При цьому індикаторний та ефективний коефіцієнти корисної дії, а також питома витрата палива залишаються практично незмінними. Виявлено, що підвищення потужності зумовлене переважно збільшенням маси робочого тіла в циліндрі, тоді як основні коефіцієнти, що характеризують процес газообміну, змінюються незначно.*

Наукова новизна. *Розроблено методику оцінювання впливу динамічного наддуву на індикаторні та ефективні показники бензинового двигуна внутрішнього згоряння з урахуванням зміни параметрів газообміну та умов впуску, що дозволяє кількісно визначати приріст потужності залежно від швидкості руху транспортного засобу.*

Практична цінність. *Запропонована методика та отримані результати можуть бути використані при проектуванні та оптимізації впускних систем швидкісних транспортних засобів, зокрема мотоциклів, спортивних автомобілів, літальних апаратів, а також при модернізації існуючих двигунів з метою підвищення їх потужнісних показників без суттєвого ускладнення конструкції.*

Ключові слова: *двигун внутрішнього згоряння, газообмін, динамічний наддув, впускна система, динамічний тиск, ефективна потужність.*

Список літератури

1. Чмир В. Аналіз способів підвищення ефективності поршневих двигунів внутрішнього згорання в ході їх застосування на автомобільній техніці під час організації автомобільних перевезень. Збірник наукових праць Національної Академії Державної прикордонної служби України. Серія :

DOI 10.15588/1607-6885-2026-2-8

військові та технічні науки. 2025. Том 99. № 2. С. 142–151. https://doi.org/10.32453/3.v99i2.1858

2. Цимбал С. В., Закорчевський А. В., Березовський Є. Е., Козак Р. О. Перспективні тенденції розвитку поршневих ДВЗ і агрегатів на їхній базі. Вінниця : ВНТУ, 2023. 8 с. https://atm.vntu.edu.ua/articles/15.pdf

3. Марченко А. П., Рязанцев М. К., Шеховцов А. Ф. Двигуни внутрішнього згорання: Серія підручників у 6 томах. Т. 1. Розробка конструкцій форсованих двигунів наземних транспортних машин. Харків : Прапор, 2004. 384 с.

4. Слинько Г. І., Сухонос Р. Ф., Слинько В. В., Лук'яненко В. П. Дослідження впливу резонансного наддуву бензинового двотактного двигуна на його швидкісну характеристику. *Нові матеріали і технології в металургії та машинобудуванні*. 2024. № 4. С. 59–66. https://doi.org/10.15588/1607-6885-2024-4-6

5. Kee R. J., Maynes B. D. J., Kenny R. G., Mackey D., Foley L. Prediction of Formula 1 Engine and Airbox Performance using Coupled Virtual 4-Stroke and CFD Simulations. SAE Technical Papers. 2002. 2002-01-3318 https://doi.org/10.4271/2002-01-3318

6. Cabello S., Baz P. Sistema aerodinámico Ram-Air: funcionamientoю Сайт «Motociclismo». 2013. URL: https://www.motociclismo.es/industria/el-ram-air_176725_102.html

7. Airboxes and Ram Effect. 2008. Сайт «Autosport». URL: https://forums.autosport.com/topic/103265-airboxes-and-ram-effect

8. Does ram air work? 2012. Сайт «Grassroots Motorsports». URL: https://grassrootsmotorsports.com/forum/grm/article-topic-does-ram-air-work/48999/page1

9. Абрамчук Ф. І., Гутаревич Ю. Ф., Долганов К. Є., Тимченко І. І. Автомобільні двигуні. Київ : Арістей. 2006. 476 с.

10. Parry L., Könözsy L., Temple C. Airbox design, analysis and improvement for a highperformance road racing sidecar. Vehicle and Automotive Engineering. Lecture Notes in Mechanical Engineering. 2018. № 2. P. 545–562. https://doi.org/10.1007/978-3-319-75677-6_48

11. Tan J., Abu Bakar N. Z. Design improvement of an airbox for a passenger vehicle. Journal of Physics: Conference Series. 2021. https://doi.org/10.1088/1742-6596/2120/1/012010

12. Teck Yap J., Abu Bakar N. Z., Shaikh Dawood N. F., Rosli M. A. Design Improvements of Acoustic Response of an Automotive Air Intake System. MATEC Web of Conferences. 2021. Vol. 335. https://doi.org/10.1051/matecconf/202133503017

13. Kawasaki Ninja ZX-10R Motorcycle Service Manual. Kawasaki Heavy Industries, Ltd. 2008. 694 p.

14. Kawasaki Ninja ZX-10R Racing Kit Manual. Kawasaki Heavy Industries, Ltd. 2006. 82 p.

15. Слинько Г. І., Сухонос Р. Ф., Іванов П. Є. Комп'ютерна програма для теплового розрахунку робочого циклу двигуна внутрішнього згорання. Інформаційні технології: теорія і практика : матеріали II Всеукр. Інтернет-конф. здобувачів вищої освіти і молодих учених, 4 квітня 2019 р. Запоріжжя : ЗНТУ, 2019. С. 96–97.

16. Слинько Г. І., Сухонос Р. Ф., Слинько В. В. Тепловий і динамічний розрахунок ДВЗ : навчальний посібник з курсового проєктування. Запоріжжя : НУ «Запорізька політехніка», 2024. 130 с.

17. Slynko G., Sukhonos R., Ivanov P. Computer Program for Calculation of the Operating Cycle of Internal Combustion Engine. Тиждень науки-2019. Транспортний факультет : щоріч. наук.-практ. конф., 15-19 квітня 2019 р. : тези доп. Запоріжжя : ЗНТУ, 2019. С. 74–75.

18. Dziubak T., Karczewski M. Experimental Study of the Effect of Air Filter Pressure Drop on Internal Combustion Engine Performance. Energies. 2022. 15(9). 3285. https://doi.org/10.3390/en15093285

DOI 10.15588/1607-6885-2026-2-8

UDC 338:658.5

Oleksandr Chechet	Deputy head of the production department at JSC “Motor Sich”, Zaporizhzhia, Ukraine, *e-mail: Chechetalex1979@gmil.com*, ORCID: 0009-0003-2070-9885
Ruslan Kulykovskyi	Candidate of Technical Sciences, Associate professor, Vice-rector, National University Zaporizhzhia Polytechnic, Zaporizhzhia, Ukraine, *e-mail: kulikovski@zp.edu.ua*, ORCID: 0000-0001-8781-2113
Serhii Chigileychik	Leading Researcher at ZMDB SE “Ivchenko-Progres”, Zaporizhzhia, Ukraine, *e-mail: ChigileychikSL@ivchenkoprogress.com*, ORCID: 0000-0002-2372-9078
Yurii Torba	Candidate of Technical Sciences, Deputy director at ZMDB SE “Ivchenko-Progres”, Zaporizhzhia, Ukraine, *e-mail: Torba.Yuriy@gmail.com*, ORCID: 0000-0001-8470-9049
Andrii Dobrovolskyi	Leading engineer at ZMDB SE “Ivchenko-Progres”, Zaporizhzhia, Ukraine, *e-mail: dobrovolskiyj5@gmail.com*, ORCID: 0009-0007-8015-821X
Nataliia Shyrokobokova	Candidate of Technical Sciences, Associate professor, National University Zaporizhzhia Polytechnic, Zaporizhzhia, Ukraine, *e-mail: nsonik11@gmail.com*, ORCID: 0000-0002-7009-6218

MICROPLASMA POWDER CLADDING FOR THE REPAIR OF TURBINE MONOWHEELS MADE OF NICKEL-BASED HEAT-RESISTANT ALLOYS

Purpose. *Theoretical justification and experimental development of a technology for the restoration of turbine blades of an aircraft engine, manufactured using the “blisk” process from heat-resistant nickel alloys, via the additive micro-plasma powder cladding method (MPC).*

Research methods*. The study employed microplasma layer-by-layer powder cladding on the end faces of plates made of the ЖС32-ВИ alloy, using the specialised robotic system STARWELD 190H. The MPC process was carried out using direct current of positive polarity (currents of 2…50 A). High-purity argon was used as the plasma-forming and shielding gas. The dimensions of the test plates were115×15×2 mm. The cladding was carried out using a reciprocating motion. After cladding, the samples were subjected to heat treatment. The mechanical properties of the samples obtained by the additive growth method were determined on standard flat specimens.*

Results*. Following mechanical testing, the specimens exhibited the following properties: average tensile strength* σ *= 1147 MPa and plasticity* δ *= 9.5%, whilst the requirements of the standard specify* $\sigma_в \geq 882$ *MPa and* $\delta = 6.0\%$*. The fracture surfaces exhibited a medium-grained structure. No defects were observed in the fracture surfaces. The microstructure of the sample material prior to heat treatment consists of γ-solid solution containing an intermetallic γ′ phase, carbides, carbonitrides, and 5 μm-sized eutectic (γ-γ′) phase, which is characteristic of the as-cast condition of the ЖС32-ВИ alloy. The microstructure of the sample material after heat treatment corresponds to the normal state of the ЖС32-ВИ alloy.*

Scientific novelty*. When manufacturing turbine wheels by casting, one of the most serious problems is casting defects, such as cracks, porosity and cavities. The use of existing repair methods, which are based on welding or surfacing using argon arc welding, for example for blades, is limited by the high susceptibility of heat-resistant nickel alloys (ЖС3ДК, ВЖЛ12) to the formation of heat-fatigue cracks due to the high content of γ′ phase. The proposed repair technology involves cutting the blade down to the location of the defect and subsequently restoring the blade profile layer by layer using the additive micro-plasma cladding method.*

Practical value*. It has been established that the repair of aircraft engine turbine blades using the additive microplasma powder cladding method ensures high mechanical properties across the entire height of the grown blade without the occurrence of casting defects.*

Key words*: turbine wheel, additive microplasma cladding, powder, γ′-phase, mechanical properties, microstructure.*

DOI 10.15588/1607-6885-2026-2-9

Introduction

One of the main areas of development for gas turbine engines is the improvement of their specific performance, including a reduction in their mass and dimensions [1]. The turbine wheels of small gas turbine engines are usually manufactured using the «blisk» process, meaning that the wheel blades and the disc section are formed as a single component (Figure 1). With this construction, the total mass of the turbine wheel is reduced compared to wheels that use individual working blades [2, 3].

The turbine wheel of a small gas turbine engine, manufactured using the “blisk” process, operates under significant thermomechanical stresses (the operating temperature of the wheel blades ~ 950 °C, maximum rotational speed of the wheel is 39000 r/min), in an environment of high-temperature combustion products from aviation fuel. Due to these demanding operating conditions, turbine wheels are manufactured from heat-resistant nickel alloys using high-precision casting [4–7].

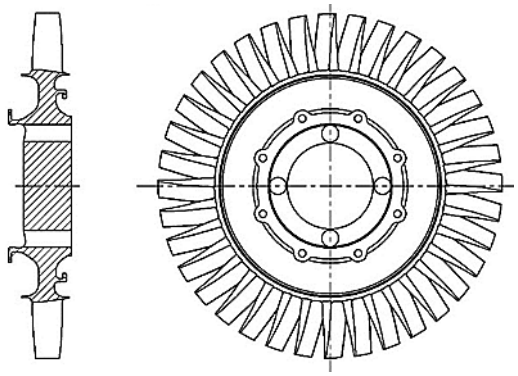

Figure 1. Turbine wheel manufactured using the “blisk” process

When manufacturing turbine wheels from heat-resistant nickel alloys ЖС3ДК and ВЖЛ12 using the casting process, difficulties arise due to the occurrence of casting defects such as cracks, porosity and cavities. It should be noted that most defects occur in the blades, particularly in the lower section near the base.

When attempting to repair such alloys using traditional methods, such as argon arc welding, cracks inevitably form in the heat-affected zone. The mechanisms behind their formation are varied: from liquation cracking during the welding process to strain-age cracking during subsequent heat treatment. This is due to the rapid kinetics of the precipitation of the strengthening phase $Ni_3(Al,Ti)$, which is accompanied by volume changes and a reduction in the material’s ductility during the relaxation of welding stresses [8].

Additive technologies, in particular microplasma powder cladding (MPC), represent a promising approach to addressing this task [9–12]. This method combines the precision of energy delivery characteristic of laser processes with the metallurgical ‘mildness’ and cost-effectiveness of arc processes. The aim of this work is a comprehensive study of the feasibility of using MPC for the repair of turbine blades made of the heat-resistant alloy ЖС32-ВИ, including the optimisation of cladding parameters and post-weld heat treatment regimes.

Analysis of research and publications

The problem of welding and cladding heat-resistant nickel alloys (superalloys) has remained a key focus for materials scientists over the past five decades. Scientific fundamental works laid the foundations for understanding the physical metallurgy of these materials. However, the main difficulty of the process lies in the fact that alloying aimed at improving high-temperature strength (increasing the volume fraction of the γ´- phase) has a diametrically opposite effect on weldability.

Alloy ЖС32-ВИ (analog to western alloys such as René and CMSX) belong to the class of dispersion-hardened materials. When heated above the solidus temperature (during welding), partial melting occurs along the grain boundaries in the heat-affected zone, caused by the presence of low-melting eutectics and the segregation of impurities (S, P etc.). During cooling, under the action of tensile thermal stresses, these liquid films open up, forming hot cracks [5, 13–15].

An even more insidious phenomenon is stress-induced ageing cracking. These cracks occur during post-weld heat treatment in the temperature range of 700…900°C. In this range, there is an intense precipitation of the secondary γ'-phase within the grains, which significantly strengthens their interior. If the grain boundaries remain relatively weak or have low ductility, the relaxation of residual stresses occurs not through plastic deformation, but through the formation of cracks along the grain boundaries.

A number of repair techniques are currently available for damaged components, each with its own advantages and disadvantages. The traditional method – argon arc welding – is widely used for repairing less alloyed alloys (e.g. Inconel 625, Inconel 718). However, for alloys with a γ'-phase content exceeding 40…50 % (which includes ЖС32), TIG welding is characterised by excessively high heat input. This leads to a wide heat-affected zone, grain growth and catastrophic cracking. Numerous studies confirm that the use of TIG welding to restore the aerodynamic profile of blades made from ЖС32 is impractical due to the low yield of serviceable parts [5, 14].

Laser technologies (laser metal deposition) ensure minimal heat input and high precision. However, high cooling rates (10^3…10^4 K/s) lead to the formation of non-equilibrium, hardened structures with high levels of internal stresses [2, 3, 14]. Furthermore, laser cladding is prone to porosity and lack of fusion if parameters are selected incorrectly, and is characterised by high equipment

DOI 10.15588/1607-6885-2026-2-9

and operating costs. Another issue is the anisotropy of properties and the need for strict control of particle size.

Electron beam welding ensures the highest metal purity, but requires a vacuum chamber, which limits productivity and part dimensions and makes it a challenging method for the layer-by-layer fabrication of complex geometries.

Microplasma powder cladding occupies a unique place. The use of a low-power compressed arc (currents of 2…50 A) allows for precise control of heat input, ensuring "gentle" mixing of the filler material with the base metal.

The works of the Ukrainian school of welding (E.O. Paton Electric Welding Institute), in particular those by K.A. Yushchenko, O.V. Yarovitsyn and others, have examined the physics of the MPC process in detail [9–12]. It has been shown that laminar plasma flow provides reliable protection of the molten pool against oxidation, which is critical for alloys containing active elements (Al, Ti, Hf).

Previous studies have demonstrated the successful use of MPC for repairing blade tip sections (build-up of up to 3…5 mm) [10, 11, 16, 17]. However, when repairing integral wheels, there is often a need to restore significantly larger volumes - for example, when cutting out a defect near the root of the blade, up to 45…50 mm of the profile to be restored. This shifts the task from the realm of «cosmetic repair» to that of «additive manufacturing on an existing substrate».

The issues of structural stability and properties during multi-layer cladding of such large volumes of the ЖС32-ВИ, as well as the selection of heat treatment regimes that would mitigate the effects of repeated thermal cycling, remain insufficiently studied. This work is specifically aimed at addressing these «gaps» in the technology.

Purpose of the study

The aim of this work is to provide a theoretical justification and experimental development of a technology for the repair of turbine blades in aircraft engines, manufactured using the «blisk» process from heat-resistant nickel alloys, by means of additive micro-plasma powder cladding.

To achieve the set objective, the following tasks must be addressed:

- to develop a methodology for the additive manufacturing of test specimens made from the ЖС32-ВИ alloy, which replicate the thermophysical conditions involved in restoring the blade profile;
- conduct a comparative analysis of the microstructure of the deposited metal in the original state and after various homogenisation annealing regimes;
- determine the effect of homogenisation temperature on the dissolution of non-equilibrium eutectic phases and prevent the formation of defects;
- to determine the mechanical properties (tensile strength, elongation) of the remanufactured metal and verify their compliance with the requirements of industry standards for cast materials;
- to investigate the failure mechanism of the remanufactured samples using fractography to confirm the absence of hidden defects of metallurgical origin.

Materials and methods

The high-temperature nickel alloy ЖС32-ВИ was selected as the subject of the study. It is one of the most advanced casting alloys for aircraft turbine blades, capable of operating at temperatures of up to 1050…1100°C.

The filler material used was spherical-shaped metal powder of the ЖС32-ВИ alloy, produced by vacuum induction gas atomisation in argon. The particle size distribution of the powder was 63…163 μm [9, 11, 12]. Choice of particle size was dictated by the requirements for a stable feed into the plasmatron: finer particles (<50 μm) are prone to agglomeration and "clogging", whilst larger ones (>160 μm) may not have time to melt completely in a low-power plasma arc.

The experimental work was carried out on a specialised robotic system the STARWELD 190H. The process MPC was performed using direct current of positive polarity (negative electrode). High-purity argon was used as the plasma-forming and shielding gas. To simulate blade repair, a strategy of layer-by-layer cladding on the end face of a plate made of the ЖС32-ВИ alloy was chosen. The plates measured 115×15×2 mm (Figure 2). The thickness of 2 mm corresponded to the average thickness of the turbine blade and vane in the repair zone. The cladding was carried out using a reciprocating motion.

Figure 2. Sample cutting plan

The mechanical properties of the specimens following heat treatment (T=1255±10°C for 1…1.5 hours), produced by additive manufacturing using microplasma powder cladding, were determined on standard flat specimens.

Results and discussion

The first stage of the study involved assessing the quality of the metal's formation immediately following the additive manufacturing process (original condition). A visual inspection of the surface of the deposited layers revealed satisfactory formation: consistent width, and no coarse burrs, undercuts or macro-cracks. The surface had

DOI 10.15588/1607-6885-2026-2-9

a characteristic structure resulting from the crystallisation of individual molten pools.

Analysis of cross-sectional micro-sections in the unetched state revealed the presence of scattered microporosity. The pores were predominantly spherical in shape, with a size not exceeding 20 μm (Figure 3). The spherical shape of the pores indicated that they were of gaseous origin. The most likely causes are either argon entrapped by powder particles during their production (gas atomisation) or microbubbles of shielding gas that entered the turbulent flows of the weld pool. It should be noted that, from the point of view of fracture mechanics, small spherical pores (up to 20…30 μm) are significantly less dangerous stress concentrators than flat oxide films or sharp hot cracks [2, 10].

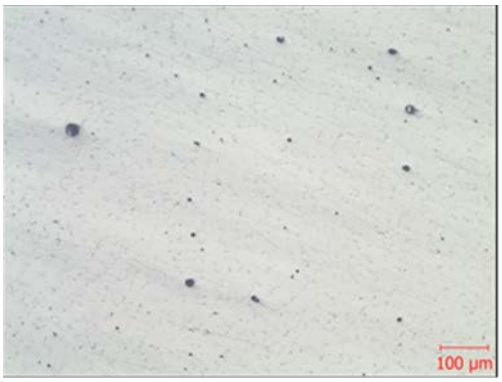

Figure 3. Microstructure of the deposited metal prior to etching

Etching revealed a dendritic structure resulting from directional crystallisation. The axes of the dendrites are predominantly oriented along the heat dissipation path (from bottom to top, away from the substrate). The microstructure of the samples prior to heat treatment consisted of a γ-solid solution containing an intermetallic γ´- phase, carbides and carbonitrides [3, 5, 6]. Particular attention was drawn to the presence of a eutectic (γ-γ´)- phase, ~5μm in size, in the inter-axial spaces of the dendrites, which is characteristic of the as-cast state of the ЖС32-ВИ alloy (Figure 4). This is a consequence of dendritic solidification, where elements with a partition coefficient k <1 (Al, Ti, Ta) are displaced by the crystallisation front into the liquid phase, enriching the final portions of the melt to the eutectic composition. It is precisely these zones that are potential weak points.

The samples were then subjected to heat treatment – homogenisation at T=1270±10°C for 1…1.5 hours. Homogenisation is necessary to equalise the chemical composition, dissolve non-equilibrium eutectics and form the optimal morphology of the strengthening γ´- phase.

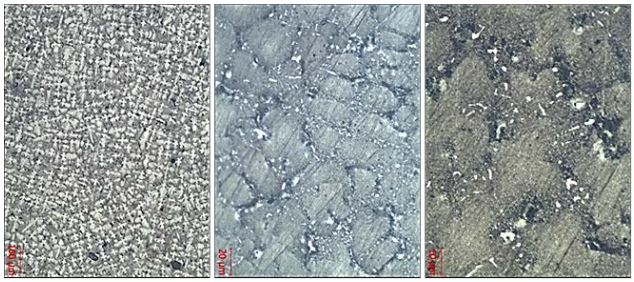

Figure 4. Microstructure of the deposited metal prior to heat treatment following etching

Metallographic analysis of samples after ageing at 1270°C revealed the presence of structural defects classified as “overheating” or “incipient melting” [3, 5, 7]. The microstructure photographs clearly show thickened grain boundaries and «islands» with traces of melting around former eutectic zones (Figure 5).

Figure 5. Microstructure of the deposited metal after heat treatment (homogenisation at T=1270±10°C)

Although the nominal solidus temperature of the ЖС32-ВИ alloy is higher than 1270°C, the deposited metal contains zones enriched with boron, carbon and liquidus elements as a result of non-equilibrium crystallisation. These localised zones have a significantly lower melting point. When heated to 1270 °C they turn to a liquid state. Upon subsequent cooling, the liquid crystallises in the form of brittle films or coarse eutectics, which drastically reduces the mechanical properties. Thus, this particular heating temperature is unacceptable for the deposited material without prior stepwise preparation.

To prevent the metal samples from overheating, the homogenisation temperature was reduced by 15 °C. Another series of samples underwent heat treatment – homogenisation at T=1255±10 °C for 1…1.5 hours. Decreasing the temperature by 15 °C allowed entry into the safe heat treatment interval. The structure after heating at 1255 °C was characterised by the absence of melting traces, a significant degree of solid solution homogenisation, a reduction in the number and size of non-equilibrium eutectics due to diffusion dissolution, and the formation of a regular γ-γ´ phase structure with a cuboid morphology, which is optimal for creep resistance and corresponds to the normal state of the ЖС32-ВИ alloy (Figure 6).

DOI 10.15588/1607-6885-2026-2-9

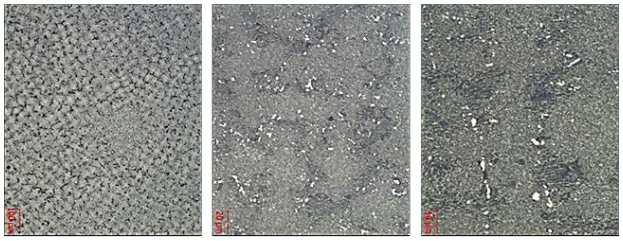

Figure 6. The microstructure of the deposited metal after heat treatment (homogenisation at T = 1255±10°C)

The results of the tensile strength tests on samples treated under optimal conditions are presented in the comparative table (Table 1).

The obtained results demonstrate that the properties of the deposited metal significantly exceed the minimum requirements. This is because rapid crystallisation during MPC resulted in a more dispersed structure compared to conventional casting, where slow cooling led to the formation of large dendrites and significant microporosity.

Table 1 – A comparative analysis of the mechanical properties of the remanufactured ЖС32-ВИ alloy and the relevant standards

Characte-ristics	Mean value (experi-ment, MPC)	Require-ments (casting, technical specifica-tions)	Deviation	Rating
Strength limit σ, MPa	1147	≥ 882	+ 30 %	excellent
Relative elongation δ, %	9.5	≥ 6.0	+ 58.3 %	excellent
Yield point $\sigma_{0,2}$, MPa *	931	-	-	-

** The yield point value is an estimate, based on the typical ratio for this class of alloys*

Examination of the fracture surfaces following rupture confirmed that metal was of a sufficiently high quality. The fracture had a matt grey hue, characteristic of ductile fracture. No defects such as lack of fusion between the cladding layers were detected (Figure 7), confirming the correct selection of the process's energy parameters (current, cladding rate).

Figure 7. Fracture patterns in specimens following tensile testing

Discussion

The obtained data made it possible to formulate a concept for the «blisk» blade remanufacturing process. The main point is to demonstrate that the MPC method can produce dense metal with properties not worse than those of cast metal, even at high build-up heights. It is important to note the role of heat treatment. In industrial conditions, higher heating temperatures (1280…1290 °C) are often used for cast blades to ensure complete dissolution of γ- phase. However, for metal formed by the MPC method, which has its own specific crystallisation characteristics, these temperatures are unacceptable [3, 5, 7]. It has been established that reducing the temperature to 1255°C is a necessary compromise that ensures a sufficient level of mechanical properties.

The economic benefits of implementing this technology are clear. The cost of a new turbine monowheel can run into tens of thousands of dollars. The cost of repair using the MPC method (powder + labour + heat treatment) amounts to 10…15% of the cost of a new part. Furthermore, this also resolves the issue of logistics and spare parts delivery times.

Conclusions

Based on the comprehensive research carried out, the following conclusions can be drawn:

1. The feasibility of using the additive MPC method to repair deep damage and fully restore the profile of the working blades of "blisk"-type turbine wheels made from the ЖС32-ВИ alloy has been confirmed.

2. The developed technology ensures the production of dense deposited metal. The residual microporosity does not exceed 20 μm, is spherical in shape and does not compromise the static strength. There are no cracks or lack of fusion..

3. The critical sensitivity of the deposited metal to the homogenisation temperature has been established. A temperature of 1270 °C is excessive and causes the eutectic phases to melt. The optimum condition has been determined to be T = 1255±10 °C (1…1.5 hours), which ensures the formation of the required microstructure.

4. The clad metal exhibits high mechanical strength (σ = 1147 MPa) and plasticity (δ = 9.5%), which significantly exceeds the specifications for the base material.

5. The results of this work form the basis for the development of standard operating procedures for the aircraft engine repair process, which will significantly extend the service life of the aircraft fleet.

References

1. Балушок К. (2024). Ремонт деталей авіаційних двигунів із жароміцних нікелевих сплавів із застосуванням адитивних технологій. Авіаційно-космічна техніка і технологія, № 5. DOI: https://doi.org/10.32620/aktt.2024.5.04

DOI 10.15588/1607-6885-2026-2-9

2. Sarkar R. et al. (2022). Additive manufacturing-based repair of IN718 superalloy and high-cycle fatigue assessment of the joint. *Additive Manufacturing*, 60, Part A, 103276. DOI: DOI: https://doi.org/10.1016/j.addma.2022.103276

3. Chen J. et al. (2025). Laser-based powder bed fusion of nickel-based superalloy designed specifically for turbine blades using high-power flat-top laser: Towards high-speed manufacturing and directional solidification. *Journal of Alloys and Compounds*, 1022(11), 179902. DOI: https://doi.org/10.1016/j.jallcom.2025.179902

4. Yarovytsyn O. V., Khuschchov H. D., Chyhileychik S.L. (2019). Estimation to optimize energy spent on a single welding pool creation in micro-plasma powder deposition process of JS32 nickel superalloy HPT blade`s bandage shelve. *International Journal of Mechanical and Production Engineering*, 7, 1, 5 IJMPE-IRAJ-DOI-14928.

5. Schulz F. et al. (2024). Gamma prime formation in nickel-based superalloy weld metal fabricated by laser beam welding. *Materials today Communications*, 38, 107905. DOI: https://doi.org/10.1016/j.mtcomm.2023.107905

6. Zhang G. et al. (2024). Research progress in repair and remanufacture of compressor blisk. *Journal of Aeronautical Materials*, 44(3). DOI: https://doi.org/10.11868/j.issn.1005-5053.2019.000153

7. China. (2023). *Integral heat treatment method for nickel-based high-temperature alloy leaf disc after laser additive repair* (Patent No. CN116944521A/B). China National Intellectual Property Administration.

8. Ющенко К. А. та ін. (2022). Дослідження і оптимізація процесу серійного ремонту робочих лопаток авіаційного газотурбінного двигуна Д-18Т микроплазмовим порошковим наплавленням. *Космічні матеріали та технології*, 28, 3, 3–16.

9. Cherviakov M., Yarovytsyn O., Khrushchov H. (2023). Expanding the Technological Possibilities of Multilayer Micro-Plasma Powder Deposition Process by Optimizing the Quality and Composition of Process Gases. *Science and Innovation*, 19(5), 89–99. DOI: https://doi.org/10.15407/scine19.05.089

10. Balushok K. et al. (2024). Developing technology of directed energy deposition of workpieces of parts of aircraft engines from heat-resistant nickel alloys by means of using layer-by-layer microplasma surfacing method. *Mechanics and Advanced Technologies*, 8, 2(101), 121–129. DOI: https://doi.org/10.20535/2521-1943.2024.8.2(101).296932

11. Yarovytsyn A. V. (2015). Energy approach in analysis of microplasma powder surfacing process parameters in restoration of blades of aircraft GTE. *The Paton Welding Journal*, 6, 28–34.

12. Yarovytsyn O.V. et al. (2024). Development and approval of the procedure of high-temperature uniaxial creep strength tests of difficult-to-weld high-temperature nickel alloys specimens with microplasma powder deposition. The Paton Welding Journal, 9, 29–37. DOI: https://doi.org/10.37434/tpwj2024.05.04

13. 10. Tan Q. et al. (2024). A review on cracking mechanism and suppression strategy in nickel-based superalloys during laser cladding. *Journal of Alloys and Compounds*, 1001. DOI: https://doi.org/10.1016/j.jallcom.2024.175164

14. Dmitrieva A. et al. (2023). Effect of the Laser Cladding Parameters on the Crack Formation and Microstructure during Nickel Superalloy. *Gas Turbine Engines Repair*. *Metals*, 13(2), 393.

15. Wang D. et al. (2024). A laser powder bed fusion-based methodology for repairing damaged nickel-based turbine blades. *Materials Characterization*, 212, 113948. DOI: https://doi.org/10.1016/j.matchar.2024.113948

16. Яровицін О. В., Чигилейчик С. Л. (2024). Формування критеріїв оцінки придатності застосування присадних матеріалів з нікелевих стопів у адитивних технологіях 3D-натоплення. *Металофізика та новітні технології*, 4, 129–149.

17. Yuschenko K.A. et al. (2017). Understanding the impact of oxygen and nitrogen content in metal powder on microplasma multilayers deposition of aircraft GTE blade edges. Proceedings of 9th International conference of young scientist on welding and related technologies, PWI NAS of Ukraine, 23–26 May, 257–261.

Received 09.04.2026
Accepted 22.04.2026
Published 07.05.2026

DOI 10.15588/1607-6885-2026-2-9

УДК 338:658.5

МІКРОПЛАЗМОВЕ ПОРОШКОВЕ НАПЛАВЛЕННЯ ДЛЯ РЕМОНТУ МОНОКОЛІС ТУРБІН ІЗ НІКЕЛЕВИХ ЖАРОМІЦНИХ СПЛАВІВ

Олександр Чечет — заступник начальника цеху, ОАО «Мотор Січ», Запоріжжя, Україна, *e-mail: Chechetalex1979@gmil.com*, ORCID: 0009-0003-2070-9885

Руслан Куликовський — канд. техн. наук, доцент, проректор з науково-педагогічної роботи та питань перспектив розвитку Національного університету «Запорізька політехніка», Запоріжжя, Україна, *e-mail: kulikovski@zp.edu.ua*, ORCID: 0000-0001-8781-2113

Сергій Чигілейчик — провідний науковий співробітник ДП ЗМКБ «Івченко-Прогрес», Запоріжжя, Україна, *e-mail: ChigileychikSL@ivchenkoprogress.com*, ORCID: 0000-0002-2372-9078

Юрій Торба — канд. техн. наук, заступник директора ДП ЗМКБ «Івченко-Прогрес», Запоріжжя, Україна, *e-mail: Torba.Yuriy@gmail.com*, ORCID: 0000-0001-8470-9049

Андрій Добровольський — провідний інженер ДП ЗМКБ «Івченко-Прогрес», Запоріжжя, Україна, *e-mail: dobrovolskiyj5@gmail.com*, ORCID: 0009-0007-8015-821X

Наталія Широкобокова — канд. техн. наук, доцент, Національний університет «Запорізька політехніка», Запоріжжя, Україна, *e-mail: nsonik11@gmail.com*, ORCID: 0000-0002-7009-6218

Мета роботи. *Теоретичне обґрунтування та експериментальна розробка технології відновлення робочих лопаток колеса турбіни авіаційного двигуна, виконаного за технологією «бліск» із жароміцних нікелевих сплавів, методом адитивного мікроплазмового порошкового наплавлення (МПН).*

Методи дослідження. *В ході дослідження було застосовано метод пошарового порошкового наплавлення з використанням мікроплазми на торцеві поверхні пластин зі сплаву ЖС32-ВИ за допомогою спеціалізованої роботизованої системи STARWELD 190H. Процес МПН здійснювався з використанням постійного струму позитивної полярності (силою струму 2…50 А). В якості плазмоутворюючого та захисного газу використовували аргон високої чистоти. Розміри експериментальних пластин становили 115×15×2 мм. Наплавлення здійснювали з використанням зворотно-поступального руху. Після наплавлення зразки піддавали термічній обробці. Механічні властивості зразків, отриманих методом адитивного нарощування, визначали на стандартних плоских зразках.*

Отримані результати. *Після механічних випробувань зразки мали наступні властивості: середні значення міцності $\sigma_в$=1147 МПа, пластичності δ= 9,5 %, при вимогах нормативної документації $\sigma_в \geq 882$ МПа, δ= 6,0 %. Злами мали середньо-кристалічну структуру. Дефекти у зламах не виявлено. Мікроструктура матеріалу зразків до термообробки являє собою γ- твердий розчин з наявністю інтерметалідної γ′-фази, карбідів, карбонітридів, а також евтектичної (γ-γ′) - фази розміром 5мкм, яка характерна для литого стану сплаву ЖС32-ВИ. Мікроструктура матеріалу зразків після термообробки відповідає нормальному стану сплаву ЖС32-ВИ.*

Наукова новизна. *При виготовленні коліс турбін методом лиття одна з найсерйозніших проблем – це ливарні дефекти, такі як тріщини, пористість, раковини. Використання існуючих методів ремонту, які основані на зварюванні або наплавленні методом аргонодугового зварювання, наприклад для лопаток, обмежені високою схильністю жароміцних нікелевих сплавів (ЖС3ДК, ВЖЛ12) до появи термовтомних тріщин через високий вміст γ′-фази. Запропонована технологія ремонту полягає у зрізанні лопатки до місця розташування дефекту і подальшому пошаровому відновленню профіля лопатки методом адитивного мікроплазмового наплавлення.*

Практична цінність. *Встановлено, що відновлення колеса турбіни авіаційних двигунів методом адитивного мікроплазмого порошкового наплавлення забезпечує високі механічні властивості по всій висоті вирощеної лопатки без виникнення дефектів лиття.*

Ключові слова: *колесо турбіни, адитивне мікроплазмове наплавлення, порошок, γ′-фаза, механічні властивості, мікроструктура.*

DOI 10.15588/1607-6885-2026-2-9

Список літератури

1. Балушок К., Чигілейчик С. Ремонт деталей авіаційних двигунів із жароміцних нікелевих сплавів із застосуванням адитивних технологій. *Авіаційно-космічна техніка і технологія*. 2024. № 5. DOI: https://doi.org/10.32620/aktt.2024.5.04

2. Additive manufacturing-based repair of IN718 superalloy and high-cycle fatigue assessment of the joint / R. Sarkar et al. *Additive Manufacturing*. 2022. Vol. 60. Part A. 103276. DOI: https://doi.org/10.1016/j.addma.2022.103276

3. Laser-based powder bed fusion of nickel-based superalloy designed specifically for turbine blades using high-power flat-top laser: Towards high-speed manufacturing and directional solidification / J. Chen et al. *Journal of Alloys and Compounds*. 2025. Vol. 1022(11). 179902. DOI: https://doi.org/10.1016/j.jallcom.2025.179902

4. Yarovytsyn O. V., Khuschchov H. D., Chyhileychik S. L. Estimation to optimize energy spent on a single welding pool creation in micro-plasma powder deposition process of JS32 nickel superalloy HPT blade`s bandage shelve. *International Journal of Mechanical and Production Engineering*. Vol. 7. Issue 1. Jan. 2019. 5 p. IJMPE-IRAJ-DOI-14928.

5. Gamma prime formation in nickel-based superalloy weld metal fabricated by laser beam welding Schulz F. et al. *Materialstoday Communications*. 2024. Vol. 38. 107905. DOI: https://doi.org/10.1016/j.mtcomm.2023.107905

6. Research progress in repair and remanufacture of compressor blisk / G. Zhang, et al. *Journal of Aeronautical Materials*. 2024. Vol. 44(3). DOI: https://doi.org/10.11868/j.issn.1005-5053.2019.000153

7. Integral heat treatment method for nickel-based high-temperature alloy leaf disc after laser additive repair: пат. CN116944521A/B China. № CN202310971641.0A; заявл. 03.08.2023; опубл. 27.10.2023.

8. Дослідження і оптимізація процесу серійного ремонту робочих лопаток авіаційного газотурбінного двигуна Д-18Т микроплазмовим порошковим наплавленням / Ющенко К. А. та ін. *Космічні матеріали та технології*. 2022. Т. 28. № 3. С. 3–16.

9. Cherviakov M., Yarovytsyn O., Khrushchov H. Expanding the Technological Possibilities of Multilayer Micro-Plasma Powder Deposition Process by Optimizing the Quality and Composition of Process Gases. *Science and Innovation*. 2023. 19(5). P. 89–99. DOI: https://doi.org/10.15407/scine19.05.089

10. Developing technology of directed energy deposition of workpieces of parts of aircraft engines from heat-resistant nickel alloys by means of using layer-by-layer microplasma surfacing / Balushok K. et al. *Mechanics and Advanced Technologies*. 2024. Vol. 8. № 2(101). P. 121–129. DOI: https://doi.org/10.20535/2521-1943.2024.8.2(101).296932

11. Yarovytsyn A.V. Energy approach in analysis of microplasma powder surfacing process parameters in restoration of blades of aircraft GTE. *The Paton Welding Journal*. 2015. № 6. С. 28–34.

12. Development and approval of the procedure of high-temperature uniaxial creep strength tests of difficult-to-weld high-temperature nickel alloys specimens with microplasma powder deposition Yarovytsyn O.V. et al. *The Paton Welding Journal*. 2024. № 9. С. 29–37. DOI: https://doi.org/10.37434/tpwj2024.05.04

13. A review on cracking mechanism and suppression strategy in nickel-based superalloys during laser cladding / Tan Q. et al. *Journal of Alloys and Compounds*. 2024, Vol. 1001 . DOI: https://doi.org/10.1016/j.jallcom.2024.175164

14. Effect of the Laser Cladding Parameters on the Crack Formation and Microstructure during Nickel Superalloy / Dmitrieva A. et al. *Gas Turbine Engines Repair. Metals*. 2023. 13(2). 393 p.

15. Wang D. et al. A laser powder bed fusion–based methodology for repairing damaged nickel-based turbine blades. *Materials Characterization*. 2024. Vol. 212. 113948. DOI: https://doi.org/10.1016/j.matchar.2024.113948

16. Яровицін О. В., Чигилейчик С. Л. Формування критеріїв оцінки придатності застосування присадних матеріалів з нікелевих стопів у адитивних технологіях 3D-натоплення. *Металофізика та новітні технології*. 2024. № 4. С. 129–149.

17. Understanding the impact of oxygen and nitrogen content in metal powder on microplasma multilayers deposition of aircraft GTE blade edges. Proceedings of 9th International conference of young scientist on welding and related technologies / Yuschenko K. A. et al. PWI NAS of Ukraine, 23–26 May 2017. P. 257–261.

DOI 10.15588/1607-6885-2026-2-9

UDC 621.791.75:621.7.01

Denys Molochkov — PhD, Senior Lecturer, Department of Integrated Technologies of Electronic Devices, National University Zaporizhzhia Polytechnic, Zaporizhzhia, Ukraine, *e-mail: molochkov@zp.edu.ua*, ORCID: 0000-0002-9030-5371

Kyrylo Krasnoselsky — PhD student of the Department of Integrated Welding Technologies and Structural Modeling, National University Zaporizhzhia Polytechnic, Zaporizhzhia, Ukraine, *e-mail: kvkras@gmail.com*, ORCID: 0009-0006-5251-9076

SHIELDING GAS OXIDATION EFFECTS ON GEOMETRY AND ENERGETICS IN WIRE ARC DEPOSITION OF HIGH-STRENGTH STEEL

Purpose. *To establish the regularities of the influence of carbon dioxide concentration (0-100% CO_2) in an argon-based shielding mixture on the external macrogeometry (width, height, waviness) and energetic parameters of low-heat-input thin-wall formation from high-strength low-alloy (HSLA) MoNiVa steel using robotic Cold Metal Transfer (CMT) additive manufacturing.*

Research methods. *The studies were conducted using a robotic system with a Fronius TPSi power source (CMT mode, WFS = 2.0 m/min, TS = 35 cm/min). To eliminate subjective errors and analyze the stochastic macrogeometry, a computer vision method (OpenCV) based on pixel-by-pixel integration of optical scans (600 DPI, absolute error of 0.045 mm) was developed. Synchronizing geometric metrics with high-frequency (10 Hz) data logging of arc energetic parameters allowed for the evaluation of Volumetric Energy Density (VED).*

Results. *A fundamental scale effect was observed during thin-wall deposition. Monogas environments proved technologically unviable: 100% argon induced severe internal porosity due to molten pool viscosity and rapid freezing, while 100 % CO_2 caused spatial meandering, hydrodynamic collapse, and a catastrophic 45 % loss of cross-sectional area. An exceptionally stable technological window was identified strictly within 5–18% CO_2, where the coefficient of variation (CV) for the width was minimized (1.30–1.87%) and a proportional bead form factor was maintained.*

Scientific novelty. *For the first time, a thermohydrodynamic "scale effect" in WAAM of complex HSLA steels is formalized, proving that under low-heat-input conditions, active gas additions do not improve wetting but rather trigger rapid crystallization and oxide barrier formation. The "energy paradox" of the process is mathematically proven: despite the 100% CO_2 mode having the lowest linear heat input (205.5 J/mm) due to synergic current suppression, it requires the highest Volumetric Energy Density (2.09 kJ/cm³) owing to critical mass transfer deterioration.*

Practical value. *The identified technological window (5-18% CO_2) and the formalized energy balance for MoNiVa thin-wall structures serve as a ready-to-use foundation for minimizing geometric defects and maximizing energy efficiency in production. The developed machine vision algorithm is suitable for implementation in closed-loop WAAM control systems for predictive real-time parameter adjustment.*

Key words*: Wire Arc Additive Manufacturing, WAAM, Cold Metal Transfer, CMT, high-strength steel, MoNiVa, shielding gas, volumetric energy density, computer vision.*

Introduction

Wire Arc Additive Manufacturing (WAAM) is currently considered one of the most promising areas of metal 3D printing for large-scale objects tailored to the needs of the aerospace and heavy engineering industries. Its main advantages are high deposition rates, relatively low equipment costs, and the ability to use standard commercial welding wires. Of particular interest to the industry is the printing of parts from high-strength low-alloy (HSLA) steels, particularly those alloyed with molybdenum, nickel, and vanadium (MoNiVa system), which provide a unique combination of strength, toughness, and cold resistance.

However, the main drawback hindering the mass adoption of WAAM is the low dimensional accuracy and significant waviness of the side surfaces of the deposited walls. Since the process relies on free-form deposition, controlling the final dimensions of the part comes down to managing the hydrodynamics of the liquid weld pool. Deviations from the specified geometry require significant allowances for subsequent machining, which negates the economic benefits of the additive approach.

Problem statement

Unlike traditional welding, in WAAM, the bead shape is formed exclusively as a result of the evolution of the liquid metal pool under the influence of surface tension forces, viscous friction, and electrodynamic forces. Traditionally, kinematic parameters such as wire feed speed (WFS) and travel speed (TS) are used to control the geometry. The shielding gas is mostly considered a passive element for isolating the molten pool. However, changing its composition, in particular by adding active carbon dioxide (CO_2), alters the oxidation potential of the plasma and the

DOI 10.15588/1607-6885-2026-2-10

rheology of the molten pool, making it a fully-fledged independent tool for influencing shape formation, which remains understudied for steels with complex alloying systems.

Analysis of research and publications

The current state of development of additive technologies shows that the product geometry in WAAM is determined by the evolution of the metal pool under a moving heat source. Unlike processes with a strictly localized molten pool of small volume (e.g., laser powder bed fusion), shape accuracy in arc deposition must be considered as a complex problem of unsteady thermohydrodynamics with a free surface [1, 2]. The final bead shape results from the interaction of surface tension forces, viscous friction, gravity, droplet transfer momentum, and the overall thermal state of the molten pool [3-5]. Most studies prove that the key factors of geometric stability are heat input, deposition strategy, and the metal transfer algorithm [6]. However, the shielding gas is often still considered primarily as a passive technological parameter to ensure arc stability and protection from the atmosphere [7]. In recent years, the paradigm has been changing. Studies show that the gas environment should be considered an active shape control tool [8, 9]. Changing the gas composition affects not only the electrical and spatial characteristics of the arc discharge but also the surface state of the pool, the nature of convective flows, and the lifetime of the liquid phase. The fundamental basis for this approach was formed in studies of weld pool physics, which proved that Marangoni thermocapillary flows have a decisive influence on the deposition geometry [3, 4]. The magnitude and direction of these flows are determined by the sign and modulus of the surface tension temperature gradient. When using pure argon, the temperature gradient is negative, which initiates centrifugal molten pool flows from the center of the pool to its edges, resulting in relatively wide but shallow penetration. However, the addition of carbon dioxide is accompanied by its dissociation in the arc and the supply of surface-active oxygen to the liquid metal. As proven in classical works, even minor additions of active gas turn the surface tension gradient positive, initiating powerful centripetal flows that pull the molten pool toward the center and downwards, radically changing the macrogeometry and heat redistribution [3, 4]. Specifically for WAAM, the impact of gas mixtures has become the subject of empirical research only recently. In particular, studies for low-carbon and stainless steels demonstrate that changing the Ar/CO_2 ratio affects layer geometry, spatter, and surface roughness [10-14]. However, most of these studies analyze specific “ready-made” industrial mixtures rather than the systematic variation of the CO_2 fraction as a control parameter. Furthermore, they focus mostly on the materials science aspect (microstructure), bypassing mechanical interpretation through changes in the hydrodynamic field and energy efficiency. A specific challenge that currently remains ignored is the use of high-strength low-alloy (HSLA) steels in WAAM [15]. The application of complex alloyed steels (like MoNiVa) introduces an additional level of thermodynamic complexity. Alloying elements (especially molybdenum and vanadium) combined with an active gas can form complex refractory oxide films on the pool surface. Unlike simple silicate slags in ordinary steels, these films locally alter molten pool viscosity, acting as a mechanical barrier that restricts spreading and impairs interlayer wetting. Conversely, synergic algorithms of modern power sources (such as CMT) automatically change the current to compensate for gas dissociation, directly affecting the specific energy intensity of the process.

Furthermore, current theoretical frameworks of Marangoni thermocapillary flows in WAAM are predominantly based on high-heat-input regimes (thick-wall deposition) with a massive molten pool. The extrapolation of these rules to low-heat-input, thin-wall structures – where the pool volume is minimal and cooling rates are extreme – remains a critical gap in the literature. It is unclear whether the active gas additions can effectively trigger centripetal spreading before the small pool completely solidifies, especially for highly viscous alloys like MoNiVa.

Thus, the current scientific literature lacks an integrated approach combining a systematic analysis of the impact of the full spectrum of CO_2 concentrations (0–100 %) on macrogeometric stability and the energy balance of free-form deposition specifically for HSLA steels with complex molten pool rheology, which justifies the relevance of this study.

Purpose of the work

To establish the regularities of the influence of active carbon dioxide concentration (from 0% to 100%) in a mixture with argon on the macrogeometric stability, stochastic waviness, bead form factor, and specific volumetric energy density of low-heat-input thin-wall deposition of high-strength low-alloy MoNiVa steel using the robotic Cold Metal Transfer process.

Material and methods of research

To implement the experimental part of the work, a specialized robotic additive manufacturing complex was used. The kinematic system was based on a six-axis industrial manipulator Yaskawa MH1440. An inverter welding system, Fronius TPS500i, equipped with a hardware module for the CMT (Cold Metal Transfer) technology, was used as the power source. The choice of the CMT algorithm is due to its ability to minimize heat input through high-frequency reciprocating wire movement, which ensures mechanical droplet detachment at reduced short-circuit currents. This is critical for multi-layer 3D printing, where heat accumulation is the main cause of geometric wall degradation.

A solid welding wire with a diameter of 1.2 mm made of high-strength low-alloy (HSLA) steel with an Mn-Ni-

DOI 10.15588/1607-6885-2026-2-10

Mo-V alloying system was used. The presence of molybdenum and vanadium provides high strength but significantly changes the molten pool rheology, increasing its viscosity and tendency to form refractory oxide films in the presence of active gases. Deposition was carried out on S355 structural steel substrates.

Kinematic parameters were specifically optimized for low-heat-input thin-wall deposition: the wire feed speed (WFS) was set to 2.0 m/min, and the travel speed (TS) was reduced to 35 cm/min to stabilize pool hydrodynamics. The contact tip to work distance (CTWD) was 13 mm, and the torch tilt angle was 0 degrees. Shielding gas flow was maintained at 14 L/min. To investigate the oxidation potential, a gradient of gas mixtures from 100 % Ar to 100 % CO_2 was applied (including intermediate values of 5, 10, 15, 20, and 25 % CO_2). The process involved depositing 20 consecutive layers. To isolate the effect of thermal accumulation, a strict temperature control protocol was applied, ensuring an interpass temperature of 85±10 °C.

To eliminate subjective human factors in measuring the stochastic macrogeometry, a software package based on the OpenCV computer vision library (Python) was developed. Transverse macrosections were digitized using an optical scanner at 600 DPI (pixel size 0.0423 mm). The algorithm included Gaussian filtering, Otsu's adaptive binarization, and morphological closing. To eliminate edge effects, the algorithm automatically cropped 3.0 mm from the top and bottom bounds. For the stabilized central zone, the exact cross-sectional area (F) was calculated via pixel-by-pixel integration. Horizontal scanning determined the effective width, width extremes, standard deviation, and coefficient of variation (CV). Additionally, the algorithm calculated the geometrical Form Factor (φ) as the ratio of the average bead width to the average layer height. Hardware validation via a 10 mm reference standard confirmed an absolute error of 0.045 mm.

Energetic parameters (welding current I, arc voltage U) were recorded via the power source's built-in data logger at 10 Hz. A script extracted stationary process segments. Linear heat input (HI) and Volumetric Energy Density (VED, kJ/cm³) were subsequently calculated by integrating the energetic logs with the cross-sectional area extracted by the computer vision system.

Research results

Initial trials utilizing 100% argon shielding were deemed unsuccessful due to the active formation of internal porosity within the deposited bead. Consequently, pure argon was excluded from further systematic quantitative analysis, and the study focused on the gradient of CO_2-Ar mixtures.

Precision analysis of the cross-sectional macro-geometry revealed a strict, linear degradation of the thin-wall profiles as the CO_2 concentration increased (Figure 1). In the range of 5% to 25% CO_2, a gradual decrease in mass transfer was observed: the total wall height dropped from 33.78 mm to 29.93 mm, while the corresponding average layer height decreased from 1.689 mm to 1.496 mm. This was accompanied by a linear reduction in the cross-sectional area (F) from 178.73 mm² to 139.73 mm². However, the transition to 100 % CO_2 resulted in a catastrophic drop in geometric indicators (Table 1). The cross-sectional area plummeted to 98.22 mm², representing a 45% loss of material compared to the 5 % CO_2 baseline, while the total height collapsed to 20.36 mm.

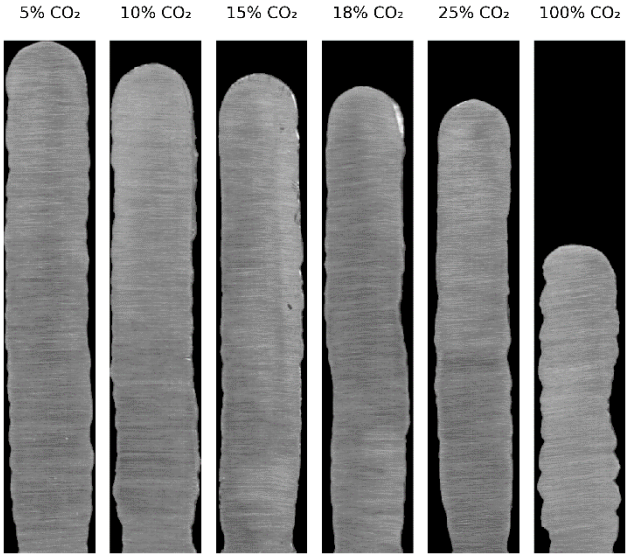

Figure 1. Macrogeometric profiles and calculated contours of the deposited MoNiVa walls as a function of CO_2 concentration

The average wall width exhibited a slightly different trend. The maximum width was recorded at 5–10 % CO_2 (5.46 mm). As the active gas fraction increased to 25 %, the bead gradually narrowed to 4.86 mm. Interestingly, at 100 % CO_2, the average width marginally increased to 4.96 mm, which, as subsequent visual analysis showed, was an artifact of severe spatial instability rather than uniform spreading. Statistical processing of the digitized bead masks provided an objective metric for assessing process stability. For the MoNiVa alloy system under thin-wall deposition parameters, an exceptionally stable technological window was identified in the range of 5–18 % CO_2. Within this zone, the coefficient of variation (CV) for the wall width was exceptionally low, ranging from 1.30 % to 1.87 % (Table 1), indicating near-perfect layer-by-layer reproducibility. A progressive collapse of stability occurred at higher CO_2 concentrations. The transition to pure carbon dioxide caused the CV to surge to 4.90 %. Macroscopic evaluation of the wall surface at 100 % CO_2 (Figure 2) demonstrated severe spatial meandering of every single bead. This longitudinal wandering led to a complete disruption of interlayer cohesion and the formation of deep interpass valleys, directly causing the aforementioned drop in total height and area.

DOI 10.15588/1607-6885-2026-2-10

Table 1 – Energetic and geometric indicators of the MoNiVa WAAM process (WFS = 2.0 m/min, TS = 35 cm/min)

Shielding gas mixture	I average, A	U average, V	P average, W	HI, J/mm	Cross-sectional area F, mm²	VED, kJ/cm³
5% CO_2	94,5	11,9	1508,5	258,6	178,73	1,45
10% CO_2	93,0	12,5	1540,4	264,1	171,13	1,54
15% CO_2	92,0	12,7	1543,2	264,5	163,20	1,62
18% CO_2	83,6	13,0	1398,3	239,7	152,59	1,57
25% CO_2	77,5	13,5	1335,8	229,0	139,73	1,64
100% CO_2	66,3	14,2	1198,5	205,5	98,22	2,09

Figure 2. Top view of the 100 % CO_2 deposited wall with severe spatial meandering

This degradation was further confirmed by the Form Factor anomaly (φ), calculated as the ratio of average width to average layer height. Within the 5–25 % CO_2 technological window, the Form Factor remained stable between 3.23 and 3.38. However, at 100 % CO_2, this indicator anomalously spiked to 4.87, serving as a mathematical reflection of the severe height collapse and erratic material deposition.

High-frequency data logging of the CMT power source parameters captured a pronounced electrical adaptation to the shielding gas effect on the process. While the wire feed speed was strictly fixed at 2.0 m/min, increasing the CO_2 concentration forced the equipment to elevate the average arc voltage from 11.9 V to 14.2 V. Simultaneously, the synergic control loop drastically suppressed the average welding current, which dropped from 94.5 A (at 5 % CO_2) to 66.3 A (at 100 % CO_2). This cyber-physical feedback directly impacted the energy balance. Contrary to expectations, the lowest linear heat input (HI) was recorded in the 100 % CO_2 environment (205.5 J/mm), whereas the optimal 10–15 % CO_2 mixtures generated approximately 264.1–264.5 J/mm. However, integrating the heat input with the cross-sectional area exposed an extreme peak in the Volumetric Energy Density (VED). The 100 % CO_2 mode required the highest amount of energy to build one cubic centimeter of metal –2.09 kJ/cm³ – compared to just 1.45 kJ/cm³ for the 5% CO_2 mixture.

Discussion

The complete failure to produce a defect-free thin wall in a 100 % argon atmosphere highlights the unique rheological challenges of HSLA steels. In pure argon, the absence of surface-active oxygen leads to a negative surface tension temperature gradient, driving centrifugal Marangoni flows. More critically, alloying elements such as molybdenum and nickel significantly increase the kinematic viscosity of the MoNiVa molten pool. In thin-wall deposition, the small pool volume cools and solidifies extremely fast. Without the “fluxing” and viscosity-reducing effects of an active gas, evolving gases (such as hydrogen) become trapped within the rapidly freezing viscous molten pool, inevitably resulting in the severe internal porosity observed during the initial trials.

A crucial finding of this study is the identified “scale effect” of heat input on the thermohydrodynamics of the molten pool. Previous theoretical frameworks regarding WAAM of carbon steels suggest that adding CO_2 improves wetting and spreading by generating active oxygen, which shifts the Marangoni flow from centrifugal to centripetal. However, our data on thin-wall structures (WFS = 2.0 m/min) proves the opposite. Under conditions of low overall heat input, the high energy demand for CO_2 dissociation drastically shortens the lifetime of the liquid phase. The molten pool “freezes” too rapidly, crystallizing before the centripetal thermocapillary flows can fully activate and redistribute the metal. Consequently, active gas additions on thin walls do not improve lateral spreading, leading instead to the observed linear degradation of the cross-sectional area. The catastrophic 45 % loss of cross-sectional area and the total loss of geometric stability (CV = 4.90 %) at 100% CO_2 are directly attributed to the complex chemical rheology of MoNiVa steel. In highly oxidizing environments, refractory oxide films of molybdenum and vanadium form instantaneously on the pool surface. Unlike simple silicate slags, these films act as a rigid mechanical shell that completely blocks interlayer wetting.

This oxide barrier, combined with the lowest heat input dictated by the CMT synergic loop, creates a molten pool with extreme viscosity. As a result, a phenomenon of severe longitudinal meandering occurs. The highly constricted arc column wanders across the pool surface searching for conductive pathways, but the viscous, oxide-covered metal cannot flow quickly enough to follow the heat source. This disconnect between the arc pressure and fluid flow tears the molten pool stream apart, triggering Rayleigh-Plateau hydrodynamic instability.

DOI 10.15588/1607-6885-2026-2-10

The recorded electrical logs – where voltage increased to 14.2 V and current plummeted to 66.3 A at 100% CO_2 – perfectly illustrate the thermodynamics of gas dissociation. The endothermic breakdown of polyatomic CO_2 molecules extracts significant heat from the arc, constricting its plasma column. To maintain a stable discharge against this cooling effect, the power source naturally elevates the voltage. To compensate for this voltage spike, the cyber-physical CMT algorithm drastically suppresses the average welding current along a strict inverse vector.

In standard GMAW processes, the current is intrinsically linked to the actual wire melting rate. We hypothesize that the synergic self-regulation of the CMT power source, by dropping the current so aggressively, effectively reduced the actual deposition rate despite the programmed WFS. This hidden drop in productivity, coupled with massive spatter caused by the arc deflecting off the oxide shell, fully explains the extreme metal deficit. Therefore, the anomalous jump of the Form Factor (φ) to 4.87 is not an indicator of a successfully flattened bead, but rather a mathematical proof of a "failed humping" effect: the spatial wandering and spatter prevented vertical buildup, leaving a disjointed track with a microscopic average layer height.

These interconnected phenomena culminate in the fundamental "energy paradox" of thin-wall WAAM. The 100% CO_2 mode exhibited the lowest linear heat input (HI = 205.5 J/mm). In traditional welding, lower heat input is often associated with better process control. However, in this free-form additive process, the constricted arc, impenetrable oxide barriers, and massive vaporization rendered the mode utterly unprofitable. The Volumetric Energy Density reached its maximum (VED = 2.09 kJ/cm³), meaning the highest amount of energy was wasted per cubic centimeter of successfully deposited metal.

In conclusion, this study establishes strict boundaries of technological robustness for precision thin-wall WAAM of complexly alloyed HSLA steels like MoNiVa. Monogas shielding is fundamentally unviable: 100% argon induces porosity due to high viscosity and gas trapping, while 100% CO_2 triggers severe meandering, spatter, and hydrodynamic collapse. The optimal balance between molten pool viscosity, surface tension, and heat input is strictly confined to a narrow technological window of 15–18 % CO_2, where perfect synergy between droplet transfer and mass assimilation is achieved.

Conclusions

This study establishes that the shielding gas oxidation potential is a critical factor governing the thermohydrodynamics of low-heat-input thin-wall WAAM for complex HSLA MoNiVa steels. A fundamental "scale effect" was identified, which inverses the typical influence of active shielding gases observed in massive depositions. Specifically, monogas environments proved technologically unviable for this alloy: 100 % argon induces severe internal porosity due to high molten pool viscosity and the rapid freezing of the small pool volume, whereas 100 % CO_2 triggers hydrodynamic collapse. The highly oxidizing environment leads to the formation of rigid, impenetrable Mo-V oxide films, manifesting as severe spatial meandering and a catastrophic 45% loss of cross-sectional area (dropping to 98.22 mm²).

Conversely, precision computer vision analysis statistically justified an exceptionally stable technological window strictly within the range of 5–18% CO_2. Within this gradient, the deposition achieves ideal layer-by-layer geometric reproducibility with minimal stochastic waviness, maintaining a coefficient of variation between 1.30 % and 1.87 % alongside a proportional and predictable bead form factor.

Furthermore, these geometric transformations are inextricably linked to the formalized "energy paradox" of the cyber-physical CMT process. To compensate for the endothermic dissociation in pure CO_2, the synergic loop drastically suppresses the average current to 66.3 A, resulting in the lowest linear heat input of 205.5 J/mm. However, due to massive material loss and spatter, this mode is actually the least energetically efficient, driving the Volumetric Energy Density to a maximum of 2.09 kJ/cm³. Ultimately, optimal energy efficiency (1.45–1.62 kJ/cm³) and stable mass transfer are achieved exclusively at 5–15 % CO_2, proving that gas chemistry and molten pool rheology, rather than electrical power alone, fundamentally dictate the geometric and economic viability of the thin-wall WAAM process.

References

1. Zhang, H., Li, R., Liu, J., Wang, K., Qiu, W., Shi, L., & et al. (2024). State-of-art review on the process-structure-properties-performance linkage in wire arc additive manufacturing. Virtual and Physical Prototyping, 19(1), e2390495. https://doi.org/10.1080/17452759.2024.2390495

2. Jafari, D., Vaneker, T. H. J., & Gibson, I. (2021). Wire and arc additive manufacturing: Opportunities and challenges to control the quality and accuracy of manufactured parts. Materials & Design, 202, 109471. https://doi.org/10.1016/j.matdes.2021.109471

3. Wang, Y., & Tsai, H. L. (2001). Effects of surface active elements on weld pool fluid flow and weld penetration in gas metal arc welding. Metallurgical and Materials Transactions B, 32, 501–515. https://doi.org/10.1007/s11663-001-0035-5

4. Lu, S., Fujii, H., & Nogi, K. (2004). Marangoni convection and weld shape variations in Ar-O_2 and Ar-CO2 shielded GTA welding. Materials Science and Engineering: A, 380(1-2), 290–297. https://doi.org/10.1016/j.msea.2004.05.057

5. Wu, F., Falch, K. V., Guo, D., English, P., Drakopoulos, M., & Mirihanage, W. (2020). Time evolved force domination in arc weld pools. Materials & Design, 190, 108534. https://doi.org/10.1016/j.matdes.2020.108534

6. Cunningham, C. R., Flynn, J. M., Shokrani, A., Dhokia, V., & Newman, S. T. (2018). Strategies and processes for high quality wire arc additive manufacturing. Additive Manufacturing, 22, 672–686. https://doi.org/10.1016/j.addma.2018.06.020

DOI 10.15588/1607-6885-2026-2-10

7. Kah, P., & Martikainen, J. (2013). Influence of shielding gases in the welding of metals. The International Journal of Advanced Manufacturing Technology, 64 (9–12), 1411–1421. https://doi.org/10.1007/s00170-012-4111-6

8. Teixeira, F. R., Jorge, V. L., Scotti, F. M., Siewert, E., & Scotti, A. (2024). A methodology for shielding-gas selection in wire arc additive manufacturing with stainless steel. Materials, 17(13), 3328. https://doi.org/10.3390/ma17133328

9. Silwal, B., Pudasaini, N., Roy, S., Murphy, A. B., Nycz, A., & Noakes, M. W. (2022). Altering the supply of shielding gases to fabricate distinct geometry in GMA additive manufacturing. Applied Sciences, 12(7), 3679. https://doi.org/10.3390/app12073679

10. Yamaguchi, M., Komata, R., Furumoto, T., Abe, S., & et al. (2022). Influence of metal transfer behavior under Ar and CO_2 shielding gases on geometry and surface roughness of single and multilayer structures in GMAW-based wire arc additive manufacturing of mild steel. The International Journal of Advanced Manufacturing Technology. https://doi.org/10.1007/s00170-021-08231-8

11. Kanishka, K., Acherjee, B., & et al. (2025). A study on the effect of shielding gases on the GMAW-WAAM process and performance of WAAM-deposited low-carbon steel. International Journal of Materials Research. https://doi.org/10.1515/ijmr-2024-0319

12. Akbarzadeh, E., Yurtışık, K., Gür, C. H., & et al. (2024). Influence of shielding gas on the microstructure and mechanical properties of duplex stainless steel in wire arc additive manufacturing. Metals and Materials International, 30(7), 1977–1996. https://doi.org/10.1007/s12540-023-01623-3

13. Marefat, F., Kapil, A., Banaee, S. A., Van Rymenant, P., & Sharma, A. (2023). Evaluating shielding gas-filler wire interaction in bi-metallic wire arc additive manufacturing (WAAM) of creep resistant steel-stainless steel for improved process stability and build quality. Journal of Manufacturing Processes, 88, 110–124. https://doi.org/10.1016/j.jmapro.2023.01.046

14. Yang, G., Deng, F., Zhou, S., Wu, B., Qin, L., & Zheng, J. (2022). Influence of shielding gas nitrogen content on the microstructure and mechanical properties of Cu-reinforced maraging steel fabricated by wire arc additive manufacturing. Materials Science and Engineering: A, 832, 142463. https://doi.org/10.1016/j.msea.2021.142463

15. Rodrigues, T. A., Duarte, V., Avila, J. A., Dias, M. R., Santos, T. G., & Oliveira, J. P. (2019). Wire and arc additive manufacturing of HSLA steel: Effect of thermal cycles on microstructure and mechanical properties. Additive Manufacturing, 27, 440–450. https://doi.org/10.1016/j.addma.2019.03.029

Received 15.04.2026
Accepted 24.04.2026
Published 07.05.2026

УДК 621.791.75:621.7.01

ВПЛИВ ОКИСЛЮВАЛЬНОЇ ДІЇ ЗАХИСНОГО ГАЗУ НА ГЕОМЕТРІЮ ТА ЕНЕРГЕТИКУ ДУГОВОГО 3D-ДРУКУ ВИСОКОМІЦНОЮ СТАЛЛЮ

Денис Молочков — доктор філософії, старший викладач кафедри інтегрованих технологій електронних засобів Національного університету «Запорізька політехніка», м. Запоріжжя, Україна *e-mail: molochkov@zp.edu.ua*, ORCID: 0000-0002-9030-5371

Кирило Красносельський — аспірант кафедри інтегрованих технологій зварювання та моделювання конструкцій Національного університету «Запорізька політехніка», м. Запоріжжя, Україна, *e-mail: kvkras@gmail.com*, ORCID: 0009-0006-5251-9076

Мета роботи. *Встановлення закономірностей впливу концентрації вуглекислого газу (0–100 % CO_2) у захисній суміші з аргоном на зовнішню макрогеометрію (ширину, висоту, хвилястість) та енергетичні показники процесу формування тонкостінних структур з низьким тепловкладенням із високоміцної низьколегованої сталі (HSLA) MoNiVa з використанням роботизованого адитивного виробництва за технологією CMT (Cold Metal Transfer).*

Методи дослідження. *Дослідження проводились із застосуванням роботизованого комплексу з джерелом живлення Fronius TPSi (режим CMT, швидкість подачі дроту 2,0 м/хв, швидкість зварювання 35 см/хв). Для усунення суб'єктивних похибок та аналізу стохастичної макрогеометрії розроблено метод комп'ютерного зору (OpenCV) на основі попіксельного інтегрування оптичних сканів (600 DPI, абсолютна похибка 0,045 мм). Синхронізація геометричних метрик з високочастотним (10 Гц) логуванням енергетичних параметрів дуги дозволила оцінити питому об'ємну енергію (VED).*

Отримані результати. *Під час тонкостінного наплавлення виявлено фундаментальний масштабний ефект. Використання моногазів виявилося технологічно недоцільним: 100% аргон провокує сильну внутрішню пористість через високу в'язкість розплаву та його швидке твердіння, тоді як 100 % CO_2 спричиняє просторове меандрування, гідродинамічний колапс та катастрофічну втрату 45 % площі поперечного перерізу. Визначено зону надвисокої технологічної стабільності в строгому діапазоні 5–18 % CO_2, де коефіцієнт варіації (CV) ширини досягає мінімуму (1,30–1,87 %) при збереженні пропорційного форм-фактора валика.*

DOI 10.15588/1607-6885-2026-2-10

Наукова новизна. *Вперше формалізовано термогідродинамічний «масштабний ефект» у WAAM-технології для складних HSLA сталей. Доведено, що в умовах низького тепловкладення додавання активного газу не покращує змочування, а навпаки, провокує швидку кристалізацію та утворення оксидних бар'єрів. Математично доведено «енергетичний парадокс» процесу: незважаючи на те, що режим 100 % CO_2 має найнижче лінійне тепловкладення (205,5 Дж/мм) завдяки синергетичному придушенню струму, він потребує найвищої питомої об'ємної енергії (2,09 кДж/см³) через критичне погіршення масопереносу.*

Практична цінність. *Виявлене технологічне вікно (5–18 % CO_2) та формалізований енергетичний баланс для тонкостінних структур зі сталі MoNiVa слугують готовим фундаментом для мінімізації геометричних дефектів та максимізації енергоефективності на виробництві. Розроблений алгоритм машинного зору придатний для імплементації в системи керування WAAM із замкненим контуром для предиктивного коригування параметрів у режимі реального часу.*

Ключові слова: *дротове дугове адитивне виробництво, WAAM, холодне перенесення металу, CMT, високоміцна сталь, MoNiVa; захисний газ, питома об'ємна енергія, комп'ютерний зір.*

Список літератури

1. Zhang, H., Li, R., Liu, J., Wang, K., Qiu, W., Shi, L., & et al. (2024). State-of-art review on the process-structure-properties-performance linkage in wire arc additive manufacturing. Virtual and Physical Prototyping, 19(1), e2390495. https://doi.org/10.1080/17452759.2024.2390495

2. Jafari, D., Vaneker, T. H. J., & Gibson, I. (2021). Wire and arc additive manufacturing: Opportunities and challenges to control the quality and accuracy of manufactured parts. Materials & Design, 202, 109471. https://doi.org/10.1016/j.matdes.2021.109471

3. Wang, Y., & Tsai, H. L. (2001). Effects of surface active elements on weld pool fluid flow and weld penetration in gas metal arc welding. Metallurgical and Materials Transactions B, 32, 501–515. https://doi.org/10.1007/s11663-001-0035-5

4. Lu, S., Fujii, H., & Nogi, K. (2004). Marangoni convection and weld shape variations in Ar-O_2 and Ar-CO_2 shielded GTA welding. Materials Science and Engineering: A, 380(1–2), 290–297. https://doi.org/10.1016/j.msea.2004.05.057

5. Wu, F., Falch, K. V., Guo, D., English, P., Drakopoulos, M., & Mirihanage, W. (2020). Time evolved force domination in arc weld pools. Materials & Design, 190, 108534. https://doi.org/10.1016/j.matdes.2020.108534

6. Cunningham, C. R., Flynn, J. M., Shokrani, A., Dhokia, V., & Newman, S. T. (2018). Strategies and processes for high quality wire arc additive manufacturing. Additive Manufacturing, 22, 672–686. https://doi.org/10.1016/j.addma.2018.06.020

7. Kah, P., & Martikainen, J. (2013). Influence of shielding gases in the welding of metals. The International Journal of Advanced Manufacturing Technology, 64 (9–12), 1411–1421. https://doi.org/10.1007/s00170-012-4111-6

8. Teixeira, F. R., Jorge, V. L., Scotti, F. M., Siewert, E., & Scotti, A. (2024). A methodology for shielding-gas selection in wire arc additive manufacturing with stainless steel. Materials, 17(13), 3328. https://doi.org/10.3390/ma17133328

9. Silwal, B., Pudasaini, N., Roy, S., Murphy, A. B., Nycz, A., & Noakes, M. W. (2022). Altering the supply of shielding gases to fabricate distinct geometry in GMA additive manufacturing. Applied Sciences, 12(7), 3679. https://doi.org/10.3390/app12073679

10. Yamaguchi, M., Komata, R., Furumoto, T., Abe, S., & et al. (2022). Influence of metal transfer behavior under Ar and CO_2 shielding gases on geometry and surface roughness of single and multilayer structures in GMAW-based wire arc additive manufacturing of mild steel. The International Journal of Advanced Manufacturing Technology. https://doi.org/10.1007/s00170-021-08231-8

11. Kanishka, K., Acherjee, B., & et al. (2025). A study on the effect of shielding gases on the GMAW-WAAM process and performance of WAAM-deposited low-carbon steel. International Journal of Materials Research. https://doi.org/10.1515/ijmr-2024-0319

12. Akbarzadeh, E., Yurtışık, K., Gür, C. H., & et al. (2024). Influence of shielding gas on the microstructure and mechanical properties of duplex stainless steel in wire arc additive manufacturing. Metals and Materials International, 30(7), 1977–1996. https://doi.org/10.1007/s12540-023-01623-3

13. Marefat, F., Kapil, A., Banaee, S. A., Van Rymenant, P., & Sharma, A. (2023). Evaluating shielding gas-filler wire interaction in bi-metallic wire arc additive manufacturing (WAAM) of creep resistant steel-stainless steel for improved process stability and build quality. Journal of Manufacturing Processes, 88, 110–124. https://doi.org/10.1016/j.jmapro.2023.01.046

14. Yang, G., Deng, F., Zhou, S., Wu, B., Qin, L., & Zheng, J. (2022). Influence of shielding gas nitrogen content on the microstructure and mechanical properties of Cu-reinforced maraging steel fabricated by wire arc additive manufacturing. Materials Science and Engineering: A, 832, 142463. https://doi.org/10.1016/j.msea.2021.142463

15. Rodrigues, T. A., Duarte, V., Avila, J. A., Dias, M. R., Santos, T. G., & Oliveira, J. P. (2019). Wire and arc additive manufacturing of HSLA steel: Effect of thermal cycles on microstructure and mechanical properties. Additive Manufacturing, 27, 440–450. https://doi.org/10.1016/j.addma.2019.03.029

DOI 10.15588/1607-6885-2026-2-10

Наукове видання

Нові матеріали і технології в металургії та машинобудуванні № 2/2026

Науковий журнал

Оригінал-макет підготовлено у редакційно-видавничому відділі НУ «Запорізька політехніка»

Комп'ютерний дизайн та верстання: Наталія Савчук

Реєстрація суб'єкта у сфері друкованих медіа:
Рішення Національної ради України з питань телебачення і радіомовлення
№ 3040 від 07.11.2024 року
Ідентифікатор медіа: R30-05583

Підписано до друку 29.04.2026. Формат 60×84/8
Папір офс. ризогр. Ум. др. арк. 11,2
Тираж 300 прим. Зам. № 307

69011, м. Запоріжжя, НУ «Запорізька політехніка», друкарня, вул. Університетська, 64

Свідоцтво суб'єкта видавничої справи
ДК № 6952 від 22.10.2019